Ph.D. Thesis

Investigations on the effect of excitonic confinement on nanomagnetic materials and studies on the optical properties of ferrofluids
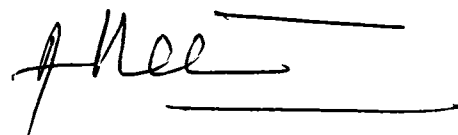
Thesis submitted to

COCHIN UNIVERSITY OF SCIENCE AND TECHNOLOGY
In the partial fulfillment of the requirements for the award of
the degree of
DOCTOR OF PHILOSOPHY

by
Swapna.S.Nair

Department of Physics
Cochin University of Science & Technology
Cochin – 686 022. India
May 2006.

CERTIFICATE

Certified that the thesis entitled *"Investigations on the effect of excitonic confinement on nanomagnetic materials and studies on the optical properties of ferrofluids"* is based on the bonafide research work carried out by Ms Swapna. S. Nair under my guidance, at the Physics Department, Cochin University of Science & Technology, Cochin – 682 022, and has not been included in any other thesis submitted previously for the award of any degree.

Dr. M. R. Anantharaman
(Supervising Guide)
Department of Physics
Cochin University of Science and Technology
Cochin-22

DECLARATION

I hereby declare that the work presented in this thesis entitled *"Investigations on the effect of excitonic confinement on nanomagnetic materials and studies on the optical properties of ferrofluids"* is based on the original research work carried out by me under the guidance and supervision of Dr. M. R. Anantharaman, Sr. Lecturer, Department of Physics, Cochin University of Science & Technology, Cochin-682 022 and has never been included in any other thesis submitted previously for the award of any degree.

Swapna. S. Nair

Cochin - 22
29-05-2006

Acknowledgements

"Reality is merely an illusion, albeit a very persistent one"-Albert Einstein

Preface

Four technologies are going to rule the world in the 21st century of which the first three are biotechnology, technology of photonics and genetic engineering which had shocked the world with their new findings in the late 90's itself and showing their potential in day to day human life. Nanotechnology is the fourth one which has the additional advantage of being interdisciplinary to the first three. Nanotechnology deals with the phenomena and structures that can only occur at the nanometer scale which is the scale to represent single atoms/molecules. Hence it can be defined as the synthesis and engineering of materials near the molecular level. Nanometric scale is used to specify materials at a size range 1 to 100nm where unique phenomena is found to be exhibited which enables novel applications. The related term nanoscience which is an extension of 'materials science' is used to describe the interdisciplinary fields of science devoted to the study of nanoscale phenomena employed in nanotechnology consisting of processing, separation, consolidation and deformation of materials and induced property change at the molecular level.

The first mention of some of the distinguishing concepts in nanotechnology was by Richard Feynman in a lecture at an APS meeting in 1959 which started with a sentence "there is plenty of room at the bottom". He described a method by which one can manipulate individual atoms and molecules in which he also talked about the role of surface in determining the bulk behavior.

Magnetic nanomaterials have become the topic of interest nowadays due to its unique application potential in versatile fields including high density storage media, magneto-optical display devices etc, due to their very high surface area. Diluted magnetic semiconductors are another promising area which has great application potential. Nanograined magnetic materials show many peculiar properties like single domain nature, superparamagnetism, spin polarized tunneling etc, which can open a new era in spin modulated electronics (spintronics). Also these ultra fine magnetic materials have potential bio-medical application including in targeted drug delivery, hyperthermia etc

due to their additional advantage of being functionalized and targeted by the application of external magnetic fields.

Also when the grain size of these nanostructures approaches Bohr radius of the materials, their band structure gets modified to a great extend giving their optical properties remarkably different from their bulk cousins. Metals if synthesized in the ultrafine regime are no more metals! They are semiconductors. Magnetic oxides which are semiconductors optically whose bandgap varies from 2.1 eV to 2.2 eV in the bulk, can be modified to a great extent if they could be synthesized with in the Bohr radius limit due to quantum confinement effects. Thus tailoring the grain size can ensure fine tuning of the magnetic and optical properties which can enhance their application potential.

The important properties that make the nanoscaled magnetic materials important from the fundamental point of view is the remarkable changes in the structural, morphological, chemical, optical and magnetic properties at the nanometric regime when compared to their bulk counter parts. Magnetic nanomaterials, especially the magnetite derivatives are thus ideal templates to study the optics, magneto-optics and magnetism at the nanolevel. Here a system of non interacting ultra fine magnetic grains are synthesized with in the confinement regime and they were characterized magnetically and optically by different procedures and their confinement effects have been studied in detail. Also their magneto-optical properties were discussed and the deviation from the non-interacting system observed in the case of concentrated systems has been studied.

Here two different templates have been chosen to study the non-interacting magnetic nanosystems, nanomagnetic composite and ferrofluids. Nanocomposites can be defined as materials consisting of a host matrix with noninteracting well separated individual nanograins as the guest substance whose dimension are of less than 100 nm. Magnetic nanocomposites have gained great interest in recent years as they possess both the magnetic properties of the inorganic component and the mechanical and physical properties of the nonmagnetic matrix. It is possible to observe quantum size effects in the magnetic and optical properties when the size is limited to 10 nm or less than that. These

materials find applications in magnetic refrigeration, ferrofluids, colour imaging magnetic recording and sensors. If these composites can be made transparent, they can be potential for magneto optical storages.

Initially magnetic nanoparticles with in the size limit 10 nm have been synthesized inside natural pores of polystyrene by chemical methods to obtain magnetic nanocomposites. Ion exchange process is adopted for the synthesis of ultra fine grains of maghemite with 'strong sulphonated polystyrene ion exchange resin' was used as the polymer template. Repetition of ion exchange process can provide better magnetization yield. Also doping of cobalt could be carried out inside the vacancies of the maghemite lattice sites with a view to enhancing the coercivity as cobalt is a material with an inherent magneto crystalline anisotropy which can enhance the coercivity. The effect of grain size on the magnetic properties could be investigated using this template. Also magnetic metal nanoparticles are encapsulated inside the polymer network by a modified reduction process.

Also due to the ultra fine nature of the magnetic particles inside the polymer network, their optical properties could be modified due to the grain size dependant modification of energy bands and quantum confinement which results in a blue shift in the energy band gap. This can result in an enhanced transparency for this system which can find application potential. More over the quantum confinement and grain size dependant blue shift was investigated in semiconductors like CdS, CdSe and CdTe while such an investigation was never attempted in magnetic nanosytems and synthesis of a near transparent magnetic material by this method thus assumes great significance.

Ferrofluids which are the stable colloidal suspension of nanomagnetic materials inside a suitable base fluid are an ideal template to study a system of non-interacting magnetic particles. Also by tuning the concentration of this system, the effect of interaction also could be studied. Hence magnetite and doped magnetite ferrofluids in organic careers was selected as the system under study. The suspended fine magnetic grains make the fluid an interesting system optically as well and tuning of these optical signals with the application of an external magnetic field open a vast field of

investigations -- magneto-optics. Ferrofluids are magnetically polarized random media in which the particles can have individual Neel rotation and hence large magneto-optical signals can be expected. Also deviation from sphericity and diluted system can affect the magneto-optical signal very much which could be investigated by the HEBM induced effects.

Also optically they are ideal system as the grain size approaches the Bohr radius limits, high quantum confinement and induced blue shift can make them optically more transparent and this confined excitons can assist in non linear absorptions. Also as a random media, this can offer induced scattering which can make them good optical limiters owing to their high shelf life and stability against agglomeration.

Thus the thesis has two parts, one deals with the magnetic nanocomposites, their magnetic and optical properties while the latter part describes the structural, morphological, magnetic, optical, dielectric, magneto-optical, and nonlinear optical properties of ferrofluids with varying composition. The thesis is divided into 11 chapters.

Chapter 1 gives an introduction about nanoscience and nanotechnology with emphasis being given to the magnetic nanostructures, their synthesis techniques, properties, anomaly at the nanolevel etc. Magnetic nanocomposites and ferrofluids are introduced with necessary details and Physics governing their properties is also discussed.

Theoretical concepts necessary to understand the present investigation including the theory behind optical properties, band theory, confinement effects, non linear optical properties and magnetic properties are provided in ***Chapter 2***. Also the theory of magneto-optics is provided in this chapter.

In ***Chapter 3*** the experimental procedures adopted for the synthesis and characterization of the magnetic nanocomposites and ferrofluids have been dealt in detail. Schematic of the experimental set-ups and description of the experimental procedures are provided in this chapter. Also brief theory of the working with necessary equation is also given.

Chapter 4 deals with the synthesis and characterization of chemically synthesized maghemite-polystyrene magnetic nanocomposite. This chapter has two parts of which the first part deals with the magnetic properties of the composites. Here effect of cobalt doping on the magnetic properties of the nanocomposite is described. In the second session grain size dependant optical confinement effects noted for this system has been reported with the necessary theory towards its explanation. Novelty of the results is noted.

The synthesis and characterization of elementary metal based magnetic nanocomposite is given *chapter 5.* Here the importance of this work and the method adopted for the synthesis is explained and the novelty of the synthesis procedure is explained.

The results, and discussions of the experiments that have been carried out starts with *Chapter 6.* Chapter 6 describes the structural and magnetic properties of the fine magnetic precursors for the ferrofluids. Magnetite, nickel doped, zinc doped as well as manganese doped magnetite are the magnetic fine particles under study and the results obtained are discussed in detail.

Chapter 7 deals with the magneto-optical characterization of ferrofluids synthesized by chemical methods. Magnetic field induced light transmission, linear dichroism, linear birefringence, Faraday rotation and Faraday ellipticity have been measured using magneto-optical null ellipsometer set ups and the results obtained are explained with necessary theory. Also the effect of interaction of suspended grains in the concentrated system has been explained. Effect of attrition on the magneto-optical signals are also investigated and explained with theory. Also the deduction of magnetic diameter, anisotropy constant etc from the magneto-optical measurements have been explained in detail. Novel results in this study have been concluded.

Dielectric characterization of ferrofluids and their magnetic field dependence is discussed in *chapter 8.* Effect of carrier, concentration, and composition are discussed. The enhancement of capacitance in presence of applied field is explained. Also permittivity and permeability in the X band has also been provided in this chapter.

Chapter 9 gives the optical characterization of ferrofluids, in which the observed blue shift is explained in terms of quantum confinement effects and the effect of nickel alloying in blue shift is discussed and the results are fitted for excitonic confinement in the weak confinement regime. The novelty of this work has been explained.

Nonlinear optical characterization of ferrofluids is provided in *Chapter 10*. The sample is analyzed by Z scan technique and the non-linear optical property of ferrofluids are assured beyond doubt and the wavelength, fluence, concentration and composition dependence has been studied. The sample shows nice limiting comparable to the limiting observed in the fullerence based optical limiters. The experiment is repeated in Femtosecond excitations too and the obtained results are analyzed and fitted for necessary theory.

Finally in *chapter 11* results obtained in this part of work with deductions are concluded with the novelty of results poiñted out. Also the application potential of the obtained results are discussed with scope for further work in this field.

Contents

CHAPTER 1

Introduction

It is well known that nanoscience and nanotechnology is the science and technology of ultrafine particles. Particles when reduced to nanometric dimensions display novel and superlative physical, chemical, electrical, optical and magnetic properties with respect to their coarser sized cousins. At these dimensions the surface area becomes very large and the ratio of surface to bulk atoms dictates the properties of the material. Grains, grain size, intergranular interaction, quantum magnetization, quantum tunneling, superparamagnetism are some of the various phenomena exhibited by particles at the nanodimension. So manipulation of properties means the understanding of these phenomena for tailoring the properties. With the emergence of nanotechnology, newer applications of these materials are conceived and are realized as products soon.

At the same time many phenomenon are not clearly understood and exclusive investigations are to be carried out.

Magnetism and magnetic materials is an area where large scope for such an activity exists. Moreover nanomagnetic materials are going to play a dominant role in the day-today life of human beings. The birth of new class of materials like diluted magnetic semiconductors (DMS), spin valve transistors, giant magneto resistive (GMR) materials, ferrofluids, giant magneto caloric materials (GMC), are all indication of these. Thus study on magnetic nanocomposites and nanomagnetic materials assumes significance and is very relevant in understanding various phenomena. This chapter provides an introduction to the various phenomena of nanomagnetism and spells out the motivation of the present work and its objectives.

1. Nanotechnology-An overview

Nanotechnology is known as the technology of the 21st century which deals with the synthesis and study of ultra fine materials and their employment in technology for various applications. It can be defined as the synthesis and engineering at the molecular level for possible device applications where nanoscience deals with the investigations of phenomena and properties exhibited by materials at the nanolevel.

The demand for smaller materials for high density storage media is the fundamental motivation for the fabrication of nanoscale magnetic materials. The idea of nanoscale molecular device is not entirely new, and has been around since days immemorial. Richard Feynmann, who addressed the issue of quantum mechanical computers once opined "at any rate, it seems that the laws of physics present no barrier to reducing the size of computers until bits are the size of atoms, and quantum behaviour holds dominant sway" – a task, considering the small size that is necessary for realizing such device.

The ultimate motive in nanotechnology is to manipulate and control the individual atoms and thereby, the programmed formation of the superstructures. However, such a definition may be extended to the organization of objects having nano-dimension such as molecules/biomacromolecules and other nanoscale matters such as quantum dots, buckyballs (also known as fullerenes) and nanotubes [1,2]

Materials consisting of particles with diameter less than 100 nm have attracted a great deal of recent research attention. Owing to their ultrafineness in size and very high surface area, these particles possess dramatic changes in physical and chemical properties as compared to their bulk counterparts which makes them ideal templates to study the physics at the nanolevel from a fundamental point of view in addition to the vast application potential in versatile fields [3,4].

Nanoparticles behave quite different from their coarser-grained counterparts of the same composition due to the high surface to volume ratio. The more loosely bound surface atoms constitute a significant fraction of the sample and their properties influence its behaviour. For example, the melting point of gold is dramatically reduced when the particle diameter drops below 5nm. Improvements can be made in the mechanical and magnetic properties of materials.

At sufficiently small domain sizes, the particle roughness increases and becomes comparable to the radius of curvature, in the case of a spherical particle. This reduces the strength of the bonding to adjacent atoms and often results in surface atoms with increased reactivity. The abundance of particle edges and corners can create non-equivalent reactive sites on a single particle.

Their magnetic and optical properties will be profoundly modified. Smaller grained magnetic materials exist as single domain because of the energy considerations. Ferro/ferrimagnetism is reduced and below a critical diameter the materials exist as

superparamagnetic. Optical properties are modified because of the quantum size effects on the band structure. Optical energy Bandgap is blue shifted for ultra fine materials. Nano sized gold is green in colour which is a semiconductor while bulk is a noble yellow metal!. We can make junctions with the same materials with different grain sizes due to the modified band structures of these ultra fine particles. This gives scope for a variety of applications in the semiconductor industry.

1.1 Particles at the nanolevel

The physical and chemical properties of materials with their grain size approaching molecular dimensions are of great fundamental interest. Hence they became hot topic of intensive research. Nanoparticles display novel physical properties resulting from surface effects. The enhancement of the magnetization per atom and decrease in the blocking temperature from the bulk values is induced by the controlled size in a superparamagnetic nanoparticle. There has been a great deal of interest in the optical and magnetic properties of ultra fine particles in recent years.

The optical properties of materials change abruptly when the grain size becomes comparable to the Bohr radius of electron-hole pairs (excitons), quantization effects can be observed due to the quantum confinement of charge carriers in the finite volume of the particles which becomes very large when the size approaches the Bohr radius limits. Interesting and novel optical properties have been observed in the case of gold and silver when their sizes are reduced to nanodimensions.

1.2 Quantum wells, quantum wires and quantum dots

When one of the dimensions in a crystal are made smaller so as to reach the nanoscale (a few nanometer), electrons and holes can be confined in space in along that direction as compared to their motion in a bulk crystal, which is equivalent to the reduction of one of the degree of freedom for the electrons/hole/quasi particles. These states can be termed as quantum well like states.

In quantum wires, two of the dimensions are cut off. Materials could be made into the nanowires in which one of the degrees of freedom is retained for the charge carriers electrons and holes. Hence the diameter of the nanometer is few tens of nanometers. Hence confinement is stronger as there is only one degree of freedom.

In a quantum dot, the crystal is miniaturized in all the three dimensions to a few nanometers. The greatest difference between a quantum dot as compared with a bulk crystal, quantum well and quantum wire is that Coulomb energy contribution to the ground state energy is non zero where as for quantum well and quantum wires, electrons are free and coulomb energy contribution tends to zero. A detailed discussion on the theoretical aspects of these materials is provided in Chapter 2.

1.3 General Methods of Synthesis

Synthesis of nanomaterials and fabrication of nanodevices is one of the major active areas of current interests in nanotechnology. The two major approaches currently being used for the generation of nanoscaled materials, viz. the "top down" ("engineering down") and "bottom up" ("engineering up") methods.

a)   Top Down Method

In the top down method, ultra fine particles are prepared from their bulk cousins by a continuous grinding process.   This is the traditional way of synthesis of nanoparticles from their bulk counterparts which in turn is synthesized by ceramic techniques. Generally, a "two roll mill" is employed for the reduction of grain size of the powder specimens. Nowadays, high energy ball milling (HEBM) is employed for attrition which can impart high momentum to the milled powders through the high speed rotation and revolution of the vials which helps in obtaining high efficiency in low milling times. Thin films consisting of nanograins could be synthesized from bulk materials by a variety of other techniques like vacuum evaporation, RF sputtering, pulsed laser ablation etc.

b)   Bottom Up Process

It is the ideal and the most commonly employed method for the synthesis of nanoparticles. In this method, nanomaterials are grown slowly from the atomic scale mostly by chemical methods in which careful control of the preparation parameters like pH and temperature is utilised to tune the grain size in a favourable way. Chemical co-precipitation and sol-gel techniques are used for the synthesis of ultra fine powder particles. There are several techniques for the growth of ultra fine grains on a substrate by atom by atom deposition. They include physical and chemical methods. For the synthesis

of fine grained thin films, processes like chemical vapor deposition, chemical bath deposition, spray pyrrolysis, Sol-gel dip coating are also employed.

Out of these two techniques, bottom up process is advantageous for the synthesis of ultra fine powder sample as it provide atom by atom growth there by reducing the surface imperfections and strain that could be imparted in the milling process and careful control of the preparation conditions could ensure systematic tuning of the grain size and other characteristics of these powder particles. Top down process like PLD and RF sputtering are routinely made use of for thin film fabrication.

1.4 General Synthesis Techniques.

There are a variety of experimental techniques for the synthesis of ultra fine magnetic particles. All these techniques need complete control over the reaction parameters.

The first technique involves the preparation of isolated particles. However ultra fine crystallites having uncontaminated free surfaces followed by a consolidation process either at room or at elevated temperatures. The specific processes used to isolate the nanostructured materials are for example, inert gas condensation, decomposition of starting chemicals and precipitation from the solutions.

1. Chemical vapour deposition (CVD), Physical vapor deposition (PVD) and some electrochemical methods have been used to deposit atoms or molecules of desired materials on suitable substrates. Nanocomposites of these materials could be synthesized in thin film form by consecutive coating of chemically different materials.

2. By introducing defects in a formerly perfect crystal another class of materials could be synthesized. This can be effected by processes like HEBM, and ion irradiation which shatters the bigger crystal.

3. The most efficient method of fine particle synthesis is the chemical co-precipitation from super saturated solutions by careful control of reaction conditions.

4. Another method being employed currently for the synthesis of metal/semi conductor oxides which is the sol-gel process in which the samples are taken in the required molar ratio and it is made into a gel and finally ignited at a higher temperature to yield nanostructured fine particles.

Of these different methods for the synthesis of nanostructured materials, inert gas condensation, physical vapour deposition, High energy ball milling and ion irradiation can be included in the physical methods for the synthesis of materials.

Chemical methods include, chemical vapour deposition, chemical bath deposition, (for thin film fabrication) chemical co-precipitation, sol-gel (for nanoparticle and composite synthesis) etc

Synthesis of metal nanoparticles comes under a separate category as the preparation process is quite tedious with more chances of contamination so that the additional provision should be given to passivate these explodingly reactive surfaces.

1.4.1. Chemical Methods

Chemical methods are the most widely employed technique [5] for the synthesis of nanostructured materials owing to the versatility in design, its economic nature and its capability for tailoring the properties by carefully controlling the grain growth as it offers mixing at the nanolevel. A basic understanding of the principles of crystal chemistry, thermodynamics, phase equilibriums, phase changes and reaction kinetics is necessary to take advantage of several benefits the chemical process offer.

The grain size and size distribution, the physical properties such as crystallinity and crystal structure, and the degree of dispersion can be affected by the reaction kinetics, pH, reaction temperature, concentration of reactions, molarity and its ratio and several other factors. There can be other factors like agglomeration of individual grains that make them unidentifiable from their bulk counter parts. There are chances of getting non stoichiometric undesired components precipitated along with the desired final product because of the slow reaction dynamics and nucleation. Hence other measures like size control, surface modification and capping are to be adopted to modify these processes.

1.4.2 Size control

Control of both grain size and grain size distribution becomes important in the synthesis of nanomaterials. The grain size could be controlled by varying the synthesis parameters like concentration, choice of reactants, temperature, pH etc. Choice of templates with natural pores for the synthesis of nanoparticles is also in use. *Insitu* surface modification using stabilizers such as thiols, phosphates, and polymers prevents further grain growth. [5-10].

6

1.4.3 Grain size distribution

The control of grain size distribution is quite important in the synthesis of nanoparticles. To narrow the size distribution, exclusion chromatography and capillary zone electrophorosis are employed [10]. These are based on the principle of charge to size ratio is different for different grain sizes. Filtration through molecular sieves of different mesh size is also used for getting the size distribution narrower.

1.4.4 Size quantization effects

Quantization in ultra fine particles originates from the confinement of charge carriers in semiconductors with potential wells of narrow dimensions less than the De-Broglie wavelength of electron and holes. Confinements could be mere electronic, excitonic or polaronic based on the grain size and excitation energy [11]. Under these conditions, the energy bands of electrons and holes becomes close to discrete energy levels as of in atom and thus a semiconductor becomes atom like. In addition to the large change in electronic/optical properties, they also exhibit change in the effective redox potentials of photo-generated carriers.

Size quantization effects on the optical properties of semiconductors are extensively studied [12-16]. In CdS nanocrystals, a blue shift in energy band gap of 1.54 eV is obtained for a particle with radius 1nm. Blue shift is observed for many other semiconductors because of the quantum confinement effects. Trapping of charge carriers is possible for the nanostructured materials [17-22]

1.4.5 Optical Properties

Optical properties of ultra fine particles are profoundly modified by the grain size dependant confinement effects. In the ultra fine regime, due to very small wave function overlapping, the energy levels tends to be discrete and when the grain sizes are reduced to the order of exciton Bohr radius limit of the material, they are near molecule like materials and hence the energy levels tend to be discrete and thus there is confinement of carriers. This will alter the band gap towards the high energy limits which can be as high as 3 eV in a 5Å particle! Thus by manipulating grain sizes, materials with same chemical formulae but different band gaps can be synthesized. The influence of grain size vis a vis quantum confinement have been investigated extensively [23-25]

1.4.6 Nonlinear optical properties

Semiconductor nanoparticles are investigated because of their excellent non linear optical properties by many researchers [26-28]. In the linear regime, photoinduced blue shift in absorption edge is observed, which causes transient bleaching in nonlinear regime [29]. Third harmonic generation, and free carrier absorption are also observed in semiconductor nanoparticles especially in CdS nanoclusters [30]. Due to near molecule like energy levels, they show strong Saturable Absorption (SA), Reverse Saturable Absorption (RSA) and multi photon absorption.

1.4.7 Surface modification of nanoparticles

Due to the high surface to volume ratio and these nanoparticles possess surfaces which are explodingly reactive. This makes it necessary that the surface of the nanoparticles should be capped properly to prevent explosive reactions and grain growth. Surface modification can be classified in to three.

1. *Deposition of metals on the nanoparticles*

Metals are deposited on synthesized nanoparticles by variety of techniques. By this the selectivity and efficiency of a photoelectrochemical reaction could be greatly enhanced by surface modification of these nanoparticles. Gold and platinum are the commonly used surface modifying metals because of their very low reactivity at the surface. Platinisation could be done by the direct photoreduction of $PtCl_6$ on the nanoparticles [31,32] or by stirring the nanoparticles by platinum colloids [33-35]. Gold layer coating could be done by employing similar techniques. Mostly this is meant for the improvement of the photocatalytic properties of the synthesized nanoparticles in addition to the protection provided by the noble metal layer to the surface.

2. *Capping with organic/inorganic molecules*

Nanoparticles could be capped most effectively using insitu capping of organic/inorganic materials on the surface of each and every particles. Thiols have been extensively used for capping the materials [36-37]. Nowadays polymers like PVPA, Polypyrrole etc have been used for the capping of materials [38-44] which provides surface passivation and modifies the electronic and optical properties because of the

presence of a thin capping layer which provides necessary electric field to act as confinement potential.

3. Surface modification with sensitizing dyes

By the surface modification of materials using sensitizing dyes, the optical response could be tuned to the low energy regime. While surface modification using metals and organic molecules provides improved catalytic/dielectric properties, this enhances optical properties of the materials in general [45-47]. The process of charge injection from the excited state into the conduction band of the semiconductor has been studied with respect to the photoresponse of large band gap semiconductor which has applications in imaging science and solar energy conversion. Erythrosine B, Eosin, Rose Bangal, Rhodomines, methlene Blue etc have been used for the surface modification.

Since the focus of this thesis is nanomagnetism and nanomagnetic materials, some of the very relevant aspects of magnetism and magnetic materials will be discussed in the ensuing sections.

1.5 Nano magnetic materials

The emergence of nanotechnology has given rise to a new class of materials called nanomagnetic materials and this is as important as semiconducting materials. Magnetic nanomaterials are important both from the fundamental as well as application point of view. From a fundamental point of view, nanomaterials, especially, magnetic nanomaterials exhibit superlative properties with respect to their, structural, magnetic, electrical, optical and magneto-optical properties as compared to their coarser sized cousins. For example magnetic materials at reduced dimensions exhibits quantum magnetization, single domain characteristics, superparamagnetism, and spin polarized tunneling. These quantum mechanical phenomenon are wisely exploited to increase the density of bit storage, make spintronics a reality, make CMR sensors for data accessing etc. A more detailed discussion of the anomaly in exhibited properties for ultra fine articles is provided in Chapter2.

Magnetism and magnetic materials find applications in almost all realms of human life. They play a vital role in making life more sophisticated and humane. The most important use of magnets in the home is the electric motors. All electric motors use

electromagnets. These motors run refrigerators, vacuum cleaners, washing machines, compact disc players, blenders, drills, race cars etc. Audiotape and videotape players have electromagnets called *heads* that record and read information on tapes covered with tiny magnetic particles. Magnets in speakers transform the signal into a sound by making the speakers vibrate. An electromagnet called a deflection yoke in TV picture tubes helps form images on a screen. [48-54].

The magnets used in the industry and business are mostly electromagnetically powered devices, such as cranes, cutters, fax machines, computers etc. Generators in power plants rely on magnets like the ones found in electric motors to produce electricity. Transformers are devices that use electromagnetics to change high-voltage electricity to low-voltage electricity needed in homes and businesses. In transportation, systems that use electromagnetics are trains, subways, trolleys, monorails, escalators, elevators etc. Scientists and engineers have developed trains that use electromagnetism to float it above the track by the principle of magnetic levitation. It eliminates friction thereby attaining higher speeds over ordinary trains.

Another important magnetic material category which attracted recent research interest are dilute magnetic semiconductors. They are potential materials for magneto-optical devices. Ferromagnetic semiconductors are obtained by doping magnetic impurities into host semiconductors with out forming islands of magnetisation. They are key materials for spin electronics (spintronics) in which the correlation between the charge and spin of electron is used to bring about spin dependent electronic functionality such as GMR and spin field effect transistor [49]. Among such materials reported so far GaAs has a T_c of about 100K.

Magnetic nanocomposites find a host of other applications because of their remarkable properties. They are used as magnetic recording media, colour imaging, ferrofluids, catalysts etc. Magnetic nanocomposite consisting of iron oxide embedded in polymer matrices are found to be behaving like transparent magnets with remarkable electrical and optical properties. Flexible magnets or rubber ferrite magnets find applications in many devices because of their easy mouldability and microwave absorbing properties [55-56].

To understand the physics that dictates various properties of magnetic nanomaterials, it is necessary to have look into the basic concepts and theories regarding the origin of magnetism in a material from the classical as well as quantum approach.

1.6 Physical origin of Magnetism

To understand the anomalous magnetic behaviours exhibited by these magnetic fine particles, it is necessary to understand the basic theories of magnetism. It is recognized that [57] the magnetic behaviour of atoms, molecules and solids is related to the orbital and spin motion of the electrons. The magnetic dipole moment associated with an electron describing a circular orbit is related to the angular momentum of the electron as:

$$\mu = \frac{e}{2m} \qquad \text{(Angular momentum).} \qquad 1.1$$

All the known magnetic materials can be classified into the following classes depending on their electronic configurations and properties.

1) Diamagnetic
2) Paramagnetic
3) Ferromagnetic
4) Antiferromagnetic
5) Ferrimagnetic

If an atom or ion contains only paired electrons, the total magnetic moment is practically zero as a result of the nullifying effect of the added orbital and spin angular moments. Such materials for which the permeability is less than unity and the magnetic susceptibility is negative are called diamagnets. If the atom or ion contains one or more unpaired electrons and thus posses a permanent magnetic moment, the material can be either paramagnetic or ferromagnetic. If there is no interaction between the adjacent magnetic moments and, thus, they can interact independently with an external magnetic field, the materials are ideal paramagnets, for which the permeability is slightly greater than unity and the susceptibility has a slight positive value and varies inversely with the absolute temperature. If a strong interaction between adjacent magnetic moments tends to

align them parallel to one another, the materials are called ferromagnetic, for which the susceptibility values are very large, positive and the magnetic induction is approximately equal to the magnetization produced in the material. Above a certain critical temperature, called the Curie temperature or Curie-Point (T_c), ferromagnetic materials become paramagnetic and follow the so-called Curie Weiss Law:

$$\chi = \frac{C}{T - \theta} \qquad\qquad 1.2$$

Where C and θ are the Curie and Weiss constants respectively.

Under certain circumstances, the interaction between neighbouring magnetic moments may lead to an antiparallel alignment resulting in a vanishing resultant moment at zero Kelvin; such materials are called antiferromagnetic. Above a certain temperature called the Neel Temperature or Neel Point (T_n), antiferromagnetic materials become paramagnetic and follow the Curie –Weiss type relation:

$$\chi = \frac{C}{T + \theta_n} \qquad\qquad 1.3$$

Where θ_n is a constant.

For some materials, the antiferromagnetic alignment may lead to a non-vanishing resultant magnetic moment. These materials are called Ferrimagnetic and become paramagnetic above the ferrimagnetic Neel Temperature (T_{fn}).

1.7 Ferro magnetic Domains

To explain the appearance of a large magnetization in a Ferro magnet on the application of even a small magnetic field, Weiss introduced the concept of "domains". A ferromagnetic sample of macroscopic dimensions contains a number of small regions called domains. Within each domain, spontaneous magnetization exists, whose value depends on the temperature. The vector sum of magnetizations of the individual domains gives the overall spontaneous magnetization of the sample. 'domain walls', called the Bloch Walls, separate the different domains. The volume of the domains is critically of the order of 10^{-8} to $10^{-12} m^3$.

1.8 The Two-sub lattice Model

A simple antiferromagnet consists of two interpenetrating sub-lattices such that the atomic or ionic spins on one sub-lattice are aligned antiparallel to those on the other and the net magnetization is zero at the absolute zero of temperature. Ferrimagnetic materials are those, which exhibit spontaneous magnetization due to antiparallel alignment between two magnetic sub lattices. The principal reasons for the non-vanishing magnetization are:

a) The two sub lattices are occupied by different types and number of magnetic ions

b) The two sub-lattices correspond to two different crystallographic sites, which may be occupied either by the same type or different types and number of magnetic ions

1.9 Ferrites:

The most important ferromagnetic material known is magnetite which corresponds to the chemical formulae Fe_3O_4 or more specifically, $Fe^{2+}Fe_2^{3+}O_4$. When one replaces the divalent ferrous ion by another divalent metal such as Mn, Co, Ni, Cu, Mg, Zn, or Cd, one obtains a ferrite of the general composition $Me^{2+}Fe_2^{3+}O_4$, where Me^{2+} is the divalent metal ion. In mixed ferrites, a mixture of ions replaces the Fe^{2+} ion.

1.10.a The structure of ferrites

The physical properties of ferrites are intimately related to the structure of these solids. They belong to the large class of compounds, which have the spinel structure. The oxygen ions with a radius of 1.32 Å, forms to be a good approximation for a close-packed cubic structure. The unit cell contains 32 oxygen ions, 16 Fe^{3+} ions, and 8 divalent metal ions. The total of 24 metal ions, ranging in radius between 0.4 and 1Å, are in eight tetrahedral interstices surrounded by four O^{2-} ions and sixteen octahedral interstices, surrounded by six O^{2-} ions. The distribution of metal ions is very important for an understanding of the magnetic properties of these materials: the following distributions may occur.

1) In the 'normal' spinel structure of a ferrite, eight divalent metal ions occupy tetrahedral positions: the sixteen trivalent iron ions occupy octahedral positions Me^{2+} $[Fe_2^{3+}]O_4$. The brackets around the $Fe^{3+}]$ ions indicate that they occupy the octahedral sites.

2) In the 'inverse' spinel structure of a ferrite, the divalent Me^{2+} ions occupy octahedral sites: the Fe^{3+} ions are distributed equally over the tetrahedral and octahedral sites. The arrangement may thus be represented by
Fe^{3+} [$Me^{2+}Fe^{3+}$]O_4.

3) In the intermediate case we have arrangement of the type;
$Fe_x^{3+} Me_{1-x}^{2+}$ [$Me_x^{2+}Fe_{2-x}^{3+}$] O_4.

In the mixed ferrites obtained from normal and inverse spinels, it may become necessary to consider as many as 10 molecular field constants. However, in practice, consideration of only three molecular field constants is often sufficient, especially when the dominant interaction is that between the A and B sub lattices [58]. When interactions become comparable in magnitude, canting of spins, becomes energetically favourable.
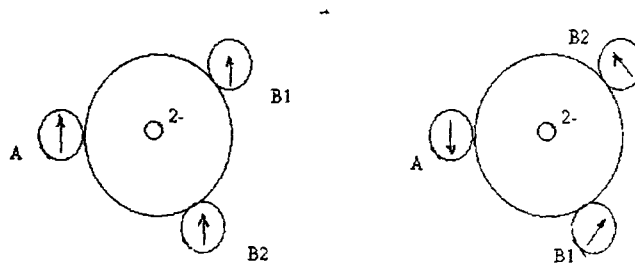
Fig.1a Exchange interactions as per "Two sub lattice model"

1.10.b Crystal Structure of Spinel ferrites

Ferrites having the spinel structure have the general formula MFe_2O_4 where M is a divalent metal. They resemble the structure of the naturally occurring mineral $MgAl_2O_4$. The oxygen anions have an fcc arrangement accommodating the smaller positive ions in the interstices. The available spaces are of two kinds. One is called tetrahedral or A site, because it is located at the centre of a tetrahedron whose corners are occupied by oxygen ions. The other is called octahedral or B sites, because the oxygen ions around it occupy the corners of an octahedron. In the mineral spinel Mg ion occupy the A site, known as tetrahedral site because it has four nearest oxygen neighbours. The B

site ions have six nearest oxygen ions (and the site is termed octahedral site) and the site is occupied by the Al ions.

The crystal structure is best described by subdividing the unit cell into 8 octants with edge a / 2 as shown in Fig.1.2. The location of oxygen ions and metal ions in every octant can be easily described. The oxygen ions are arranged in identical manner in all octants. Each octant contains four oxygen ions in the body diagonal and they lie at the corners of a tetrahedron. Positions of metal ions are different in the two octants sharing a face. In the case of octants sharing only an edge the location is the same. Hence a complete picture of the location of metal ions is obtained if position of ions is drawn in two adjacent octants is also shown in Fig 1.1b.

(a) Tetrahedral A site   (b) Octahedral B site

• Metal ion in tetrahedral site

• Metal ion in octahedral site

● Oxigen ion

(c)

(d)
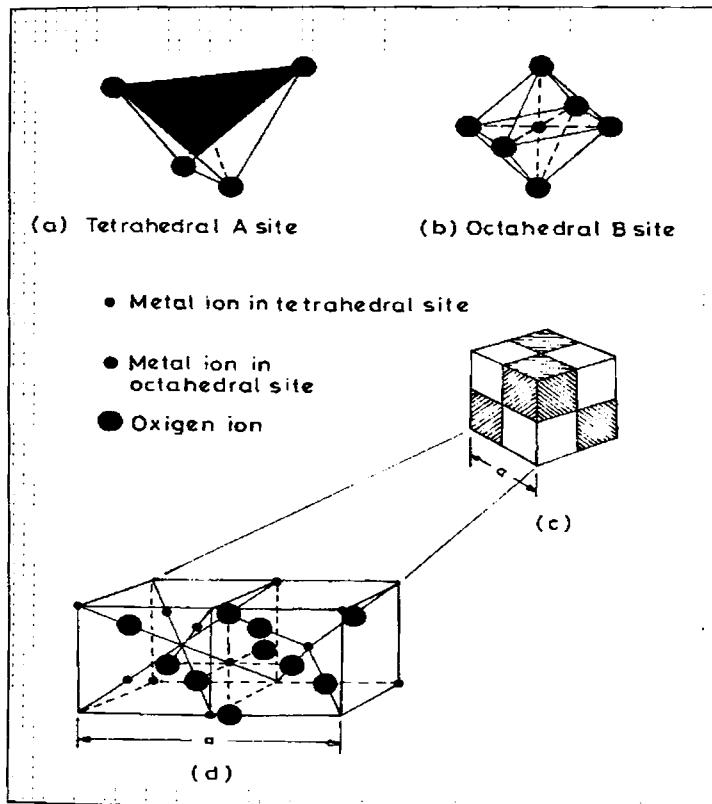
Fig.1.2.b Crystal structure of a cubic ferrite

The distribution of metal ions is very important for an understanding of magnetic properties of these materials. Not all available sites are occupied by metal ions. Only one fourth of the A sites and one half of the B sites are occupied. In the case of mineral spinel, Mg^{2+} ions are in the A site and Al^{3+} ions are in B sites. Such an arrangement is called normal spinel structure in which the divalent ions are on B sites and trivalent ions are on the A sites. $ZnFe_2O_4$ is a normal spinel in the micron regime. The structure in which divalent ions are in the A sites and trivalent ions are equally distributed between A and B sites, is called an inverse spinel structure. $CoFe_2O_4$ and $NiFe_2O_4$ ferrites have inverse structure and they are all ferrimagnetics.

1.11 Superparamagnetism

A particle of ferromagnetic material below a critical particle size would consist of a single magnetic domain. For a spherical sample, this size limit is around 100Å The treatment of the thermal equilibrium magnetization properties of an assembly of isotropic single domain particles is analogous to the Langevin treatment of atomic Paramagnetism. It differs only in that the moment μ we are dealing with is not that of a single atom, but rather of a single domain ferro/ferrimagnetic particle, which may contain more than 10^5 atoms ferromagnetically coupled with exchange forces.

Since one of the central themes of this thesis is magnetic fluids, a brief insight into the various aspects of magnetic fluids will be provided in the subsequent subsections.

1.12 Magnetic Fluids

A homogeneous fluid with magnetic characteristics has been the dream of researchers and scientists for quite sometime which remained unfulfilled as efforts for producing a liquid out of a solid by melting the metallic magnets became impractical because all the magnetic materials have a property of loosing their magnetic properties if heated above a certain temperature called the Curie temperature. These particles have melting point much greater than the Curie temperature, twice as that of the value of its Curie temperature. This makes the process of producing magnetic fluids by melting, a non-viable one.

The dream of producing a liquid that possess strong magnetic properties was not realized until the early 1960s, when Stephen Papell of National Aeronautics and Space Administration (NASA) developed a colloidal system. Papell's fluid consists of finely divided particles of magnetite suspended in kerosene. To keep the particles from

clumping together, Papell added oleic acid, an organic substance that served as surfactant or dispersing agent [59].

This kerosene-based fluid had a high evaporation rate and was not suitable for industrial applications. After a few years of NASA funded magnetic colloid research at AVCO, Ferrofluid Corporation was founded by Rosensweig and Moskowitz, to commercialise this technology. Magnetic fluids are of great interest, since they possess the properties of a fluid and act as a ferromagnetic material. [60]

1.13 Components of a Magnetic Fluid

The unique combination of fluidity and the capability of interacting with a magnetic field is achieved in magnetic fluids because of their composition. Three components are required to synthesize a magnetic fluid namely, a liquid base (or in other words, a carrier liquid), single domain magnetic particles of a colloidal size and a stabilizer to prevent colloid particles from aggregating. Each of these components must satisfy certain requirements [61].

(a) Base Fluid

A carrier liquid is chosen to conform to its field of application. Thus for lubrication and sealing systems, mineral oils and silicon organic bases are used. For medical applications, water is used as base fluid. Liquid bases need to be of low evaporation, non toxic, resistant to corrosive media, insoluble in specified media and so on [61]

(b) Single Domain Magnetic Particles

Ferromagnetic particles in colloidal dispersion make the fluid act like a ferromagnetic material. They may be cobalt, iron, nickel or one of their magnetic compounds or alloys. The most usual material is magnetite. Typically magnetic fluids contain 10^{20} particles per litre [59,61].

The size of the particles must be sufficiently small, for preventing agglomeration and precipitation. The thermal motion of the particles ensures the stability of magnetic fluid and this thermal motion increases with decreasing particle size. At the same time the particles must not be too small, since at sizes less than 1-2 nm, their magnetic properties disappear [61].

(c) Surfactant (Stabilizer)

The surfactant must prevent particles from aggregating. To this end long chain molecules are used with functional groups OOH, H_2OH, H_2NH_2 and so on. A stabilizer is chosen so that its molecules interact with magnetic particles, via bonds of functional group, to form a tightly bonded monomolecular layer around the particles [59,61].

1.14 What is a Ferrofluid?

Ferrofluids are stable colloidal suspension of single domain magnetic particles in a base fluid, which is magnetically passive. The number density of the particle in a typical ferrofluid is of the order of 10^{23} particles per m^3. The particles are so small in nature and the size of the particles is of the order of 100 Å [59,61,62].

To synthesize ferrofluids, at least two components, mono domain magnetic particles and a suitable carrier liquid are required. Since randomising Brownian energy may not be enough to counteract attraction owing to van-der-Waal and dipole- dipole forces, aggregation and sedimentation are prevented by providing suitable repulsive forces either by Coulomb repulsion or by steric repulsion. In the former case particles are either positively charged or negatively charged and the fluid is called 'ionic ferrofluid', while in the later case each particle is coated with an appropriate surfactant and resulting ferrofluid is classified as 'surfacted' ferrofluid. The ionic fluid requires a polar medium like water as base fluid; the surfacted fluid can use any carrier liquid like oil, water and hydrocarbons [62].

The choice of the carrier liquid depends on the application. For a surfacted ferrofluid, selection of surfactant is crucial for its stability. A surfactant molecule consists of a polar head and a tail of hydrocarbon chain. An example is oleic acid

$$CH_3(CH_2)_7 CH\text{-}CH(CH_2)_7C\diagup^{OH}_{\diagdown O}$$

The anchor polar group is adsorbed on the particle while the chain performs thermal movement in the carrier. When a second particle with a similar chain approaches closely, the movement of the chains is restricted and results in steric repulsion.

→ Magnetic particle

→ Surfactant

→ Carrier fluid
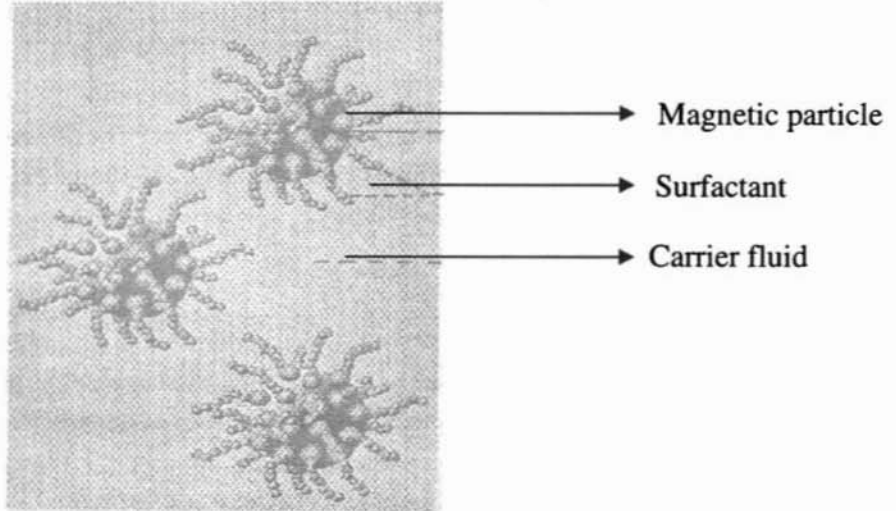
Fig.1.3 Magnetic particles suspended in a carrier liquid.

Rosenweig gives a simplified estimate for the entropic effect for the short chains

$$E_s = \frac{2}{3}\pi N k_B T \left[\delta - \frac{x}{2}\right]^2 \frac{\left(1.5D + 2\delta + \frac{x}{2}\right)}{\delta} \qquad 1.4$$

where N, is number of molecules per unit area, δ, is the thickness of the stabilized layer, x is the distance between two surfaces, and D is the diameter of the particle. The equation is useful to calculate δ which gives a reasonable barrier of $25k_BT$ to prevent agglomeration [62, 59].

1.15 Physics of Ferrofluids

Many of the properties of the ferrofluids can only be well understood by studying the physical laws governing the behaviour of these special fluids. So a brief discussion of major physical laws governing their special properties becomes relevant here. This section mainly consists of three parts, namely, Modified Bernoulli's equation, Kinematics of ferrofluids and Brownian motion of the particles in a ferrofluid.

1.15.1 Stability criteria for the magnetite based ferrofluids

Stability against settling of the suspended particles is achieved if the ratio of thermal energy to magnetic energy is greater than 1, ie,

$$\frac{k_B T}{\mu_0 MHV} \geq 1 \qquad\qquad 1.5$$

where M is the magnetisation, H is the applied magnetic field and V the volume of the particles. Assuming the particles to be spherical, the diameter of individual particles is given by

$$d \leq \left(\frac{6k_B T}{\pi\mu_0 MH}\right)^{1/3} \qquad\qquad 1.6$$

so that with a permanent magnet having a magnetic field of 8 x 10^4 A/m, we can separate the aggregates to have an average particle diameter around 80 Å.

Stability against individual particle agglomeration is achieved if the thermal energy becomes at least equal to the dipole-dipole energy:

$$\frac{\mu_0 M^2 V}{24} \leq k_B T \qquad\qquad 1.7$$

and for magnetite particles the magnetization M= 4.46 x 10^5 A/m, giving the maximum size limit for an agglomeration less ferrofluid as 100 Å.

1.15.2 Modified Bernoulli's Equation

The equation presented by the Swiss mathematician Daniel Bernoulli in his Hydrodynamica of 1738, is one of the most useful relations in ordinary fluid mechanics. This equation relates the pressure, the velocity and the elevation of a fluid in a gravitational field. Bernoulli showed that the sum of the three forms of energy; pressure energy, kinetic energy and gravitational energy inherent in the flow remains constant, provided, the effects of friction are negligible [59].

The Bernoulli's equation is

$$P + \frac{1}{2}\rho v^2 + \rho gh = const.$$ 1.8

Hydrodynamically magnetic fluids follow the Bernoulli's equation, modified by adding a term, which takes the magnetic properties into consideration. The pressure energy, potential energy and magnetic energy are constant along the streamline flow. It is expressed by the modified Bernoulli's equation,

$$P + \frac{1}{2}\rho v^2 + \rho gh - \mu_0 \int_0^H M dH = const.$$ 1.9

Where P is the pressure energy, ρ is the mass per unit volume, μ_0 is the permeability of free space, M is the magnetization and H is the magnetizing field. From this equation it is clear that in the absence of magnetic field, the magnetic fluid acts like other liquids, but in magnetic field an additional force appears and affects the fluid. [59,63].
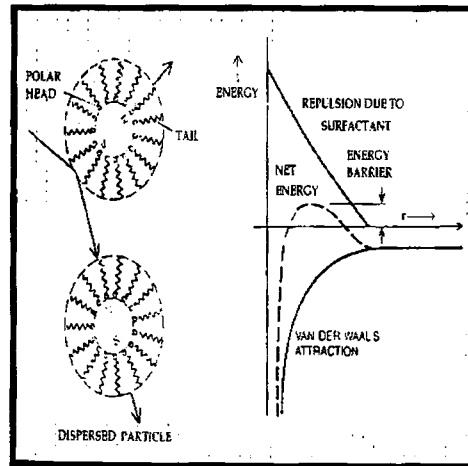
Fig. 1.4 Various interaction energies those are significant in the prevention of particle agglomeration.

1.15.3 Kinematics of ferrofluids

The kinetic theory of matter suggests that sufficiently fine particles of matter can remain suspended indefinitely in a liquid even though the particle density is much higher

than that of the liquid. This is due to the continuous collisions of the particles with molecules of liquid, which are in thermal motion. When many particles are present in the same volume of the liquid, agglomeration may take place, creating a heavy particle, since the ratio of the thermal energy (kT) to the gravitational energy (ρgh) is reduced.

The forces of attraction that affects the particles in a ferrofluid are magnetic force and Van der Waal's force. Due to the extremely small size of the particles, the magnetic force is very weak. But Van der Waal's force of attraction arises between the dipoles, which are created by the fluctuations in electronic structure. According to Fritz London, the energy needed to overcome the Van der Waal's force is inversely proportional to the sixth power of the centre-to-centre separation of the particles. Hence to overcome this force, the particle must be kept well apart. In preparing ferrofluids the necessary separation can be achieved by coating each particle with a molecular film that acts as an elastic cushion. [59].

1.15.4 Brownian Motion of Particles

The problem of agglomeration of the particles in a ferrofluid due to Van der Waal's force is overcome by the coating of the surfactant layer on each particle. But to avoid the gravitational settling of the particles, the gravitational energy must be exactly balance the viscous force of the base fluid. For that, there is a maximum limit for the size of the suspended particles. Then only there is a stability of the fluid by means of the vigorous non-uniform zigzag motion of the particles inside the base fluid. This is called the 'Brownian motion' of the particles. [59]

For balancing the viscous force, which acts upward must at least be equal to the gravitational force.

Viscous force = gravitational force

$$6\pi\eta av = mg \qquad\qquad 1.10$$

Where mg is the weight of the particle, which acts in downward direction.

$$6\pi\eta av = \frac{4}{3}\pi a^3 \rho g \qquad\qquad 1.11$$

Here ρ is the density of the particle, η is the co-efficient of viscosity, 'a' is the radius of the particle. Substituting the typical values, assuming the number density is of the order of 10^{23} per m^3, we get the particle size maximum of 100Å [59].

1.15.5 Physical Properties of Ferrofluids

* The size of the particles in the ferrofluid is of the order of 100Å. They are single domain particles and exhibits superparamagnetism.
* The number density of the ferrofluids is of the order of 10^{23} per m^3. It is comparable with the number of molecules in air at STP (ie; 2.7×10^{23}/m^3)
* Physical properties of the ferrofluids like specific gravity, viscosity, magnetization, dielectric constant etc. are modified with the application of a magnetic field.
* Depending on the choice of the surfactant and base fluid, density of ferrofluid varies with the density of water to twice its value.
* Magnetic fluids have zero remanance and coercivity.
* They spike under the influence of a magnetic field.
* Cluster Formation:

    In the absence of magnetic field, the particles are well dispersed. When a weak field is applied, particle tends to form tiny clusters elongated parallel to the field. These are called micro clusters. Further increase in the magnetic field results in a growth of clusters, and forms the so-called macro clusters. Under the influence of strong magnetic fields, well elongated macro clusters repel each other, thus forming an ordered arrangement. This cluster formation leads to the remarkable magneto-optical properties such as dichroism and birefringence. [64-68].

1.16 Optical Properties of Ferrofluids

Magnetite based ferrofluids are black and practically opaque; however thin layers exhibit the magnetic field effect both on isotropic optical properties such as extinction and anisotropic optical properties such as birefringence, dichroism etc, when they are exposed to its effect. For high concentration fluids, a difference in refractive indices of the ordinary and extraordinary rays attains 5×10^{-3} and dichroism amounts to 4×10^{-3}. That

is, the magnetic fluid displays the pronounced properties of an optically single axis crystal in an external field.

1.17 Synthesis of magnetic Nanoparticles.

Generally the magnetic nanocomposites are prepared by the following techniques.

a. Ceramic Method

It is the physical mixing of reactants in the appropriate molar ratio in an acetone-mixing medium. By the heat treatment of the above mixture at a high temperature, highly crystalline ferrite particle of micron scale is formed.

b. Co precipitation Method.

In Cold co-precipitation method the precursor materials are taken in the appropriate molar ratio in aqueous medium maintaining an appropriate pH and temperature. In aqueous medium the reactants are in ionized form, and thus the ferrites formed are in the nanoscale. [69-76]

c. Sol-Gel synthesis

In sol-gel technique, the precursor materials are completely dissolved in a suitable solvent and the solution is allowed to react at low temperature until a gel is formed. The gel is then heated at a higher temperature to obtain the desired final product. Mainly oxides are synthesized by this technique.

1.18 High energy ball milling

High energy Ball Milling is a method for the synthesis of nanograins out of bulk by the top-down approach. Here due to the very high rotation and revolution, the momentum imparted is very high as compared to the conventional low energy milling techniques.

The properties of the nanophase materials synthesized by high energy ball milling are dependant on the ball milling conditions. Among the key parameters characterising the process, the impact speed of the balls is of the most important one in determining the rate of energy transfer. The deformation is   by the impact of a body on a target material can be characterized by a dimension less number called "Best number" (B.N)

24

$$B.N = \frac{\rho V^2}{Y_d},$$ 1.12

where ρ and Y_d are the density and dynamical field strength of the target material. Here V is the impact velocity of the body. B.N values below 10^{-5} correspond to the deformation in the elastic range where as for B.N > 10^{-4} plastic deformation prevails.

In the plastic deformation range, a correlation can be established between the relative impact velocity V of a sphere with the target material and the indentation radius 'a' assuming normal impact and the hardness of the material of the sphere greater than that of the target. With ball mass m and ball radius R,

$$V^2 = \frac{4.5\pi n Y a^4}{2R}$$ 1.13

Momentum of the balls in each grinding, means the correlated impulsive force "F" is key parameter in the plastic deformation produced by the high-energy ball milling. This momentum is correlated to the impulsive load

F=mV/t where the ball-vial contact time. Such load F determines the mechanical energy transfer to the grains during grinding. 'F' can be varied by adjusting the rpm and duration of the milling. The transferred energy to the vial is a factor that determines the particle size distribution

Chemically synthesized nanomaterials if subjected to a high energy ball milling will enhance its shape anisotropy. Magnetic particles exhibit superparamagnetism below its critical size. At these submicroscopic scales, the material exists strictly as single domains. Magnetic, dielectric, and the conductive properties highly depend on the particle size. At this particular size scale novel properties are exhibited mainly dependant on their surface to volume ratio and magnetic interaction.

1.19 Magnetic Nanocomposites

Nanocomposites are composite materials containing a phase with one or more average dimension smaller than 100nm, like multiplayer or monolayer films, nanograined

metals, etc [77]. The improved magnetic properties of such materials can be accounted as follows.

Reduction in the size of materials causes long-range magnetic order to be replaced by some other magnetic state. It is a consequence of the increased uncertainty in momentum and energy of electrons in the ordered region. The uncertainty in momentum is given by:

$$\Delta P = \frac{\eta}{d} \qquad\qquad 1.14$$

Where 'd' is the uncertainty in the position of the electron, which is determined by the particle dimension. This results in an uncertainty in energy. When this energy uncertainty equals the magnetic ordering energy, the long-range order is no more energetically favourable. The gross magnetic behaviour becomes either paramagnetic or super paramagnetic as the sizes of the magnetic species are well reduced.

Ease in control of the magnetic behaviour of these composite materials by controlling the processing parameters present great possibilities for the atomic engineering of materials with specific magnetic properties. They are potentially important to the magnetic recording industry for high-density information storage and in the refrigeration industry for their potential for enhancing the efficiency of magnetic refrigeration cycles.

As already mentioned, when the size becomes smaller and smaller, properties of materials become different from that of their bulk counterparts. The discovery of nanoscopic materials has opened up new vistas in the frontier areas of material science and technology. The recent advances in nanotechnology has made it possible to devise newer materials with novel chemical, magnetic and electrical properties [69,78].

Particles possessing nanometric dimensions, lying in the range 1-10 nm are found to be exhibiting superior physical properties with respect to their coarser sized cousins. The properties of nanostructured materials are determined by the complex interplay among the building blocks and the interfaces between them.

Single nanosized magnetic particles are mono-domains and one expects that in magnetic nanophase materials the grains correspond with domains, while boundaries on the contrary to disordered walls. Magnetic nano-composites have been used for mechanical force transfer (ferrofluids), for high density information storage and magnetic refrigeration [69,70,79-80]. Multilayers and other types of materials containing

nanocomposites are found to exhibit properties like GMR and magnetocaloric effect. A research team led by Ron Ziolo [70] developed a composite material consisting of 5 to 10-nm magnetic iron-oxide particles lodged in a polymer matrix. This nanocomposite material consists of tiny magnetic particles dispersed in a lightweight, insulating polymer solid. They serve as transparent magnets and can be converted into magnetic fluids. Other than serving as a lossless transformer, the nanomagnets could act as miniature switches or sensors in smart materials, or as a form of microwave shielding. These materials are expected to have novel acoustic, thermal, and optical properties. Besides these the magnetic nancomposites can find applications in medical diagnostics, digital information storage, leak free sealing and detection and sensing devices [69,70,78-79]

1.20 Different schemes of preparation of magnetic nanocomposites

There are different schemes available for the synthesis of magnetic nanoparticles/ nanocomposites. Some of the important methods of preparation will be discussed here.

a) Inert gas evaporation

In the inert gas evaporation method [11,69] a metal is evaporated in an inert atmosphere at a reduced pressure and then condensed in the gas phase to form metal clusters or nanocrystals. These could be collected on the cold finger and can be oxidised to fine ceramic powder which can be scrapped off. If a bicomponent composite is to be synthesized two different metals are to be evaporated.

b) Solution chemical route

In the solution chemical route [11,69], molecular mixing is accomplished by aqueous solution of suitable precursors. The solution mixture is aerosolised and rapidly spray dried to get extremely fine mixture of salts. These precursor powders are reduced with hydrogen and then reacted with CO in a fluidized bed reactor to yield nanophase metal carbide powder. Nanocomposites with impressive properties can be prepared by dispersing nanoparticles either inside the larger grains of a second ceramic or in between the grains.

c) Rapid thermal decomposition of precursors in solution (RTDS)

27

Rapid thermal decomposition of precursors in solution (RTDS) method is yet another synthesis scheme which can be used to make nanophase powders of NiO and $Ni(OH)_2$. The RTDS process applies a high temperature and pressure to a rapidly flowing solution containing dissolved precursors to synthesize ultra fine particles.

d) Sol-gel method

Recently sol-gel method is gaining popularity and can be made use of for the dispersion of small metal, metal oxides or alloy particles in non-metallic matrixes. In this method, precursor materials are dissolved in a suitable solvent and a wet gel is made by slow heating process and finally the gel is ignited at a high temperature to yield the required nanoparticles/alloys [81-82].

e) Ion exchange method

Another important method used for the preparation of magnetic nanocomposite is the ion exchange method [70,75-76].

In this method the nanoscopic magnetic components are dispersed in the nonmagnetic matrix of the ion exchange resin. Here in the present study the ion exchange method [83] will be employed to prepare magnetic nanocomposites containing dispersions of iron oxide in a nonmagnetic matrix. Therefore the details are discussed in more detail in the next section.

1.21 Preparation of nanocomposites by ion exchange method.

Nanometer sized γ-Fe_2O_3 particles were embedded in a polymer matrix by the method of ion exchange followed by reduction. The method adopted here is a modification of the preparation scheme reported by Ziolo et al [70]. The polymer matrix employed is a cross linked polymer of sulphonated polystyrene and divinyl benzene, which have exchangeable H^+ ion containing $SO_3^-H^+$ groups. The detailed synthesis technique employed and schematic of a polystyrene structure is given in Chapter 3 (Fig.3.1)

1.22 Some Applications of magnetic nanocomposites

Nanocomposites promise to be the wave of the future having major implications industry and technology. A number of companies all over world particularly in Japan has been utilizing their application potential in versatile fields. Nano Dyne, a US based company has started utilizing their properties to employ them in cutting tools and wear resistant devices. Nanocomposite based superlattice structures become promising candidates for the next generation information storage devices. The nanocomposites which are superparamagnetic, will in general by theory could provide the same magnetocaloric effect at a given field which is given by a natural paramagnet, but the transition temperature will be much higher so that they can be employed as magnetic refrigerant materials at the same temperature they need only a small applied magnetic field. Polymer based nanocomposites can be employed used as a dielectric layer in electronic packaging applications.

1.23 Motivation for the present study

Having brought out the importance of nanomagnetic materials and its applications, it is imperative that the motivation for the present investigation is spelled out. From the foregone discussions it can be seen that any study in materials science requires preparation of pristine as well as single phasic compounds. The approach of synthesizing newer compounds and its characterization at various points of preparation using various analytical techniques is advantageous in extracting useful Physics.

The history of materials synthesis and reaction condition plays a vital role as far as the interpretation of the results is concerned and hence it is mandatory that the materials under investigation are prepared by the researcher himself/herself. Thus in this investigation, emphasis was laid in synthesizing pure nanomagnetic materials by adopting ingenious techniques.

This is an investigation in the realm of nanomagnetic materials and ferrofluids and hence pure materials are to be prepared in the ultra fine regime. It has already been mentioned in the earlier sections of this chapter that magnetism presents an indomitable challenge to physicists and chemists in explaining and understanding various phenomena like quantum magnetization, quantum tunneling, spin polarized tunneling, and superparamagnetism. In order to understand various phenomena occuring at the nanolevel, appropriate templates are necessary. While choosing such templates, the researcher has to keep in mind the various surface phenomena occurring at the

nanodimensions. This means that synthesized particles are to be protected by appropriate passivation techniques to prevent oxidation. Thus preparation of self protected nanoparticles is a viable solution and this can be achieved by incorporating ferrites like maghemite and magnetite in matrixes like sulphonated polystyrene. The method of ion exchange can be utilized to incorporate maghemite. Under normal circumstances, incorporation of magnetic materials in matrixes like sulphonated polystyrene using strong ion exchange resin results in weakly magnetic composites. In order to have better magnetic characteristics, cycling of magnetic materials (ion/nickel/cobalt cycling) can be employed. The *insitu* incorporation of magnetic materials in matrixes relies on the pore size offered by the polymer matrix. The nanopores inside the matrixes limit nucleation and growth and thus aid the synthesis of self protected nanocomposites. These studies not only provide templates for studying magnetism at the nanolevel, but also help to synthesize composites for magneto caloric application and in magneto-optical devices. This is a major motive of the present study.

It is known that a transparent magnetic material does not exist in nature and hence alternate techniques are to be employed to realize it. With the advent of nanotechnology, phenomenon like grain size dependant quantum confinement and alloying induced quantum confinement can be successfully employed to induce transparency in magnetic materials. This is important from a fundamental point of view. Thus preparation of a transparent magnetic composite using sulphonated polystyrene by size reduction is another motive of the present investigation.

In composites containing maghemite and sulphonated polystyrene, though magnetisation can be manipulated by cycling process, another important performance characteristic of a magnetic material is coercivity and this also need to be tuned. 'Cobalt' is an ideal dopant because of its large magneto-crystalline anisotropy. It can be incorporated inside the lattice of maghemite-sulphonated polystyrene nanocomposites. Incorporation of cobalt in the maghemite lattice not only modifies coercivity but also alters the optical band gap. So modification of saturation magnetization, coercivity and optical band gap is possible by the synthesis of cobalt containing maghemite-polystyrene nanocomposites.

3d transition metals like Co, Fe, and Ni are magnetic materials that are employed extensively for various applications. Studying the finite size effects on the magnetic properties assumes significance since various novel phenomena are expected to occur at

reduced dimensions. However, usual synthesis of these particles at the ultra fine regime results in nonmagnetic metal oxides immediately after synthesis because of their large surface area. Hence it was thought that nanocomposites containing cobalt/iron/nickel can be synthesized using sulphonated polystyrene. An ingenious method of synthesis was conceived where in, a reducing agent like $NaBH_4$ is utilized to arrive at passivated and self protected metal nanoparticls. This is another motive of the present work.

Ferrofluids are commercially important materials which can be employed for a number of engineering applications. Since the individual particles in a ferrofluid are typical of the order of 100Å or less and are self protected using a surfactant, they serve as ideal templates to study magnetism and non-interacting magnetic systems. Phenomena like quantum size effects, excitonic confinement and wave function overlapping and its influence on the optical properties of ferrofluids, alloying induced quantum confinement and enhanced optical transparency can also be studied by using ferrofluid templates. All these phenomena can be studied by synthesizing magnetite and nickel doped magnetite ferrofluids by using oleic acid as surfactant and kerosene as the carrier liquid. The synthesis and characterization of magnetite based ferrofluids is another mandate of this thesis.

Thin films made of ferrofluid (ferrofluidic thin film) display interesting magneto-optical properties like zero field birefringence, field induced birefringence, field induced dichroism, and Faraday rotation. These measurements enable us to extract very useful information like anisotropy constant, rotary diffusion coefficient, and magneto-optical diameter. Since facility for the evaluation of these properties does not exist in the department of Physics, setting up of a full fledged magneto-optics laboratory with vibration isolation table and optical bread board and all its accessories is another task which will be undertaken as part of the investigation. Using this set-up, field induced transmission, measurement of dichroism, birefringence, and Faraday rotation in various ferrofluid systems could be carried out.

It is known from literature that capped silver/gold nanoparticles exhibit useful optical limiting properties. However they are not stable and lack good shelf life. Hence it was thought that ferrofluid with oleic acid coating can be a useful optical limiter. So studies relating to non-optical properties of ferrofluids are also envisaged as a part of this investigation and this forms yet another motive for the present investigation.

A correlation of these properties is always handy in understanding the fundamental properties in the nanolevel and also in proposing new applications in the field of nanophase materials and ferrofluids. So the objective of present investigation can be enlisted as follows.

Objectives of the present work:

- ➢ Synthesis of ultra fine maghemite inside natural pores of polystyrene
- ➢ Optimization of the reaction conditions
- ➢ Tuning of optical parameters by manipulating grain size to the Bohr radius limit
- ➢ Insitu doping of cobalt with a view to enhancing the coercivity of the samples
- ➢ Correlation of the results
- ➢ Synthesis of self protected elementary magnetic metal nanoparticles inside polymer pores
- ➢ Optimization of reaction conditions
- ➢ Evaluation of structural and magnetic properties of the synthesized metal nanocomposites
- ➢ Synthesis of magnetite and doped magnetite ferrofluids by direct precipitation technique
- ➢ Optimization of reaction parameters for fine tuning the grain size
- ➢ Evaluation of their structural, magnetic, and dielectric properties
- ➢ Analysis of the magnetic field dependence of dielectric studies
- ➢ Setting up of magneto-optical laboratory for measurements
- ➢ Magneto-optical characterization of the synthesized ferrofluid samples
- ➢ Investigation on the effect of attrition on the magneto-optical signals
- ➢ Evaluation of the magneto-optic diameter, anisotropy etc from magneto-optic data
- ➢ Correlation of the results obtained from the magneto-optical measurements
- ➢ Study of their absorptive nonlinearities by closed aperture z scan technique
- ➢ Analysis of the results obtained

References

1. Jhunu Chatterjee, Yousef Haik, Ching-Jen Chen, J. Magn Magn. Mater. **246** (2002), 382

2. Q A Pankhurst, J Connolly, S K Jones and J Dobson, J. Phys. D:Appl.Phys.**36** (2003) R167

3. Masashige, Shinkai, Mitsugu Yanase, Masataka Suzuki, Hiroyuki, Honda, Thoshihiko Wakabayashi, Jun Yoshida, Takeshi Kobayashi, J. Magn Magn. Mater.**194**, (1999), 176

4. Urs O Hafeli, Gayle J. Pauer, J.Magm Mag. Mater. **194** (1999),76

5. T. Rajh, O.I Micic, A.J Nozik, J. Phys.Chem, **97**, (1993) 11999,

6. Y.Nosaka, K. Yamaguchi, H.Miyama, H. Hayashi, Chem.Lett, (1988) 605

7. S. Mahamuni, A.A Khosravi,M. Kundu, A Khirsagar, A Bedekar, D.B Avasare, P. Singh, S. K Kulakarni, J. Appl. Phys, **73**, (1993) 5237

8. H. Matsumoto, T. Sakata, H. Mori and H. Yoneyama, J. Phys. Chem, **100**, (1996)13781

9. C.Murray, D. Norris, B.Bawendi, J. Am. Chem. Soc, **115**, (1993) 8706

10. H.Matsumoto, H. Uchida, T.Matsunaga, K.Tanaka, T.Sakata, J. Phys.Chem, **98**, (1994) 11549

11. Harisingh Nalwa, Nanostructured materials and nanotechnology, Academic Press London

12. A Henglein, Chem Rev **89**,(1989) 1861

13. H. Weller, H.M Schmidt, U. Koch, A. Fojtik, S. Baral, A Henglein, W. Kunath, K. Weiss, E. Diemen, Chem. Phys. Lett, **124**, (1986) 557

14. H Weller, Adv.Mater, **5**, (1993) 88, Y Nosaka, K. Yamaguchi, H. Miyama, H Hayashi, Chem.Lett, (1988) 605

15. D Heyes, O.I Micic, T Nenadovic, V Swayambhunathan, D Miesel, J. Phys. Chem, **93**, (1989) 4603

16. C.H Fischer, A. Henglein, J. Phys. **93**, (1989) 5578

17. R.V. Kamat and B Patrick, J.Phys.Chem, **96**, (1992) 6829

18. I Bedja, S.Hotchandani, P.V.Kamat, J. Phys.Chem, **97**, (1993) 11064

19. J.Bedja, S Hotchandani, P.V kamat, **98**, (1994) 4133

20. D.E Skinner, D.P.J Colombo, J.J Cavelcri, R.M Bowman, J.Phys.Chem, **99**, (1995) 7853

21. J.G Zhang, R.H.O' Neil, T.W Robertie, J.Phys.Chem, **98**, (1994) 3859

22. J.Z Zhang, R.H.O' Neil, T.W Roberti, J.L McGowan, J.E Evans, Chem.Phys.Lett, **218**, (1994) 479

23. C. Allan, M. Delerue, M. Lannoo, Appl. Phys. Lett, **70**, (18), (1997) 2437

24. M. Goryll, L Vescan, K. Schmidt, S. Mesters, H. Luth, and K Szot Appl. Phys.Lett, **71** (3) (1997)410

25. G. Allan, C. Delerue, M. Lannoo Appl. Phys. Lett, **71**(9)((1997), 1189

26. L.T Cheng, N.Herron, Y.Wang, J.Appl.Phys, **66**, (1989) 3417

27. C.Y Yeh, S.B Zhang, A Zunger, Appl.Phys.Lett, **64**, (1994) 3545

28. A.J Heliweil, R.M Hochstrasser, J.Chem.Phys, **82**, (1985) 179

29. E.F Hilinski, P.A Luca, Y Wang, J. Chem. Phys, **89,** (1988) 3435

30. L.T Cheng, N.Herron, Y.Wang, J.Appl.Phys, **66,** (1989) 3417

31. B Kraeutler and A. J Bard J. Am. Chem. Society, **100,** (1978) 4317

32. R. Palmans and A. J Frank, J. Phys. Chem., **95,** (1991) 9438

33. D. Duonghong, E. Borgarello, and M. Gratzel, J. Am. Chem.Soc, **103,** (1981) 4685

34. A Mills and G Porter, J. Chem. Soc, Faraday Trans. **78,** (1982) 3659

35. T. Sakata, T. Kawai, and K. Hashimoto, Chem. Phys. Lett, **88,** (1982) 50

36. C.P Lafrance, S. Kaliaguine D. Meisel, Isr.J. Chem, **33**(1993) 53, R.R Chandler and J.L Coffer, J. Phys.Chem, **97** (1993) 9767

37. P.V kamath, M. de Lind and S. Hotchandani, Isr.J. Chem, **33**(1993) 47

38. K.R Gopidas and P.V Kamath, Mater Lett, **9** (1990) 372

39. K.R Gopidas and P.V Kamath Proc.Ind.Acad. Sci (Chem.Sci) **105** (1993) 505

40. J.P Kuenzynski, B.H Milosavljevic, J.K Thomas, J. Phys.Chem, **88** (1984) 980

41. Y. Nosaka M.A Fox, Langmuir, **7**(1987) 1147

42. T. Rajh, J. Rabani, Langmuir **7** (1991)2054

43. F.R.F Fan, H.Y Liu, A.J Bard, J.Phys.Chem, **89** (1985) 4418

44. M.D Butterworth, S. P Armes, A.W Simpson, J. Chem.Soc;chem..commun, (1994) 2129

45. P.V Kamat, Chem. Rev **93** (1993) 267

46. B.O Regan and M. Gratzel, Nature, **353,** (1991) 737

47. P.V Kamat and M.A Fox, Chem. Phys. Lett, **102,** (1983) 379

48. Ph.D.Thesis, Adrian Richard Muxworthy, Dept. of Earth Sciences, University of Oxford, 1998

49. Yuji Masumoto, M.Murukami et al Science 291, 2Feb, 2001

50. D.Ralph, Science, **291** , 9 Feb 2001, 9990

51. Hartley et al Science 290, 15Dec, 2000

52. B.D.Cullity, 'Magnetic Materials' Addison-Weisley Publishing Company, Inc (1972)

53. S.Henze, Science **288**, 9 June2000, 1805

54. E.C.Snelling and A.D Giles Ferrites For Inductors and Transformers, Research studies press. John Wiley and sons,1983

55. V.Provenzano and R.L.Holtz, J.Material Science and Engineering **A204** (1995) 125

56. Maurice Gell J.Material Science and Engineering **A204** (1995) 246-251

57. A. J Dekker, Solid state Physics, Addison Wesley New York

58. Smit. J and H.P.J.Wijn, 'Ferrites', 1959, Philips Technical library

59. R. E. Rosenswieg; Magnetic Fluids, Oxford University press, 124

60. K. Raj and A. F Chorney Ind. J. of Eng. And materials Sciences, **5**, Dec.1998, 372

61. B. M. Berkovsky, V. F. Medvedev, M. S, Krakov; Magnetic Fluids, Engineering Applications; Oxford University Press. 1993

62. R. V.Mehta and R.V. Upadhyay, Current Science,76, No 3, Feb 1999, 305

63. Jan Burcan, Indian. J. Of Eng. And Mat. Sciences, 5, Dec.1998, 390

64. S. Chikazumi, S. Taketomi, M. Ukita, M. Mizukami, H. Miyajima, M. Setogawa, and Y. Kurihara; J. Magn.Magn.Mater. 65 (1987) 245

65. Horng H.E, Chin–Yih Hong, Yang S.Y, Yang H.C, 2001, J. Phys. and Chem. of Solids, 62, 1749.

66. Promislow J.H.E, Gast.A.P, Fermingier M, 1995, J. Chem. Phys, 102, 5492

67. Wu K.T, Yao Y.D, April 1999, J. of Appl. Phys, 85, 5959

68. Tengda Do, Weili Luo, April 1999, J. of Appl. Phys, 85, No.8, 5953

69. Ron Dagani, Nanostructured Materials Promise To Advance Range of Technologies, Science/Technology, 1992, 18

70. R. F.Ziolo, E.P.Giannelis, B.A Weinstein, Michela P. O'Horo, B.N.Gaguly, V.Mehrotra, M.W.Russel, D.R.Huffman. Science 257, (1992) 219

71. G.C.Hadjipanayis and R.W. Seigel (Edt) Nanophase Materials – Synthesis properties and applications, Kluwer Academic Publishers (1994),

72. Y.Shi, J.Ding, X.liu and J.Wang J.Magn.Magn.Mater. 205 (1999) 249

73. D.Niznansky,J.L.Rehspringer and M.Drillon, IEEE Trns. On magnetics, 30, no 2. (1994) 821

74. W.Gong, G.C.Hadjipanayis and R.F.Krause, J.Appl.Phys. 75 (10) 1994, 6649

75. R.F Ziolo, E.P.Giannelis and R.D.Shull, J.Nanostructured materials,.3,(1993), 85

76. J.K.Vassilovu, V.Mehrotra, M.W.Russel and E.P.Giannelis, Mater. Res.Soc. Symp.Proc.206, (1991) 561

77. Aihua Chen, Haiqiar Wang, Bin Zhoio, Xiaoyer Li, Synth. Met, 2003, 223

78. J.H.Paterson, R. Devine ,A.D.R.Phelps, J. Magn. Magn. Mater. 196-197 (1999) 394,

79. D.Chakravorty Bull.Mat.Sci. 15, no.5, 1992 411 |A Henglein, Chem Rev 89 (1989) 1861

80. R.D.Shull and L.H.Bennet, Nanocomposite magnetic materials, J.Nanaostructured Materials 1(1992), 83

81. M.George, A.M. John, S.S. Nair, P.A. Joy, M.R. Anantharaman, J. Magn. Magn. Mater, 302, (2006) 190

82. Structural Magnetic and electrical properties Of Sol-Gel Synthesized LiFe$_2$O$_4$ fine particles, M.George, Swapna.S.Nair, A.M. John, P.A. Joy, M.R. Anantharaman , J. Phys.D: Apply.Phys, 39, (2006) 900

83. K.A Malini, Ph.D Thesis, 2002, Dept of Physics, CUSAT, India

Introduction

CHAPTER 2

Theoretical Concepts

This chapter briefly discusses the theory and the related phenomenon that are central to this thesis. An outline of the brief Physics involved n the various experimental techniques are also dealt with.

2.1 Magnetic properties of materials

2.1.1 Magneto crystalline anisotropy.

Magnetization curves for single crystal iron at 18°C are shown in figure. It can be seen that, along the [100] direction, a very small magnitude of the magnetic field is required to produce a large magnetization; in other words it is 'easy' to magnetize an iron crystal along [100] direction, while it is 'hard' to do so along the other directions.
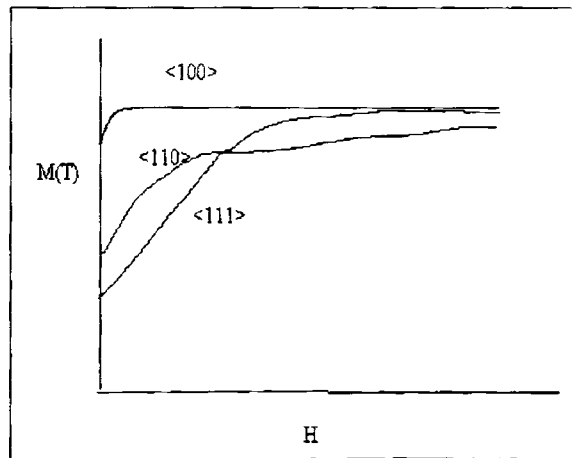
Fig 2.1 Magnetisation Curve for Fe (18°C)

The preference of spontaneous magnetization for a specific, easy direction may be taken as an evidence of a thermodynamically stable, minimum energy state. Now, if an external magnetic field is applied so as to rotate the magnetization vector out of its easy direction the energy of the system will tend to increase. This increase in energy may be called the magneto crystalline energy. If 'θ' is the angle between the easy direction and the

magnetization vector the anisotropy energy will be zero for θ=0, and it will increase with increase in 'θ' values. While the exchange energy is isotropic in nature, since it is determined by the relative directions of the adjacent magnetic spins only, the anisotropy energy is believed to be due to spin orbit coupling. As a result of this L-S coupling in the presence of a crystal field, atomic spins align themselves along a preferred direction with respect to the unit cell (crystal) axes. When an external magnetic field rotates the spins, the residual, unquenched orbital magnetization vector also rotates with the spin magnetization. This rotation alters the orbital overlap of the adjacent magnetic atoms or ions. This change in the overlap, in turn, affects electrostatic coulombic and the exchange energies. As a consequence, the total energy of the system increases.

For cubic crystals, the anisotropy energy may be expressed as:

$$E=K_1(\alpha_1^2\alpha_2^2+\alpha_2^2\alpha_3^2+\alpha_3^2\alpha_1^2)+K_2\alpha_1^2\alpha_2^2\alpha_3^2$$

Where K_1, K_2, are constants and α_1, α_2, α_3 are the direction cosines of the magnetization vector with respect to the unit cell axes. For uniaxial crystals such as Cobalt,

$$E=K_1 sin^2\theta+K_2 sin^4\theta,$$

Where θ is the angle between the easy and the magnetization directions [1-6].

2.1.2 Exchange Interactions

J.Frenkel made the assumption that the origin of strong, ferromagnetic interactions is due to what are called as exchange interactions. It is a characteristic quantum effect having no parallel in classical physics. Given below is a brief account of the various types of exchange interactions present in solids [2-4].

2.1.3 Direct-exchange interaction

This mechanism is operative between the adjacent atoms/ions and leads to a strong magnetic coupling. The total energy of the system corresponds to two situations:

a) Symmetric state corresponding to antiparallel spins
b) Antisymmetric state corresponding to parallel spins.

The corresponding energies can be described by:

$$E_A = 2E_O + \frac{E_C + E_{ex}}{1 + S^2} \qquad\qquad 2.1$$

$$E_B = 2E_O + \frac{E_C - E_{ex}}{1 - S^2} \qquad\qquad 2.2$$

Here $2E_O$ is the total energy of the isolated atoms (A, B), E_C the Coulombic interaction between electrons, nuclei and electrons-nuclei, E_{ex} the exchange energy associated with the process of exchanging electrons and S the overlap integral, whose value lies between 0 and 1.The magnitude of E_{ex} is always much larger than that of E_C and, therefore, the stability of the symmetric/antisymmetric state depends on the term E_x. In turn, E_{ex} depends on two factors:

1) The dot product, Si.Sj where Si and Sj are the total spins of the adjacent atoms.
2) The exchange integral J_{ex}, which represents the probabilities of exchange of electrons.

J_{ex} is obviously a sensitive function of overlap of electronic wave functions and its sign can be either positive or negative. If $J_{ex}>0$, parallel alignment of the neighboring spins is favored and this corresponds to the ferromagnetic case. If $J_{ex}<0$, neighboring spins will align themselves antiparallel, corresponding to antiferromagnetic behavior [2-4].

2.1.4 Indirect or Super-exchange Interaction

The value of the exchange integral depends on the ratio of the inter-atomic distance (a) to the diameter of the 3d orbital (D). The ferromagnetism of Fe, Co and Ni can be attributed to this direct exchange.

As the degree of overlap of d–orbitals decreases, J_{ex} becomes positive. This is true for values of a/D>1.5.If a/D<1.5, indirect exchange interaction leads to antiparallel alignment of adjacent atomic magnetic moments, resulting in the antiferromagnetic ordering [1-4].

2.1.5 Magnetism at the nano level

At the nanolevel the properties of the material changes from that of the bulk. Some of the interesting phenomena are explained below [2,4,7].

2.1.6 Coercivity of fine particles

In magnetic studies on fine particles the single property of most interest is the coercivity, for two reasons:

1. It must be high, at least exceeding a few hundred Oersteds, and
2. It is a quantity which comes quite naturally out of theoretical calculations of the hysteresis loop.

The coercivity of fine particles has a striking dependence on their size. As the particle size is reduced, it is typically found that the coercivity increases, goes through a maximum, and then tends towards zero.
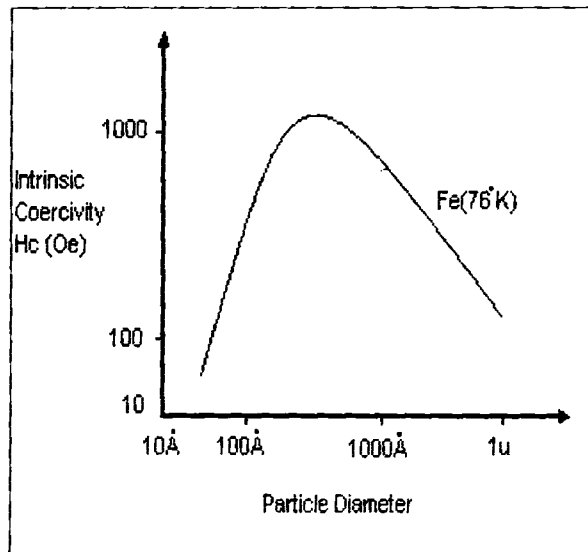
Fig. 2.1: Variation of coercivity with particle size

Beginning at large sizes, we can distinguish the following regions:

1. Multidomain: magnetization changes by domain wall motion. For most materials the size dependence of the coercivity is experimentally found to be given approximately by

$$H_{ci} = a + \frac{b}{D}$$
2.3

where a and b are constants

40

2. Single-domain: Below a critical distance D_s, which is not well defined, the particles become single domains, and in this size range the coercivity reaches a maximum. Particle of size D_s and smaller change their magnetization by spin rotation, but more than one mechanism of rotation can be involved.

    a. As particle size decreases below D_s the coercivity decreases, because of thermal effects, according to

$$H_{ci} = g - \frac{h}{D^{3/2}}$$

2.4

   where g and h are constants.

    b. Below a critical diameter D_p the corecivity is zero, again because of thermal effects, which are now strong enough to spontaneously demagnetize a previously saturated assembly of particles. Such particles are called superparamagnetic.
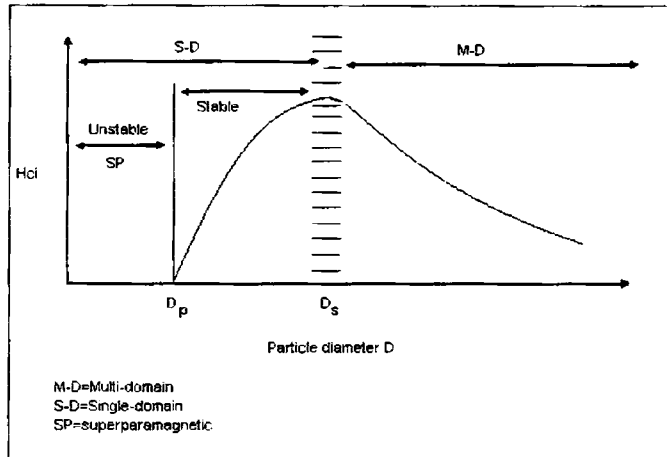
Fig. 2.2 Variation of intrinsic corecivity H_{ci} with particle diameter D (schematic)

2.1.7 Superparamagnetism

   In ferromagnetic materials there is spontaneous magnetization, which arises due to the interaction between the neighbouring atomic magnetic dipoles. It is called spin exchange interaction and is present in the absence of external magnetic field. The

41

exchange interaction aligns the neighbouring magnetic dipole moments parallel to one another and this spreads over a finite volume of the bulk. This small volume is called the domain. Each domain is spontaneously magnetized, the magnetization being appropriate to temperature T. In an unmagnetised piece of ferromagnet the domains are not aligned. When external field is applied magnetization of the specimen may occur either by the growth of one domain at the expense of another i.e. by the motion of domain walls.

If the size of the ferromagnetic particle is reduced below a critical particle size it would consists of single magnetic domain. This single domain particle is in a state if uniform magnetization at any field. Let us consider such a particle whose total magnetic moment is directed at an angle θ to an applied field H.

a) Isotropic single
domain particle

(b) Single domain particle
with uniaxial anisotropy
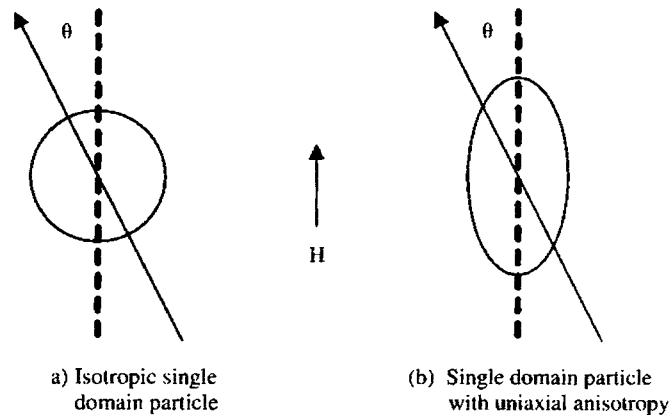
Fig. 2.3 Single domain Particles in magnetic field

For the sake of simplicity let us consider only one preferential direction (direction of easy magnetization) and let us call V the particle volume and θ the angle between the easy axis and the magnetic moment directions. The anisotropy energy,

$$E = KV\sin^2\theta \qquad\qquad 2.5$$

K is also sometimes called anisotropy constant but one must keep in mind K may depend drastically on temperature.

Consider an assembly of aligned uniaxial particles that are fully magnetized along the easy symmetry axis. After the field is removed the resulting remanance will vanish as,

$$M_r = M_s \exp\left(-\frac{t}{\tau}\right)$$

2.6

M_s is the full magnetization

t is the time after the removal of field

τ is the relaxation time for the process

The relaxation time is given by

$$\frac{1}{\tau} = f_0 \exp\left[-\frac{KV}{kT}\right]$$

2.7

As the particle volume V becomes smaller, the relaxation rate increases. Hence let us consider an observation time τ_m, characteristic of the measurement technique. If τ_m >>τ, the measurement result is averaged over a great number of reversals. For example under zero fields the magnetic moment of a particle is averaged to zero. This is the superparamagnetic state. If $\tau m <<\tau$, the magnetic moment appears blocked in one of the two directions of the easy axis. This is the blocked state. Hence, depending on the values of the anisotropy constant, the particle volume and the characteristic measurement time, it may be possible to evidence the transition from the superparamagnetic to the blocked regime by decreasing the temperature. The temperature at which this transition occurs is called the blocking temperature [2,4,8].

However the two main aspects of superparamagnetism are

1. Magnetisation curves measured at different temperatures superimpose when M is plotted as a function of H/T.
2. There is no hysteresis, i.e., both the retentivity and corecivity are zero.

2.1.8 Thermal equilibrium properties of single domain particles.

Consider a particle whose total magnetic moment μ is directed along an angle θ to an applied field H. If there are no anisotropic terms in the energy, the energy of this particle is $-\mu H\cos\theta$. In nature, single domain particles are not fully isotropic in their properties, but will have anisotropic contributions to their total energy associated with the external shape of the particle, imposed stresses or the crystal structure itself. Consider an anisotropy that is uniaxial in symmetry of the form: $E_k = KV \sin^2\theta$. Here θ is the angle between the moment and the symmetry axis of the particle, V is the volume of the particle and K is the anisotropy energy per unit volume. For an applied field H along the symmetry axis, the energy of the particle is given by: $KV \sin^2\theta - \mu H\cos\theta$. Here we have a

different Boltzmann distribution of θ's in thermal equilibrium than we had with out the anisotropy term and the magnetization curve will no longer be a simple Langevin function [2,4].

2.1.9 Approach to thermal equilibrium.

Consider an assembly of aligned uniaxial particles that are first fully magnetized along the easy symmetrical axis On the removal of the field, the resulting remanance will vanish as $M_r = M_s \exp(-t/\tau)$ where Ms is the saturation magnetization, t is the time after removal of the field and τ is the relaxation time for the process, given by

$$\frac{1}{\tau} = f_0 \, exp \, (-KV/kT), \qquad\qquad 2.8$$

where f_0 is the frequency factor of the order of 10^9 sec^{-1}. To approach the thermal equilibrium, a sufficient number of particles should be reversed by thermal activation over the energy barrier KV, the probability of which process is proportional to exp (-KV/kT).

For particles with an anisotropy of cubic symmetry, the energy barrier between adjacent easy directions will appear in the exponential. Using standard definitions of the first order cubic anisotropy constant, the barrier is KV/4 for K>0.([100] easy direction)

Because of the exponential dependence of τ on particle volume, there is a fairly well defined particle size at which the transition to stable behaviour occurs. There will be in general, only a narrow range of particle sizes in which the relaxation times, for which measurable "magnetic viscosity" effects would be expected. As a rough measure of the size corresponding to τ = 10^2 sec. This occurs when the energy barrier is equal to approximately 25KT. For a given particle, the temperature at which this occurs has been called the "blocking temperature".

Consider an assembly of uniaxial particles which is in an initial state of magnetization M_i by an applied field. Now the field is reduced to zero at a time t=0. Some particles in the assembly will reverse their magnetization as their thermal energy is larger and the magnetization of the assembly tends to decrease. The rate of decrease at any time is proportional to the magnetization existing at that time and the Boltzmann factor.

Therefore

$$-\frac{dM}{dt} = f_0 M e^{\frac{-KV}{kT}} = \frac{M}{\tau} \qquad 2.9$$

The proportionality factor is called the frequency factor and it has a value of $10^9 sec^{-1}$.

The constant τ is called the relaxation time.

Rearranging the above equation and integrating we arrive at

$$M_r = M_i e^{\frac{-t}{\tau}} \qquad 2.10$$

and hence relaxation time τ can be defined as the time for remanence M_r to decrease to 1/e of its initial value. From equation 2.99, we can write

$$\frac{1}{\tau} = f_0 e^{\frac{-KV}{kT}} \qquad 2.11$$

Thus it is clear that τ is strongly dependent on V and T.

If we put relaxation time as 100sec, then from equation 2.11 we arrive at

$$\frac{KV}{kT} = 25 \qquad 2.12$$

Hence transition to stable state occurs when energy barrier equals 25kT and also the upper limit of the particle volume for Superparamagnetism for uniaxial particles is given by

$$V_p = \frac{25kT}{K} \qquad 2.13$$

For a particle assembly of constant size there will be particular temperature called the superparmagnetic blocking temperature, below which magnetization will be stable. For a uniaxial particle assembly,

$$T_B = \frac{KV}{25k} \qquad 2.14$$

Now we can consider the effect of an applied field on the approach to equilibrium. Assume an assembly of particles with their easy axis parallel to the z axis. Let it be initially saturated in the +z direction and let us now apply a field in the −z direction. Then the Ms in each particle will make an angle θ with the z axis. Then the total energy per particle is

$$E = V(K\sin^2\theta + HM_s\cos\theta) \qquad\qquad 2.15$$

The energy barrier for reversal is the difference between the maximum and minimum values of E and it can be obtained as

$$\Delta E = KV(1 - \frac{HM_s}{2K})^2 \qquad\qquad 2.16$$

The particles with sizes larger than D_p are stable in zero filed and will not thermally reverse in 100s. But when the field is applied the energy barrier can reduce to 25kT. This will be the coercivity and is given by

$$\Delta E = KV(1 - \frac{H_{ci}M_s}{2K})^2 = 25kT \qquad\qquad 2.17$$

$$H_{ci} = (\frac{2K}{M_s})\left[1 - (\frac{25kT}{KV})^{1/2}\right] \qquad\qquad 2.18$$

When V is very large or T is zero $H_{ci}=(2K/M_s)$

Putting this limiting value as

$H_{ci,0}$ and substituting for $25k_BT/K$ as V_p, we get

$$h_{ci} = \frac{H_{ci}}{H_{ci,0}} = 1 - (\frac{V_p}{V})^{1/2} = 1 - (\frac{D_p}{D})^{3/2} \qquad\qquad 2.19$$

Similarly equation (2.19) can also be used for variation of coercivity with temperature for particles of constant size. For this we assume that particle with critical size V_p have zero coercivity at their blocking temperature T_B.

We get

$$h_{ci} = \frac{H_{ci}}{H_{ci,0}} = 1 - (\frac{T}{T_B})^{\frac{1}{2}}$$ 2.20

Particles larger than V_P have finite retentivity as thermal energy cannot reverse their magnetization in 100s. To find a relation between retentivity and size we can combine equations 2.9 and 2.10 to get

$$\ln\frac{M_r}{M_i} = -\frac{t}{\tau} = -10^9 e^{-KV/kt}$$

2.21

which gives the grain size dependence of magnetic properties which varies with temperature [2,4].

2.1.10 Spin-Glass and spin glass clusters

Crystalline alloys comprising of a small percentage of the magnetic ions in a nonmagnetic matrix show some peculiar magnetic behaviour when cooled below a critical temperature T_f, the spins can order speromagnetically and this effect is named as spin glass freezing typical examples being Fe or Mn in Cu or Au matrix. A characteristic feature of the so called spin glass, is that a cusp is seen in the low field susceptibility - temperature curve at T_f. As the constituent elements in glass are frozen randomly, the spins are frozen at random in this alloy and hence the name spin-glass.

For a single domain particle, below a critical volume, the energy barriers become comparable to the thermal energy and thus a total magnetic moment of the particle can fluctuate between the easy directions. In real systems the moments of the particles interact between them and there is always a particle size and shape distribution, as well as distribution of particle environments, depending on the topology of the system. This leads to a distribution of the total energy barriers of particles, because of the different values of the various contributions and thus to a distribution of the blocking temperature T_B. At enough low temperatures ($T<T_{Bmin}$), below which all the particles moments are blocked along their anisotropy axes, (small fluctuations around them are still possible: collective magnetic excitations) a disordered magnetic arrangement will result, recalling the frozen disordered magnetic state of spin-glass systems.

Neel superparamagnetic model was proposed to explain the macroscopic properties of the spin glass state which implies the existence of a distribution of magnetic

clusters, the passage from the paramagnetic to spin-glass state is described in terms of a progressive blocking of clusters moments [2].

2.1.11 Surface magnetism

Fine particles provide an attractive platform for the study of the magnetic properties at the surface. They possess variety of advantages over the thin films. Their Surface to volume ratio is very high and can be varied over a relatively wide range. It may be possible to distinguish between the surface, close to surface and bulk properties. Also fine particles have only one interface while, thin films have two and at least one of these, contact with the substrate. Interface of fine particles are of vacuum, gas, liquid or solid surfactant, or the contact with a binder. Fine particles may be superparamagnetic, a phenomenon that depends on both the volume and the anisotropy. Any change in the surface anisotropy can be monitored by superparamagnetism measurements. They are widely employed in a number of applications, for example magnetic fluids, particulate magnetic-recording media, and catalysis in which the surface properties may be important.

The determination of the saturation magnetization M_s, of fine particles is one way of seeking information on the magnetic structure near the surface. A saturation magnetization less than the bulk value suggest that a change in the dipole arrangements has occurred. Mossbauer spectroscopy provides a rather direct way for the investigation of magnetic structures. Fine particles can also contribute to determination of the hyperfine field magnitude at the surface. The chemical composition or the morphology is the most important factor influencing the non-collinear magnetic structure in fine particles. Particle morphology is important, and must be considered in any detailed analysis of surface magnetism [8-10].

2.2 Dielectric studies

Dielectric measurements provide an insight into the conduction mechanism on these nanomaterials. The dielectric results are important when we intend to apply these materials in electronic applications.

A material is said to be dielectric if it has the ability to store energy when an external electric field is applied. If a dc voltage source is placed across a parallel plate

capacitor, more charge is stored when a dielectric material is inserted between the plates than if no material is between the plates. The dielectric material increases the storage capacity of the capacitor by neutralizing charges at the electrodes, which ordinarily would contribute to the external field.

In any dielectric material there will be some power loss because of the work done to overcome the frictional damping forces encountered by the dipoles during their rotations.

If an AC sinusoidal voltage source is placed across the capacitor, the resulting current will be made up of a charging current and a loss current that is related to the dielectric permittivity. Here we are interested only in the relative permitivity (ε_r) of the material. Relative permittivity describes the interaction of a material with an electric field. The complex relative permittivity is given by

$$\varepsilon_r^* = \frac{\varepsilon^*}{\varepsilon_0} = \frac{\varepsilon^1 - j\varepsilon^{11}}{\varepsilon_0} \qquad\qquad 2.22$$

Where 'ε_0' is the permittivity (electric constant) of free space, which is 8.854×10^{-12} F/m in SI units. The real part of dielectric permittivity (ε^1) is a measure of how much energy from an external electric field is stored in a material. The imaginary part of the dielectric permittivity (ε_r^{11}) is called the loss factor. It is a measure of the energy dissipation or heat generation in the material when an external electric field is applied. The dielectric loss is given by,

$$\text{Tan}\delta = \varepsilon''/\varepsilon' \qquad\qquad 2.23$$

The dielectric properties of the nanomaterials prepared were studied by using a homemade conductivity cell and an impedance analyzer (Model: HP 4285A) in the frequency range 100 KHz to 8 MHz. The samples prepared were made in the form of pellets of 12mm diameter and is loaded in to the dielectric cell. The capacitance values at different frequencies ranging from 100 KHz to 8 MHz were noted.

The dielectric constant was calculated using the formula

$$\varepsilon_r = \frac{Cd}{\varepsilon_0 A} \qquad\qquad 2.24$$

where 'A' is the area of cross section of the sample pellet, 'd' is the thickness, 'ε_0' and 'ε_r' are the dielectric permittivity of the air and sample material respectively and 'C' is the measured capacitance.

A capacitor when charged under an ac voltage will have some loss current due to ohmic resistance or impedance by heat absorption. If 'Q' be the charge in coulombs due to a potential difference of 'V' volts between two plates of a capacitor of area of A and inter plate distance is 'd', then ac conductivity (σ_{ac}) due to ac voltage $v(v_0\,e^{\,j\omega t})$ is given by the relation

$$\sigma_{ac} = \frac{J}{E} \qquad\qquad 2.25$$

where 'J' is the current density and 'E' is the electric field strength vector. But we know that the electric field vector

$$E = \frac{D}{\varepsilon} \qquad\qquad 2.26$$

where 'D' is the displacement vector of the dipole charges. 'ε' is the complex permittivity of the material. Also the electric field intensity (E) for a parallel plate capacitor is the ratio of potential difference between the plates of the capacitor and the inter plate distance.

$$E = \frac{V}{d} \qquad\qquad 2.27$$

Since the current density $J = \dfrac{dq}{dt}$ where q is given by $\dfrac{Q}{A} = \dfrac{V\varepsilon}{d}$

$$\therefore J = \frac{dq}{dt} = \frac{d}{dt}\left(\frac{V\varepsilon}{d}\right) = \frac{\varepsilon}{d}\frac{dV}{dt}$$

$$\therefore J = \frac{\varepsilon}{d}Vj\omega \qquad\qquad 2.28$$

Substituting for E and J in equation

$$\sigma_{ac} = \frac{J}{E} = \varepsilon j\ \omega \hspace{4cm} 2.29$$

Since 'ε' being a complex quantity

$$\sigma_{ac} = (\varepsilon' - j\varepsilon'')j\omega\ = \varepsilon\ j\ \omega + \omega\ \varepsilon'' \hspace{2cm} 2.30$$

To make ac conductivity a real quantity the term containing 'j' has to be neglected hence

$$\sigma_{ac} = \omega\ \varepsilon'' \hspace{5cm} 2.31$$

Substituting ε'' from equation

$$\sigma_{ac} = \omega\ \varepsilon'\tan\delta \hspace{4cm} 2.32$$

Putting $\varepsilon' = \varepsilon_0\varepsilon_r(\omega)$ as a frequency dependant term, and substituting $\omega = 2\pi f$,

$$\sigma_{ac} = 2\pi f\ \tan\delta\ \varepsilon_0\ \varepsilon_r(\omega) \hspace{3cm} 2.33$$

This equation is used to calculate the ac conductivity by employing the values of dielectric constant and tan δ at a given frequency [11-13].

2.3 Theory of microwave absorption

Microwaves constitute only a small portion of the electromagnetic spectrum, but the applications have become increasingly important to the investigate the material properties. Measurement of material properties like permeability, permittivity, conductivity etc will serve as a tool for investigating the intermolecular and intra molecular mechanisms of compounds.

Bethe and Schwinger suggested the cavity perturbation theory for the first time. According to them, the perturbation was caused by the insertion of small dielectric sample in to the cavity and by a small deformation of the boundary surface of the cavity. By quantifying the perturbation occurred, various material properties can be measured. The fundamental idea is that the change in the overall configuration of the electromagnetic fields upon the introduction of the sample must be low. Based on this

assumption, detailed derivation of the perturbation equation for the frequency shift upon introduction of a sample into a cavity was given by Waldron and Harrington.

The permittivity and permeability of a material in general is a complex quantity such as $\varepsilon_r = \varepsilon_r' - j\varepsilon_r''$ and $\mu = \mu' - j\mu''$. The real and imaginary part of the permittivity are obtained from the perturbation equation for the frequency shift as,

$$\varepsilon_r' + 1 = \frac{(f_0 - f_s) V_c}{2 f_s} \frac{V_c}{V_s} \qquad\qquad 2.34$$

$$\varepsilon_r'' = \frac{V_c}{4 V_c} \left(\frac{1}{Q_s} - \frac{1}{Q_0} \right) \qquad\qquad 2.35$$

Here Q_0 and f_0 represent the quality factor and resonance frequency of the cavity in the unperturbed condition respectively. Q_s and f_s are the corresponding parameters of the cavity loaded with the sample.

To study the dielectric properties of liquid, a container is required. For this purpose, a capillary tube of low- loss, fused silica is used. If the frequency shift is measured from the resonance frequency f_t of the cavity loaded with an empty capillary tube rather than that with an empty cavity alone, the above equation becomes

$$\varepsilon_r' + 1 = \frac{(f_t - f_s) V_c}{2 f_s} \frac{V_c}{V_s} \qquad\qquad 2.36$$

$$\varepsilon_r'' = \frac{V_c}{4 V_c} \left(\frac{1}{Q_s} - \frac{1}{Q_t} \right) \qquad\qquad 2.37$$

Here, Q_t represent the quality factor of empty tube.

Similarly, the real and part of the complex permeability is given by,

$$\mu_r' + 1 = \left(\frac{\lambda^2_g + 4a^2}{8a^2}\right)\frac{(f_t - f_s)}{f_s}\frac{V_c}{V_s} \qquad 2.38$$

where f_s and f_t are the resonant frequencies of the cavity with the sample and with the empty tube, respectively and a represent the λ_g is the guided wavelength and is given by

$$\lambda_g = \frac{2d}{p} \qquad 2.39$$

where $p = 1,2,3,......$

2.4 Electron States in a crystal

Probabilities of optical transitions in molecules and crystals are determined by the properties of atoms and their spatial arrangement. Electron in a solid possesses a set of energy levels which results in narrow absorptions and emissions. Elementary excitations in an electron subsystem of a crystal, that is an electron and a hole, possess many properties of free particles.

A lot of features connected with the absorption of light can be studied by the quantum confinement approach. In this approach, a nanocrystal is considered as a three dimensional potential box in which photon absorption and emission results in an electron subsystem [14-16].

2.4.1 Particle in a potential well

To understand different confinement mechanisms, a quantum mechanical approach is necessary. Time dependant Schrödinger equation for an electron in a one dimensional potential well can be written as

$$-\frac{\eta^2}{2m}\frac{\partial^2}{\partial x^2}\psi(x) + U(x)\psi(x) = E\psi(x) \qquad 2.40$$

where 'm' is the particle mass, E is the energy and the potential U(x) is of the form of a rectangular well of infinitely high walls. By elementary quantum mechanics, the solutions of even and odd types are of

$$\psi^{(-)} = \frac{\sqrt{2}}{\sqrt{a}}\cos\frac{1}{\eta}\sqrt{2mE} \quad \text{(for n=1,3,5............)} \qquad 2.41$$

$$\psi^{(+)} = \frac{\sqrt{2}}{\sqrt{a}}\sin\frac{1}{\eta}\sqrt{2mE} \quad \text{(for n=2,4,6............)} \qquad 2.42$$

The most important result obtained through this approach is that it gives discrete values for
energy levels.

$$E_n = \frac{\pi^2\eta^2}{2ma^2}n^2 \qquad 2.43$$

which means that there is no zero point energy. If a particle exists the quantity $\psi^*\psi$ must be nonzero somewhere. So no state with n=0 is admissible

Thus the particle is restricted to a region of space $\Delta x = a$. Hence uncertainty in momentum is $\Delta p \geq \eta/2a$.

2.4.2 Particle in a spherically symmetric potential well

For a spherically symmetric potential well, Schrödinger equation can be rewritten as

$$-\frac{\eta^2}{2m}\nabla^2\psi + U(r)\psi = E\psi \qquad 2.44$$

where '∇' has its usual meaning in spherical polar coordinate.

Here energy eigen states are spherical harmonics, and the state is represented by three quantum numbers, *n,l*, and *m* [16]. However as the radial function is insensitive to inversion, (r remains the same), energy eigen values are

$$E_{nl} = \frac{\eta^2\chi_{nl}^2}{2ma^2} \qquad 2.45$$

2.4.3 Electron in a Coulomb potential well

For a particle in a Coulomb type potential well, the potential assumes the form

$$U(r) = -e^2/r \qquad 2.46$$

Then the Schrödinger equation for radial part of the wave function can be written as

$$[\frac{d^2}{d\rho^2} + \varepsilon + \frac{2}{\rho} - l(l+1)]u(\rho) = 0 \qquad\qquad 2.47$$

$$\rho = \frac{r}{a_0} \text{ , and } \varepsilon = \frac{E}{E_0}$$

$$a_0 = \frac{\eta^2}{m_0 e^2} \approx 0.5292 \text{ Å} \qquad\qquad 2.48$$

Hence $E_0 \sim 13.6$ eV, where m_0 is the electron mass

$$\varepsilon = -\frac{1}{(n_r + l + 1)^2} \equiv \frac{1}{n^2} \qquad\qquad 2.49$$

where $n=n_r+l+1$ is called the "principal quantum number" which take positive values only from '1'. n_r the radial quantum number determines the quantity of nodes of the corresponding wave function. For every 'n' value, exactly 'n' states exist differing in l, from $0-(n-1)$. Additionally, for every given l value, $(2l+1)$ degeneracy is there for energy values.

Total degeneracy is given by

$$\sum_{l=0}^{n-1}(2l+1) = n^2 \qquad\qquad 2.50$$

The wave function obeys a spherical symmetry with a_0 corresponds to the most probable distance where an electron can be found. For E>0, a particle exhibits an infinite motion with a continuous spectrum and electron and proton experience an infinite motion.

The problem of a 'particle in a spherical potential well' and of 'hydrogen atom' are very important for further consideration. The former is used to model an electron and a hole in a nanocrystal and the latter is essential for excitons in a bulk crystal and in a nanocrystal [16].

2.4.4 Electron in a periodic potential well

Consider a particle in a potential of the type

U(x) = U(x+a) which shows translational invariance, Schrödinger equation can be written as

$$-\frac{\eta^2}{2m}\nabla^2\psi(x+a)+U(x)\psi(x+a)=E\psi(x+a) \qquad 2.51$$

which satisfies the probability criteria

$|\psi(x+a)|^2 = |\psi(x)|^2$ and the solutions for the Schrödinger equation assumes the

form $\psi(x)=e^{ikx}u_k(x)$ and $u_k(x)=u_k(x+a)$ which means that the eigen function of the Hamiltonian with in a periodic potential is a plane wave modulated with the same period as the potential. This is Bloch's theorem.

The wave numbers k_1, k_2 differ by a value

$k_1 - k_2 = \frac{2\pi}{a}n$, where '$n'= \pm1,\pm2,\pm3,\dots\dots\dots\dots$, This is a direct consequence of a

translational symmetry of the space. Therefore, the whole multitude of the k values exists consisting of equivalent intervals

$$-\frac{\pi}{a}<k<\frac{\pi}{a}; \qquad \frac{\pi}{a}<k<\frac{3\pi}{a}; \qquad \frac{3\pi}{a}<k<\frac{5\pi}{a}; \dots\dots\dots$$

with the width of "$2\pi/a$". Each of these intervals contains the full set of the nonequivalent k values and is called "Brillouin Zone". The energy spectrum and the dispersion curve differ from those of a free particle. Dispersion curves have discontinuities at

$$k_n = n\frac{\pi}{a} \qquad 2.52$$

At this k value wave function is a standing wave that arises as a result of multiple reflections from the periodic structure. For every k value satisfying the standing wave solution, two standing waves exist with different potential energies. This gives rise to forbidden energy levels for which no propagating waves exist. We have,

$$E_k = \frac{\eta^2 k^2}{2m^*(k)}$$ where $\hbar k$ is the quasi momentum and m^* is called effective

momentum. For every periodic potential, there exist maxima in the band structure.

If the energy is measured from E_0, that $E_0=0$, the wave number is measured k_0, $dE/dK=0$ at the maximum, we obtain

$$E(k) = \left|\frac{1}{2}k^2\frac{d^2E}{dk^2}\right|_{k=0} + \dots\dots\dots \qquad 2.53$$

Neglecting contribution from terms higher than k^2, we obtain parabolic bands.

$$m^{*-1} = \frac{1}{\eta^2}\frac{d^2 E}{dk^2} = cons\tan t.$$ 2.54

For a free particle, m*=m.

Hence the particle could be described by a plane wave modulated by the periodic potential. Secondly the particle state is characterized by the quasi momentum. The energy spectrum thus consists of wide continuous band separated from each other by forbidden gaps. A particle in a periodic potential exhibits quasi free motion with out acceleration. The particle behaviour can be understood from the effective mass approximation theory.

It has been found from experiments that there are two distinct energy bands in semiconductors. The lower band is almost full of electrons and can conduct by the movement of the empty space, the hole. The band originates from the valance electron state which contributes the covalent bond holding the atom together in the crystal. In many ways, electric charge in a solid resembles a fluid, and the analogy for this and, labeled the valance band is that the empty states behave like bubbles within the fluid-hence their name holes. Analogous to energy bands in bulk materials, in quantum well systems the energy domains associated with confined levels are referred to as "subbands"
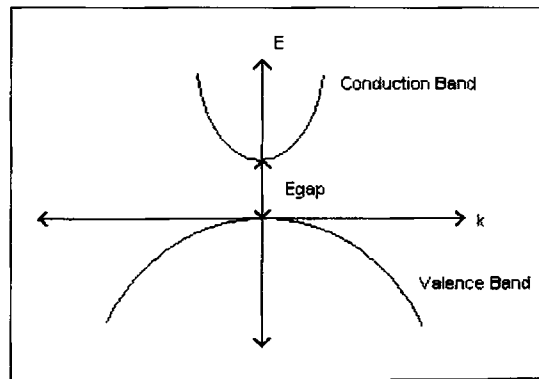
Fig. 2.4 : The energy versus wave vector for an electron in the conduction band and a hole in the valence band.

The energy difference between the two bands is known as the band gap, labeled as E_{gap}. Single quantum wells, stepped quantum wells symmetric and asymmetric double

quantum wells, multiple quantum wells etc are some band alignments which have quantum properties [14-16].

2.5 Quasi particles-electron, hole and excitons (Crystal approximation)

Electrons in conduction band can be represented with charge e, spin ½, and effective mass m* and quasi momentum. $\hbar k$. But electron in a crystal will not have the same values that it possess in vacuum whose properties are governed by several interactions in a many body system in which there are a large number of positive nuclei and electrons. Many body system can be replaced by large number of interacting particles or by small number of non-interacting quasiparticles, which are elementary excitations of the system. Elementary excitation is a *hole* which is a quasiparticle equivalent to an ensemble of electrons in the valence band from which the electron is removed [14,16].

2.6 Excitons

If photon of energy comparable to the band gap are incident on a semiconductor then they can be absorbed by the electrons forming atomic bonds between neighboring atoms, and so provide them with enough energy to break free and move around in the body of the crystal. With in the band theory of solids, this would be described as "exciting an electron from the valence band across the band gap into the conduction band". If the energy of the photon is larger than the band gap, a free electron is created and an empty state is left within the valence band. The empty space within the valence band behaves very much like an air bubble in a liquid and rises to the top-the lowest energy state. This hole behaves as though it was positively charged and hence often forms a bond with a conduction-band electron. The attractive potential leads to a reduction in potential energy of the electron and hole. This bound electron-hole pair is known as an exciton [14-16].

2.7 Crystal to clusters-effective mass approximation

It is reasonable to consider the quasiparticles featuring the properties inherent in an infinite crystal, and then include its finite size effects (of a given crystallite) as the relevant potential jump at the boundaries. As the length parameters of quasiparticles (the De Broglie wavelength and constant a_i) are too small in nanoclusters, particle/quasiparticle wave functions will have vanishing values away from the

boundaries meaning their complete confinements with in that small volume. Therefore, if mesoscopic particles with dimensions comparable to or even less than a_B in one, two or all the three dimensions, due to change in the degree of freedom, and as the hole becoming more and more localized, quasi momentum and hence quasi effective mass changes abruptly for ultra fine particles having all the three dimensions in nanometric regime less than the Bohr radius of exciton.

2.8 Quantum Confinements

In general, three regimes of quantization can be defined depending on whether the charge carriers are confined in 1, 2, or 3 dimensions. Confinement in 1-D creates structures that have been termed as quantum wells; this is because the first such structure could be described by the elemental quantum mechanics of a particle in a one dimensional box; these structures have also been labeled as "quantum films". Carrier confinement in 2-Ds produces "quantum wires", and in 3-D produces "quantum dots" (also called nanocrystals or quantum boxes). The dimensionality of confinement affects many aspects of quantization.

Since their discovery/invention by Esaki and Tsu in the 1970s semiconductor quantum wells and superlattices have evolved from scientific curiosities to a means of probing the fundamentals of quantum mechanics, and more recently into wealth creating semiconductor devices.

For an electron in vacuum away from the influence of electromagnetic fields, the total energy is just the kinetic energy [14-16].

2.8.1 Weak and strong confinements

To reveal the principal quantum confinement effects within the framework of the nanocrystal, it is reasonable to deal with the simplest three dimensional potential well which is the spherical potential box with infinite potential and electrons and holes are considered to possess isotropic effective mass. Then there exist two limiting cases, weak confinement regime and strong confinement regime. Weak confinement regime corresponds to the case when the particle radius is very small, still higher than several times of the exciton Bohr radius a_B. In this case quantization of the exciton centre of mass occurs. A detailed theory is provided in *Chapter 4.*

In strong confinement regime, the grain size is much less than the Bohr radius of the excitons. This means that the confined electron and hole have no bound state corresponding to the hydrogen like exciton and zero point kinetic energy of electron and hole due to strong confinement is much larger resulting in a very high shift in energy band gap. For strong confinements to happen, there should be quantum dot like states with monodisperse grains. Coulomb interactions do not vanish in quantum dots. Moreover the coulomb term contribution to the ground state energy is even greater than in the bulk monocrystal. This is the fundamental difference of quantum dots when compared to a single crystal, quantum well and quantum wire, is that the coulomb energy of an electron and hole pair is zero. Hence elementary excitations in a quantum dot possess high confinement energies. Here it can be seen by energy considerations that the hole is immovable and localized completely at the centre of the dot [16].
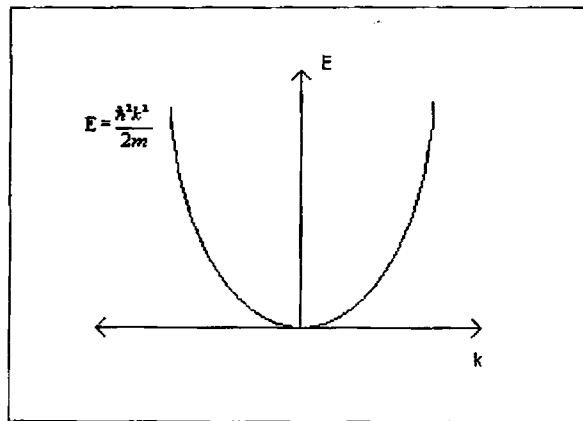
Fig.2.5 Parabolic approximation for filled states (devoid of unharmonic terms)

2.9 Absorption processes in a medium

There are lots of processes which determine optical absorption in a material. They are fundamental absorption, free carrier absorption excitonic absorption etc. This is dealt in detail in the ensuing sections

2.9.1 *Fundamental absorption*

Transitions in which an electron is excited from the valance band to the conduction band with the absorption of photon of energy approximately equal to the energy band gap is known as fundamental absorption. This type of absorptions could be broadly divided into two types, direct transitions and indirect transitions

In a direct band gap material, the minimum of the conduction band occurs at the same value of the wave vector as that of the maximum of the valence band so that the absorption of energy is not a phonon assisted process. But in indirect band gap materials, this condition is not matched and so the absorption process is a phonon assisted process.

2.9.2 *Direct transitions*
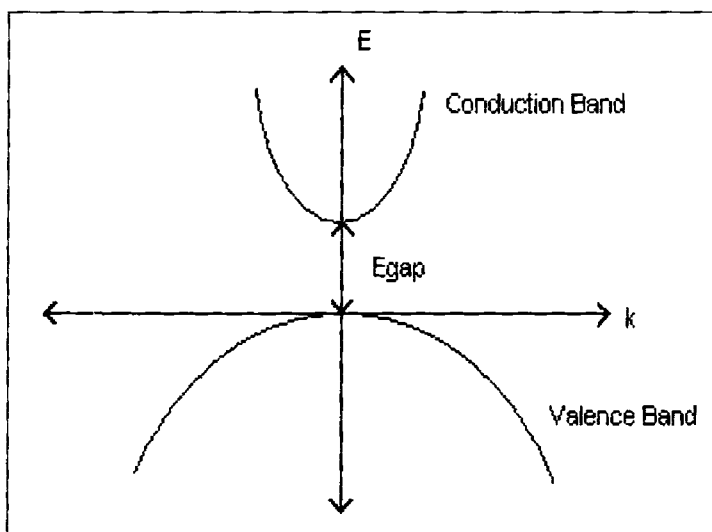
Fig. 2.6 Direct transitions

A direct transition is shown in Fig. 1. It occurs with out practically any change in the wave vector of electron since the wave vector of photon is negligibly small. This process is also termed as vertical transition. (an electron of energy k_BT, at room temperature will possess a wave vector of approximately 10^7 cm^{-1} while a photon in the

infrared has a wave vector of 10^3 cm^{-1} which makes only a negligible change in electronic wave vector according to momentum conservation laws.

Treating the problem quantum mechanically, the transition probability involves the exponent $[exp(i/\eta(E_f-E_i-E_{ph})t]^2$ which is when integrated over time leads to the delta function $\delta(E_f-E_i-E_{ph})$ and thus leads to the energy conservation law

$$(E_f-E_i)=E_{ph} \qquad\qquad 2.55$$

Thus the absorption spectrum has a sharp threshold. The absorption coefficient at frequencies larger than the threshold is given by

$$\alpha = A \ P_k[\ \eta\omega_{ph} -(E_f-E_i)]^{1/2} \qquad\qquad 2.56$$

where P_k is the transition probability. The $E^{1/2}$ dependence arised from the fact that the density of electrons at the top of the valance band is proportional to $E^{1/2}$ and at the bottom of the conduction band it is nearly a constant.

The above analysis assumes that transitions from the valance band states to the conduction band states are allowed. This is so if the valance band wave functions are derived from atomic s-states and the conduction band wave functions from the atomic p-states on the other hand, if they are from 's' and 'd' states, the transitions are forbidden. Even in this case of forbidden transitions, absorption is still possible if it takes place at a wave vector $k \neq 0$.

Then

$$\alpha = A \ P_k[\ \eta\omega_{ph} -(E_f-E_i)]^{3/2} \qquad\qquad 2.57$$

2.9.3 Indirect transitions:

In direct transitions [14-16] occur with a change in electron wave vector which is equivalent to a phonon assisted transitions implied that there is an intermediate level, real or virtual through which absorption process happens with the help of a phonon assisted energy transfer. Hence the absorption spectrum has only a broad threshold

$$\alpha = A \ P_k[\ \eta(\omega_{ph-}\omega_{phonon}) -(E_f-E_i)]^2 \qquad\qquad 2.58$$

2.10 Optical properties of materials.

2.10.1 Optical constants

The propagation of light through a non magnetic medium is determined by the four Maxwell's equations.

To describe optical effects, the wave equation obtained from Maxwell's equations can be written as follows [17],

$$\nabla^2 E = \frac{\varepsilon_1 \partial^2 E}{c^2 \partial t^2} + \frac{4\pi\sigma}{c^2}\frac{\partial E}{\partial t} \qquad \qquad 2.59$$

Consider the solution of the form of plane wave

$$E = E_0 \, exp[i(\, K.r - \omega t)] \qquad \qquad 2.60$$

This leads to,

$$K = \frac{\omega}{c}[\varepsilon_1 + i\frac{4\pi\sigma}{\omega}]^{1/2} \qquad \qquad 2.61$$

A complex quantity refractive index N can now be defined as

$$N = [\varepsilon_1 + i\frac{4\pi\sigma}{\omega}]^{1/2} \qquad \qquad 2.62$$

so that

$$\overline{K} = \frac{\omega}{c/N} \qquad \qquad 2.63$$

The propagation vector is thus modified from the value k=ω/c to $\overline{K} = \dfrac{\omega}{c/N}$ so that the new velocity through the medium comes as

$$v = c/N \qquad \qquad 2.64$$

where N is the complex refractive index of the material which can be expressed as

$$N=n+ik \qquad\qquad\qquad 2.65$$

Squaring (7) and comparing with (5)

$$\left.\begin{array}{l} \varepsilon_1 = n^2 - k^2 \\[2.5em] \dfrac{4\pi\sigma}{\omega} = 2nk = \varepsilon_2 \end{array}\right\} \qquad\qquad 2.66$$

Complex dielectric constant is given by

$$\varepsilon = N^2 = (\varepsilon_1 + i\varepsilon_2) \qquad\qquad 2.67$$

which shows that the dielectric constant and conductivity determines the real and imaginary part of the optical constant N. Real part is often termed as the refractive index 'n' and the imaginary part the extinction coefficient 'k'. Thus propagation of electromagnetic wave through a medium is determined by the optical constants 'n' and 'k'.

Hence when we consider propagation through a medium, it is found that refractive index is no longer an integer, but a complex quantity in which the real part describes the velocity of light in the medium while the imaginary part deals with the absorption of light in the medium both of which are important from the fundamental point of view.

2.10.2 Polarization of light

The phenomenon of polarisation has helped to establish beyond doubt the transverse nature of optical vibrations. Polarisation is the direction of the electric field vector of the light beam when considered as a wave. Ordinary light has optical disturbance in all possible directions. So it can be called as unpolarized light. Optical disturbance can physically be treated as the direction of the electric field vector of the material.

.2.10.2a Linear polarization

Two orthogonal optical disturbances could be explained as

$$E_x = i \ E_{ox} \cos(kz - \omega t)$$ 2.68

$$E_y = j \ E_{oy} \cos(kz - \omega t + \varepsilon)$$ 2.69

where ε is the relative phase difference between the waves.

The resultant optical disturbance could be written as

$$E(z,t) = E_x(z,t) + E_y(z,t)$$ 2.70

The waves will be in phase only when ε is '0' or 2π so that the resultant amplitude is

$$i \ E_{ox} + j \ E_{oy}$$

So they are linearly polarized [17].

2.10.2b Circularly polarized light

If both the constituent waves have equal amplitudes, and their relative phase difference is

$$\varepsilon = -\pi/2 + 2m\pi$$ 2.71

(where m=0,1,2 etc).

$$E = E_0 [i \ \cos(kz - \omega t) + j \ \sin((kz - \omega t)]$$ 2.72

They are right circularly polarized waves for $\varepsilon = 3\pi/2$, $7\pi/2$ etc

If $\varepsilon = \pi/2$, $5\pi/2$, $9\pi/2$ etc. they become left circularly polarized light and the direction is changed and new electric field vector is

$$E = E_0 [i \ \cos(kz - \omega t) - j \ \sin((kz - \omega t)]$$ 2.73

Thus from two circularly polarized lights of opposite polarization direction (a combination of right handed and left handed polarized circular light waves) a linearly polarized light could be generated. Or in converse, any linearly polarized light wave could be treated as a combination of right handedly and left handedly circularly polarized wave.

2.11 Theory of magneto-optical effects

2.11.1 Birefringence and dichroism

Birefringence is the anisotropy in the refractive index measured against parallel and perpendicularly polarized light beams with respect to the applied magnetic field directions while dichroism is the measure of anisotropy in the selective absorptions of the light [17].

Birefringence and dichroism effects in any colloidal suspensions may originate from the intrinsic anisotropy or the shape anisotropy of the individual particles, which are suspended in the base fluid.

In a magnetic fluid to which a magnetic field is applied, the physical process which are likely to occur are that some pre existing aggregates align along the direction of the applied field and with increasing fields, these clusters grow in size resulting long periodic chains, which are responsible for strong magneto optical properties [18-24].

The dichroism of a sample can be explained by the modified version of the classical oscillating dipole model. Here we assume that magnetic particles are optically isotropic spherical and behave like permanent magnetic dipoles forming some linear head to tail aggregates due to static magnetic forces between them. In the electric field of a laser beam (polarized) these individual particles may be considered as oscillating dipoles, which interact with one another, which is symmetric depending upon the orientation of the aggregates to the direction of the light polarization. The asymmetry produces an optical anisotropy, which is the key reason for dichroism in ferrofluids.

Magneto optical properties shown by these smart fluids depend only on the properties of magnetic fine particles that is suspended inside the base liquid. According to Rayleigh theory, particles that are small compared to the wavelength of light will behave like oscillating dipoles when irradiated by a light beam [19]. Excited dipole moments of the particle has the following relationship with local electric field vector of the laser

$$p=\varepsilon_0\alpha E \qquad\qquad\qquad 2.74$$

where 'α' is the polarisability, 'p' the Dipole moment. For an anisotropic medium, 'α' is a tensor.

Consider N such particles are there in the medium. Consider no aggregation is there for the particles. Then 'N' will be the number of dipoles so that the total polarization P can be written as

$$P = Np \qquad 2.75$$

The change in polarization induces a change in refractive index of the medium. The complex refractive index of the sample can be written as

$$N^2 = (1 + N \langle \alpha \rangle) \qquad 2.76$$

where $\langle \alpha \rangle$ is the average polarisability which can be calculated using a statistical distribution which can be related to the distribution of particle size of the particles. For nanosized particles whose size is much lower than the wavelength of the laser used

$$K^2 = \omega^2 \mu_0 \varepsilon_1 (1 + N \langle \alpha \rangle) \qquad 2.77$$
$$n^2 = n_1^2 (1 + N \langle \alpha \rangle) \qquad 2.78$$

where ε_1 is the dielectric constant, n_1 is the refractive index of the carrier.

Assume the particles are fully spherical and cubic so that the intrinsic optical anisotropy is almost neglected. Then electrical polarisability can be written as:

$$\alpha_p = 3 \frac{\varepsilon_p - \varepsilon_1}{\varepsilon_p + 2\varepsilon_1} v_p = \chi_0 v_p \qquad 2.79$$

where v_p is the volume of the particle, ε_1 is the dielectric constant of the carrier, ε_p is the dielectric constant of the particles and χ_0 is the optical polarizability per unit volume.

So far we have been discussing about the isolated particles. But in dense ferrofluids, magnetic particles forms linear aggregates due to the magnetostatic interparticle interactions. The particle in an aggregate forms an array of oscillating dipoles when acted on by an electric field. The dipoles interact with each other.

Now consider aggregates consisting of only two dipoles. Then

$$E_p = \frac{1}{4\pi\varepsilon_1 |r_0|^3}[3(p.r_0)r_0 - p_0]$$

2.80

Consider a pair of dipoles. We can take in to account the interaction effects of the dipole moments p_1 and p_2.

$$p_1 = \varepsilon_1\alpha_p(E + E_{p2})$$ 2.81a

$$p_2 = \varepsilon_1\alpha_p(E + E_{p1})$$ 2.81b

Taking the interaction also into account, we can write the total dipole moment as

$$P = \varepsilon_1\overline{\alpha_p}E_0$$

2.82

$$\overline{\alpha_p} = \begin{matrix} \alpha_\perp & 0 & 0 \\ 0 & \alpha_\perp & 0 \\ 0 & 0 & \alpha_x \end{matrix} \qquad \text{is a tensor.}$$

2.83

$$\alpha_\perp = \frac{2\chi_0 v_p}{1 + k_\perp\chi_0}$$

2.84a

$$\alpha_\Pi = \frac{2\chi_0 v_p}{1 - k_\Pi\chi_0}$$

2.84b

Where $k_\perp = \frac{v_p}{4\pi d^3}$ and $k_\Pi = 2k_\perp$

So interaction of two dipoles produces an anisotropic polarizability giving rise to magnetic field induces optical effects. The complex refractive index now becomes a tensor with its diagonal values non-vanishing

$$n_x^2 = n_1^2\{ 1 + N[\alpha_\perp + (\alpha_{11} - \alpha_\perp)\langle\sin^2\theta\cos^2\phi\rangle]\}$$ 2.85a

$$n_y^2 = n_1^2\{ 1 + N[\alpha_\perp + (\alpha_{11} - \alpha_\perp)\langle\sin^2\theta\sin^2\phi\rangle]\}$$ 2.85b

$$n_z^2 = n_1^2\{ 1 + N[\alpha_{11} + (\alpha_{11} - \alpha_\perp)\langle\cos^2\theta\rangle]\}$$ 2.85c

Here θ is the angle that the symmetry axis making with z axis and φ is the angle between the projection of the symmetry axis on y direction and the x-y plane make with the x axis. Now the change in refractive index is given by: $\Delta n = n_z - n_y$

$$\Delta n \approx \frac{1}{2} n_1 N(\alpha_x - \alpha_\perp) \int (\cos^2\theta - \sin^2\theta \sin^2\phi) f(\theta,\phi) d\theta.d\phi \qquad 2.86$$

where f(θ,φ) denotes the orientation of the particles which obey a Boltzmanian function.

$$f(\theta,\phi) = A \exp(U / kT) \qquad 2.87$$

and;

$$A \int \exp(\frac{U}{kT}) d\theta.d\phi = 1 \qquad 2.88$$

U= -2μH cosθ, which is the potential energy of a pair of magnetic particles constituting a dipole having a magnetic moment 2μ in the applied magnetic field and θ is the azimuthal angle of the symmetry axis of a pair of dipoles with respect to the applied field.

$$\Delta n \approx \frac{1}{2} n_1 N(\alpha_x - \alpha_\perp)[1 - \frac{3}{x}\coth(x) + \frac{3}{x^2}] \qquad 2.89$$

ie, $$\Delta n \approx \frac{1}{2} n_1 C(\chi_\Pi - \chi_\perp)[1 - \frac{3}{x}\coth(x) + \frac{3}{x^2}] \qquad 2.90$$

where C=N v_p and x= 2μH/kT,

So the refractive index change depends mainly on the orientation of the particles and the applied magnetic fields.

In the weak field region, we can approximate this in to,

$$\Delta n = \frac{15}{2} n_i C(\chi_{\parallel} - \chi_{\perp}) x^2 \qquad\qquad 2.91$$

which is linearly proportional to the square of the applied field strength in the low field approximation and the anisotropy in the susceptibility. This change in refractive index results in birefringence while anisotropy in the optical absorption of ordinary and extra ordinary rays results in dichroism for a sample.

2.11.2 Faraday Rotation and Faraday Ellipticity

The Faraday rotation is the first indirect observation that domains exist inside a magnetic material [17-20]. A transparent optical medium when placed in a powerful magnetic field, acquires the property of rotating the plane of polarization when light traverses the medium in the direction of the lines of magnetic forces. Thus Faraday rotation is the rotation of plane of polarization of light by the medium in presence of a magnetic field. It differs from natural optical activity in the sense that it depends on the polarization direction of light as well as the direction of magnetic force of lines. So in Faraday rotation, the rotating angle doubles when the light is allowed to be reflected back through the medium.

The rotation could be explained by analyzing the plane polarized light beam divided into two circularly polarized light beam traveling with varying velocity. Generally for a non magnetic material, the rotation is observed to be dependant on the applied magnetic field strength. But if the material is ferromagnetic in nature, this quantity will be dependant on the saturation magnetization of the sample. This is because in other materials, the dia/para magnetic susceptibility is negligibly small so as to interact with the polarization direction of light used. But in ferro/ferri magnetic materials, the magnetic moment is so large, so that the rotation will be a function of magnetic moment strictly (as the material gets magnetized with applied magnetic field along the field direction until a saturation in magnetization is attained). As the suspended particles are magnetic in nature, the rotation angle will depend on the domain structure and magnetic moment of the fine magnetic particles. So rotation will be dependant on the saturation magnetization of the sample if the sample is a ferromagnetic one.

The angle through which the plane of vibration is rotated is given by the relation

$$\theta = VBd, \qquad\qquad\qquad 2.92$$

where 'V' is Verdet's constant, B is the flux density of the applied field.

Assume when the incident light is circularly polarized and monochromatic, an elastically bound electron will take on a steady state circular orbit driven by the electric field of the light beam. The introduction of large constant applied field perpendicular to the plane of orbit will result in a radial force on the electron. Thus for a given magnetic field, there can be two possible value of the electric dipole moment, polarization and permittivity, and hence refractive index due to the fact that the force can either point towards or away from the circle centre.

Primarily Faraday rotation was observed for transparent isotropic materials so that there was negligible amount of absorption within the material. Then polarization direction is altered due to the difference in velocity of the right and left handed circularly polarized beams. However if light suffers an absorption loss with in the material which is non negligible, the additional relative absorption change of the two beams will result in a change in the shape of the index ellipsoid into an elliptically polarized beam.

Faraday ellipticity is the anisotropy in absorption of a sample when place in a magneto-longitudinal mode of applied field. As the applied field increases, the rotation of plane of polarization increases. This gives the linearly polarized light to be converted in to an elliptically polarized light. The angle through which the plane of polarization is turned is a function of the length of the path of light through that medium and so it is dependant on the sample cell thickness and concentration.

2.12 Non linear optical properties of materials.

2.12.1 The Regime of Linear Optics:

Nonlinear optics is a study that deals mainly with various new optical effects and novel phenomena arising from interactions of intense coherent optical radiation with matter. Nonlinear optical effects could not be experimentally observed in the pre-laser era, since the field strengths of conventional sources have been much too small to perturb the atomic and inter atomic fields. Naturally, light waves with low intensities are not able to affect atomic fields to the extent of changing optical parameters. Thus the assumption of linearity of an optical medium has the following far reaching consequences: the optical

properties, such as the refractive index and the absorption coefficients are independent of the light intensity; the frequency of light cannot be altered by its passage through the medium; and light cannot interact with light; that is, two beams of light in the same region of a linear optical medium have no effect on each other.

The nonlinear optical properties of materials play a crucial role in today's technology .For example, optical switching which is necessary for optical computing maybe realizable via the non-linear processes of materials. Another example is optical storage, where laser light is used as a means of reading or writing information. If the wavelength of the laser light is halved the storage capacity of the device will quadruple. This may be achieved by frequency doubling the fundamental wavelength in a nonlinear material through nonlinear second harmonic generation. Clearly, the nonlinearity of materials enhances our optical capability and allows us to improve our optical devices [25-31].

The behavior of a dielectric medium through which an electromagnetic (optical) wave propagates is completely described by the relation between the polarization density vector $P(r,t)$ and the electric field vector $E(r,t)$. A transparent dielectric medium placed in an electric field becomes electrically polarized, and the displacement of the electron density away from the nucleus results in a charge separation (an induced dipole) with dipole moment P_i . With small applied fields the linear response approximation holds, so that the displacement of charge from equilibrium position is proportional to the strength of the field;

$$P_i = \alpha' E \qquad\qquad 2.93$$

here α' is the linear polarizability of the molecule or atom, and E is the applied electric field. If the field oscillates with a frequency then the induced polarization will have the same frequency and phase if the response is instantaneous. Also, the dipole moment vector per unit volume (i.e. the polarization density) P is given by $P = \Sigma P_i$, where the summation is over the dipoles in unit volume. For a linear dielectric medium,

$$P = \varepsilon_0 \chi E \qquad\qquad 2.94$$

where ε_0 is the permittivity of free space and χ is the dielectric susceptibility of the medium. The quantity χ is a constant only in the sense of being independent of E; its magnitude is a function of frequency.

2.12.2 Nonlinear Optics:

However, after the advent of lasers, the coherence of the laser beam enabled an examination of the behavior of light in optical materials at intensities higher than that was previously possible. Irradiation of a medium with high intensity laser radiation is, in principle equivalent to the application of a large electric field to the material. Many experiments revealed that the optical media do in fact exhibit nonlinear behavior. Under such circumstances the following phenomena takes place

The refractive index consequently the speed of light in an optical medium does change with intensity

1. Light can alter its frequency as it passes through a nonlinear optical material
3. Light can control light; photons can be made to interact.

Thus, when a molecule is subjected to strong laser radiation, the molecule's polarization is being driven beyond the linear regime. The modified nonlinear polarization P_m (which is a function of the applied field and leads to nonlinear effects) is expressed as

$$P_m=\alpha'E+\beta'E^2+\gamma'E^3+\ldots\ldots\ldots\ldots \qquad 2.95$$

where,

α'= linear polarizability of the molecule or atom

β'= first molecular hyperpolarizability (second order nonlinearity term)

γ'= third order nonlinearity term

E= electric field acting on the molecule

With increasing field strength, nonlinear effects become observable due to the presence of the higher powers of E in eqn.2.95. (α is usually much greater than β and γ) Eqn.2.94 also gets generalized to

$$P_m=\varepsilon_0(\chi^{(1)}E+\chi^{(2)}E^2+\chi^{(3)}E^3+\ldots\ldots) \qquad 2.96$$

where $\chi^{(1)}$ is the first order susceptibility ,and $\chi^{(n)}$ is the nth order nonlinear optical susceptibility. Thus optical characteristics of a medium such as dielectric permittivity, refractive index, etc, which depend upon susceptibility, also become functions of the field strength E. It may be noted here that optical nonlinearity is a property of the medium through which light travels, rather than a property of light itself.

Suppose that the field incident on a medium has the form $E=E_0 \cos(\omega t)$ .Putting this in eqn.2.96 we get,

$$P = \varepsilon_0 \left(\chi^{(1)}E_0 \cos(\omega t) + \chi^{(2)}E_0^2 \cos^2(\omega t) + \chi^{(3)}E_0^3\cos^3(\omega t) + \ldots\ldots\ldots\ldots\right) \quad 2.97$$

Using the trigonometric relations,

$$\cos^2(\omega t) = [1+ \cos(2\omega t)] / 2 \text{ and } \cos^3(\omega t) = [\cos(3\omega t) + 3\cos(\omega t)] /4 \qquad 2.98$$

the above relation can be written as,

$$P=(1/2)\ \varepsilon_0\chi^{(2)}E_0^2 + \varepsilon_0[\chi^{(1)} +((3/4)\chi^{(3)}E_0^2]\ E_0\cos(\omega t) + (1/2)\varepsilon_0\ \chi^{(2)}\ E_0^2\cos^2\ (2\omega t) +$$
$$(1/4)\varepsilon_0\chi^{(3)}E_0^3\cos(3\omega t)+\ldots\ldots\ldots\ldots \qquad\qquad 2.99$$

The first term is a constant term. It gives rise to a d.c.field across the medium, the effect of which is of comparatively little practical importance. The second follows the external polarization and is called first or fundamental harmonic of polarization; the third oscillates at a frequency 2ω and is called the second harmonic of polarization; the fourth is called the third harmonic of polarization and so on.

These higher harmonics of the dielectric polarization, results from the optical nonlinearity of the medium, leads to various optical nonlinear phenomena. Some of these effects are discussed below.

2.12.3 Second Order Nonlinearity:

In the case of anisotropic materials (e.g.: uniaxial crystals), all the quadratic, cubic and higher order terms will be active. However, generally the cubic and higher

order terms are substantially smaller than the second order term and may be ignored. For such materials, we can write

$$P = \varepsilon_0(\chi^{(1)}) E + \chi^{(2)} E^2) \qquad 2.100$$

and the medium is said to have second order nonlinearity.

In anisotropic materials, the polarizability depends on the direction of the beam propagation, polarization of the electric field and the relative orientation of the optic axis. Since the vectors P and E are not necessarily parallel in them, the coefficients must be treated as tensors. The second order polarization, therefore may be represented by a relation of the type

$$P_i^{(2)} = \varepsilon_0 \Sigma\chi^{(2)}_{ijk} E_j E_k \qquad 2.101$$

where, i,j,k represents the coordinates x,y,z. However most of the coefficients χ_{ijk} are usually zero so that normally only one or two components need be taken into account.

2.12.4 Second harmonic Generation

Second Harmonic Generation (SHG) is an important application of the second order optical nonlinearity. It can be shown that when two beams of frequencies ω_1 and ω_2 interact with a second order nonlinear medium, the resultant polarization contains the sum ($\omega_1 + \omega_2$) and the difference ($\omega_1-\omega_2$) frequencies as given through the expression $2\varepsilon_0\chi^{(2)}E_1E_2$ [cos ($\omega_1+\omega_2$)t +($\omega_1-\omega_2$)t]. SHG is the sum of frequency generation when $\omega_1=\omega_2$. The second harmonic beam thus produced is emitted in the same direction as the incident beam.

2.12.5.Third Order Nonlinearity

In case of centro-symmetric materials, i.e., the materials that exhibit inversion symmetry (liquids, gases atomic or molecular vapors etc.) the electric polarization can contain only odd powers of electric field amplitudes. Considering the lowest non-vanishing nonlinear polarization, which is a cubic term in the applied field magnitude, eqn 2.58 reduces to

$$P = \varepsilon_0 \chi^{(1)}E +\varepsilon_0 \chi^{(3)}E^3 \qquad 2.102$$

The third order susceptibility term ($\varepsilon_0 \chi^{(3)}E^3$) will be present with varying strengths in

essentially all optical materials irrespective of structural symmetry. Using the above equation, the electric displacement D in the medium can be written as

$$D = \varepsilon_o E + P = \varepsilon_0(1+\chi^{(1)}) E + \varepsilon_0\chi(3)E^3 = \varepsilon_0(1 + \chi^{(1)} + \chi^{(3)}E^2) E \quad 2.103$$

Now, the dielectric constant is a nonlinearly varying quantity given by $\varepsilon = \varepsilon_1 + \varepsilon_0\varepsilon_2 E^2$ where,

$$\varepsilon_l = \varepsilon_0(1+\chi^{(1)}) \qquad \textit{linear dielectric constant} \qquad\qquad 2.104$$

$$\varepsilon_2 E^2 = \chi^{(3)}E^2 \quad : \quad \text{nonlinear change in dielectric constant produced by the applied}$$
field.

Since, the optical index of refraction n is related to the optical frequency value of ε by
$n = (\varepsilon/\varepsilon_0)^{1/2}$, we can also view this as a nonlinear dependence of refraction on the applied signal strength given by

$$n=n_0+n_2I \qquad\qquad\qquad 2.105$$

where
$n_0 = (\varepsilon_1/\varepsilon_0)^{1/2}$: linear refractive index and
n_2I is the intensity dependent part of the nonlinear refractive index.

The effect depicted by eqn. 2.104 is known as the **optical Kerr effect** because of its similarity to the electro-optic Kerr effect. The optical Kerr effect is a self-induced effect in which the phase velocity of the wave depends on the wave's own intensity.

The order of magnitude of n_2 (in units cm^2/W) is 10^{-16} to 10^{-14} in glasses, 10^{-10} to 10^{-8} in organic materials, 10^{-14} to 10^{-7} in doped glasses and 10^{-10} to 10^{-2} in semiconductors. It is sensitive to the operating wavelength and depends on the polarization. Thus for a centrosymmetric nonlinear medium, the absorption coefficient and the refractive index n must be modified to include intensity dependent terms such that $\alpha(I) = \alpha + \beta I$ and $n= n_0 + \gamma I$, where α (cm^{-1}) and n_0 are the linear terms, and I (W cm^{-2}) is the incident radiation intensity.

The instantaneous two-photon absorption coefficient β (cm W^{-1}) and the nonlinear refractive index parameter γ (cm^2 W^{-1}) are related to the corresponding nonlinear susceptibility by the equations

$$\text{Im } \chi^{(3)} \text{ (esu)} = 10^{-7} c^2 n_0^2 \beta / 96 \, \pi^2 \omega, \text{ and}$$

$$\text{Re } \chi^{(3)} \text{ (esu)} = 10^{-6} c \, n_0^2 \gamma / 480 \, \pi^2,$$

where c is the speed of light in cm/s and ω is the fundamental frequency in cycles/seconds.

2.13 Application of non linear optical properties

The ability to control the intensity of light in a predetermined and predictable manner is a fundamental and important requirement with applications ranging from optical communications to optical computing. Although there are numerous methods that can be used to switch, limit, amplify or modulate the amplitude of an optical signal, all of these may be broadly classified into two groups, viz. dynamic and passive methods. Optical limiters have been utilized in a variety of circumstances where a decreasing transmission with increasing excitation is desirable. These devices can be used for various pulse shaping applications. An optical limiter consisting of a reverse saturable absorber can be used for passive mode locking [32]. The amplitude modulated pulse can be smoothed by an optical limiter [33]. In this application, a long optical pulse with short intensity pikes incident on the limiter will have the spikes preferentially attenuated with respect to average pulse shape.

It is proposed that an optical limiter together with a saturable absorber can be employed for improved pulse compression [32] in which the leading edge of the pulse is preferentially attenuated by the saturable absorber while the trailing edge will be preferentially attenuated by the optical limiter. The latter is activated by the energy absorbed from the leading portion of the pulse resulting in a more temporally coherent symmetric pulse.

Also slow optical limiters finds applications in reducing the background in pulsed IR laser excited photothermal spectroscopy [34].

However the most important application of optical limiters are in eye/sensor protecting coatings especially in optical systems such as direct viewing devices (telescopes, googles, gunsights etc), focal plane arrays, night vision systems etc. All photonic systems including eye have an intensity level above which damage occurs. Using an optical in the system prior to the sensor extends the dynamic range of the sensor and allows the sensor to continue its operation with out which it could be damaged permanently.

A device that uses some form of active feedback accomplishes dynamic control. A photo sensor, which controls an iris that restricts the intensity of light incident on an optical system, is an example for dynamic control. Dynamic devices suffer from a number of disadvantages, such as higher complexity and slower speeds than passive devices. The higher complexity results from the need for multiple components that must communicate with one another. A device designed for dynamic intensity control generally requires a sensor, a processor and an actuation module that require time to operate in a serial manner and to communicate between the modules.

By contrast, passive control is typically accomplished using a nonlinear optical material in which the sensing, processing and actuating functions are inherent. Since the optical control function is a part of the physical characteristics of the material, the speed is not limited by the communication between the individual modules and the device can be potentially very simple and fast. Such devices are crucial for controlling short optical pulses .Two important and distinctly different types of passive devices used to control the amplitude of an optical signal are "all optical switches and optical limiters". An ideal passive optical switch is a nonlinear optical device that is activated at a set intensity or fluence threshold, whereupon the device becomes completely opaque .By contrast, an ideal optical limiter exhibits a linear transmission below a certain threshold intensity, but above this threshold the output intensity is a constant. The response of an optical limiter and an optical switch are shown in figures. These responses are those of ideal devices to ideal optical pulses that are uniform in both space and time. Pulses with realistic temporal and spatial profile will modify these responses. Under realistic conditions the limiter activation threshold is less well defined, and the output fluence will not be perfectly clamped at a constant value. For any realistic switch, the leading edge of a fast optical

pulse will pass through the device before activation, yielding a response intermediate between a limiter and an ideal switch.

(a)   (b)   (c)
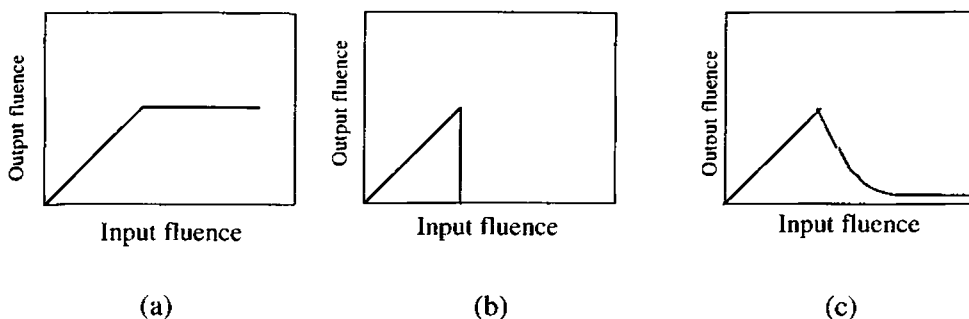
Fig. 2.7 shows the optical response of (a) an Optical Limiter (b) an ideal

Optical Switch (c) A Realistic Optical Switch to the incident fluence.

2.13.1 Mechanisms for Passive Optical Limiting

There are a variety of non-linear optical phenomena that can be used to construct an optical limiter. These include non-linear absorptive process such as two photon (multi-photon), excited state and free carrier absorption; nonlinear refractive processes such as self-focusing and photo refraction and optically induced scattering.

2.13.2 Two Photon Absorption

Two-Photon Absorption (TPA) is an instantaneous non-linearity that involves the absorption of a photon from an electromagnetic. field to promote an electron from its initial state to a virtual intermediate state, followed by the absorption of a second photon that takes the electron to its final real state . Since the intermediate state for such transition is virtual, energy need not to be conserved in the intermediate state but only in the final state. For TPA, the material response is of the order of an optical cycle and is therefore independent of the optical pulse length for a fixed intensity. The device will respond virtually instantaneously to the pulse. On the other hand, because of the low value of the TPA co-efficient β (where $\beta=(3\omega/2\ \epsilon_0\ c^2\ n_0^{2})$ Im $[\chi^{(3)}]$ with $\omega=$ the circular

79

frequency of the optical field n_0 –the linear index of refraction and c- the speed of light in vacuum) in usual materials, high intensities are required to realize significant TPA in them . Since the intensity is essentially the energy density divided by the pulse duration, short pulses are required to achieve limiting with TPA for energy densities that may be high enough to damage an optical sensor. Thus, TPA acting alone is not a practical approach to device protection for nano second and longer threat pulses.

2.13.3 Reverse Saturable Absorption

Reverse Saturable Absorption (RSA) or Excited State Absorption generally arises in a system when an excited state absorbs stronger than the ground state. The process can be understood by considering a system that is modeled using three vibronically broadened electronic energy levels. Let the cross section for absorption from the ground state 1 is σ_1, and σ_2 is the cross section for absorption from first excited state 2 to the second excited state 3. The lifetime of the first excited state is σ_2 (seconds). As light is absorbed by the material, the first excited state begins to become populated and contributes to the total absorption cross section. If σ_2 is smaller than σ_1, then the material becomes more transparent and bleaches .Such materials are known as saturable absorber. If σ_2 is larger than σ_1 then the total absorption increases and the material is known as reverse saturable absorber. Reverse saturable absorbers are good optical limiters.

2.13.4 Free Carrier Absorption

Once charge carriers are optically generated in a semiconductor, whether by single photon or two-photon absorption, these electrons (holes) can be promoted to states higher (lower) in the conduction (valence) band by absorbing additional photons. This process is often phonon assisted, although depending on the details of the band structure and the frequency of the optical excitation it may also be direct. The phonon-assisted phenomenon is referred to as free carrier absorption and it is analogous to the excited state absorption in a molecular system. It is clearly an accumulative non-linearity, since it depends upon the build up of carrier population in the band as the incident optical pulse energy is absorbed.

Free carrier absorption always plays some role in the operation of a semiconductor limiter, if the excitation process results in the generation of significant free carrier populations in the band. It certainly contributes to the limiter performance and its inclusion is important in the precise modeling of the response of such devices. Just as in the case of TPA, its importance typically plays in comparisons with non- linear refractive effects, whether single photon or two-photon transition, generates the carriers.

2.13.5 Nonlinear Refraction

Optical limiters based on self-focusing and defocusing form another class of promising devices. The mechanism for these devices may arise from the real part of $\chi^{(3)}$ or from nonlinear refraction associated with carrier generation by either linear or two photon absorption in a semiconductor. Both self focusing and defocusing limiters operate by refracting light away from the sensor as opposed to simply absorbing the incident radiation. Compared to strictly absorbing devices, these limiters can there fore, potentially yield a larger dynamic range before damage to the limiter itself happens.

Here a converging lens is used to focus the incident radiation before it passes through the non- linear medium. The output passes through an aperture before impinging on the detector .At low input levels, nonlinear medium has little effect on the incident beam, and the aperture blocks an insignificant portion of the beam, thus allowing for a low insertion loss for the device. When the nonlinear refraction occurs however the non-uniform beam profile within the medium results in the generation of a spatially non-uniform refractive index. This act as either a negative or positive lens depending on the refractive non-linearity causing the incident beam to either focus or defocus. In a properly designed system this lensing results in a significant amount of energy being blocked by the system aperture thereby protecting the sensor. Since self-focusing can lead to catastrophic damage to the non linear medium itself self defocusing media may have an advantage in practical devices by providing a self protecting mechanism for the limiter itself.

A self-focusing limiter works best if the nonlinear medium is placed approximately at Rayleigh range before the intermediate focus of the device. For a self-defocusing material, the optimum geometry is approximately at one Raleigh range after the focus. This geometric dependence can be exploited to determine not only the sign of

the nonlinear refraction in a given medium but the magnitude as well. This is the principle behind the Z- Scan technique [35-40].

2.13.6 Induced Scattering

Scattering is a mechanism that has been extensively studied. Scattering is caused by light interacting with small centers that can be physical particles or simply the interfaces between the groups of non-excited and excited molecules. This scattering can be highly directional or fairly uniform depending on the size of the scattering centers. It is obvious that if an optical signal induces scattering centers in a given medium, the transmission of the medium measured in a given solid angle will decrease. Hence, optical scattering can be used in optical limiters for sensor protection. Induced scattering limiters usually rely on liquid media, because the process in such media is often reversible. That is, if chemical or structural decomposition has not occurred, the excited liquid can readily return to equilibrium. Even when the decomposition does occur, the illuminated volume can be refreshed by either diffusive processes or by circulation. However, when the scattering centers are generated in solids, they are usually due to irreversible decomposition processes that can lead to degradation in the linear operation of the device.

When light impinges on a particle (an atom, molecule or cluster) the electric field interacts with the particle causing the electric charges within to oscillate. The oscillation in turn leads to radiation. This scattered radiation is symmetric with respect to forward and backward scattering. Scattering is of two types: Rayleigh scattering that can be applied to particles much smaller than the wavelength of light or where the particle is nonabsorbing (refractive index real). For particles where size is either comparable or larger than the wavelength of light, then Mie scattering occurs. The essential point is that as the size of the scattering particle increases, a larger percentage of the scattered radiation is forward scattered. Hence, limiting based on Mie scattering will be less effective than Rayleigh scattering [35-40].

2.14 Z-Scan Technique

Z scan is a technique employed for the detection of optical nonlinearities associated with the medium. Details are provided in Chapter 3.

References

1. C.Radhakrishnamurty, *Magnetism and Basalts*, Geological Society of India, Banglore, (1993).

2. B.D.Cullity, *Introduction to Magnetic Materials* Addison-Wesley Publishing Company, Inc (1972).

3. Soshin Chikazumi, *Physics of magnetism , John Wiley and sons, Inc., New York*.

4. David Jiles, *Introduction to magnetism and magnetic materials, Chapman and hall,London*.

5. Hadfield D, *'Permanent Magnets and Magnetism'*, 1962, John Wiley and sons, Inc., London.

6. Neel. L *Properties magnetiques des ferrites, ferrimagnetisme et antiferromagnetism*, Ann. Phys. **31**(948), 137.

7. S. Gangopadhyay, G. C. Hadjipanyas, C. M. Soresen and K. J. Klabunde, *Nanophase Materials – Synthesis properties and applications* (G. C. Hadjipanayis and R.W. Scigel (Edt.)), Kluwer Academic Publishers (1994) 573

8. Qi Chen, Adam. J. Rondinone, Bryan. C. Chakoumakos, Z. John. Zhang (1999) *J.Magn.Magn.Mater* **194**

9. J.C.Ho,H.H.Hamdeh, Y.S.Chen, S.H.Lin, Y.D.Yao, R.J.Willey, S.A.Oliver (1995) *Phys.Rev.B* **52** 10122

10. H.Hamdeh, J.C.Ho, S.A.Oliver, R.J.Willey, G.Oliveri, G.Busca **81** (1997) *J.Appl.Phys* 1851

11. Ronald F.Soohoo, *Theory and application of ferrites*, Prentice hall Inc, New Jersey.

12. Xavier Battle, Amilcar Laborta *J.Phys.D.Appl.Phys* **35** (2002) R15

13. Tareev B *Physics of Dielectric Materials* (Mir Publishers) Moscow (1979)140

14. Richard Turton, *The Physics of solids*, Oxford Univ. Press, (2000)

15. John Singleton *Band theory and electronic properties of solids*, Oxford Univ. Press, (2001)

16. S. V Gaponenko, *Optical properties of semiconductor nanocrystals*, Cambridge studies on modern optics press, (2002)

17. Eugene Hecht and Alfred Zajac, *Optics*, Addisson Wesley Publishing Company, London, (1979).

18. E. Hasmonay, J Depeyrot, *J. Appl.Phys.* **88**, No 11 (Dec. 2000), 6628.

19. A.F Bakuzis, M.F Da Silva, P.C Morais, L.S.F Olavo, and K. Skeff Neto, *J. Appl. Phys* **87**, (5), March 2000, 2497.

20. H.C Yang, I.J Jang, H.E Horng, J.M Wu, Y.C Chiou, Chin-Yih-Hong, *J. Magn. Magn. Mater.* **201**, (1999), 215.

21. M. Xu and P.J Ridler, *J. Appl. Phys.* **82** (1), (1997 July), 326.

22. H.E Horng, Chin-Yih-Hong, H.C Yang, I.J Jang, S.Y Yang, S.L Lee, and I.C Kuo, *J. Magn. Magn. Mater.* **201,** (1999), 215.

23. S. Taketomi, *Jpn. J. Appl. Phys*, **22**(1983) 1137.

24. H.E Horng, Chin-Yih-Hong, S.Y Yang, and H.C Yang, *J. Phys. And Chem. Solids*, **62** (2001) 1749.

25. Y.B Band, D.J Harter and R. Bavli, *Chem. Phys. Lett*, **126,** (1986) 280

26. S.E Bialkowski, *Opt. Lett*, **14,** (1989) 1020

27. HelenW.Davies and Patrick Llewellian, *J. Phys. D, Appl. Phys*, 12, 1979, 1357.

28. S Couris, E. Koudoumas, A A Ruth and S. Leach, *J.Phys.B, At.Mol.Opt.Phys.* 28 (1995) 4537.

29. Tutt L W and Kost A *Nature* **356** (1992),225

30. kost A Tutt L W, Klein M B Dougherty T K, and Elias W, *Optics Letters*, **18** (1993) 334.

31. Mc Lean D. G, Sutherland R L, Brant M.C, Brandelik D M, Fleitz P A and Pottenger T, *Optics Letters*, **18** (1993) 858.

32. D.J Harter and Y.B Band, Springer Series, *Chem. Phys*, **38,** (1984) 102

33. D.J Harter, M.L Shand and Y.B Band, *J. Appl. Phys*, **56,** (1984) 865

34. Lin F, Zhao J, Luo T, Jiang M, Wu Z, Xie Y, Qian Q and Zeng H *J. Appl. Phys*, **74** (1993) 2140.

35. Justus B L, Kafafi Z H, and Huston A L, *Optics Letters*, **18** (1993) 1603.

36. R.Philip, G.Ravindra Kumar, N.Sandhyarani, T.Pradeep, *Phys.Rev.B.* **62** (2000) 13160

37. S.Link, C.Burda, Z.L.Wang, M.A.El-Sayed, *J.Chem.Phys.* **111** (1999) 1255

38. P.V.Kamat, M.Flumiani, G.V.Hartland, *J.Phys.Chem.B.* **102** (1998) 3123

39. C.Zhan, D.Li, D.Zhang, W.Xu, Y.Nie and D.Zhu, *Opt.Mat.* **26** (2004) 11

40. K.S.Bindra, S.M.Oak and K.C.Rustagi, *Opt.Commun.* **124** (1996) 452

CHAPTER 3
Experimental Techniques

This chapter deals with the details of the experimental techniques employed for the synthesis and characterization of magnetic nanoparticles, ferrofluids and magnetic nanocomposites. Brief theory supporting the experimental techniques is also provided. Schematic diagrams of the experimental set-ups are also provided in this chapter. Novelty of experimental techniques opted in the synthesis and characterization of the magnetic nanomaterials is also discussed.

The synthesis procedures could be divided into two parts. One includes the synthesis and characterization techniques employed in understanding the physics governing the properties of ferrofluids while the second part describes the synthesis and characterization techniques used in magnetic nanocomposites.

3.1 Synthesis

Magnetic Nanocomposites

1) Synthesis of Magnetic nanocomposites

Nanoparticles of γ-Fe_2O_3 (maghemite) particles were incorporated inside a polymer matrix by the method of ion exchange followed by controlled oxidation [1]. The method adopted here is a modification of the preparation scheme reported by Ziolo et al [2] and similar to that of [3,4]. The polymer matrix employed is a cross linked polymer of sulphonated polystyrene and divinyl benzene, which have exchangeable H^+ ion containing $SO_3^-H^+$ groups. The schematic of a polystyrene structure is given in Fig.1.

The ion exchange resin was exchanged with Fe ions from an aqueous solution of $FeSO_47H_2O$ and these exchanged Fe ions were then converted into $Fe(OH)_2$. This was then oxidized to yield, presumably, γ-Fe_2O_3. Drop wise addition of dilute aqueous solution of hydrogen peroxide (H_2O_2) accelerated the conversion to oxide. The resin was then washed with water and then dried. Strong ion exchange process has been employed for the synthesis of entire set of samples [1-4].
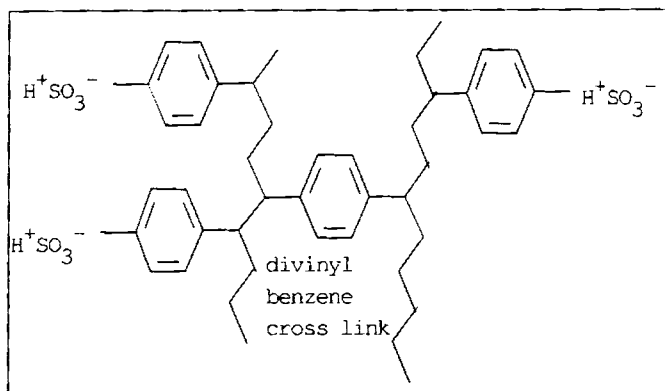
Fig.3.1 schematic of sulphonated polystyrene

Ion Exchange Cycling

The above procedure of Ion exchange cycling is repeated for different cycles to enhance the magnetization of the sample [5]. More and more 'Fe' ions will get exchanged and hence a higher yield of maghemite is achieved. The ion exchange process has been repeated till cycle 10. The ion exchange process is carried out both at room temperature and at higher temperatures of 65^0C [6]. For the high temperature exchange process, the reaction was carried out in a water bath with provisions for temperature tuning.

Doping

Insitu doping of any other metal along with maghemite could be performed by a reaction similar to that described in the earlier section. For that sulphates of that metal should be taken in appropriate atomic percentages and the reaction could be carried out. Here cobalt have been selected as the dopant material to be incorporated inside the vacancies of the maghemite lattice because of its inherent magneto-crystalline anisotropy which can substantially enhance the coercivity of the composite. A schematic picture of the ion exchange process for the doping is provided. Cobalt was added in the maghemite lattice in the atomic percentages 1%, 2%, 4%, 6%, 8% and 10%. Ion exchange cycling was carried out for all set of samples up till the 10th cycle [6].
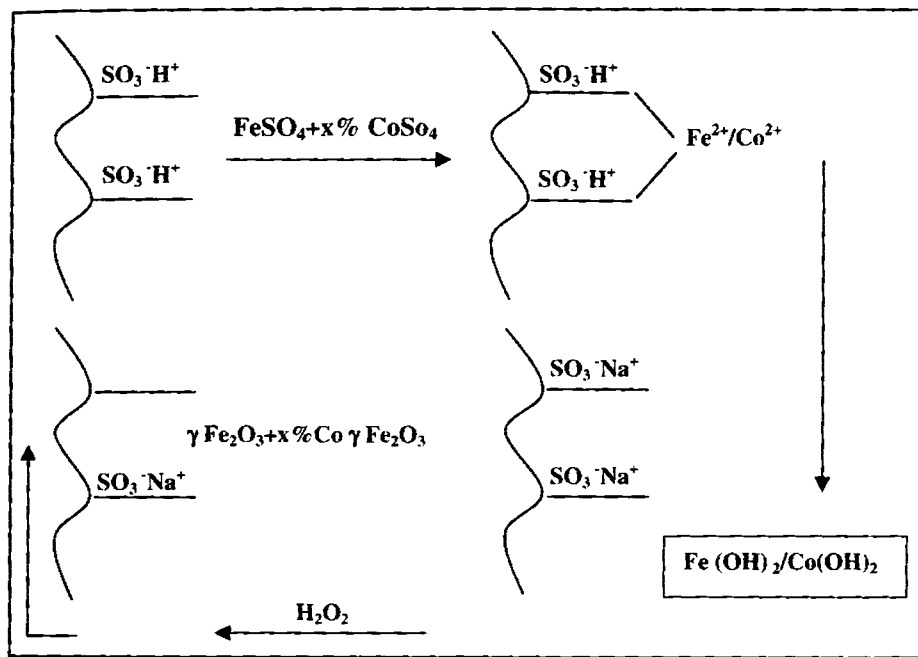
Fig.3.2 Scheme of preparation of nanocomposites

Novel method for the synthesis of magnetic metal nanoparticles (elementary cobalt)

Metal nanoparticles are highly reactive and prone to oxidation instantly on their synthesis due to their large surface area. Hence insitu capping is essential for their synthesis at the nanolevel for passivation. Especially cobalt a metal with inherent crystalline anisotropy will have higher reactivity at the surface due to the high surface energy due to the high c/a ratio. Here a novel method has been developed for the synthesis of self protected cobalt nanoparticles inside the polymer pores. Here also the sulphonated polystyrene has been employed as the template for the host matrix.

The ion exchange strong resins have been soaked inside the $CoCl_2$ solutions for 24 hours. Insitu reduction was carried out with a very strong reducing agent $NaBH_4$. It is assumed that in the first reduction cycle, more particles will be trapped in surface pores which may be oxidized. Hence reduction cycles were repeated to enhance the yield.

2) Synthesis of Ferrofluids

a) Synthesis of ferrofluids by co-precipitation aided by high energy ball milling (HEBM)

i)Preparation of magnetic fine particles

Fine particles of nickel iron ferrite belonging to the series ($Ni_xFe_{1-x}Fe_2O_4$) where 'x' varies from 0.1 to 0.7, and zinc iron ferrite ($Zn_xFe_{1-x}Fe_2O_4$) which are the precursor material for the preparation of the ferrofluids, were synthesized by the cold co-precipitation. For this, $NiSO_4$. $6H_2O$, $FeSO_4$. $7H_2O$ and $FeCl_3$ (all AR grade chemicals) in the molar ratio of x M, (1-x) M, and 2 M respectively were employed. pH was maintained at 10.5 under room temperature conditions [7-13].

ii)Suspension of particles by High Energy Ball Milling (HEBM)Process

High Energy Ball Milling process was utilised for further reduction of grain size. For the preparation of ultra fine particles, 'Fritsch pulverisette 7 planetary micro mill' was employed. In this, 800 rotations per minute can be achieved and hence the momentum imparted to the particles will be very high. The ball to powder ratio was maintained at 1:8 to impart a high momentum to these fine particles. This helps the required size reduction within two to three hours of time. This results in excellent grinding of the particles at considerably shorter grinding times. Here the HEBM is successfully employed to provide the surfactant coating to these ultrafine magnetic materials synthesized. Oleic acid with a long polar tail is used for providing the stereic repulsion between adjacent interacting magnetic nanograins [14-16].

iii) Ferrofluid preparation

Ferrofluids were prepared by milling the powder samples prepared by cold co precipitation with the surfactant oleic acid. Oleic acid provides the necessary steric repulsion by its polar ends, thus preventing the agglomeration of fine particles. Finally these samples were milled with kerosene for around three hours to obtain a uniform stable dispersion with a reduced particle size. The samples were centrifuged well to remove the sedimented particles and placed in an ultrasonic vibrator to enhance Brownian motion, which provides stability to the ferrofluid. Oleic acid, kerosene and nickel ferrite particles were optimally employed to ensure good quality ferrofluid.

Ferrofluid thus prepared exhibited typical characteristics like spiking, which is a sure test for the formation of ferrofluids.

b) Synthesis of ferrofluids by co-precipitation and *insitu* coating with surfactant

i) Ferrofluid preparation

To synthesize ferrofluids co-precipitation and *insitu* coating technique was employed in this project work. In this method, the required amount of precursor materials was weighed in the appropriate molar ratio. Through the normal chemical reactions, the magnetic particles were made precipitated. One monolayer coating of oleic acid is provided to the magnetic nanoparticles and this was achieved *insitu*. The resulting particles were mixed with carrier liquid and stirred well to get a uniform dispersion of magnetic particles. It must be noted here that, in this method, control of pH and temperature, and purity of chemicals are very essential to maintain the stoichiometry of the particles.

For the synthesis of Fe_3O_4 ferrofluids, a solution containing 1M in $FeSO_4.7H_2O$ and 2M in $FeCl_3$ were prepared. A 25% NH_4OH solution was added to the above solution until the pH becomes 10.5ml Oleic acid was added to the solution for providing a monomolecular coating and heated for thirty minutes. The pH was maintained during heating process. In order to coagulate the oleic acid coated particles, a concentrated solution of hydrochloric acid (HCl) was added. After decantation of the solution, the resulting product was washed many times with distilled water to remove impurities and free radicals. Finally uncoated oleic acid and water were removed by washing with acetone. This acetone-wet slurry was dispersed in around 5ml of household grade – kerosene and stirred for 30 minutes to produce ferrofluids [7-13].

For the preparation of ferrofluids based on ($Ni_xFe_{1-x}Fe_2O_4$), where 'x' varying from 0.1 to 0.7, a mixed solution of x M in Nickel Sulphate, (1-x) M in Ferrous Sulphate and 2M in Ferric Chloride is used. Here 'x' varies from **0.1 to 0.7**. Further variation of Ni concentration yielded particles, which were only feebly magnetic and could not be used for ferrofluids. Same procedure was adopted for the synthesis of ferrofluids based on ($Mn_xFe_{1-x}Fe_2O_4$ also.

b) Separation of Magnetic Particles from Ferrofluids

Good quality, stable ferrofluids were prepared using co-precipitation technique, by the chemical reaction of suitable chemicals that were taken in the appropriate molar ratio. These ferrofluids were tested for their stability and quality. For the structural characterization, a portion of each sample was taken and these were washed many times with acetone to remove the carrier liquid. The magnetic particles were separated by decantation and these wet samples were dried with a hair drier. These dried powder samples were used for the structural characterization [8-9].

3.2. Structural Characterization

a) X-Ray diffraction studies

The magnetic nanoparticles were separated from the ferrofluid using reversible flocculation using acetone and the wet slurry obtained is dried. Dried ferrofluids were analyzed using X-Ray Diffractometer (Rigaku Dmax-C) using Cu-K$_\alpha$ radiation of wavelength 1.5418Å.

In the second system of ferrofluids, the synthesized ultra fine magnetic nanoparticles using co-precipitation technique is directly analyzed using X-Ray Diffractogram.

The magnetic nanocomposites were milled in a high energy ball milling (HEBM) unit for some minutes with water and dried and maghemite were separated using magnetic separation and analyzed by X Ray diffraction technique.

Grain size can be estimated from the line broadening of the central maxima of X-Ray diffraction patterns [16-17]. From the spectrum the glancing angle at which maximum diffraction was obtained. Knowing the value of glancing angle, we can find the spacing between the planes using *Bragg's Law:*

$$n\lambda = 2d \sin \theta \qquad\qquad\qquad 3.1$$

where '**n**' is the order of diffraction, 'λ' is the wavelength of the light used and '**d**' is the interplanar spacing.

Lattice parameter (a) was calculated assuming cubic symmetry and planes were identified by matching interplanar spacing values (d) with standard tables (JCPDS-ICDD C, 1990). Average grain size could be estimated using Debye-Scherrer's formulae

$$D = \frac{0.9\lambda}{\beta\cos\theta} \qquad\qquad 3.2$$

where λ= Wave length of X-ray used in Å, β = FWHM in radians of the XRD peak with highest intensity, D = particle diameter in Å, θ= the angle of diffraction in radians, where

$$\beta = \frac{FWHM}{180} \times \pi \qquad\qquad 3.3$$

and **FWHM** is the Full Width at Half of the Maximum intensity peak.

b) *Atomic Absorption Spectroscopy (AAS)*

Atomic absorption spectroscopy is used for the determination of exact atomic percentage of any metal ion. Percentage of divalent metal as well as zinc/nickel in ferrofluids has been determined using this method [5].

c) *Atomic Force Microscopy*

Atomic force microscopy is a powerful mechanical profiling technique which gives three dimensional maps of surfaces by scanning a sharp probe attached to a cantilever. The tip of the cantilever determines the resolution of the AFM images in general. The forces, which exist in between the surface of the cantilever and surface to be scanned, are used to control the vertical distance. The resolution of AFM is determined by the atomic wave function of the probe tip and the sample. AFM can respond to all the electrons including the core electrons, which is its advantage over an STM. Because electrons at the Fermi level are loosely bound than the electrons at the core, the special resolution of AFM should be greater and it is experimentally proved in simultaneous measurements.

The forces that exist between tip and sample were often orders of magnitude higher than the forces of a tip with a single front atom and thus true atomic resolution is limited in AFM. But it can be widely used as a surface profiling tool.

In contact mode AFM, the tip feels small repulsive forces from the sample surface. The cantilever should be softer than the bonds between the surface atoms to

obtain a decent deformation for the cantilever when it touches a surface atom, or the surface atom will be deformed more than the cantilever. This method is highly used for atomic scale resolution. But the tip and surface of the sample should be chemically non-reacting in this method.

Here ferrofluids have been surface profiled using contact mode AFM technique. Both surface profiling as well as depth profiling is carried out (3D AFM).

d) Transmission Electron Microscopy

The synthesized ferrofluids have been dried by washing with acetone and were analyzed for their grain size and grain size distribution using transmission electron microscopy (TEM), (Model JOEL FE-TEM-2010 F). The electron diffraction (ED) spectrum was also recorded and the lattice planes were identified using the ED spectrum. Here a thin specimen is irradiated with an electron beam of uniform current density. Electrons are emitted from an electron gun and illuminate the specimen through a two or three stage condenser lens system. The electron intensity distribution behind the specimen is magnified with a three or four stage lens system and viewed on a fluorescent screen. The image can be recorded by direct exposure of a photographic film [18].

The electron diffraction technique is a powerful technique to characterize samples at the nanolevel. Lattice planes could be identified and using a HRTEM image, lattice defects/contraction also could be observed.

e) High Energy ball Milling (HEBM)

Particle size reduction was carried out employing by High Energy Ball Milling. For the preparation of ultra fine particles, 'Fritsch pulverisette 7 planetary micro mill' was employed. In this, 800 rotations per minute can be achieved and hence the momentum imparted to the particles will be very high. The ball to powder ratio was maintained at 1:8 to impart a high momentum to these fine particles. This will enable the required size reduction within two to three hours. This results in excellent grinding performance at considerably shorter grinding times.

3.3. Magnetization Studies

Vibrating Sample Magnetometry (VSM)

The magnetic characterization of the samples was carried out using a Vibrating Sample Magnetometer (VSM), model: EG & G Par 4500. The main parts of a VSM and the simplified block diagram are given in Fig 3.3 and Fig. 3.4. Saturation magnetization (M_s), Retentivity (M_r) and Coercivity (H_c) were evaluated from the hysteresis loops.
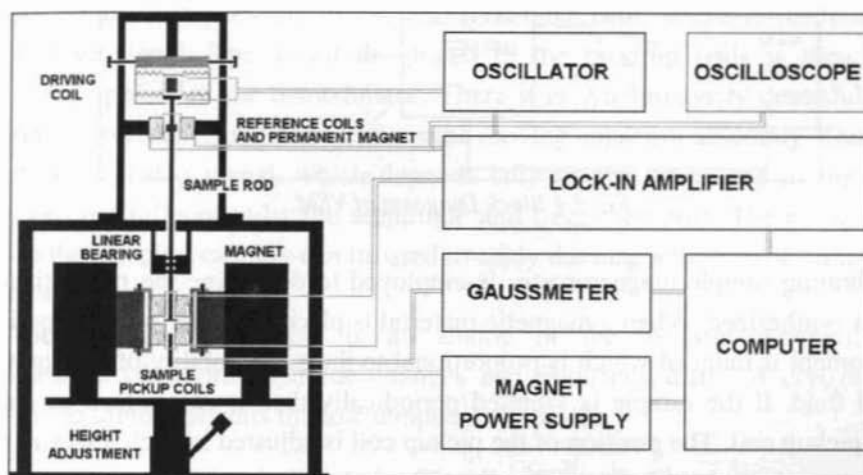
Fig. 3.3 Main Parts of VSM

The magnetic nanoparticles are kept in the sample holder, which is centered in the region between the pole pieces of an electromagnet. A slender vertical sample rod connects the sample holder with a transducer assembly located above the magnet. The transducer converts a sinusoidal ac drive signal into a sinusoidal vertical vibration of the sample rod and the sample thus made to undergo sinusoidal motion in a uniform magnetic field. Coils mounted on the pole pieces of the magnet pick up the signal resulting from the sample motion. This ac signal at the vibrating frequency is proportional to the magnitude of the moment induced in the sample. Thus, the pick up coil output accurately gives an account of the moment level of the sample [19-22].

Fig 3.4 Block Diagram of VSM.

Vibrating sample magnetometry is employed to determine the magnetization of the samples synthesized. When a magnetic material is placed in a uniform magnetic field, a dipole moment is induced which is proportional to the susceptibility of the sample and the applied field. If the sample is vibrated periodically then it can induce an electrical signal in a pickup coil. The position of the pickup coil is ad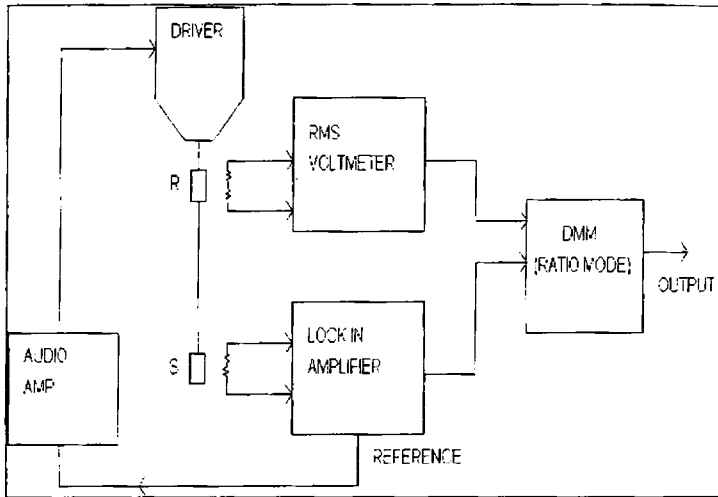justed in such a way as to give the maximum induction without much noise. The induced signal in the pickup coil will be proportional to the magnetic moment produced in the sample and the vibrating frequency of the sample. This is the basic principle used in the design of a VSM to measure the magnetic properties. The material under study is loaded in the sample holder, and it is placed at the centre region of the pole pieces of a laboratory electromagnet. A slender vertical sample rod connects the sample holder with a transducer assembly located above the magnet, which in turn supports the transducer assembly by means of sturdy adjustable support rods.

A transducer is used to convert the electrical oscillations into mechanical vibrations. An electronic oscillator circuit produces a constant frequency and it is fed to the transducer to vibrate the sample rod. The vibrating sample in the uniform magnetic field induces a signal in the pickup coils mounted to it. The strength of the ac signal at the vibrating frequency is proportional to the magnetic moment induced in the sample. However, vibration amplitude and frequency also will have some contributions to the

induced emf. A servomechanism is used to stabilize the amplitude and frequency of the drive so that the output accurately tracks the moment level without degradation due to variation in the amplitude and frequency of the oscillator.

This servo technique uses a vibrating capacitor located beneath the transducer to generate an ac control signal that varies solely with the vibration amplitude and frequency. The signal, which is at the vibration frequency, is fed back to the oscillator where it is compared with the drive signal so as to maintain constant drive output. It is also phase adjusted and routed to the signal demodulator where it functions as the reference drive signal. The signal developed in the pick up coils is then buffered, amplified and applied to the demodulator. There it is synchronously demodulated with respect to the reference signal derived from the moving capacitor assembly. The resulting dc output is an analog signal, which depends only on the magnitude of the magnetic moment, and not influenced by the amplitude and frequency drift. The cryogenic setup attached to the sample assembly can be used to study the magnetization of samples at low temperatures.

The resulting dc output is an analog of the moment magnitude alone, uninfluenced by vibration amplitude changes and frequency drifts. A cryogenic setup attached to the sample permits the low temperature studies.

Principle & Theory Involved in VSM

When a sample is placed in a magnetizing field 'H', it will respond with a magnetic induction 'B'

$$B_{sample} = \mu_0 (H+M)$$ 3.4

where 'M' is the magnetization in the sample. The magnetization and the magnetic moment 'm' and the volume ' v ' to get:

$$B_{sample} = \mu_0 \left[H + \frac{m}{v} \right]$$ 3.5

In free space, outside the sample, a magnetic induction 'B $_{by\ sample}$' is proportional to the magnetic moment 'm' of the sample present:

$$B_{by\ sample} = gm$$ 3.6

where 'g' is a proportionality constant depending on the position of the point in space. The total magnetic induction at a point in space is:

95

$B_{space} = B_{ext.} + B_{by\ sample} = B_{ext} + gm$ (2), where $B_{(ext.)}$ is the magnetic induction of free space due to the magnetizing field 'H'. Note that when the external field 'B_{ext} is varied, the pick up coils do not pick up the change due to the fact that the coil pairs are wound in opposite directions. When the sample is moved near a pickup coil, a voltage is induced in the coil:

$$V = -NO \frac{dB_{space}}{dt} = -NO \frac{d}{dt} \cdot (B_{ext.d} + gm) \qquad 3.7$$

where N is the number of turns and O is a constant depending on the geometry of the coil. Note that only the components of the field normal to the area of the coil are included in this and all subsequent expressions. Since the magnetizing field H and consequently the magnetic induction B_{ext} due to the field is constant, we can write:

$$V = -NO \frac{dg}{dt} m \qquad 3.8$$

Here g is not a constant and it depends on the position of the sample and is a function of time. If the sample is in a sinusoidal motion we can write:

$$V = -NOhA \frac{de^{\omega x}}{dt} m \qquad 3.9$$

Here *h* is proportionality constant. $-NOh$ is substituted by a constant 'k' and taking the derivative we get:

$$V = k\omega Ae^{\omega x} m \qquad 3.10$$

It can be seen that a voltage 'V', proportional to the magnetic moment, 'm' is induced in the coil.

A VSM uses an electromechanical driver (voice coil) to move a vertical drive rod with a small amplitude 'A', and frequency 'ω' mounted on the drive rod of the sample holder S, and a small permanent magnet or small coil with a constant dc excitation current of constant magnitude as reference magnetic moment R. Pick-up coils near R will have an induced voltage

$$V_R = k_R \omega Ae^{\omega x} m_R \qquad 3.11$$

where 'k_R' is a constant depending on coil geometry, and 'm_R' is the constant magnetic moment of reference R. 'V_R' is in the millivolt range and easily measured by a rms voltmeter. Similarly, the sample pick-up coils will see a voltage

$$V_s = k_s \omega A e^{\omega x} m_s \qquad\qquad 3.12$$

where 'k_s' is a constant depending on the sample coil geometry and 'm_s' is the magnetic moment of the sample coil S. An RMS-to-dc conversion is performed on both 'V_R' and 'V_S' by the RMS voltmeter and lock-in amplifier, respectively. The ratio of these two dc voltages is then taken by a digital multimeter (DMM) which has ratio capabilities. Taking the root-mean-square average of the previous two equations, it is seen that the dependence on frequency 'ω', and drive amplitude 'A', cancel and the DMM output is

$$V_{out} = \frac{\langle V_S \rangle_{rms}}{\langle V_R \rangle_{rms}} = km_s \qquad\qquad 3.13$$

where 'k' is the calibration constant which has absorbed 'k_R', 'k_S', 'm_R', as well as any amplifications of the reference signal and the sample signal by the lock-in amplifier. Since the magnetic moment 'm' is related to the magnetization 'M' and the volume 'v' of the sample we can write:

$$V_{out} = kvM_s \qquad\qquad 3.14$$

We can directly read off the magnetization of the sample 'M_S' by writing:

$$M_s = \frac{V_{out}}{kv} \qquad\qquad 3.15$$

Fig. 3.5 shows the schematic diagram of the instrumental set up used for ac susceptibility measurements consisting cryostat assembly with coil system. Here the change in the mutual inductance of a primary and two identical but oppositely wound secondary coils is measured when a sample is placed in it. This change is a measure of the magnetic susceptibility of the sample.

3.4. Optical studies

Optical absorption spectrum was recorded using a Hitachi U-3410 UV-VIS-NIR spectrophotometer for the pure as well as cobalt doped samples and the band gap was determined for all the synthesized samples. For a semiconductor, the absorption coefficient near the band edge is given by the equation

$$\alpha = \frac{A(h\nu - E_g)^{1/2}}{h\nu},$$ where A is a constant and E_g is the energy band gap.

When $\alpha h\nu = 0$, $E_g = h\nu$.

So using an extrapolation to the X axis of the pot of "$(\alpha h\nu)^2$ vs $h\nu$", gives the band gap of the material if it is a direct transition. These are termed as Tauc plots.

However the error in the calculation of band gap using Tauc plots may vary from 0.01 eV to 0.08 eV which may be much higher a value comparing with the shift in energy band gap. So a more accurate way for the determination of band gap using a first differential analysis is employed which could be applicable for both the direct and indirect transitions. Here $h\nu$ is plotted along X-axis and $ln(\alpha h\nu)$ is plotted along Y-axis and by obtaining the first derivative of the curve, both fundamental and excitonic absorption edge could be found out exactly [23].

3.5. Dielectric Measurements

The dielectric property of a material is significant from an application point of view. In the case of ferrofluids, the applications are numerous, especially in electrical devices. Speaker fluid is such an example. Under such situations the ferrofluids should work as a good dielectric.

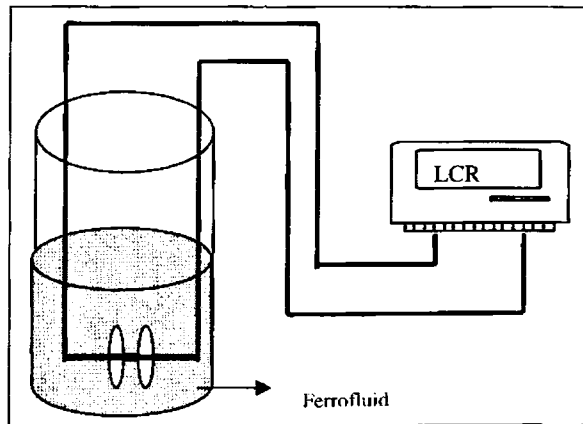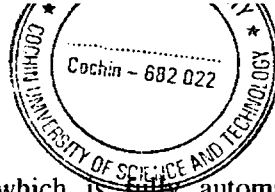

Fig. 3.5 Experimental set up for the Dielectric measurements of Ferrofluids

Here we have tried to perform dielectric measurements in the frequency range of 100 KHz to 3 MHz. The measurements were performed using a dielectric cell and a **HP**

4285A PRECISION LCR METER, which is fully automated using LABVIEW package [24-25]. The schematic representation of the dielectric cell is shown in Fig 3.5. The parallel plate capacitor is kept in air and the capacitance in air is measured. Later the parallel plate capacitor is immersed in the fluid sample to measure the fluid capacitance. The ratio of these two capacitances yielded the dielectric values.

If the parallel plate capacitor is placed in air, then the capacitance is given by

$$C_a = \frac{\varepsilon_0 A}{d} \qquad\qquad 3.16$$

ε_0 is the permittivity in air, d is the distance between the plates and A is the area of the plates. When the sample is between the plates the capacitance is given by

$$C_s = \frac{\varepsilon_0 \varepsilon_r A}{d} \qquad\qquad 3.17$$

Therefore comparing these two equations the dielectric constant of the fluid is given by

$$\varepsilon_r = \frac{C_s}{C_a} \qquad\qquad 3.18$$

Measurement of magnetic field assisted dielectric change.

The dielectric measurements are also carried out at room temperature for the ferrofluids. For that a sample cell is fabricated and the dielectric constant is measured using automated system in varying magnetic field using an electromagnet, which produce a maximum magnetic field of 3,000 Oe.

The entire data acquisition and evaluation of the dielectric constant were automated by using a package called LabVIEW which in turn is based on G programming. LabVIEW is programming language for data acquisition, analysis, simulation or computer control of instruments, techniques or processes. LabVIEW is an acronym for Laboratory Virtual Instrument Engineering Workbench and is a proprietary item owned by National Instruments. LabVIEW is an object-oriented language and its style, syntax and data flow is different from conventional linear programming languages. Appropriate modifications were incorporated in the software so as to enable the data acquisition automatic and visual observation of the graphs on the computer screen. It has

been possible to acquire 20,000 data points or more in a matter of 5 to 10 minutes by using the modified package.

Measurements of Permittivity and Permeability of Ferrofluids in the X band

Permittivity and permeability measurements were carried out using an HP 8510 B network analyzer. A rectangular cavity, designed to obtain X-band frequencies (8.-12GHz) is connected to the two ports of the HP 8514B S-parameter test set of the measuring system. It is operated in the TE_{10p} mode. The network analyzer generates the microwave oscillations of specific frequencies. With the help of an HP 9000/300 series instrumentation computer the measurements at different resonant frequencies were carried out. For measuring permittivity values the following procedure was employed.

The resonance frequency f_t and the unloaded quality factor Q_t of the cavity resonator are measured with the empty capillary tube inserted in the cavity at the position of maximum electric field as shown in Fig. 3.6 The sample liquid is filled in the capillary tube and then sealed. It is positioned at the maximum electric field. The resonance frequencies f_s and loaded quality factor Q_x are measured. The inner diameter of the capillary tube is measured. ε'_r and ε''_r of the liquid sample are calculated .
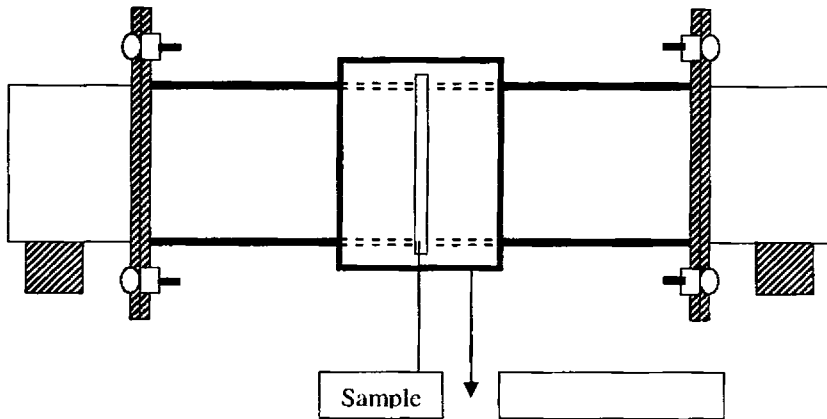
Sample

Fig. 3.6 Cavity for the permittivity measurements (cylindrical cavity)

The procedure was repeated for all the available resonant frequencies in the X band resonator. Ferrofluid samples with different Zinc concentrations were analyzed.

Permeability measurements were performed using the same X band resonator [26]. In this case the sample material is placed at the position of maximum magnetic field as shown in Fig. 3.10.

Fig. 3.7 Top View of the Rectangular cavity for Permeability measurements

Permeability and permittivity can be calculated using the equations

$$\varepsilon'_r + 1 = \frac{(f_t - f_s)V_c}{2f_s}\frac{V_c}{V_s} \qquad\qquad 3.19$$

$$\varepsilon''_r = \frac{V_c}{4V_s}\left(\frac{1}{Q_s} - \frac{1}{Q_t}\right) \qquad\qquad 3.20$$

Here, Q_t represent the quality factor of empty tube.

Similarly, the real and part of the complex permeability is given by,

$$\mu_r' + 1 = \left(\frac{\lambda_g^2 + 4a^2}{8a^2} \right) \frac{(f_t - f_s)}{f_s} \frac{V_c}{V_s}$$

3.21

3.6. Magneto-optical measurements

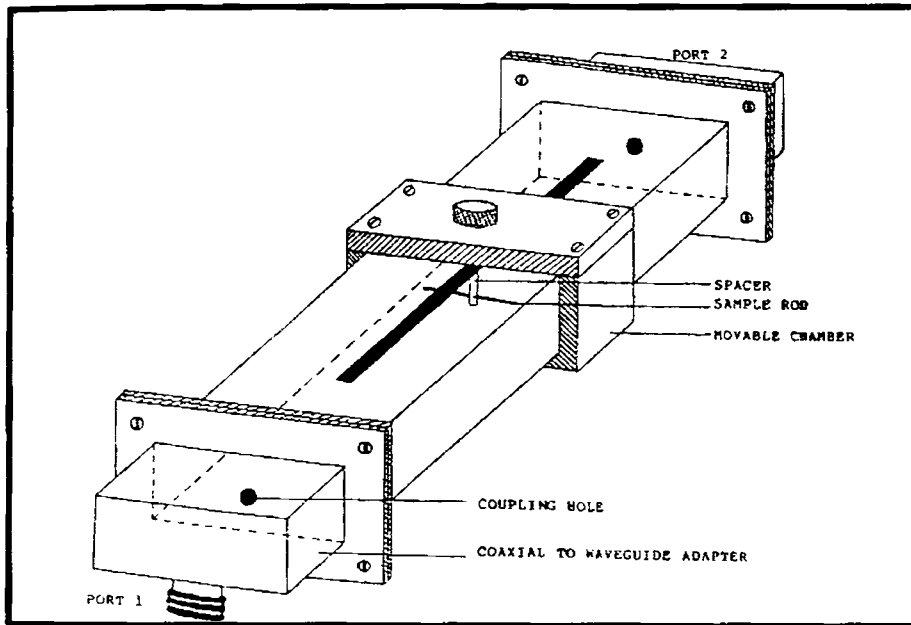In order to evaluate the magneto-optical properties of the synthesized ferrofluids a full fledged magneto-optics laboratory was set-up with a vibration isolation table, bread board and optical instruments. Electromagnets which can go up to 0.1 T, 0.3 T and 0.7 Tesla are employed for the application of magnetic field.

Laboratory was set-up both for magneto-transverse (magnetic field of lines are perpendicular to the line of propagation of laser light) and as well as magneto-longitudinal mode (line of propagation of laser is through the direction of magnetic field of lines [27-33]. For allowing optical signal passing through the electromagnet in the magneto-longitudinal mode, a magnet was designed with an axially drilled hole. He-Ne laser (17 mW polarized out put) was employed as the light source, while Photomutiplier tube (PMT) was used as the detector.


Fig. 3.8 Magnetic field induced laser transmission studies

Magnetic field induced laser transmission studies

Liquid thin films of ferrofluids were made by sandwiching and encapsulating known volumes of ferrofluid between two optically smooth and ultrasonically cleaned glass slides. The thickness of the fluid films can be calculated from the plate area and the volume of the fluid.

This film was then suspended between the poles of a water cooled electromagnet which can go up to a maximum magnetic field is 1Tesla. The ferrofluid film sample was irradiated with a polarized He-Ne laser having a power of 5mW, and wavelength 632 nm. The fluid film was aligned in such a way that the applied magnetic field is perfectly parallel to it. The laser beam is transmitted normally through the film sample and the transmitted light from the ferrofluid film sample was focused on to a white screen, placed at a distance of 0.25m from the film. The entire experimental set up is shown in the Fig 3.9. The intensity of the transmitted beam was measured using a laser power meter (OPHIR-PD 200) in the gradually increasing magnetic field. The exact field was measured each time with a digital Gaussmeter (Model DGM-102). The magnetic field was calibrated in terms of the optical output intensity for all these fluid film samples belonging to the series $Zn_xFe_{1-x}Fe_2O_4$ and $Ni_xFe_{1-x}Fe_2O_4$.
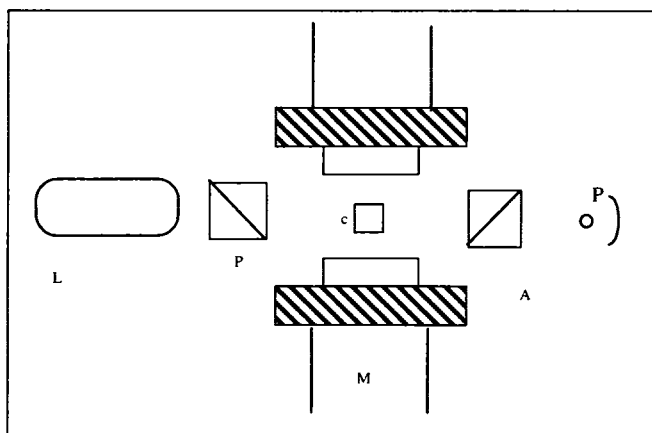
L-Laser, P-Polariser, C-Sample cell, A-Analyzer, M-Magnet, PMT (Photo Multiplier Tube)

Fig. 3.9 Schematic of the experimental set-up for studying Magnetic field assisted light transmission

Birefringence

Ferrofluids synthesized by both techniques are taken in sample cells of 1mm thickness. The samples were diluted with the carrier (to known volume fraction) so as to minimize the dichroic effects and the birefringence signal with normalized volume fraction is measured. The retardation is measured using a system including an analyzer, Soleili Babinet compensator, PMT and oscilloscope mounted on an optical bench and the applied magnetic field direction is always kept transverse to the light propagation. A schematic of the set-up is shown in Fig. 3.10
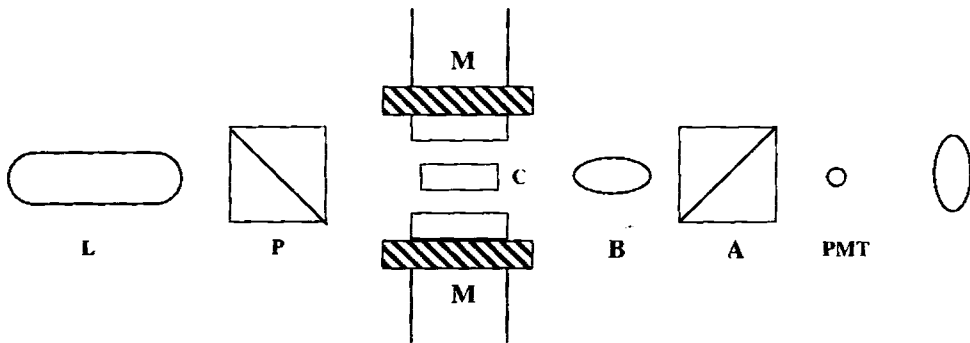
Fig. 3.10 Experimental set-up for linear birefringence.(L-Laser, P-Polarizer, M-Magnet, C- Sample Cell, B- Babinet Compensator, A-Analyzer, PMT-Photomultiplier Tube, and O-storage Oscilloscope)

The optic axis of the polarizer should be identified and the polarizer should be set for polarization direction in the direction of applied magnetic field

Soleili Babinet compensator helps to have a direct measurement of the phase retardation of the perpendicular and parallel polarized waves. Birefringence is calculated from the phase retardation of the components light with planes of polarization parallel and perpendicular to the applied field

$$\Delta n = \lambda \delta / 2\pi l \qquad\qquad 3.22$$

Where 'δ' is the relative retardation of the two mutually perpendicular polarization components of light (directly measured with Babinet's compensator) λ the

wavelength of light used and 'l' is the length of propagation of light through the sample, which is the thickness of the fluid film,

The birefringence is measured with different applied magnetic field values for the chemically synthesized as well as mechanically milled samples. The same experimental set up is employed to study the variation of birefringence with sample volume fraction also.

Linear dichroism:

The experimental set up for measuring linear dichroism is shown in Fig. 3.11.
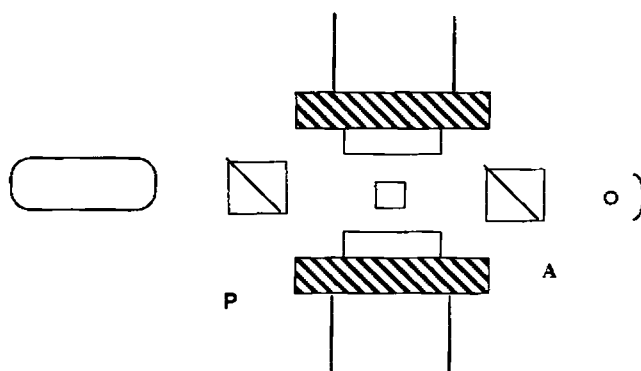
Fig. 3.11 Experimental set-up for measuring Linear Dichroism in ferrofluids.

The intensities of transmitted light with planes of polarisation parallel and perpendicular to the applied field are measured using photo multiplier tube. The corresponding intensities for the zero fields is also measured.

Hence the change in absorbance of the sample caused by turning the magnetic field on for the parallel light beam is

$$\Delta A_{||} = -\ln(I_{||}/I_0) \qquad 3.23$$

Where $I_{||}$ is the transmitted intensity when the magnetic field is turned on and I_0 is the intensity of transmitted light with zero field.

Similarly for the plane of polarization perpendicular to the field direction

$$\Delta A_{\perp} = -\ln\left(\frac{I_{\perp}}{I_0}\right) \qquad 3.24$$

The intrinsic dichroism of the sample can be calculated using the formula

$$\Delta K = (\Delta A_{\parallel} - \Delta A_{\perp})(\frac{\lambda}{4\pi l})$$
                                                                    3.25

Where 'λ' is the wavelength of the source used and 'l' is the thickness of the sample.

Faraday rotation

Faraday rotation is measured using the standard ellipsometer arrangement shown in Fig. 3.15 In this configuration applied field is longitudinal. So we used magnetic poles with a hole of diameter 2mm drilled through them. If the unpolarized laser beam is allowed to pass through a Nicol polarizer, the emerging light will be plane polarized along the optic axis of the polarizer. With the introduction of a quarter wave plate in the optical path of the linearly polarized beam, the linearly polarized beam is changed in to an elliptically polarized beam. The angular setting of the analyzer (θ) is adjusted to obtain a minimum photo multiplier output. To obtain a circularly polarized beam, analyzer is placed after the quarter wave plate and the quarter wave plate is rotated slowly to obtain complete extinction of light.
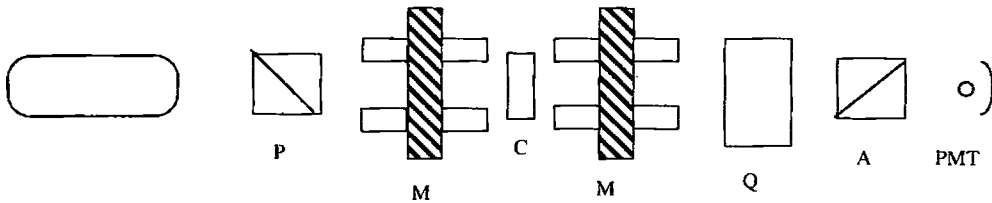
Fig. 3.12 Experimental set up for Faraday rotation and Ellipticity (circular dichroism) measurements.

Now the sample is introduced with the magnetic field through the line of propagation of light. Circularly polarized beam is allowed to pass through the sample. Now with the application of the field the analyzer is readjusted for a minimum photo multiplier output and from these readings the rotation of plane of polarization of light '$\Delta\theta$' is calculated.

Faraday ellipticity

The experimental arrangement of ellipticity is the same adopted for the measurements of Faraday rotation. If there is an ellipticity introduced together with the

106

rotation of plane of polarization of light, The analyzer and quarter wave plate are adjusted to obtain a minimum photomultiplier output with and without the application of the magnetic field. From these readings the changes in readings of analyzer ($\Delta\theta$) and quarter wave plate ($\Delta\phi$) are calculated. Hence the faraday ellipticity is

$$E_F = \tan (\Delta\theta-\Delta\phi) \qquad\qquad 3.26$$

Imaging of the chain formation

The thin ferrofluid film was kept in different magnetic fields and allowed to dry in the respective applied fields. These dried ferrofluidic thin films were viewed with the help of a CCD camera (Model No. G P KR 222) and an optical microscope and the pattern obtained was imaged on a colour video monitor and recorded photographically.

3.7. Measurement of nonlinear optical properties using z scan technique

Characterization of the nonlinear optical properties of materials is of utmost interest in several fields of physics, both from the fundamental and the applied points of view. In particular, great effort has been devoted to the determination of the third-order nonlinear optical susceptibility,$\chi^{(3)}$, responsible for phenomena such as third harmonic generation or optical phase conjugation. In media with inversion symmetry (such as gases, liquids and non-crystalline materials), third order nonlinearity is the lowest order nonlinearity allowed under the electric-dipole approximation. Third harmonic generation, phase conjugation, saturation, self-focusing, optical Kerr effect, and two-photon absorption can all be attributed to this optical nonlinearity. There has been a great deal of research directed to investigating these phenomena in various materials and in pursuing their application. The nonlinear intensity index of refraction n_2 and the two-photon absorption coefficient β are normally used to quantitatively characterize these kinds of self-action nonlinear optical behavior. Many experimental techniques have been developed to measure the magnitude and dynamics of third order nonlinearities. Two most commonly used methods are Degenerate Four Wave Mixing (DFWM) and beam distortion measurements (Z-scan). DFWM directly measures the third order nonlinear susceptibility and usually involve a complicated experimental set up. The Z-scan method utilizes the self-focusing effects of the propagation beam to measure the nonlinear refractive index. The most commonly used method to extract β, is the nonlinear transmittance method

which measures the transmittance of the laser medium as a function of the laser's intensity [34-40].

Among the many methods of measuring $\chi(3)$, the Z-scan technique is the simplest and deserves the most attention. As stated above, the Z-scan technique is a simple and popular experimental technique to measure intensity dependent nonlinear susceptibilities of materials. Moreover, it is a highly sensitive single beam technique for measuring both non-linear refractive index and nonlinear absorption coefficients for a wide variety of materials. In this method, the sample is translated in the Z-direction along the axis of a focused Gaussian beam, and the far field intensity is measured as function of sample position. Analysis of the intensity versus sample position Z-scan curve, predicated on a local response, gives the real and imaginary parts of the third order susceptibility. In this technique the optical effects can be measured by translating a sample in and out of the focal region of an incident laser beam. Consequent increases and decreases in the maximum intensity incident of the sample produce wave front distortions created by nonlinear optical effects in the sample being observed. Moving the sample along a well defined focused laser beam, and thereby varying the light intensity in the sample one obtains the z-scan. By varying the size of an aperture kept in front of the detector, one makes the z-scan transmittance more sensitive or less sensitive to either the real or imaginary parts of the nonlinear response of the material, i.e., nonlinear refractive index and nonlinear absorption, respectively. The z-scan method is an experimental way to obtain information of nonlinear refractive index and nonlinear absorption properties of materials. With nonlinearity, here we simply mean the intensity dependent response of the material, which can be used to obtain an optical limiting device, either by nonlinear refraction or absorption.

The other widely used technique, degenerate four-wave mixing (DFWM), involves a far more complex experimental apparatus but provides several advantages. The fact that the setup includes temporal and spatial overlapping of three separate beams permits increased flexibility, such as the possibility of measuring different tensor components of $\chi^{(3)}$, and a straight forward study of temporal behavior.

When the Z scan was originally devised, it was used to characterize the nonlinear susceptibility of transparent bulk materials. Nevertheless, its use has now been extended to the study of a wide variety of samples. In particular, it is often used to study absorbing media. Among the latter, its use for the assessment of materials consisting of

semiconductor or metal crystallites of nanometer size embedded in dielectric matrices has been very common. These composites are currently the object of intensive research, their most direct application being related to their high third-order nonlinear susceptibility, $\chi^{(3)}$, which makes them promising candidates for the development of all-optical switching devices.

Z-scan is based on the principles of spatial beam distortion and offers simplicity as well as very high sensitivity. There are two types of Z-scan techniques, namely, the 'Closed aperture' Z-scan and the 'Open aperture' Z-scan.

3.8 The Z-scan experimental setup

In a typical experimental setup, a lens initially focuses a laser beam with a transverse Gaussian profile. The sample, the thickness of which is kept less than the Rayleigh range, is then moved along the axial direction of the focused beam in such a way that it moves away from the lens, passing through the focal point. At the focal point, the sample experiences the maximum pump intensity, which will progressively decrease in either direction of motion from the focus.
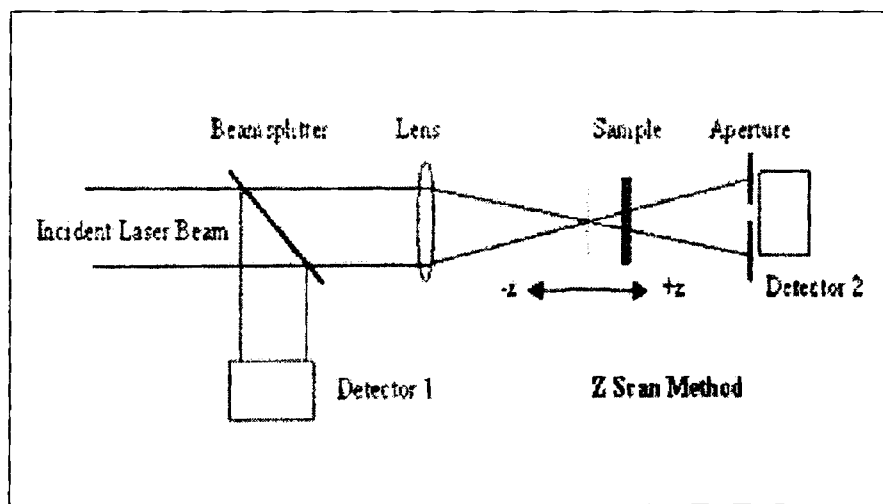
3.13 Schematic representation of the Z scan experimental set-up

A suitable light detector is placed in the far field and the transmitted intensity is measured as a function of the position of the sample, to obtain the open aperture Z-scan curve. Then

an aperture of suitable S value is placed closely in front of the detector, and the experiment is repeated to obtain the closed aperture Z-scan. The absorptive nonlinearity is first determined from the open aperture data, and then the refractive nonlinearity is determined from the closed aperture data.

Closed Aperture Z-Scan:

In this method, a single Gaussian beam in tight focus geometry is allowed to pass through a non-linear medium as shown in Fig 3.17. The sample is moved along the z-direction so that it passes through the focal region of the beam. The transmitted beam is passed through an aperture placed in the far field, and then measured by the detector, for different values of sample position z. This method gives quantitative information on the non-linear refraction of the sample.

Assume, for example, a material with a negative non-linear refractive index and a thickness smaller than the diffraction length of the focused beam (a thin medium). This can be regarded as a thin lens of variable focal length. Starting the sample scan from a distance far away from the focus and close to the lens (negative z), the beam irradiance is low and negligible non-linear refraction occurs. Hence the transmittance (D_2/D_1 in Fig 3.16) remains relatively constant. As the sample is brought closer to the focus, the beam irradiance increases, leading to self-lensing in the sample (As the sample is moved towards the focus, the intensity increase, since the width of the beam decreases towards the focus and the entire energy concentrates into a small area.). A negative self-lensing prior to focus will tend to collimate the beam, causing a beam narrowing at the aperture, which results in an increase in the measured transmittance. When the sample passes the focal plane to positive z, the same self-defocusing results in a more diverged beam at the aperture, causing a decrease in transmittance. This suggests that there is a null as the sample crosses the focal plane. This is analogous to placing a thin lens at or near the focus, resulting in a minimal change of the far field pattern of the beam. The Z-scan is completed as the sample is moved away from the focal plane to the far field in the positive z direction. In the far field since the beam radius is large, the irradiance is again low so that only linear effects will be present.

A prefocal transmittance maximum (peak) followed by a postfocal transmittance minimum (valley) is therefore, the Z-scan signature of negative refractive index nonlinearity.

Positive nonlinear refraction, following the same analogy, gives rise to the opposite valley-peak configuration. It should be noted here that the sensitivity to nonlinear refraction is due to the presence of the aperture, and removal of the aperture will completely eliminate the effect. Thus an extremely useful feature of the Z-scan method is that the sign of the nonlinear index is immediately obvious from the data. Furthermore, its magnitude can also be readily estimated using a simple analysis for a thin medium. For a transparent nonlinear medium, the Z-scan curve will be symmetrical about the z = 0 point. However, if absorptive non-linearities are present, the symmetry will be lost. For example, multiphoton absorption will suppress the peak and enhance the valley, while saturable absorption leads to the opposite effect [41-44].

Analysis of the Z-scan Data

In general, non-linearities of any order can be considered: for simplicity, first examine the case of a cubic non-linearity where the index of refraction n is expressed in terms of non-linear indices n_2 (esu) or γ (m^2/W) through

$$n = n_0 + (n_2/2)| E |^2$$
$$= n_0 + \gamma I \qquad\qquad 3.27$$

where, n_0 = linear index of refraction

E = the peak electric field (cgs)

I = the irradiance of the laser beam within the sample (MKS)

n_2 and γ are related through the conversion formula,

n_2 (esu) = (c n_0 /40π) γ (m^2/W)

where c = speed of light in vacuum measured in m/s

Assuming a TEM$_{00}$ Gaussian beam of beam waist radius w_0 traveling in the + z direction, we can write E as

$$E (z, r, t) = E_0(t) w_0/w(z). \exp[-(r^2/w^2(z))-(ikr^2/2R(z))] \exp (-i\phi(z,t)) \qquad\qquad 3.28$$

where,

E_0 (t) = radiation electric field at the focus and temporal envelope of the laser pulse.

111

$w^2(z) = w_0^2 (1 + z^2/z_0^2)$, $w(z)$ is the beam radius .

$R(z) = z (1 + z^2/z_0^2)$, $R(z)$ the radius of curvature of the wave front at z.

$Z_0 = kw_0^2 / 2$,the diffraction length of the beam.

$K = 2\pi / \lambda$,the wave vector and λ is the laser wavelength, all in free space.

The term exp ($- i\phi(z, t)$) contains all the radially uniform phase variations. As we are only concerned with calculating the radial phase variation $\Delta\phi(r)$, the slowly varying envelope approximation (SVEA) applies, and all other phase changes that are uniform in r are ignored.

If the sample length L is small enough that changes in the beam diameter within the sample due to either diffraction or non-linear refraction can be neglected, the medium is regarded as thin. The SVEA can be applied if this condition is satisfied, thus making the analysis much simpler. The amplitude $\sqrt{I}$ and the phase ϕ of the electric field as a function of z' are now governed in the SVEA by a pair of simple equations:

$$d(\Delta\phi)/dz' = \Delta n(I) k \qquad\qquad 3.29$$

$$dI/dz' = - \alpha(I) I \qquad\qquad 3.30$$

where, z' is the propagation depth in the sample and $\alpha(I)$ in general, includes linear and non-linear absorption terms.

In the case of a cubic non-linearity and negligible non-linear absorption, eqns 3.29 and 3.30 are solved to give the phase shift $(\Delta\phi)$ at the exit surface of the sample which simply follows the radial variation of the incident irradiance at a given position of the sample z. Thus,

$$\Delta\phi (z,r,t) = \Delta\phi_0 (z, t) \exp. (-2r^2/w^2(z)) \qquad\qquad 3.31$$

with

$$\Delta\phi_0 (z, t) = \Delta\phi_0 (t) /(1+ z^2/z_0^2) \qquad\qquad 3.32$$

$\Delta\phi_0$ (t) , the on-axis phase shift of the focus, is defined as

$$\Delta\phi_0 (t) = k \, \Delta n_0(t) \, L_{eff} \qquad\qquad 3.33$$

where, $L_{eff} = (1 - e^{-\alpha L}) / \alpha$

where, L being the sample length and α the linear absorption coefficient.

Here, $\Delta n_0 = \gamma \, I_0(t)$

With $I_0(t)$ being the on-axis irradiance at focus (i.e., z = 0) .

Now, the complex electric field exiting the sample E_e now contains the non-linear phase distortion

$$E_e (r , z , t) = E (z , r , t) \, e^{-(\alpha L / 2)} \, e^{i\Delta\phi(z, r, t)} \qquad\qquad 3.34$$

To obtain the far field pattern of the beam at the aperture plane, a convenient method called Gaussian Decomposition (GD) Method is applied to Gaussian input beams. This method decomposes the complex electric field at the exit plane of the sample into a summation of Gaussian beams through a Taylor series expansion of the non-linear phase term $e^{i\Delta\phi(z, r, t)}$ is,

$$e^{i\Delta\phi(z, r, t)} = \sum_{m=0}^{\infty} [(i\Delta\Phi_0(z,t))^m / m!] \exp[-2mr^2 / w^2(z)] \qquad\qquad 3.35$$

Each Gaussian beam can now be simply propagated to the aperture plane where they will be resummed to reconstruct the beam. When including the initial beam curvature for the focused beam, the resultant electric field pattern at the aperture has to derived as

$$E_a(r, t) = E(z, r=0,t) \ e^{-\alpha L/2} \sum_{m=0}^{\infty} [(i\Delta\Phi_0(z,t))^m / m!] \exp(-2mr^2/w^2(z)) \qquad 3.36$$

$$\exp[(-r^2/w_m^2) - (ikr^2/2R_m) + i\theta m]$$

Defining d as the propagation distance in free space from sample to the aperture plane and g = 1 + d / R(z), the remaining parameters are expressed as

$$w^2_{m0} = w^2(z) / (2m+1)$$

$$d_m = k \ w^2_{m0}/2$$

$$w_m^2 = w^2_{m0} \ [g2+(d^2/d_m^2)]$$

$$R_m = d \ [1- g /(g^2+d^2/d_m^2) \ ]^{-1}$$

and $\qquad \theta_m = \tan^{-1} [d / (d_m/g)]$

Eqn. 3.35 is a general case in which a collimated beam(R = ∞) is considered for which g=1. Actually, this method is very useful for the small aperture distortions detected with the Z-scan method since only a few terms of sum in eqn 3.35 are needed. This method is also easily extended to higher order nonlinearities.

The transmitted power through the aperture is obtained by spatially integrating $E_a(r, t)$ up to the aperture radius r_a, giving,

$$P_T(\Delta\phi_0(t)) = c\varepsilon_0 n_0 \pi \int_0^{r_a} |E_a(r,t)|^2 \ rdr \qquad 3.37$$

where ε_0 is the permittivity of vacuum.

Including the pulse temporal variation, **the normalized Z-scan transmittance T(z)** can be calculated as

$$T(z) = \frac{\int\limits_{-\infty}^{\infty} P_T \left(\Delta \Phi_0(t) \right) dt}{S \int\limits_{-\infty}^{\infty} P_i(t) dt}$$ 3.38

where, $P_i(t) = w_0^2 I_0(t) / 2$ is the instantaneous input power with in the sample a $S = 1 - \exp.(-2r_a^2/w_a^2)$ is the open aperture linear transmittance with w_a denoting the beam radius at the aperture in the linear regime.

Open aperture z scan

Let us analyze two-photon absorption (2PA) . In this context,

$E_g < 2h\omega < 2E_g$, for semiconductors, where E_g is the band gap energy and ω is the optical frequency.

Here, the third order nonlinear susceptibility is assumed to be a complex quantity, which can be written as:

$$\chi^{(3)} = \chi_R^{(3)} + i\chi_I^{(3)}$$ 3.39

Here, the real part is given by $\chi_R^{(3)} = 2 n_0 \varepsilon_0 c \gamma$

And, the imaginary part is given by, $\chi_I^{(3)} = n_0^2 \varepsilon_0 c^2 \beta / \omega$

where γ is the nonlinear index of refraction and

β is the two photon absorption coefficient

To calculate the irradiance distribution and the phase shift of the beam at the exit surface of the sample, substitute,

$$\alpha(I) = \alpha + \beta I$$ 3.40

Now, on re-examining eqns (3.29) and (3.30),

$$dI/dz' = -(\alpha + \beta I) I \qquad\qquad 3.41$$

i.e. $dI/[(\alpha + \beta I) I] = -dz'$

i.e. $dI/(\beta I^2 + \alpha I) = -dz'$,where $I = I(z',r,t)$

$\therefore \int [dI/(\beta I^2 + \alpha I)] = -\int dz'$

The value of $\int[dx/(ax^2+bx)] = [\ln(x)]/b - [\ln(b+ax)]/b$

Hence the above integral leads to

$[\ln(I)]/\alpha - [\ln(\alpha + \beta I)]/\alpha = -z' + c$

when $z'=0$, $c = \ln[I'/(\alpha + \beta I')]$, where I' is the intensity of the Gaussian beam at the axial point; i.e, $I' = I(z,r,t)$

On substituting the value of c also, we get

$[\ln(I)]/\alpha - [\ln(\alpha + \beta I)]/\alpha = -z' + [\ln(I')]/\alpha - [\ln(\alpha + \beta I')]/\alpha$

i.e., $(1/\alpha)[\ln(I/(\alpha + \beta I))] = -z' + (1/\alpha)[\ln(I'/(\alpha + \beta I'))]$

i.e., $(1/\alpha)[\ln[I(\alpha + \beta I')/I'(\alpha + \beta I)]] = -z'$

i.e., $\ln[I(\alpha + \beta I')/I'(\alpha + \beta I)] = -\alpha z'$

i.e., $I(\alpha + \beta I') = I'(\alpha + \beta I) e^{(-\alpha z')}$

i.e., $I\alpha + I I'\beta = I'\alpha e^{(-\alpha z')} + I'I\beta e^{(-\alpha z')}$

i.e., $I(\alpha + I'\beta - I'\beta e^{(-\alpha z')}) = \alpha I' e^{(-\alpha z')}$

$\therefore I(z',r,t) = \alpha I' e^{(-\alpha z')} / [(\alpha + I'\beta - I'\beta e^{(-\alpha z')})]$

$\qquad = I' e^{(-\alpha z')} / [1 + (\beta/\alpha)I' - (\beta/\alpha)I'(e^{(-\alpha z')})]$

$$= I' e^{(-\alpha z')} / [1 + (\beta/\alpha)I'(1 - e^{(-\alpha z')})] \qquad\qquad 3.42$$

where I' is I(z,r,t), which is the intensity of the Gaussian beam at the front face of the sample. The intensity at the exit surface of the sample can be determined from eqn.3.42 by putting   z'=L

$$\therefore I_{exit} = I(L,r,t) = I_{e=} [I(z,r,t)\ e^{-\alpha L}] / [1+ I(z,r,t)(\beta/\alpha)(1- e^{-\alpha L})]$$

$$(1-e^{-\alpha L})/\alpha = L_{eff}$$

$$\therefore \quad I_e = [I(z,r,t)\ e^{-\alpha L}]/[1+(I(z,r,t)\beta\ L_{eff})]$$

i.e., $I_e = [I(z,r,t)\ e^{-\alpha L}]/[1+q(z,r,t)]$ 3.43

and the phase shift caused to the beam after passing through the sample can be obtained as

$$\Delta\phi(z,r,t) = (k\gamma/\beta)\ \ln(1 + q(z,r,t))$$ 3.44

where $q(z,r,t) = \beta\ I(z,r,t)\ L_{eff}$

Then the complex electric field at the exit face of the sample can be obtained by combining eqns. (3.43) and (3.44) as;

$$E_e(z,r,t) = E(z,r,t)\ e^{-\alpha L/2}\ (1+q)^{(jk\gamma/\beta\ -1/2)}$$ 3.45

for |q| < 1, following a binomial series expansion in powers of q, eqn (3.45) can be expressed as an infinite sum of Gaussian beams (similar to the purely refractive case as discussed before) as

$$E_e = E\ (z,r,t)\ e^{-\alpha L/2} \sum_{m=0}^{\infty}(q^m(z,r,t)/m!)[\prod_{n=0}(ikr/\beta)-1/2-n+1]$$ 3.46

Where the Gaussian spatial profiles are implicit in q (z, r,t) and E(z,r,t). The complex field pattern at the aperture plane can be obtained in the same manner as above.

117

The result can be represented by eqn (2.78) if we substitute the $(j\Delta\phi_0(z, t)^m/m!)$ terms in the sum by,

$$f_m = [j\Delta\phi_0(z,t))^m]/m![\prod_{n-0}^{m}(1 + j(2n-1)\beta/2k\gamma)] \qquad 3.47$$

with $f_o = 1$. The coupling factor $\beta/2k\gamma$ is the ratio of the imaginary to the real parts of the third order nonlinear susceptibility

As evident from eqn (3.45), the absorptive and refractive contributions to the far field beam profile and hence to the Z-scan transmittance is coupled. When the aperture is removed, the Z-scan transmittance is insensitive to beam distortion and is only a function of nonlinear absorption. The total transmitted fluence in that case (S=1) can be obtained by spatially integrating eqn.(3.45) at z over r ;

$$P(z,t) = P_i(t) e^{-\alpha L} \ln(1 + q_0(z,t))/q_0(z,t) \qquad 3.48$$

$$\text{where, } q_o(z,t) = \beta I_0(t)L_{eff}/[1+(z^2/z_0^2)]$$

For a temporally Gaussian pulse, the normalized energy transmittance can be expressed as,

$$T(z,s=1) = [1/\sqrt{\pi} q_0(z,0)] \int_{-\infty}^{\infty} \ln[1 + q_0(z,0)\exp(-\tau^2)]d\tau \qquad 3.49$$

Thus, once an open aperture (S=1) Z-scan is performed the nonlinear absorption coefficient β can be deduced. When β is known, the closed aperture Z-scan (S<1) can be used to extract the remaining unknown, namely the nonlinear refraction coefficient γ.

References

1. Ron Dagani, Nanostructured Materials Promise To Advance Range of Technologies, Science/Technology, 1992, 18.

2. R. F.Ziolo, E.P.Giannelis, B.A Weinstein, Michela P. O'Horo, B.N.Gaguly, V.Mehrotra, M.W.Russel, D.R.Huffman. Science **257**, (1992)219

3. D.Chakravorty Bull.Mat.Sci. **15**, no.5, (1992) 411

4. R.D.Shull and L.H.Bennet, Nanocomposite magnetic materials, J.Nanaostructured Materials **1**(1992), 83

5. K.A Malini, *PhD thesis, Dept.of Physics, Cochin University of Science & Technology, Cochin-22,* 2001

6. Effect of Cobalt Doping on The Magnetic Properties of Superparamagnetic γ-Fe_2O_3 - Polystyrene Nanocomposites, **Swapna.S.Nair**, Mercy Mathews, P.A. Joy[$], S. D Kulkarni and M.R. Anantharaman, Journal of magnetism and magnetic materials, **283**, (2004) 344

7. Sutharia G.M, Siblini.A, Blanc-Mignon. M.F, Jorat. L, Parekh. K, Upadhyaya R.V, Mehta R.V, and Noyel. B, J. Magn. Magn. Mater **234**, (2001) 90.

8. B. M. Berkovsky, V. F. Medvedev, M. S, Krakov; Magnetic Fluids, Engineering Applications; Oxford University Press. 1993

9. R. E. Rosensweig; Ferro hydrodynamics; Cambridge University Press. 1985.

10. R. E. Rosenswieg; Magnetic Fluids; 124-132.

11. S. Chikazumi, S. Taketomi, M. Ukita, M. Mizukami, H. Miyajima, M. Setogawa, and Y. Kurihara; , J. Magn. Magn. Mater **65** (1987) 245.

12. R. V.Mehta and R.V. Upadhyay, Current Science, **76**, No 3, (Feb 1999), pp305-312.

13. K. Raj and A. F Chorney Ind. J. of Eng. And materials Sciences, **5**, (Dec.1998) 372

14. H.J.Fecht 1994 Proceedings of the NATO Advanced study institute on Nanophase materials-syntheses, properties and applications, Kluwer academic publishers 125

15. Suryanarayana C, Guo-Hao Chen and Sam Froes F H 1992 Scripta Metallurgica **26** 1727

16. B D Cullity, 1978 *Elements of X-ray diffraction 2nd edition, Addison Weisley Publishing Company Inc., Phillipines*

17. Manojkumar and Sekhon S S *J.Phys.D.Appl.Phys* **34** (2001)2995

18. M Watt 1997 The principles and practice of electron microscopy, second edition, Cambridge university press 60

19. Joseph A. Pesch, Rev. Sci. Instrum, **54**, No.4 (1983) 480

20. E P Giannelis, V Mehrotra, J K Vassiliou, R D Shull, R D MacMichael, R F Ziolo Proceedings of the NATO Advanced study institute on Nanophase materials-syntheses, properties and applications, Kluwer academic publishers (1994) 617

21. Simon Foner, Rev. Sci. Instrum. **30**, No.7 (1959) 548

22. R.V.Krishnan and A.Banerjee, *Rev. Sci. Instrum.*, **70** No.1 (1999) 85

23. Eugene Hecht and Alfred Zajac, Optics, Addisson Wesley Publishing Company, London, 1979

24. S.D Shenoy, PhD thesis, Dept.of Physics, Cochin University of Science & Technology, Cochin-22, 2005

25. E M Mohammed, PhD thesis, Dept.of Physics, Cochin University of Science & Technology, Cochin-22, 2001

26. Mathew George, PhD thesis, Dept.of Physics, Cochin University of Science & Technology, Cochin-22, 2004

27. H.W Davies& J.P. Llewellyn, J. Phys.D, Appl.Phys, **13**, (1980), 2327

28. M. Xu and P. J. Ridler, J.Appl. Phys. **82** (1) July 1997, 326-

29. V.S. Abraham, S. Swapna Nair, S. Rajesh, U.S. Sajeev and M.R. Anantharaman, Bull. Mater. Sci. **27** (2) (April 2004) 155.

30. H.E Horng, Chin-Yih-Hong, H.C Yang, I.J Jang, S.Y Yang, S.L Lee, and I.C Kuo, J. Magn. Magn. Mater. **201**, (1999), 215.

31. S. Taketomi, Jpn. J. Appl. Phys, **22**(1983) 1137.

32. [8]H.E Horng, Chin-Yih-Hong, S.Y Yang, and H.C Yang, J. Phys. And Chem. Solids, **62** (2001) 1749.

33. Sutharia G.M, Siblini.A, Blanc-Mignon. M.F, Jorat. L, Parekh. K, Upadhyaya R.V, Mehta R.V, and Noyel. B, J. Magn. Magn. Mater **234**, (2001) 90

34. Tutt L W and Kost A Nature **356** (1992),225

35. kost A Tutt L W, Klein M B Dougherty T K, and Elias W, Optics Letters, 18 (1993) 334.

36. Mc Lean D. G, Sutherland R L, Brant M.C, Brandelik D M, Fleitz P A and Pottenger T, Optics Letters, 18 (1993) 858.

37. D.J Harter and Y.B Band, Springer Series, Chem. Phys, **38**, (1984) 102

38. D.J Harter, M.L Shand and Y.B Band, J. Appl. Phys, **56**, (1984) 865

39. Lin F, Zhao J, Luo T, Jiang M, Wu Z, Xie Y, Qian Q and Zeng H J. of applied physics, **74** (1993) 2140.

40. Justus B L, Kafafi Z H, and Huston A L, Optics Letters, 18 (1993) 1603.

41. R.Philip, G.Ravindra Kumar, N.Sandhyarani, T.Pradeep, Phys.Rev.B. 62 (2000) 13160

42. S.Link, C.Burda, Z.L.Wang, M.A.El-Sayed, J.Chem.Phys. **111** (1999) 1255
43. .V.Kamat, M.Flumiani, G.V.Hartland, J.Phys.Chem.B. **102** (1998) 3123
44. C.Zhan, D.Li, D.Zhang, W.Xu, Y.Nie and D.Zhu, Opt.Mat. **26** (2004) 11

CHAPTER 4

Structural, magnetic and optical characterization of γFe_2O_3 –Polystyrene magnetic nanocomposites

This chapter deals with the synthesis and characterization of magnetic nanocomposites synthesized by ion-exchange technique. Superparamagnetic nanocomposites based on γFe_2O_3 and sulphonated polystyrene has been synthesized by ion exchange process and the preparation conditions were standardized and optimized. These samples were subjected to cycling to study the effect of cycling on the magnetic properties of these composites. The structural and magnetization studies have been carried out. Magnetization studies show the dependence of magnetization on the number of ion exchange cycles. Doping of cobalt in the atomic percentage range in to the γFe_2O_3 lattice was effected *insitu* and the doping was varied in the atomic percentage range 1-10. The exact amount of cobalt dopant as well as the iron content was estimated by Atomic Absorption Spectroscopy (AAS). The effect of cobalt in modifying the properties of the composites was then studied and the results indicate that the coercivity can be tuned by the amount cobalt in the composites. The tuning of both the magnetization and the coercivity can be achieved by a combination of cycling of ion exchange and the incorporation of cobalt.

Optical characterization is also carried out using UV-Vis-NIR spectrophotometer and an observed blue shift of optical band gap is observed due to grain size dependant quantum confinement. Optical band gap could be tuned by the addition of cobalt as the dopant. The results are correlated and explained.

4.1. Introduction

Nanocomposites can be defined as materials consisting of a host matrix along with identifiable, discrete nanoparticles guest substance having dimensions of the order of 100 nm. Elemental nanocomposites are the least complex nanoparticles by composition. Review of articles for nanocomposites reveal that Magnetic nanocomposites in which magnetic particles, which are in the nano regime, embedded in a nonmagnetic matrix, have gained great interest in recent years as they possess both the magnetic properties of the inorganic component and the mechanical and physical properties of the nonmagnetic matrix. Particles possessing nanometric dimensions in the range of 1-10 nm show superior properties compared to their bulk counter parts [1,2]. It is possible to observe quantum size effects at finite temperatures in these ultra fine particles. Their quantum size effects include shift in the energy gap and also quantum magnetic tunneling. Their large surface to volume ratio also provides some excellent modification of their physical properties due to the large reduction in linear dimensions [3,4]. These

peculiar properties include their single domain and super paramagnetic nature at the nanolevel [5]. Optical properties also change enormously including the band gap due to the small wave function overlapping resulting from their extremely small sizes. These materials find applications in magnetic refrigeration, ferrofluids, colour imaging magnetic recording and sensors [6,7]. If these composites can be made transparent, they can be potential candidate for magneto optical storages.

Gamma ferric oxide belongs to the class of inverse spinels and it exhibits a vacancy ordered spinel structure, where the vacancies are exclusively on the octahedral (B) sites [8]. This material has been extensively used for enormous applications in the bulk due to its very high saturation magnetization and remanance. But they exhibit novel behaviour at the nanolevel due to its vacancy ordered structure. This helps to tailor the magnetic and structural properties of γ-Fe_2O_3 since cations having a strong octahedral site preference with appropriate ionic radius can occupy the B site. This possibility gives maneuverability for modifying the saturation magnetization and coercivity.

The structure of gamma ferric oxide can be written as, Fe^{3+} $[Fe^{3+}_{5/3}$ $\Box_{1/3}]$ O_4^{2-} where $\Box$ represents vacancies and are exclusively on the octahedral sites. Nanocomposites can be synthesized by different methods like high energy ball milling, sol-gel method and ion exchange method.

It has been reported recently that the magnetization of these nanocomposite samples can be increased by ion cycling up to saturation, which depends on the vacant sites in the polymer matrix [9]. However a systematic study on their coercivity variation by doping of nanocomposites is seldom seen in the literature.

It is known that coercivity originates from the irreversible motion of domain walls. The coercivity of magnetic particles is one of the important parameters that determine the usefulness of these materials for different applications including magnetic recording. The coercivity should be at least a few hundred Oersteds to be of any importance for useful applications. However in nanoparticles and nanocomposites, the particles are in single domain/ superparamagnetic state and hence the coercivity and remanance tends to zero and the hysteresis exhibits almost zero loss [10].

Here ion-exchange method is used for the preparation of magnetic nanocomposites, which is a chemical method in which polystyrene polymer beads are used as nonmagnetic polymer matrix. The polystyrene matrix is chosen because of the large number of pores and these pores restrict the growth of the magnetic inorganic component and the size anisotropy induced will hence be a minimum. These composites can be synthesized by weak ion exchange process as well as strong ion exchange process employing hydrogen peroxide or hydrazine hydrate as oxidizing agents, out of which the strong ion exchange process is chosen here [9]. In the present system, as the pore size is the limiting size for the growth of the γFe_2O_3 nanoparticles, which is inherent for a

system of polystyrene beads, the coercivity cannot be controlled by the size anisotropy contribution.

In the case of γFe_2O_3 nanoparticles, the shape cannot be controlled in the ion exchange process and the γFe_2O_3 particles formed are assumed to be spherical. So the size anisotropy contribution is neglected here, as it cannot be controlled in a system of nanoparticles. So in order to increase the coercivity of a sample, it is desirable to dope it with a material, which possesses a large uniaxial symmetry for which cobalt is the best candidate.

In our present investigation, attempts are made to acquire expertise on the synthesis of these single domain super paramagnetic magnetic nanocomposites whose average size lies in the limits 60Å and 90Å, and gain control over its magnetic properties so as to tailor materials for potential applications. Attempts are made to explain the magnetization and coercivity behaviour of these composites at the nanolevel. Our motivation is to study the effect of cobalt doping in a matrix containing γFe_2O_3 and the effect of cycling in the amount of Co/Fe in the matrix. It is also intended to modify the existing method of ion exchange process to incorporate cobalt in the atomic percentage range in order to tune the coercivity of the fine particles.

Attempts are also made to tune the optical bandgap of these nanocomposites, over a vast visible region, by the addition of cobalt, which was never reported to the best of our knowledge. The possibility of making a transparent magnetic composite is bright if one understands the mechanism of strong exciton confinement property in magnetic materials.

Thus this chapter gives an idea of magnetic and optical properties of γFe_2O_3 nanoparticles grown inside the porous network of polystyrene whose pore size limits the growth of the nanocrystals and thus making non-interacting systems.

4.2 Experimental Techniques

4.2.1 Synthesis of γFe_2O_3 magnetic nanocomposites:

The samples were synthesized by ion exchange process using sulphonated polystyrene. The details are cited elsewhere [11]. Cycling was effected using $FeSO_4$ $7H_2O$ solution. The ion exchange cycling was carried out both at room temperature and at a higher temperature of 65^0C for the determination of the change in magnetization with the cycling temperature. The schematic diagram of a typical ion exchange process is depicted in Fig. 1
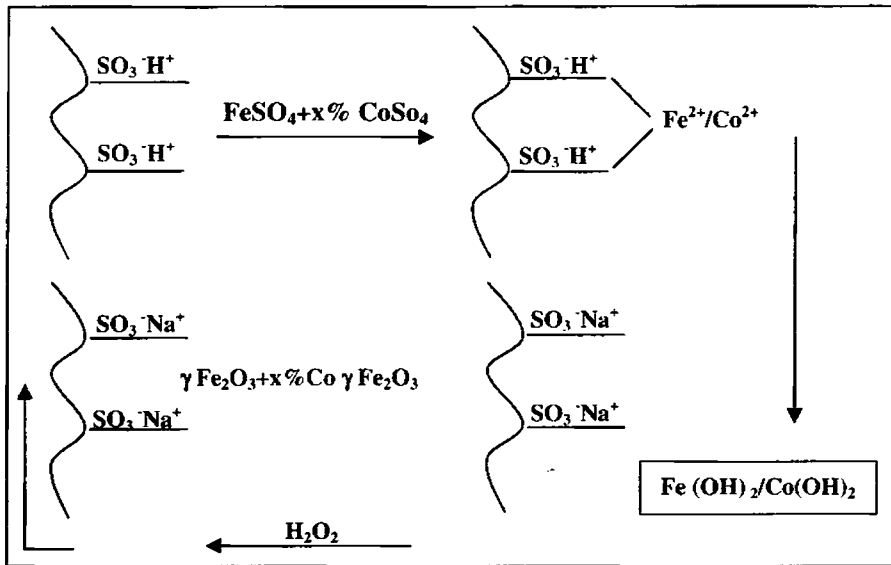
SO$_3^-$H$^+$

SO$_3^-$H$^+$

FeSO$_4$+x% CoSo$_4$

SO$_3^-$H$^+$

SO$_3^-$H$^+$

Fe^{2+}/Co^{2+}

SO$_3^-$Na$^+$

γ Fe$_2$O$_3$+x%Co γ Fe$_2$O$_3$

SO$_3^-$Na$^+$

SO$_3^-$Na$^+$

SO$_3^-$Na$^+$

Fe (OH)$_2$/Co(OH)$_2$

H$_2$O$_2$

Fig.1 A schematic diagram of the ion exchange process.

4.2.2. Doping

Doping with Co was carried out using the same iron exchange process previously described using CoSO$_4$ in the appropriate molar ratio. Doping was effected in the atomic percentage 1- 10%. Cycling of cobalt was carried out using CoSO$_4$ and upto the tenth cycle for each atomic percentage of cobalt.

4.2.3 XRD Studies

The cycled nanocomposites were ball milled in a high energy ball milling unit in an aqueous medium for which FRITSCH PULVERISETTE (P-7) PLANETARY MICRO MILL was employed and the samples were dried to obtain them in the powder form. The XRD spectra of the samples were recorded using an X-ray diffractometer (Rigaku D-max-C) using Cu Kα radiation (λ=1.5405Å). The particle size was estimated by employing Debye-Scherer's formula,

$$D = \frac{0.9\lambda}{\beta \cos \theta},$$

where λ = Wave length of X-ray used, β = FWHM of the XRD peak with highest intensity, D = particle diameter, θ = glancing angle.

126

4.2.4 VSM Studies

The magnetic characterization of the composites containing γFe_2O_3 and Co γFe_2O_3 were carried out by using vibrating sample magnetometry (VSM) (model: EG & G PAR 4500). The saturation magnetization (M_s), Retentivity (M_r) and coercivity (H_c) were measured at room temperature.

4.2.5. Iron and cobalt content estimation

The nanocomposite samples were analysed by Atomic Absorption Spectroscopy (AAS) for the determination of exact percentage of Iron in the samples. From the relative intensities of the absorption lines, the percentage of iron in the polymer globules can be determined. The samples were analysed for each and every cycle of ion exchange in order to determine whether there is an increase in iron content with cycling. The same method is employed for the measurement of the exact percentage of cobalt that has got incorporated into the composite sample. Estimation was carried out for samples with Co in the atomic percentage 1, 2, 4, 6 and 10 for representative ion exchange cycles 1 and 10.

4.2.6. Preparation of aqueous ferrofluids and thin films

Aqueous ferrofluids were synthesised from these synthesised nanocomposites by high energy ball milling (HEBM) process using FRITSH PULVERSITE 7 MICROMILL at a rotational speed of 600 rpm with known amount of water. Thin films were prepared by dip coating method and the parameters like concentration and temperature have been optimised.

4.2.7. Optical studies

Optical absorption spectrum was recorded using a Hitachi U-3410 UV-VIS-NIR spectrophotometer for the pure as well as cobalt doped samples and the band gap was determined for all the synthesised samples. In order to calculate the band gap (assuming direct band gap), it may be noted that for a semiconductor, the absorption coefficient near the band edge is given by

$$\alpha = \frac{A(h\nu - E_g)^{1/2}}{h\nu}$$

where A is a constant and E_g is the energy band gap.

When $\alpha h\nu = 0$, $E_g = h\nu$.

So using an extrapolation to the X axis of the pot of "$(\alpha h\nu)^2$ vs $h\nu$", gives the bandgap of the material if it is a direct transition which is the Tauc plots .

4.3. Results and discussions
a) *Magnetic characterization-Tuning of magnetization parameters by cobalt doping*

The X-ray diffraction pattern indicates that the composites exhibit semi amorphous nature due to the presence of large polymer content of the host matrix polystyrene and the particle size, calculated by employing Debye Scherer's formula, lies in the range 70-85Å for all the synthesized samples. The cycling of iron resulted in an increase in the crystallinity. The detected phases were that of γ Fe_2O_3 only with no detectable impurity peaks. Representative X-Ray diffraction spectrum is depicted in Fig.2.
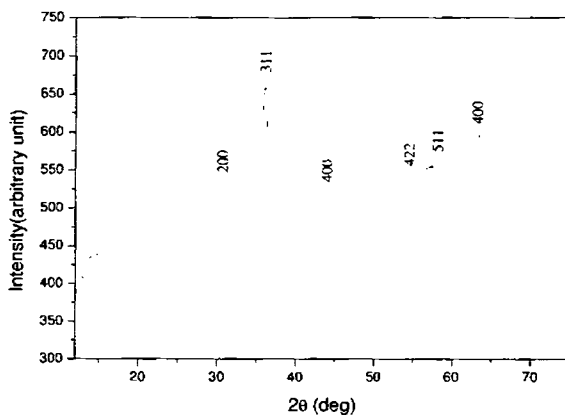

Fig.2 Representative XRD spectrum of γFe_2O_3 polystyrene magnetic nanocomposites.

The iron content measurements by atomic absorption spectroscopy indicates an increase in iron content with cycling of ferrous sulphate and this attains a saturation for cycle 8 and after that a slight decrease in iron content is observed on further increase in Fe cycling. This result is analogous to the one reported [9]. The saturation may be the result of occupation of all the vacant sites inside the polymer matrix by the Fe^{2+} ions and their subsequent oxidation to gamma Fe_2O_3. Further increase in the cycling process may push out some of the gamma Fe_2O_3 molecules previously occupied in the vacant sites. A graph plotted with the iron content against number of ion exchange cycles is shown in Fig. 3
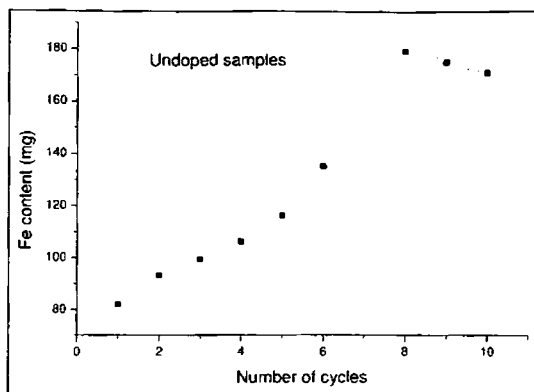
Fig.3 Fe content in different cycles of ion exchange with Fe²⁺ ion.

Magnetization studies:

The magnetization studies using vibrating sample magnetometer show that the undoped magnetic nanocomposites synthesized by ion exchange process are superparamagnetic in nature with remanance and coercivity approaches zero. Mössbauer measurements were carried out in the laboratory and these results confirm superparamagnetic behaviour. The results are not included in this thesis. Also from this measurement an increase in magnetization with increase in iron content is observed up to cycle number 8 and then it decreases.
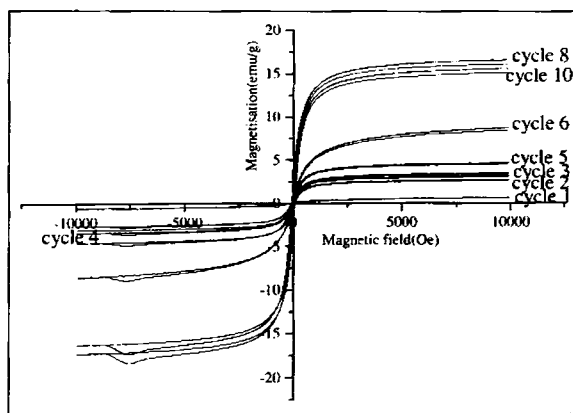

Fig.4 Hysteresis loops of undoped samples in different cycles of ion exchange with Fe³⁺ ion.

This behaviour is analogous to the iron content estimation result in which there is a slight decrease in the content of iron after the 8th cycle. This confirms the absence of αFe_2O_3 phase in the sample in a detectable amount. The X ray analysis also shows no

additional peaks. The magnetization reaches a maximum of 16.5 emu/gm and then decreases slightly for undoped samples. The hysteresis loops for the undoped samples are depicted in Fig. 4

A graph plotted with the saturation magnetization vs no of ion exchange cycles (Fig. 5) shows a similar behaviour as in Fig. 3.
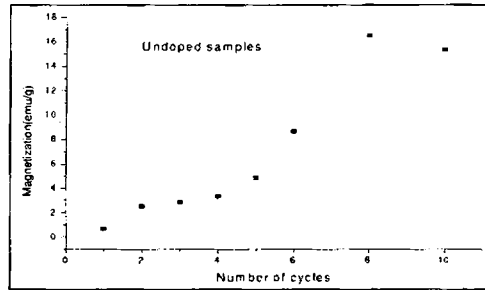

Fig.5 Saturation Magnetization in different cycles of ion exchange with Fe^{3+} ion.

It is observed that the iron content and magnetization increases if the cycling is carried out in higher temperature instead of room temperature. The samples that were left for ion exchange for 4 hours at a temperature of 65^0C possess a saturation magnetization comparable or even higher than the samples allowed for ion exchange for 24 hours. The representative hysteresis loops (Fig. 6) clearly shows that the ion exchange process as well as the yield of γFe_2O_3 is higher at 65^0C, which is evident from the magnetisation curve (Fig. 6).
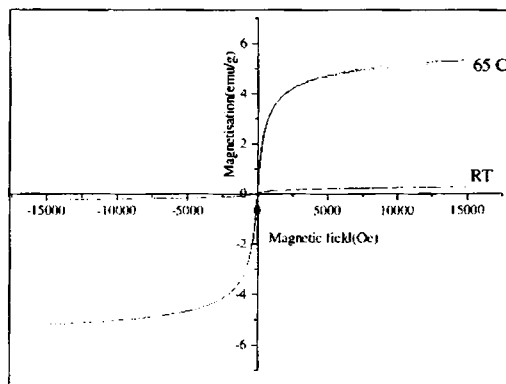

Fig. 6 Hysteresis loop showing increase in magnetization with increase in temperature of ion exchange cycling.

Analysis of the results of Atomic Absorption Spectroscopy (AAS) carried out on the doped samples suggests that the cobalt content increases in the sample in each cobalt cycling. The samples with cobalt in the atomic percentage 1%, 2%, 4%, 6% and 10% with respect to γFe_2O_3 were also investigated by AAS for the estimation of cobalt content. The cobalt content estimation shows an increase with addition of cobalt percentage indicating the proper ion exchange and doping. So doping is made easy with insitu addition of the cobalt salt along with an iron salt maintaining proper pH and temperature, which are optimized.

The magnetization studies of the doped samples show an increase in coercivity of the doped samples and the detectable change in coercivity of the sample is noted for higher cobalt doping, ie, 4%, 6% and 10%. Representative magnetization curves are shown in Fig. 7 and Fig. 8.
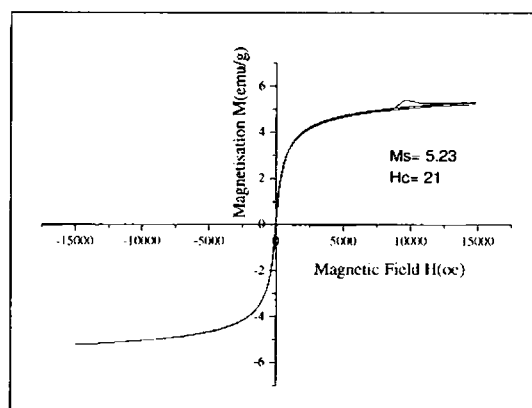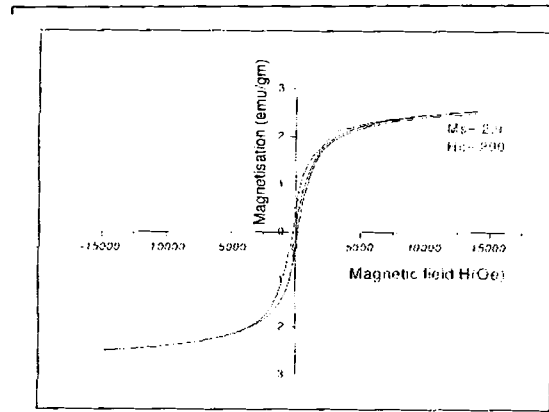

Fig.7 Hysteresis loop of the sample with Co (0.304% as determined by AAS)

It may be noted that the coercivity of the nanocomposites containing cobalt and γFe_2O_3 enhanced from 20 Oe to 300 Oe by cobalt doping. It is obvious from the figure that the coercivity increases almost linearly with increase in cobalt in the low doping regime. But the increase in coercivity is not that high for higher doping.

The variation of coercivity with percentage of cobalt is depicted in Fig. 9

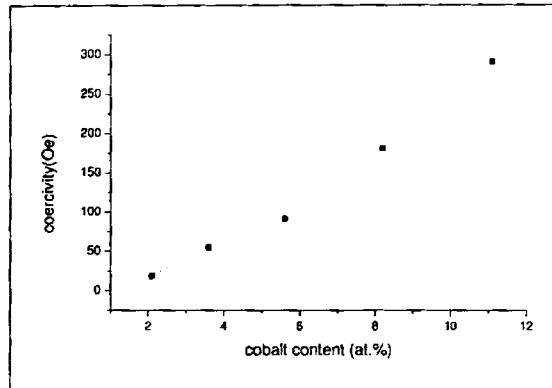*1 Fig.8 Representative hysteresis loop of the sample with Co 1.484%*

Fig. 9 The variation of coercivity with percentage of Co (As determined by AAS).

One of the probable reasons for this special behaviour in higher doping is that although there is higher cobalt content the ion exchange process may not be complete and some amount of cobalt may still exist in the unionized state itself.

Coercivity of magnetic samples has a striking dependence on their size. As the particle size decreases the coercivity increases and reaches a maximum and then decreases. The increase in magnetization is attributed to its change from the multi domain nature to the single domain [10].

The size dependence of coercivity is experimentally deducted and is as follows

$H_c = a + b/D$ 4.1

132

where 'a' and 'b' are constants and 'D' is the diameter of the particle if it is assumed to be spherical.

But as the particle size decreases below D_s (which is the critical size for a single domain magnetic particle) the coercivity decreases because of thermal effects. As the particle size decreases, H_c tends to zero below a critical particle size as governed by the equation

$$H_{ci}= g-h/D^{3/2} \qquad\qquad 4.2$$

where 'g' and 'h' are constants.

Below a critical diameter, the coercivity tends to zero again because of the thermal agitation which are now strong enough to spontaneously demagnetise the previously magnetized assembly of particles and such systems, which have the coercivity and remanence tending to zero, are termed as superparamagnetic.

So it is difficult to achieve very large coercivities in the nanoregime below a critical diameter. Enhancing coercivities by other means has to be resorted to.

The coercivity also arises from anisotropies present in the crystal. It is known from literature that shape, size and magneto crystalline anisotropy contribute to this [8].

Shape anisotropy can be expressed as

$$H= h (N_a-N_c) M_s, \qquad\qquad 4.3$$

Where N_a and N_c are the demagnetizing coefficients along 'a' and 'c' axes. If $N_a=N_b$, no shape anisotropy is there and its contribution can be neglected if the particles in general possess a spherical shape.

The anisotropy arising out of the stress created can also play a role in increasing the coercivity of a material as the stress induces magnetostriction, which increases the anisotropy there by contributing an increase in the coercivity of the sample.

Stress anisotropy can be mathematically expressed as

$$H=h (3\lambda_{si}\sigma/M_s) \qquad\qquad 4.4$$

λ_{si} is the magnetostriction, σ the stress .

Out of the three major anisotropies contributing to the coercivity, only crystal anisotropy or magneto crystalline anisotropy is intrinsic to the material and all others are induced anisotropies. In any crystal, the direction of easy magnetization is the direction of spontaneous domain magnetization in the demagnetized state. Because of the applied field doing work against the anisotropy force to turn the magnetization away from the

easy direction there must be energy stored in the crystal and this energy is termed as magnetocrystalline energy.

Magneto crystalline anisotropy is mainly due to spin orbit coupling neglecting the contributions from spin-spin and orbit-lattice coupling as they are too strong to be changed even by large applied fields and so isotropic.
The magneto crystalline anisotropy can be mathematically expressed as

$$H = h \, (2K_1/M_s) \hspace{6cm} 4.5$$

where K_1 is the anisotropy constant, assuming K_2 is small and applying conditions of minimum energy.

In cubic crystals like Fe_3O_4 there are more than one easy axis of magnetization there by reducing the magneto crystalline anisotropy. But in a hexagonal crystal like Cobalt, there is only one magnetic easy axis, which is directed along the hexagonal 'c' axis. So the anisotropy and hence the coercivity is very high in case of a uniaxial crystal like cobalt which possess a positive K_1 value.

It is in this context that incorporation of Co in a polymer matrix consisting of γ-Fe_2O_3 assumes significance. It is envisaged that the incorporation of cobalt into the lattice of γ-Fe_2O_3 in the polymer matrix will significantly modify the coercivity because of its magneto crystalline anisotropy there by offsetting the finite size effects of the particle media on the coercivity of the matrix.

γFe_2O_3 particles can be prepared in both acicular (Needle like) and spherical form . Needle shaped γFe_2O_3 particles can be synthesized by using complexing media [12] or by starting from Geothite [13]. But in the ultrafine regime, the normal tendency of the particles is to be in spherical shape, so that the contribution from the size anisotropy arising from the needle like shape of the particles is a minimum. In our present system, γFe_2O_3 is trapped inside the pores of polymer network by chemical route and these pores, which are spherical, limit the growth and shape of the nanoparticles. There are also various reports ensuring the spherical shape of the particles in their ultrafine form. Vassiliou et al reported the Transmission Electron Microscopy images of these samples showing the spherical nanoparticles [14]. Thus it can be concluded that the enhancement of coercivity observed in our present system is due to the magnetocrystalline anisotropy introduced by the dopant cobalt.

Thus in magnetic nanoparticles, the increase in coercivity for probable applications can be obtained by the addition of an element/crystal possessing large magneto crystalline anisotropy for which cobalt is the best candidate. Ion exchange method can be successfully employed for tuning both magnetization and coercivity of the samples. The decrease in magnetization caused by the doping is due to the exchange of iron with cobalt in the occupied states. The magnetization can be increased by ion

exchange cycling with iron, which enables to fill the vacant sites for the doped samples. Thus complete tuning of the magnetic parameters is possible by a combination of the ion exchange cycling and appropriate cobalt doping.

b) Optical studies: Evidence for blue shift in optical absorption spectrum due to quantum confinement effects
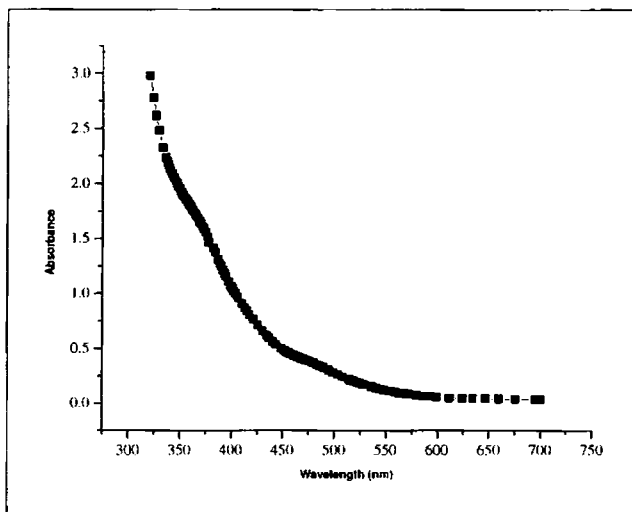

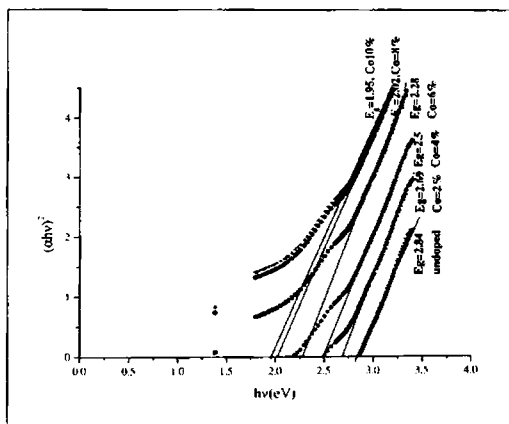*Fig. 10 Absorption spectra of γFe₂O₃-polystyrene nanocomposites*

Fig. 11 Optical bandgap determination of the pure as well as cobalt doped samples using Tauc plots

The optical absorption spectra of the pristine and the doped samples were recorded (Fig.10) and their optical bandgaps were determined using Tauc plots. They are shown in Fig.11 [15].

Co in atomic percentage (Intended)	As detected by AAS
2	2.1
4	3.6
6	5.6
8	8.2
10	11.1

Table.1 cobalt content intended and estimated

Cobalt Doping (Atomic percentage)	Optical bandgap in eV
Bulk*	2.2
Ultrafine#	2.84
2	2.69
4	2.5
6	2.25
8	2.02
10	1.95

Table. 2 Cobalt content against Optical bandgap

$* = $ Bulk γFe_2O_3 :   # Ultrafine γFe_2O_3 in the polymer matrix.

A large blue shift of 0.64 eV for the undoped samples ($E_g=2.84$ eV) is observed as compared to the bulk value. The details are included in table 2.

Optical absorption spectrum of many of the nanocrystalline semiconductors exhibits a blue shift mainly due to the quantum confinements. The confinements in these nanostructured semiconductors could be broadly divided into two extremes, namely the strong and the weak confinement. In the strong confinement regime, the grain size is less than $2a_0$ where a_0 is the exciton Bohr radius of the material and in the weak confinement regime, the grain size is larger than $4a_0$. In between these limiting cases, both electron and hole confinement and their Coulomb interaction should also be considered.

In the weak confinement regime, quantisation of exciton centre of mass comes into play, Starting from the dispersion law of an exciton in a crystal, the energy of a free exciton is replaced by a solution derived for a particle in a spherical potential well[15]. The energy of an exciton in the weak confinement case is then of the form

$$E_{nml} = E_g - \frac{Ry*}{n^2} + \frac{\eta^2 \chi_{ml}^2}{2Ma^2}$$

4.6

E_g is the bandgap, Ry^* is the Rydberg's constant.
For the lowest state (n=1, m=1, l=0) the energy can be expressed as

$$E_{1s1s} = E_g - Ry* + \frac{\pi^2 \eta^2}{2Ma^2}$$

4.7

which could be rewritten as,

$$E_{1s1s} = E_g - Ry* \left[1 - \frac{\mu}{M} \left(\frac{\pi^2 a_B^2}{a} \right) \right]$$

4.8

where μ is the reduced mass of the electron-hole pair. The value $\chi_{10} = \pi$, and the relation for confinement energy becomes,

$$\Delta E_{1s1s} = \frac{\mu}{M} \left(\frac{\pi a_B}{a} \right)^2 Ry*$$

4.9

which is, however, small compared with Ry* so far as

$a >> a_B$

holds. This is the quantitative justification of the term "weak confinement".

Taking into account of photon absorption which can create an exciton with zero angular momentum, the absorption spectrum will then consist of a number of lines corresponding to states with l=0. Therefore, the absorption spectrum can be derived from eqn (4.9) with $\chi_{m0} = \pi m$

$$E_{nm} = E_g - \frac{Ry*}{n_2} + \frac{\eta^2 \pi^2}{2Ma^2} m^2$$

4.10

the "free" electron and heavy hole have the energy spectra

$$E_{ml}^e = E_g + \frac{\eta^2 \chi_{ml}^2}{2m_e a^2},$$

4.11

$$E_{ml}^h = \frac{\eta^2 \chi_{ml}^2}{2m_h a^2}$$

4.12

therefore, the total excess energy for the lowest electron and hole in 1s state is

$$\Delta E_{1s1s} = \left(\frac{\pi a_B}{a} \right)^2 Ry*$$

4.13

Or in terms of effective mass of the exciton (electron-heavy hole pair) and grain radius, using eqn 4.12 confinement energy can be written as

$$E_{sh} = \frac{h^2\pi^2}{2m_{eff}R^2},$$ 4.14

where R is the nanocrystalline radius and m_{eff} is the effective mass of the exciton in weak confinement. Thus confinement energy is clearly a function of the nanoparticle radius and varies as $1/R^2$.

Actually the exciton of 1s electron-heavy hole has comparable values of effective mass m_{eff} for almost all the semiconductors and thus the energy shift variation becomes a function of the nanoparticle radius in the weak confinement regime.

From eqn 4.14 could be concluded that mere quantum confinement in the weak regime can itself account for an energy shift of 0.64 eV in the material as compared to the bulk value when the grain size is limited in the size limit of R=40 Å as calculated by line broadening of the X ray diffraction spectrum.

Hence the blue shift in the absorption spectrum obtained in nanocrystalline pure nanocrystalline γ-Fe$_2$O$_3$ could be fitted to the quantum confinement in the weak confinement regime with the reduced mass m_{eff} is 0.6 m_0 along the longitudinal.

The band gap shows a gradual red shift in the optical absorption edge for the Co-doped samples in comparison with the pure sample and this red shift is in accordance with the doping percentage. The red shift in absorption edge (as compared to the undoped samples) can be attributed to the pressure induced effects [16], which is manifested in nanoparticles and this extreme small size results in an increased surface pressure and hence increased lattice strain which decreases the bandgap as,

P = 2γ / R 4.15

Where γ is surface tension and P, the pressure due to surface tension and for particle of diameter around a 100 Å, the pressure of 0.4 G Pa is calculated. Thus a red shifted absorption edge can be expected. In undoped samples due to the weak exciton confinement, there is an enhancement of bandgap observed. But the presence of an atom like cobalt with large magneto-crystalline anisotropy increases the total strain effects, which helps in shifting the spectrum towards higher wavelength side, and thus the spectrum gets red shifted and the red shift gets further enhanced with the dopant amount in the lattice.

The pressure induced effects will contribute to the lattice strain and thus results in reduced bandgap. The pressure induced effects is rather very small compared to the actual shift obtained in the doped samples in comparison with the undoped samples. So in order to account for this large red shift, we have to consider the additional intermediate dopant energy levels. This can reduce the bandgap to a considerable amount.

Presence of cobalt at the vacancies of γ-Fe_2O_3 could create energy states in the band gap region that may develop into a narrow energy band as dopant concentration increases. Then the effective gap for transitions between this narrow band and other localised states or the conduction band would then definitely will be smaller than the undoped samples. Also the increase in concentration of the dopants increase the stress anisotropy and its effect on its magnetic properties have been studied and was reported elsewhere [17].

Thus in nanocrystalline γ-Fe_2O_3 doped with cobalt, two opposing effects determine the shift in band gap. One of them is the weak exciton confinement leading to the blue shifted absorption edge for the undoped samples. But as the dopant concentration increases, due to the large crystalline anisotropy, the stress induced effects comes into play. Also the small energy states formed in between the band gap grows as a narrow band and thus reducing the energy band gap of the material.

In some semiconductors it is reported that [11] the band gap decreases with increase in the pressure and strain induced effects and eventually the band gap closes and the semi conductor undergoes a semiconductor to metal transition at critical pressures which is a factor determined by the material. Here nanocrystalline γ-Fe_2O_3 were synthesised with large blue shifted absorption edge with weak exciton confinements, and tuning of both optical and magnetic parameters are effected with the addition of a specific dopant like cobalt, which becomes very important from the application point of view 18].

4.4. Conclusion

The undoped magnetic nanocomposites synthesized by ion exchange process are superparamagnetic in nature with remanance and coercivity almost zero. The magnetization can be increased by cycling process in which more vacant sites in the polymer matrix can be made occupied by the maghemite molecules. The addition of cobalt, which possesses large magneto crystalline anisotropy, is found to increase the coercivity of the samples. It is evident from the magnetization measurements that there is a cation redistribution, which changes the magnetization, which is already reported for ultrafine particles of spinel ferrites. Thus the magnetization and coercivity can be successfully tuned by doping in the nanocomposites for possible device applications. The method of strong ion exchange resin can be adopted for the incorporation of cobalt into the matrix containing γFe_2O_3. Cycling of iron and cobalt can be achieved to obtain an optimum magnetization M_s and H_c of the matrix. The incorporation of cobalt in the lattice modifies the coercivity and this is useful for tailoring the coercivity of nanocomposites whereby this offset the finite size effect on the coercivity.

Absorption edge of ultra fine γ-Fe_2O_3-polystyrene magnetic nanocomposites synthesized by chemical route was blue shifted by an amount of 0.64 eV due to weak exciton confinement. Strong confinement can result in a theoretical blue shift of around

1.45 eV (in a quantum dot confinement); but that may reduce the magnetic properties and thus not favoured under the application point of view. Thus transparent magnetic nanocomposites (in the visible range) could be synthesized by size reduction of the order of the Bohr radius limits, which can throw open a wide field with versatile application potential. Also tuning of optical bandgap is made possible which is reported for the first time in these magnetic nanocomposites by doping with Co and the spectrum gets red shifted more and more with increased doping and finally gets saturated due to the formation of a complete dopant level in the intermediate

References
1. R.F. Ziolo, E.P.Giannelis, B.A. Weinstein, M.P O'horo, B.N. Gganguly, V. Mehrotra, M.W. Russel and D. R Huffmann, Science, **219** (1992) 257.
2. R.D Shull and L.H Bennet, Nanostructured Materials, 1, (1992) 83.
3. E.M. Chudnovsky, and L. Gunther, Phys.Rev.B, **37** (1998) 9455
4. Rupali Gangopadhyay and Amitabha De, Chem. Matter (2000), vol 12, 608.
5. A. Ezzir, J.L Dormann, H. Kachkachi, M. Nogues, M. Godinho, E. Tronc and J.P Jolivet, J. Magn. Magn.Mater, **196**, (1999) 37.
6. R.D mcMichael, R.D. Shull, L.J Swartzendruber, L.H. Bennet and R.E. Watson, Journal of magnetism and magnetic materials, **111**(1992).
7. K.A Gscheidner, and V.K Pecharsky, J.Appl.Phys **85** (8) (1999) 5365
8 Ferrites, Smit and Wijn, Philips technical library, 1959.
9. K.A. Malini, M.R. Anatharaman, S.Sindhu, C.N. Chinnasamy, N. Ponpandian,   A. Narayanasamy, B. Balachandran and V.N. Shivasankarapillai, Journal of Material Science, **36** (2001) 821.
10. Introduction to Magnetic materials B.D Cullity, Addison Wesley publishing company (1972).
11. R.F. Ziolo P. Giannelis and R.D Shull, Nanostructured Materials, **3**, (1993) 85.
12. M.R. Anantharaman, K.V Joseph and H.V Keer, Bull. Mater. Science, **20**, No.7, (Oct.1997), 975.
13. M.R.Anantharaman, K.Sheshan, S.N Shringi and H.V. Keer, Bull. Mater. Science. **6**, No 1, (Feb 1984), 59.
14. John K Vassiliou, Vivek Mehrotra, Michael W Russel, Emmanuel P. Giannelis, R.D Mc Michael, R.D Shull and Ronald F. Ziolo, J. Appl. Phys, **73** (10), (15 May 1993), 5109.
15. Richard Turton, *The Physics of Solids*, Oxford University Press, New York (2000).
16. John K Vassiliou, Vivek Mehrotra, Michael W Russel, R.D Mc Michael R.D Shull and Ronald F. Ziolo, D.K Smith and C Mailhiot *Rev. Mod. Phys*, **62**, (1990) 173
17. S. Swapna. Nair, Mercy Mathews, P.A Joy and M.R. Anantharaman, *J. Magn. Magn. Mater.* **283**, Issue 2-3, (Dec 2004) 344.
18. Swapna S Nair, Mercy Mathews And M.R Anantharaman, Chem. Phys. Lett, **406** (2005) 398.

CHAPTER 5

Synthesis of self protected Cobalt nanoparticles by
a novel Chemical Route

This chapter deals with the synthesis and characterisation of self protected elementary magnetic metal nanoparticles by a novel ingenious technique. Elementary cobalt based ultra fine metal magnetic particles have been synthesised inside a porous polymer network through a novel chemical route using a reduction process. Chemical process is employed here for the synthesis of nanoparticles as it provides a bottom up process which could yield controlled grain growth. Sulphonated polystyrene with natural nanopores of about 25% is employed as a template for the synthesis of these metal nanoparticles. Capping or passivating the high surface area metal nanoparticles could be thus avoided and the grain size and size distribution could be controlled by the pore size limitation of the polymer network. The goal of obtaining a higher amount of metal nanoparticles is achieved by repeating the reduction cycle for several days. Their structural characterisation was carried out using X-Ray Diffraction technique which shows the crystalline nature of the synthesised metal nanoparticles with no detectable impurity peak. Their magnetisation measurements show that the cobalt based polymer nanocomposites synthesised possess fairly good coercivity even in the as prepared state. Both magnetisation and coercivity got enhanced by repeating the cycling of reduction process. This novel method for the synthesis of cobalt polymer nanocomposites, paves way to variety of applications in recording and are potential candidates for magnetic refrigeration owing to their very good coercivity and magnetisation even in its ultra fine as prepared form.

5.1Introduction

Over the last few years magnetic properties of fine ferromagnetic particles (Fe, Co, Ni) have been widely studied, as they present an interest both from the fundamental physics point of view and for applications [1-5]. Magnetic nanocomposites are quite important from a fundamental point of view to study the magnetism at the nano level of non-interacting particles. The general requirements would often be of magnetic particles displaying a large magnetic susceptibility, while keeping inter particle interactions low so they do not agglomerate.

Metal nanoparticles which are magnetic, possess added advantage of having possessing good conductivity. Metals like Iron, Cobalt and Nickel are ferromagnetic

at room temperature. However, the magnetic properties will vary as the bulk metal is broken into finer and finer pieces. Nanophase metals are often much stronger than their poly crystalline counterparts. The magnetic properties of nanometals can be very different, manifesting softer magnetism or single domain magnetism with a much greater coercivity. If small enough, they can also be tested the superparamgnetic limit of matter.

Magnetic properties of metal nanoparticles are important from the application point of view as they are potential candidates in magnetic storage media. The finite size effects on various physical properties of materials was investigated first by Kubo in 1962 [6] in which is shown that when the grain size is reduced to the order of 5nm, the energy level spacing of the quantised electronic states is comparable to thermal energy contribution and thus quantum size effects can be observed even at room temperature. In addition, the large reduction linear dimensions together with the boundary and surface conditions play a major role in small particles. Such changes in physical properties brought out by dimensional manipulations make them attractive candidates in variety of applications like in ceramics, magnetic recording, catalysis, medical applications, ferrofluids etc [7-11]

Several synthetic techniques have been adopted to synthesize magnetic metal (Fe and Co) nanoparticles, including thermal and sonachemical decomposition of organometallic precursors [12] high-temperature decomposition of metal carbonyls [13], and polyol process [14]. Also metal nanoparticles were synthesised by vapour liquid chemical reaction [15]. Some research groups have employed laser ablation methods and prepared magnetic nanoparticles (Co, Ni, Fe) of 40-500 atoms.

Reduction methods were extremely useful for the synthesis of metal nanoparticles as they provide tenability of grain size and size distribution by careful variation of the synthesis parameters like reaction rate, temperature, pH and concentration of reducing agents. Typical reducing agents commonly used for the synthesis of metal nanoparticles are $NaBEt_3H$, $LiBEt_3H$ and $NaBH_4$ [16]. The reactive medium chosen was either Tetrahydrofuran (THF) or toluene.

However, these bare nanoparticles were not stable in air due to oxidation and aggregation if not passivated by other organic or inorganic molecules. Ultra fine metal particles are highly explosive due to very high surface area if synthesised uncapped. But capping of metal nanoparticles makes the synthesis technique tedious and modifies many of their inherent properties.

In cubic crystals there is more than one easy axis of magnetization there by reducing the magneto crystalline anisotropy. But in a hexagonal crystal like Cobalt, there is only one magnetic easy axis, which is directed along the hexagonal 'c' axis. So the anisotropy and hence the coercivity is very high in the case of a uniaxial crystal like cobalt which possess a positive anisotropy constant (K_1) value. It is in this context that incorporation of Co in a polymer matrix assumes significance so as to study the anisotropy and enhanced coercivity even in its nanoregime.

Here, in the present investigation, a modified procedure was developed for the synthesis of metal nanoparticles as suggested by [16] for synthesising the metal nanoparticles inside the natural pores of a polymer network and thus the grain growth and the process of *in situ* capping of the materials using polymers could be avoided. Also the yield of metal nanoparticles could be enhanced by repeating the reduction cycle which was reported for the first time which provides excellent application potential. Although the exact pore diameter is not known, quantum confinement effects are observed in maghemite nanoparticles synthesised by this route earlier hinting that the pore diameter is of the order of a 10 nm. Here THF is deliberately avoided and water is used as the reaction medium so as to avoid generation of peroxides in contact with air and easily flammable.

The synthesis and characterisation of polymer based magnetic nanocomposites has been reported first by R.D Mc Michael and R.D Shull [17] and studied in plenty by other researchers also. However such an attempt was never taken for the synthesis of self protected elementary metal nanoparticles. Here attempts are taken for the synthesis of elementary metal nanoparticles inside natural pores of polystyrene with a modified reduction technique which was never reported elsewhere.

5.2 Experimental Techniques

5.2.1 Synthesis of elementary cobalt based magnetic nanocomposites:

Ultra fine cobalt particles were synthesized by a reduction process using sulphonated polystyrene as the template which is reported for the first time. Strong reducing agent $NaBH_4$ is employed for reducing the metallic salts. Both AR grade sulphates and chlorides have been used for the reduction process in which sulphates results in better yield. Precipitation cycling was effected using $CoSO_4 \, 7H_2O$ solution [18]. The schematic diagram of a typical reaction process is depicted in Fig. 1

5.2.2 XRD Studies

The cycled nanocomposites were ball milled in a high energy ball milling unit in an aqueous medium for which FRITSCH PULVERISETTE (P-7) PLANETARY MICRO MILL was employed and the samples were dried to obtain them in the powder form. The XRD spectra of the samples were recorded using an X-ray diffractometer (Rigaku D-max-C) using Cu Kα radiation (λ=1.5405Å). The particle size was estimated by employing Debye-Scherer's formula,

$$D = \frac{0.9\lambda}{\beta \cos\theta},$$

where λ = Wave length of X-ray used, β = FWHM of the XRD peak with highest intensity, D = particle diameter, θ = glancing angle.

5.2.3 VSM Studies

The magnetic characterization of the composites containing elementary Cobalt were carried out by using vibrating sample magnetometry (VSM) (model: EG & G PAR 4500). Hysteresis loop is traced and the saturation magnetization (M_s), Retentivity (M_r) and coercivity (H_c) were measured at room temperature.

5.2.4. Cobalt content estimation

The nanocomposite samples were analysed by Atomic Absorption Spectroscopy (AAS) for the determination of exact percentage of Iron in the samples. From the relative intensities of the absorption lines, the percentage of iron in the
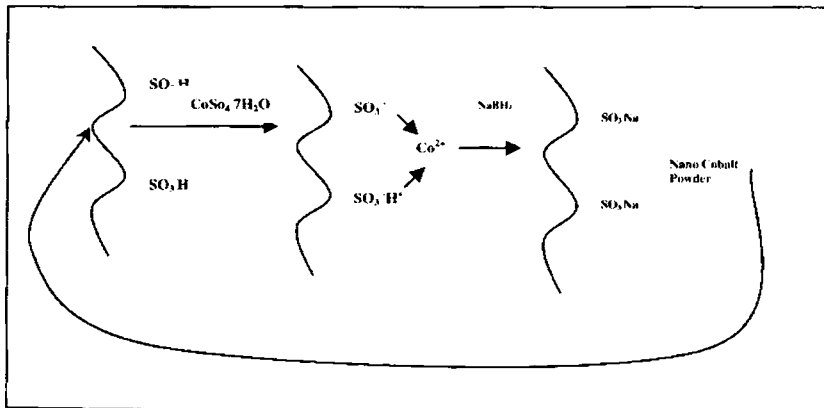

Fig.1 Schematic representation of the chemical reaction inside polymer network.

polymer globules can be determined. The samples were analysed for each and every cycle of ion exchange in order to determine whether there is an increase in iron content with cycling. The same method is employed for the measurement of exact percentage of cobalt that has got incorporated to the composite sample. Estimation was carried out for samples with Co in the atomic percentage 1, 2, 4, 6 and 10 for representative ion exchange cycles 1 and 10 [19].

5.3 Results and Discussion

Structural studies

The as prepared samples were analysed for the determination of their structure, presence of impurity etc by X-ray diffraction technique.
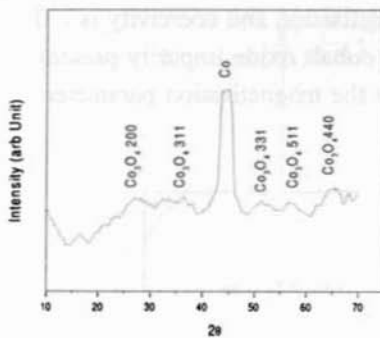
Fig. 2a   Fig. 2b

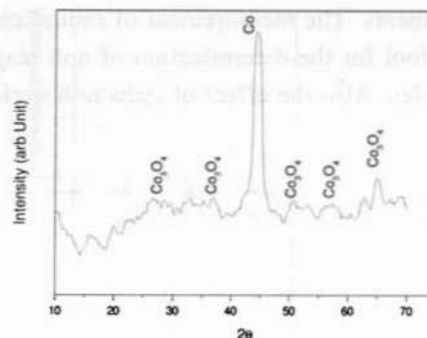*Fig. 2a X Ray diffraction spectra of elementary cobalt-polystyrene nanocomposite-cycle-1- (As prepared)*

Fig. 2b X Ray diffraction spectra of elementary cobalt-polystyrene nanocomposite-cycle-1- (Fired 473 K)

The representative X-ray diffraction spectrum is depicted in Fig. 2a, and 2b. This shows that the as synthesised particles are in the nanoregime with traces of impurity of cobalt oxide. The grain sizes have been estimated by employing Debye Scherrer's approximation using line broadening of the central maxima. The effect of strain is also accounted and eliminated. The grain size is about 9 nm for the synthesised samples. The spectrum shows only trace of cobalt oxide peaks which shows the synthesised cobalt nanoparticles are well capped inside the porous network of polystyrene. The ultra fine cobalt formed on the surface of natural pores of polystyrene may be oxidised to cobalt oxide.

Sintering studies

In order to study the crystallisation process, the samples were sintered at low temperatures so as to prevent high surface oxidation. The results show that sintering enhances the crystallinity, but enhances the impurity content cobalt oxide also which is undesirable. The presence of cobalt in as prepared samples is negligibly small in comparison with the sintered samples.

Magnetisation studies

Magnetisation measurements were carried out in as prepared samples and the hysteresis curves were depicted for representative cycles. The sintered samples which showed high percentage of impurity were not employed for magnetisation measurements. The measurement of saturation magnetisation and coercivity is a fine indirect tool for the determination of non magnetic cobalt oxide impurity present in the samples. Also the effect of reduction cycling on the magnetisation parameters is studied.
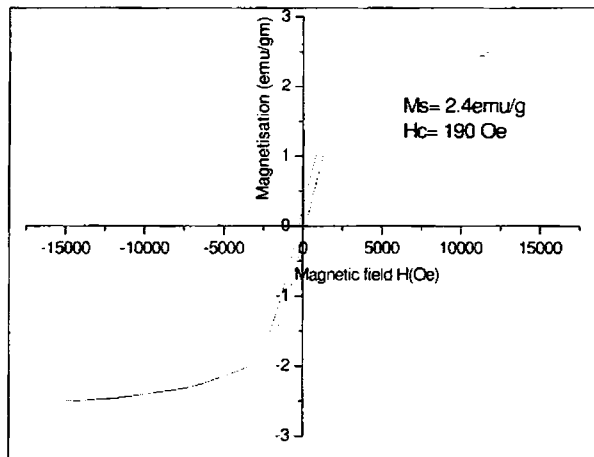

Fig. 3 Magnetisation cycle of elementary cobalt-polystyrene nanocomposites (Cycle-1)

Fig. 3 shows the magnetisation curve plotted for elementary cobalt nanoparticles inside the polymer network for the first reduction cycling. This shows that there is formation of elementary cobalt magnetic nanoparticles in the first reduction cycle itself. And an appreciable coercivity is observed for the nanomagnetic material.

Normally at the nanolevel, below a critical diameter, the materials prefer to be in single domain superparamagnetic state where remanance and coercivity tends to zero. Ultra fine magnetic materials which have a very high surface area as compared to their volume can be utilized in magneto-optical as well as magnetic recording purposes. However due to the very low remanance and coercivity at the nanoregime, their application potential is limited.

Cobalt which has an inherent magneto-crystalline anisotropy thus emerges as a suitable candidate for nanomagnetic materials for storage media die to its high coercivity and Remanance even in its ultra fine form.
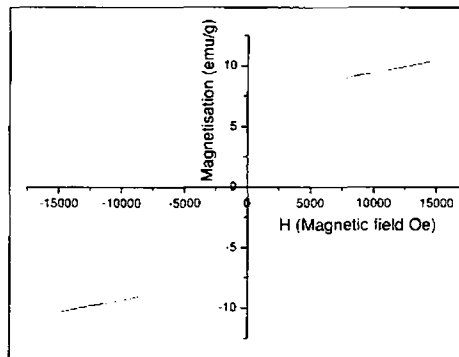

Fig. 4 Magnetisation cycle of elementary cobalt-polystyrene nanocomposites (cycle-6)
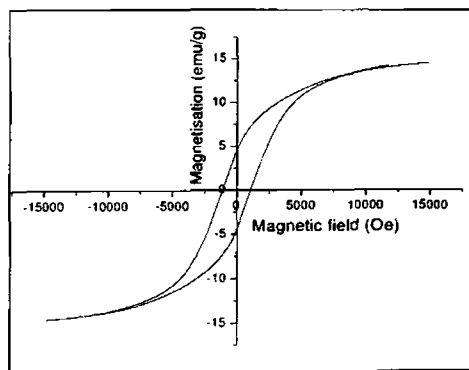

Fig. 5 Magnetisation cycle of elementary cobalt-polystyrene nanocomposites (cycle-10)

The hysteresis loop for the elementary nanocobalt in polystyrene network for precipitation cycle 1,6 and 10 is depicted in Fig. 3, 4 and Fig. 5 respectively. The saturation magnetisation, remanance, and coercivity are measured for representative samples (cycle 1, 4, 6 and 10)
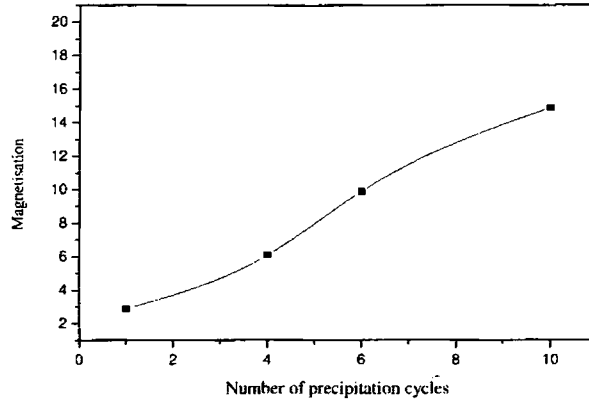

Fig. 6 Magnetisation vs no of precipitation cycles

Here in our system, the magnetic particles obtained in the as prepared form is of very small grain size, which shows an appreciable amount of coercivity which make them ideal for applications are concerned. The coercivity, remanance and saturation magnetisation increases with repetition of reduction cycles which shows the possibility of tuning the magnetisation parameters by the repetition of reduction cycles.

This magnetisation study of the elementary cobalt has been carried out and the variation of saturation magnetisation with number of precipitation cycles is depicted in Fig. 6. This shows that the magnetisation is enhanced by repeating the chemical cycles because of the opening of more pores and hence resulting in a higher yield. The enhancement of magnetisation is in a peculiar way that in initial cycles, the enhancement of magnetisation is slow whereas after that magnetisation enhancement is fast. Assuming 25% porosity, the magnetisation should be around 47 emu/g for the composite. However a low yield of 15.1 emu/g is achieved here after 10th repeating cycling of the chemical precipitation. Also the magnetisation values shows an increasing trend, with no saturation till the precipitation cycle number 10 which shows that higher precipitation cycle may result in a saturation magnetisation close to the theoretical predictions.
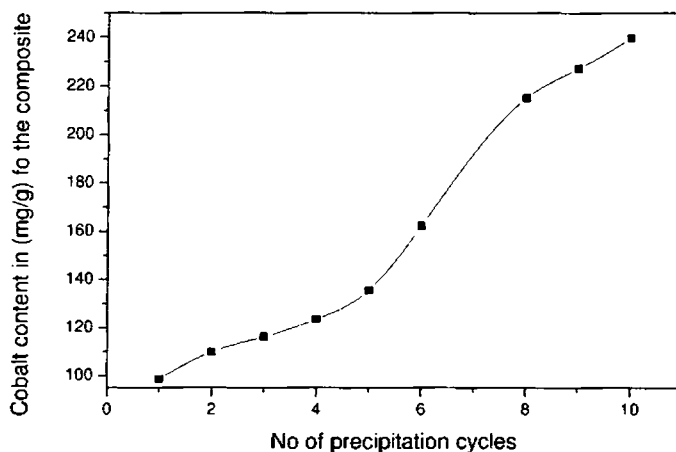
Fig. 7 Cobalt content (in mg/g) vs no of precipitation cycles

Fig. 7 shows the variation of cobalt content with number of precipitation cycles. Cobalt content estimation (which was determined by Atomic Absorption spectroscopy) also indicates that at lower precipitation cycles, there is a high Co content/magnetisation ratio showing the presence higher amount of Co_3O_4 formed. However this ratio seems to be lowered with increasing number of precipitation cycles because of the opening of more and more inner pores thus confirming our earlier assumption.

This can be explained by assuming a core shell model for these ultra fine cobalt particles which are synthesised inside the porous network of polystyrene. Normally cobalt in its ultra fine form possesses high surface area and hence there is a chance of very high surface oxidation if not passivated using capping. But there is an additional chance of getting an auto capping of CoO thereby protecting the inner cobalt nanoparticle core. Here in lower precipitation cycles there is a chance of obtaining the nanoparticles adhering to the surface, than getting trapped inside the polymer network as less number of pores inside are opened. On increasing the precipitation cycles, more and more inner pores get opened and hence formation of CoO is prevented and hence a higher yield is obtained.

In this investigation, due to the formation of cobalt inside the inner pores of the polymer, the necessity of giving additional capping for surface passivation is eliminated thereby making the synthesis procedure easier and effective.
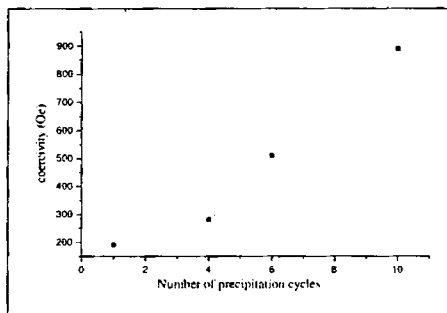

Fig. 8 Coercivity vs Number of precipitation cycles

A fairly good coercivity is obtained for elementary cobalt samples even in its ultra fine form which is promising from the application point of view. This is due to the high magneto crystalline anisotropy of cobalt. It is reported [19] that the coercivity is found to be enhanced by an order by the incorporation of elementary cobalt inside γ-Fe_2O_3-polystyrene nanocomposite. Here a very large coercivity of 890 Oe is observed for the cobalt nanoparticles (for the 10th precipitation cycle). The lower value of coercivity in samples with initial cycles may be due to the formation of cobalt oxide which is non-magnetic.

Thus elementary auto capped high surface area cobalt nanoparticles could be synthesised by a simple method by the *insitu* formation and growth process inside natural pores of a polymer polystyrene. Their magnetic properties could be enhanced by the repetition of the precipitation cycles and the large coercivity obtained is quite important from the application point of view. Also their optical properties can also be modified a lot by the size dependant quantum confinement effects which make them semiconductor like in the near molecule approximations. Such confinement effects and band structure modification has been reported in plenty for semiconductor materials [20-22] and in magnetic materials like maghemite [23].

5.4 Conclusion

High surface area, self protected elementary cobalt nanoparticles could be successfully synthesised inside the natural pores of polystyrene by a novel simple, cost effective reduction process. They are about impurity free except for the shell

formation of cobalt oxide at the surface. The magnetisation and coercivity could be enhanced by repeating the precipitation cycles by opening more and more inner pores. Initial reactions are centred at the surface thereby reducing the yield due to surface oxidation. By repeating the precipitation cycles, inner pores are exposed and the yield of metal nanoparticles are enhanced. Also the synthesis of high surface area cobalt by a simple technique by growing them inside the natural pores of polymers can throw a new area of applications including their catalytic application for the synthesis of carbon nanotubes. Scope exists for further modification of the synthesis technique to obtain a more pure self protected nanometal magnet with slightly modifying the experimental parameters with the addition of $NaBH_4$ in excess with a provision to provide a nitrogen atmosphere for controlling the oxidation process.

References

1. Masashige, Shinkai, Mitsugu Yanase, Masataka Suzuki, Hiroyuki, Honda, Thoshihiko Wakabayashi, Jun Yoshida, Takeshi Kobayashi, J. Magn Magn. Mater.**194**, (1999), 176.
2. Urs O Hafeli, Gayle J. Pauer, J.Magm Mag. Mater. **194** (1999),76.
3. Jhunu Chatterjee, Yousef Haik, Ching-Jen Chen, J. Magn Magn. Mater.**246**(2002),382.
4. Q A Pankhurst, J Connolly, S K Jones and J Dobson, J. Phys. D:Appl.Phys.**36**(2003) R167.
5. R. Mendoza-Resendez, O.Bomati-Miguel, M P Morales, P Boonville and C J Serna, Nanotechnology **15**(2004) S254.
6. Ryogo Kubo, J. Phys. Soc. Jap, **17**, (1962), 975
7. E Matijevic, Mat.Res.Bull (1989) 18,
8. M. Ozaki, Mat. Res Bull (1989) 35.
9. R.M White, Science **229**, (1985), 11.
10. Manfred E schabes, J. Magn.Magn.Mater, **95**, (1991) 249.
11. W. P Halperin, Rev. Mod. Phys, **58**, (1986) 533.
12. T. W Smith and D Wychick, J. Phys. Chem, **84**, (1980)1621.
13. B.S Clausen, S Morup, H Topsoe, Sur. Scie, **106**, (1981) 438.
14. F Fievet, J.P Lagier, B Dumont and M Figlarz, J. Mater, chem., **3**, (1993) 627.
15. I Nakatani, M. Hijikata, K. Ozawa, J. Magn.Magn.Mater, **122**, (1993) 10.
16. G.A Haber, J.L Crane, W E Buhro, C A Frey, S.M.L Sastri, J. L balbach, and M.S Cornadi, Adv. Mater, **8**, (1996) 163.
17. R.D McMichael, R.D. Shull, L.J Swartzendruber, L.H. Bennet and R.E. Watson, J.Magn. Magn. Mater, **111**(1992).

18. K.A. Malini, M.R. Anatharaman, S.Sindhu, C.N. Chinnasamy, N. Ponpandian, A. Narayanasamy, B. Balachandran and V.N. Shivasankarapillai, Journal of Material Science, **36** (2001) 821.

19. Swapna S Nair, Mercy Mathews, P A Joy, S D Kulkarni, M R Anantharaman, J.Magn. Magn. Mater, **283**, Issue 2-3, (Dec 2004) 344.

20. G. Allan, C. Delerue, M. Lannoo, Appl. Phys. Lett, **70,** (18), (1997) 2437.

21. M. Goryll, L Vescan, K. Schmidt, S. Mesters, H. Luth, and K Szot Appl. Phys.Lett, **71** (3) (1997) 410.

22. G. Allan, C. Delerue, M. Lannoo, Appl. Phys. Lett, **71**(9)((1997), 1189.

23. Swapna.S.Nair, Mercy Mathews, M.R Anantharaman, Chem.Phys.Lett, **406** (2005) 398.

CHAPTER 6

Structural, Morphological and Magnetic Studies of Ferrofluids Synthesized via HEBM via surfactant coating

This chapter deals with the synthesis of ferrofluids belonging to the series $Ni_xFe_{1-x}Fe_2O_4$ and $Zn_xFe_{1-x}Fe_2O_4$ (where 'x' varies from '0' to '0.6' in steps 0.1) and their structural, morphological and magnetic characterization. Also preliminary magneto-optical studies like magnetic field assisted cluster/chain formation and magnetic field assisted laser transmission studies were carried out and the results are explained and the measurement of magnetic and magneto-optical signals are correlated .

Fine particle precursors for ferrofluid synthesis, belonging to the series $Ni_xFe_{1-x}Fe_2O_4$ and $Zn_xFe_{1-x}Fe_2O_4$ (where 'x' varies from '0' to '0.6' in steps 0.1) were prepared using cold co-precipitation technique and their structural properties were evaluated. These fine particles were then subjected to high energy ball milling (HEBM) with oleic acid, which is used as surfactant, and finally with kerosene, the base fluid. Ferrofluids were then made into liquid thin films and magnetic field induced laser transmission through the film was studied. The transmitted light intensity decreases at the centre with the applied magnetic field, in a linear manner in lower fields. The pattern exhibited by the film in the presence of different magnetic fields were recorded with the help of a CCD camera and photographed. The analysis of the results confirms the chain formation of particles in the presence of an applied magnetic field and their saturation in higher magnetic fields. This set up can be modified to be employed as an optical Gauss meter at lower fields whose limiting value is determined by the saturation magnetization (M_s) value, of the powder precursors which in turn is related to the 'x' value in the series.

6.1 Introduction

Ferrofluids are stable suspensions of nanomagnetic particles in a suitable base fluid. These fluids can be synthesized by dispersing fine particles of ferro or ferrimagnetic materials precoated with suitable surfactant in a base fluid like kerosene.

They are of great research interest because of their numerous physical, engineering and medical applications [1-3]. These smart fluids show many interesting magneto optical

properties. Some of the engineering applications of these rheological fluids are in making rotary seals, pressure sensors and loud speakers. They are also widely used in bio-medical fields especially in cancer therapy [1].

The optical and magnetic properties of these rheological fluids have been widely studied [4-6]. Magnetic field induced structural anisotropy gives rise to many special magneto optical properties like field induced optical birefringence, linear and circular dichroism, Faraday rotation and ellipsometry [7]. They also exhibit magnetic field independent properties like zero field birefringence [7-8]. The chain formation saturates in higher fields, giving thin long chains of varying thickness leading to optical anisotropy, which contributes to the optical birefringence. The effect of a magnetic field on these thin films will have a profound influence on the birefringent properties of these fluid films. If an external magnetic field is applied parallel to the ferrofluidic thin films, they form tiny clusters that grow in size in increasing fields, which contributes to optical birefringence.

The cold co-precipitation technique is an excellent method for the preparation of powder precursors for ferrofluids. Many of the mixed ferrites can be prepared by cold co-precipitation technique and they can be further ground by HEBM for reducing the particle size further and they can serve as precursors for ferrofluid preparation. It is expected that cold co-precipitation of a series similar to $Ni_xFe_{1-x}Fe_2O_4$ will result in fine particles and further high energy ball milling (HEBM) will enable to prepare ultra fine particles with various particle dimensions.

Nickel ferrite crystallizes in an inverse spinel configuration with nickel having exclusive octahedral site preference [13-14] in its bulk form. The nickel ferrite nanoparticles show many distinctive magnetic properties. They exhibit superparamagnetism, characteristic of a nanoferrite having the size distribution of a few nanometers [15-16]. In nickel ferrite nano particles, due to a non-collinear spin structure, there is a strong reduction in the magnetization value compared with the bulk value. It is reported that due to the spin-glass-like layer wrapped around a uniformly magnetized core, hysteresis loop often shows open loop behaviour even at very high applied fields [17].

Zinc ferrite on the other hand is a normal spinel in its bulk form. However in its ultrafine form cation redistribution occurs and cations migrate to other sites resulting in a drastic change in the magnetic as well as structural properties.

Series belonging $Ni_xFe_{1-x}Fe_2O_4$ and $Zn_xFe_{1-x}Fe_2O_4$ with increasing 'x' content in steps of 0.1 will exhibit a behaviour different from that shown by the parent Fe_3O_4 in a serial manner due to the increasing 'Ni'/'Zn' content. Moreover the variation of optical behaviour with the 'x' value can be studied. The optical and magnetic properties can be compared by the investigation of magnetic field induced laser transmission through these ferrofluid films. Due to these peculiar properties, these two series are chosen for the preparation of the ferrofluids.

A survey of the literature reveals an absence of a systematic study on the optical properties of ferrofluidic thin films prepared from a series similar to $Ni_xFe_{1-x}Fe_2O_4$ and $Zn_xFe_{1-x}Fe_2O_4$. Moreover a correlation of the observed optical properties of these ferrofluidic thin films with the magnetic properties of the precursors will throw a deeper insight as regard cluster formation under the influence of an external magnetic field.

6.2. Experimental:

6. 2.1 Preparation of magnetic fine particles
Fine particles of nickel iron ferrite (Zinc iron ferrite), which are the precursor materials for the preparation of the ferrofluids, were synthesized by the cold co-precipitation. For this, $NiSO_4$. $6H_2O$ ($ZnSO_4$. $7H_2O$), $FeSO_4$. $7H_2O$ and $FeCl_3$ (all AR grade chemicals) in the molar ratio of x:(1-x):2 M were employed. Co-precipitation was carried out in an alkaline medium with a pH of around 10.5 ensuring the lowest possible particle size using 8 N ammonium hydroxide (NH_4OH). The precipitate was washed thoroughly with distilled water and finally with acetone to remove excess NH_4OH [18-20]. The obtained precipitate is dried and powdered. The details are described in detail in chapter 3.

6.2.2 Structural analysis
6.2.2 a: X Ray Diffraction
X-ray diffraction of the samples were recorded in an X-ray diffractometer (Rigaku Dmax-C) using Cu Kα radiation (λ=1.5418 Å) [21]. Lattice parameter (a) was calculated assuming cubic symmetry [22] and planes were identified by matching interplanar spacing values (d) with standard tables [23]. The average particle sizes of these powder samples were estimated by employing Debye Scherer's formula

$$D = \frac{0.9\lambda}{\beta \cos\theta}$$ where λ= Wave length of X-ray used in Å, β = FWHM in radians of the XRD peak with highest intensity, D = particle diameter in Å, θ= the angle of diffraction in radians.

6.2.2b: Atomic force microscopy

Atomic force microscopy is a powerful mechanical profiling technique which gives three dimensional maps of surfaces by scanning a sharp probe attached to a cantilever. The tip of the cantilever determines the resolution of the AFM images in general. (Details are provided in Chapter 3). (Model Nanoscope E, contact mode)

6.2.3 *Reduction of particle size*

Particle size was reduced by High Energy Ball Milling. For the preparation of ultra fine particles, 'Fritsch pulverisette 7 planetary micro mill' was employed. In this, 800 rotations per minute can be achieved and hence the momentum imparted to the particles will be very high. The ball to powder ratio was maintained at 1:8 to impart a high momentum to these fine particles. This will enable the required size reduction within two to three hours. This results in excellent grinding performance at considerably shorter grinding times.

6.2.4 Ferrofluid preparation

Ferrofluids were prepared by milling the powder samples prepared by cold co precipitation with the surfactant oleic acid. Oleic acid provides the necessary steric repulsion by its polar ends, thus preventing the agglomeration of the fine particles. Finally these samples were milled with kerosene for around three hours to obtain a uniform stable dispersion with a reduced particle size [3]. The samples were centrifuged well to remove the sedimented particles and placed in an ultrasonic vibrator to enhance Brownian motion, which provides stability to the ferrofluid. Oleic acid, kerosene and the nickel ferrite particles were optimally employed to ensure good quality ferrofluid. Ferrofluid thus prepared exhibited typical characteristics like spiking, which is a sure test for the formation of ferrofluids.

6.2.5 Ferrofluid film preparation

Liquid thin films of these ferrofluids were then made by sandwiching and encapsulating $2mm^3$ of ferrofluid between two optically smooth and ultrasonically cleaned glass slides. The thickness of these fluid films was of the order of a few thousands of angstroms.

6.2.6 Experimental set up for field induced laser transmission through the ferrofluid film.

The ferrofluidic film was suspended between the poles of a powerful electromagnet whose magnetic field strength is precalibrated. The electromagnet can go upto a field of 7500Gauss with water circulation for cooling. The film sample was then irradiated with a diode laser having a power of 3mW. The wavelength was in the range (630 -670 nm). The details are given in Chapter 3.
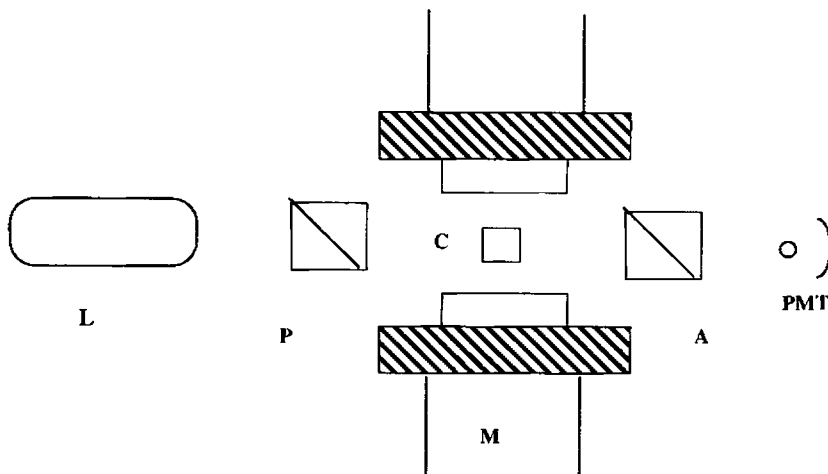
L-Laser, P-Polariser, C-Sample cell, A-Analyzer, M-Magnet, PMT (Photo Multiplier Tube)

Fig 1. Experimental set-up for Field induced laser transmission through the ferrofluid thin film. (Normal incidence and detection with respect to the sample)

6.2.7 Imaging of the chain formation

The thin ferrofluid film was kept in different magnetic fields and allowed to dry in the respective applied fields. These dried ferrofluid films were viewed with the help of a CCD camera (Model No. G P KR 222) and an optical microscope and the pattern obtained was imaged on a colour video monitor and was recorded photographically.

157

6.3. Results and Discussions:

The analysis of the X-ray diffraction results indicates that the prepared compounds crystallize in a spinel phase. The particle size evaluation employing Debye Scherer's formula suggests that they lie in the range 50-95 Å for different samples with varying nickel content. It must be noted that the phase formation is complete in the cold precipitated state itself. The particle size and lattice parameter variation for all the series is given in table 6.1.

x (Composition)	FWHM (Degrees)	Particle size Å	Lattice parameter Å
0.1	1.048	94	8.418
0.2	1.192	82	8.410
0.3	1.649	59	8.402
0.4	1.899	52	8.394
0.6	1.270	77	8.381

Table 6.1 Composition vs Particle size for $Ni_xFe_{1-x}Fe_2O_4$

The lattice parameter variation is plotted with composition (x), which shows a linear decrease of lattice parameter with composition for the series $Ni_xFe_{1-x}Fe_2O_4$ and $Zni_xFe_{1-x}Fe_2O_4$ (Fig. 2).
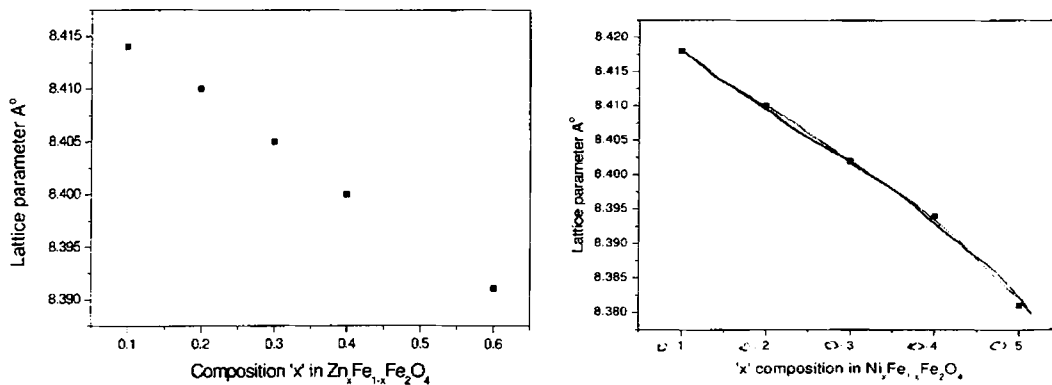

Fig. 2 Lattice parameter vs Composition

This is in accordance with the Vegard's law [13]. According to Vegard's law, the lattice parameter of a solid solution is directly proportional to the atomic percentage of the solute present in it. Here in the series $Ni_xFe_{1-x}Fe_2O_4$, and $Zn_xFe_{1-x}Fe_2O_4$ as 'x' increases, the atomic percentage 'Fe' decreases which reduces the lattice parameter value. A typical XRD spectrum is shown in Fig. 3.
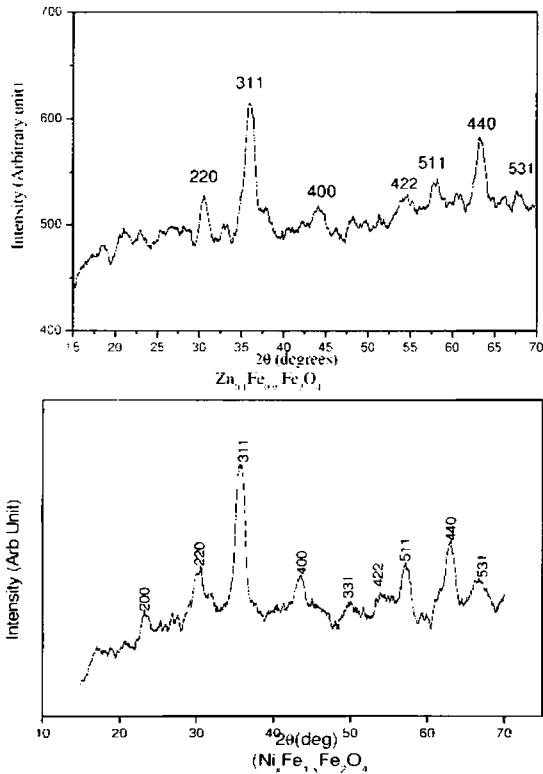

Fig. 3a Typical X Ray diffraction spectrum of dried ferrofluids

AFM pictures gives a qualitative analysis of the ferrofluid sample with grain distribution provided in a 3-dimensional manner. Although the exact grain size prediction may be difficult because of the larger AFM tip employed for the profiling, average qualitative analysis can be made possible. The evaluation of the particle size is important at various states of milling in ferrofluid preparation as it controls many of the peculiar properties exhibited by these fluids and it has been shown that particles below a critical

size of 100Å will be single domain in nature and have superparamagnetic characteristics. Moreover these particles will undergo Brownian motion, thereby increasing their stability, if dispersed in a carrier liquid only under this critical size value.
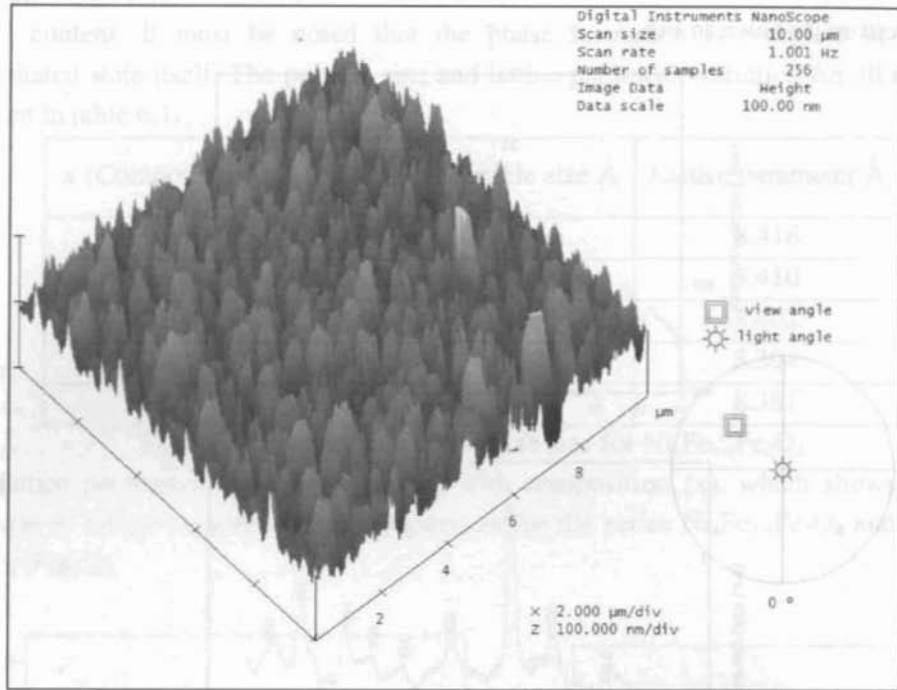

Digital Instruments NanoScope	
Scan size	10.00 μm
Scan rate	1.001 Hz
Number of samples	256
Image Data	Height
Data scale	100.00 nm

view angle
light angle

μm

8

6

4

2

X 2.000 μm/div
Z 100.000 nm/div

0 °

Fig. 3b Typical AFM (3D) image of dried ferrofluids

As the ferrofluid liquid film restricts the motion of particles in a plane, application of a magnetic field increases structural anisotropy of these particles and agglomeration starts at a very low magnetic field and the particles self assemble themselves in presence of applied magnetic field, yielding long chains and this process gets saturated at higher fields giving rise to a two dimensional quasi continuous grating [7,8,24]. Thin long chains of varying thickness are formed leading to optical anisotropy, which contributes to optical birefringence.

This is an example of field induced assembling of nanomaterials. The chain formation is confirmed by photographs taken in different applied fields with the help of a ccd camera and are shown in Fig (4). The chain formation saturates in higher fields.
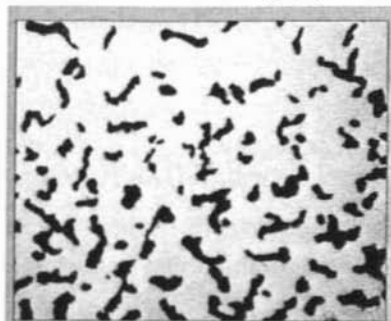

Fig 4a. Mag.Field =300G	Fig.4b. Mag.Field= 800G
Fig.4c Mag.Field =1500 G	Fig.4d Mag.Field = 2400 G

Scale factor ——— 5μm

Fig. 4a-4d Magnetic field induced cluster formation in different applied magnetic field

It is observed that the diffracted light intensity increases with the applied magnetic field. This is due to the increase in cluster formation in the ferrofluidic thin film with increasing magnetic field [8,24]. This can diminish the central spot intensity which is measured as a function of magnetic field (Fig. 5).
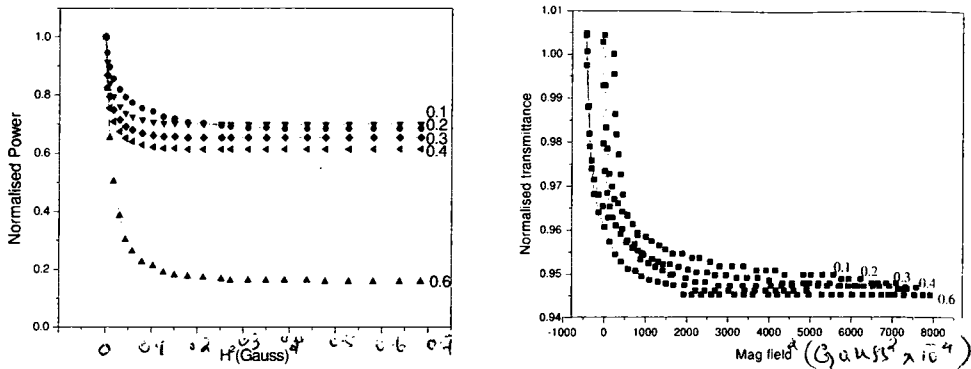
Fig 5. Normalized power vs Square of the applied field (H^2) in ferrofluidic thin films based on a) $Zn_xFe_{1-x}Fe_2O_4$ b) $Ni_xFe_{1-x}Fe_2O_4$

As the field increases the central spot intensity decreases in a linear manner and then attains a steady value indicating saturation of the cluster formation.

As the magnetic field is increased the particles are aligned and that increases the transparency and more and more clusters are formed [25,26]. The light gets diffracted by these narrow wires of ferrofluid clusters acting as a quasi continuous grating and a streak of light is obtained as the transmitted ray. This phenomenon of diffraction of light by the ferrofluid thin film can be explained by treating the film in the presence of the applied magnetic field as a system of thin wires with variable thicknesses and spacing in between them. Then the different orders of the diffracted beam overlaps and a streak of light is obtained on the screen. This is similar to a diffraction pattern obtained from a thick wire. The diffraction is governed by the relation

$$2d \sin\theta = n\lambda$$

Here, as there are a lot of thin wires of irregular thickness inside the film in the presence of a magnetic field, the situation is similar to the case of 'θ', the angle of diffraction becoming very large. This may be one of the reasons for getting a continuous streak of light. There is also a possibility for optical birefringence caused by the anisotropy created by the application of magnetic field. This is mainly due to the anisotropy in the formation of long chains in the applied magnetic field in addition to the anisotropy induced by the application of a magnetic field in the individual particles.

It is reported [27] that there is a time dependence of the transmitted light intensity for the laser beam in the zero applied field. But no such behaviour is observed in our set of experiments. However, they used a high power laser. It must be noted that we employed a 5mW laser (Diode laser- Red) and also the spot diameter here is very large (of the order of 1mm on the ferrofluid film sample) so that heating and drying up of fluid film sample by the irradiation is quite low and is negligible. The field sweep rate is kept constant here. So the time dependence of the transmitted light intensity is not observed here.

The normalized intensity vs applied magnetic field is plotted for the ferrofluid liquid thin films corresponding to x = 0.1, 0.2, 0.3, 0.4, 0.6. They are shown in Fig (5a, 5b). The saturating field (H_s) is determined for each of the composition (x) and is plotted for varying 'x'. They are shown in Fig (6).
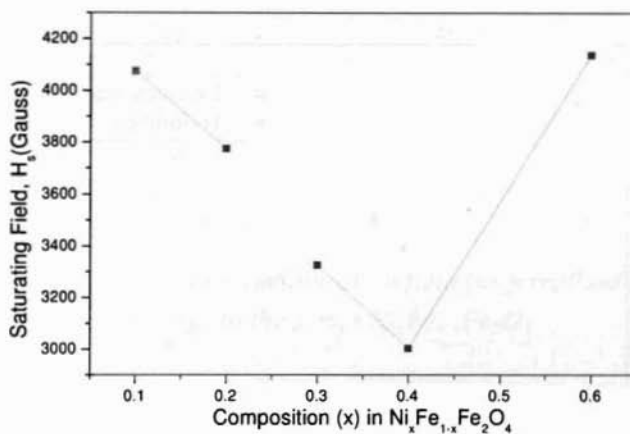

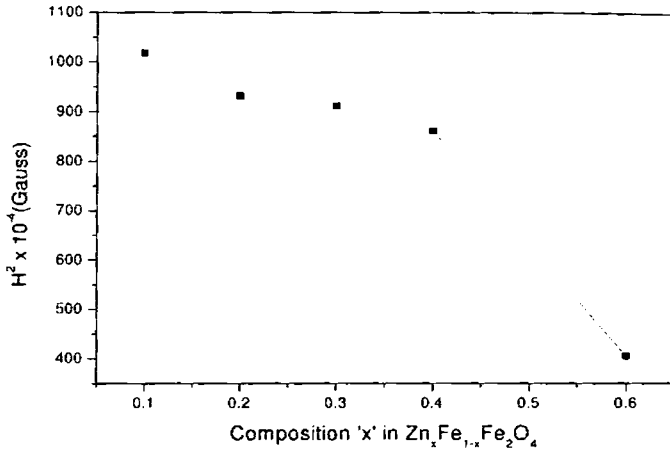*Fig. 5b. Saturating field vs. composition*

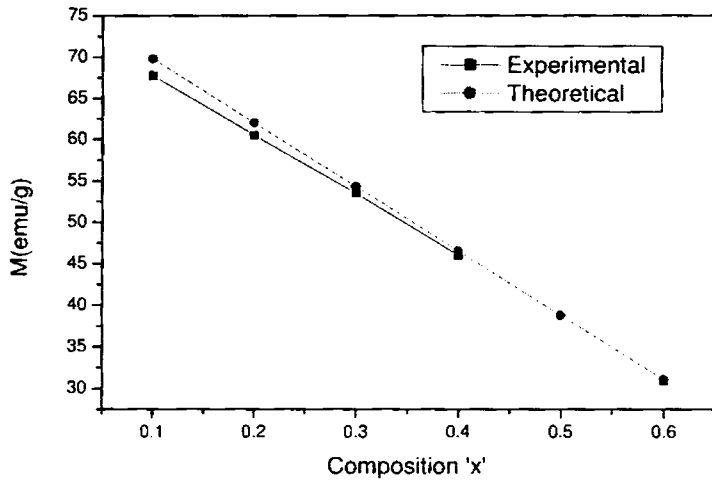*Fig. 6 Saturating magnetic field for cluster formation in ferrofluids*

Fig. 7 Saturation magnetization vs Composition of the precursor powder samples belonging to the series $Zn_xFe_{1-x}Fe_2O_4$.

x (Composition)	Calculated magnetic-moment in μ_B	M_s (emu/gm) (Calculated)
0.1	2.3	55.41
0.2	1.8	43.41
0.3	0.9	21.68
0.4	0.2	4.811
0.5	1.0	23.99
0.6	1.8	43.20

Table 6.2. Calculatedsaturation magnetization for $Ni_xFe_{1-x}Fe_2O_4$ using Neel's two sublattice model. $\left[Fe^{3+}, Fe^{2+}_{1-x} \right]_A \left[Ni_x, Fe^{3+} \right]_B O_4$

x (Composition)	Saturation field(Gauss)
0.1	4076
0.2	3776
0.3	3328
0.4	3004
0.6	4138

Table 6.3. Composition vs Saturation field for ferrofluidic film Belongs to the series $Ni_xFe_{1-x}Fe_2O_4$.

The normalized power decreases in a linear manner with the applied magnetic field in the low magnetic field values for each composition (x). This result can be explained by studying the saturation magnetization values of these ferrofluid film samples.

The saturation magnetization (M_s) of these compounds can be theoretically calculated by employing Neel's two sublattice model [13]. In this model, it is assumed that the ferrimagnetic properties arise as a result of the interaction of the tetrahedral (A) and octahedral (B) sublattices. A general cation distribution for the series is assumed and is as follows.

$[Fe^{3+}, Fe^{2+}_{1-x}]_A [Ni_x, Fe^{3+}]_B O_4^{2-}$, where 'x' varies from 0.1, 0.2, 0.3, 0.4 and 0.6.

The magnetic moment of ferrites is due to the interactions of the moments of the ions in A and B sites and the net magnetic moment value for the bulk sample using the Neel's two sublattice model is given by

$$\mu = M_A - M_B,$$

where M_A is the total magnetic moment of the A site and M_B that of the B site. The saturation magnetization in emu/gm of the samples is calculated by employing the formula

$$M_s = \frac{5585\mu}{Mol.wt},$$

where μ is the net magnetic moment in emu of that composition.
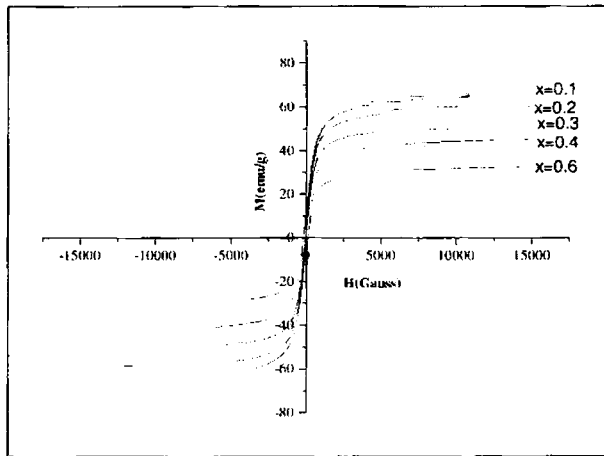Magnetisation curves plotted are shown in figure.

Fig. 8 Magnetization curves of the precursor samples belonging to the series $Zn_xFe_{1-x}Fe_2O_4$

This relation is derived as per the above mentioned cation distribution, which has been verified to be valid for the coarser sized $Ni_xFe_{1-x}Fe_2O_4$. However there are recent where in they have found a totally different cation distribution in fine $Ni_xFe_{1-x}Fe2O_4$ with respect to their coarser sized counterparts [12]. Nickel may not always occupy the B site in many of these nano particles. It must be noted that the absolute values of 'M_s' in the

fine particle regime can produce deviation from that of the bulk, but the overall variation pattern for various 'x' will remain the same.

A graph is plotted with calculated saturation magnetization (M_s) against the composition 'x'. This shows a linear decrease with the 'x' value in the series $Ni_xFe_{1-x}Fe_2O_4$ up to x =0.4 and increases there after which is shown in Fig (7). This graph shows similar variational pattern for saturation field (H_s). However a more detailed analysis for the ferrofluid system $Zn_xFe_{1-x}Fe_2O_4$ shows that there is a grain size dependence in the variation pattern shown by these fluids, which is an indication for the fact that it is the average magnetic moment of particles the deciding factor than the saturation magnetization. The variation pattern for magnetic moment with 'x' exactly resembles that of the saturation field vs composition (x) (Fig.6 and Fig.7).

These results indicate that the saturation field H_s in the series is determined by the saturation magnetization M_s that in turn is decided by the composition 'x'. From Fig (5a and 5b) it can seen that the linear part in the graph can be employed to sense the magnetic fields and the maximum field that the film can sense is determined by the 'x' value. With appropriate modifications these liquid thin films containing ferrofluids made up of $Ni_xFe_{1-x}Fe_2O_4$ / $Zn_xFe_{1-x}Fe_2O_4$ can be employed as optical gauss meters, in the linear low field region and the saturation field value can be tuned by changing 'x' value in the $Ni_xFe_{1-x}Fe_2O_4$ series.

6.4. Conclusions:

Complex behaviour is observed in the field induced laser transmission through nickel and zinc doped derivatives of magnetite ferrofluid thin films. Structural and magnetic characterization of the precursor ferrite powder samples shows that the magnetization varies as per the Neel's two sublattice model. Also they are superparamagnetic with zero remanance and coercivity and hence zero loop loss which are typical of nanomagnetic materials. Lattice parameter agrees with the Vegards low. All the synthesized samples are lying with in the size limit 10 nm. The diffracted light intensity is increased by the application of the magnetic field while the intensity of the central spot decreases. The output intensity of the central spot decreases in a linear manner till the saturation occurs in the cluster formation and this saturation field is dependent on the average magnetic moment of ferrofluid samples. Tuning of the maximum sensing capability of these films can be achieved by controlling the 'x' values

Structural, morphological......

170

CHAPTER 7

Magneto-optical properties of ferrofluids synthesized via various routes.

This chapter deals with the magneto-optical properties such as birefringence, dichroism, Faraday rotation and ellipticity of ferrofluids synthesized by different techniques and the results are correlated with the theory. Brief description of experimental set-ups and details of the results with comparison of magneto-optical signals of ferrofluids synthesized by various techniques is provided.

Magnetite (Fe_3O_4) and $Ni_xFe_{1-x}Fe_2O_4$ ferrofluids were synthesized by standard co-precipitation techniques and have been structurally characterized by XRD, TEM, and AFM. Ferrofluids were also synthesized by grinding the fine powder samples synthesized by co-precipitation using a high-energy ball milling (HEBM) unit with a view to understanding the effect of strain and size anisotropy on the magneto-optical properties of ferrofluids. Birefringence and dichroism measurements were carried out using a standard ellipsometer arrangement together with a PMT and lock in amplifier to detect the phase change. Dichroism and birefringence measured in chemically synthesized as well as ball milled samples were compared and the reason for deviation is explained and the signals are fitted to the second Langevin function. The observed discrepancies are examined and carefully discussed.

For measuring the Faraday rotation and Faraday ellipticity, longitudinal magnetic field is necessary for which an electromagnet is modified with axial hole through which the laser is transmitted. Also the effect of interparticle interaction on the magneto-optical signals was discussed by studying the Faraday rotation curves of the diluted and non diluted magnetic fluid systems. From the birefringence measurements, magneto-optical grain size and anisotropy constant were estimated. By correlating all the magneto-optical measurements, dielectric parameters could be estimated.

The magneto optical measurements can thus reveal many of the important properties of the magnetic nanograins dispersed in the career and thus come important from the fundamental point of view in addition to its vast application potential.

7.1 Introduction

Magneto-optical characterization of a sample is the measurement of optical signal changes/alterations (both by magnitude and direction) while passing through the sample and the study of their variation in presence of an applied magnetic field.

Magneto-optical signals are not the exclusive inherent property of ferro/ferrimagnetic materials. It could be observed in almost all the materials in which there is a structural anisotropy is present. But when it comes to the case of a

ferro/ferrimagnetic material, the saturation magnetization is so high that almost all the magneto-optical signals will be magnetic moment dependant.

Ferrofluids under the influence of a magnetic field induces magneto-optical anisotropy, and they contribute to the birefringence and dichroism [1-5]. In the magneto transverse mode, the eigen modes are linearly polarised waves making the dependence quadratic in the presence of an applied magnetic field [5]. The difference in speed and absorption gives rise to linear birefringence and dichroism. These properties dictate the usefulness of these materials for probable applications in devices such as light intensity modulator, magnetic field controlled switches and magnetic field induced gratings [6,8,9].

Now we can examine in detail various magneto-optical properties shown by these materials such as linear dichroism, birefringence, Faraday rotation and Faraday ellipticity.

Birefringence:

Birefringence in a material can be defined as the anisotropy in refractive index along different direction of incident polarization. The refractive index is thus not a sphere, but an ellipsoid considering it in 3D space. The anisotropy in refractive index is due to the optical anisotropy arising due to the difference in the electronic arrangement in the crystal. Also shape anisotropy is a prominent factor in the determination of magneto-optical signal if the medium is magnetically polarisable.

In an isotropic crystal, all the electrons could be visualized to be oscillating with a constant spring constant. When the material is irradiated with a laser beam, plane polarized along a particular direction, the electrons are driven by the electric field vectors of the incident beam. If all the electrons are isotropic, they will be driven alike by the incident beam. Consider a case where there is an electron oscillating away from equilibrium with a varying spring constant. Then there is an anisotropy created and the material thus becomes direction dependant as far as optical signals are concerned. There can be a lagging/leading of individually polarized waves because of this anisotropy and thus there is a change in refractive index. This change is maximum along the anisotropy axis and the least along the principal axis/optic axis which is defined as the isotropic plane inside the crystal in which all the electrons are oscillating with the same spring constant thereby resulting in a complete anisotropy as far as optical signals are concerned. In fact optic axis is not an axis, but a direction.

Dichroism:

Due to this difference in refractive index, there could be more than one diffracted ray for an incident ray, which is termed as double refraction. Some of these birefringent materials show some selective absorption of one of the ray, which is termed as dichroism.

In a purely dichroic material, one of the diffracted rays will be completely absorbed. Then the phenomenon could be visible only by the difference in intensity of the out put ray. Thus in general, dichroism is measured as the selective absorption of the incident beam along different polarization directions.

Faraday rotation and ellipticity:

Faraday rotation and ellipticity are magneto optical properties observed in the longitudinal mode in which the direction of propagation of polarized light and the magnetic field are the same. Faraday rotation is the rotation of the plane of polarization of light by the medium in presence of an applied magnetic field. Hence it can be redefined as the interaction of light with matter in presence of an applied magnetic field.

When the medium can be magnetically polarized to a great extent, the simple theories on light matter interaction fails and magneto-optical signals are thus magnetization dependant because of the individual moment interaction and their alignment along magnetic field direction. If the medium is a random media with suspended particle with full rotational degree of freedom, the obtained signals are far more strong than in thin films (In thin films, individual free rotation/movement of moments are restricted thereby reducing the magneto-optical signals).

In linearly polarized geometry, the eigen modes are circularly polarized waves make their magnetic field dependence linear. i.e., the magneto-optical effects in longitudinal mode are directly proportional to the applied field strength while that in transverse mode depends quadratically on applied magnetic field.
A more detailed theory on the light polarization and the magneto-optical properties is provided in chapter 2.

7.2. Experimental
7.2.1 Synthesis of ferrofluids
   a)   Co-precipitation method:
Ferrofluids belonging to the series $Ni_xFe_{1-x}Fe_2O_4$ have been synthesized by co-precipitation technique [9] with oleic acid as the surfactant. The obtained wet slurry was then successfully dispersed in kerosene with known volume fraction to obtain ferrofluids of desired concentration.   Detailed experimental procedure is provided in chapter 3 (Experimental techniques)
   b)   High Energy Ball Milling method (HEBM):
Fine magnetic particles have been synthesized by co-precipitation method and dried at an elevated temperature. The as prepared particles were then subjected to HEBM by employing FRITSCH PULVERISETTE 7 PLANETARY MICRO MILL first with the surfactant oleic acid and then with the carrier kerosene [10]. Detailed experimental procedure is provided in chapter 3 (Experimental techniques)

7.2.2 X Ray diffraction studies

The synthesized ferrofluids were structurally characterized using X Ray diffraction technique using Rigaku D-Max X Ray diffractometer using Cu $(K\alpha)$ wavelength by placing a thin drop of ferrofluid film on a chemically and ultrasonically cleaned substrate. The grain size was estimated by employing Debye Scherrer's formula.

7.2.3 Measurements of birefringence

Ferrofluids synthesized by both techniques are taken in sample cells of 1mm thickness. The samples were diluted with the carrier (to known volume fraction) so as to minimize the dichroic effects and the birefringence signal with normalized volume fraction is measured. The retardation is measured using a system including an analyzer, Soleili Babinet compensator, PMT and oscilloscope mounted on an optical bench and the applied magnetic field direction is always kept transverse to the light propagation. Details with schematic of the experimental set ups are provided in Chapter 3.

Soleili Babinet compensator helps to have a direct measurement of the phase retardation of the perpendicular and parallel polarized waves. The retardation is also measured with the help of a Lock in Amplifier (DSP 7260) using a chopped light beam Birefringence is calculated from the phase retardation.

$\Delta n = \lambda \delta / 2\pi l$

Where 'δ' is the relative retardation of the components of light (directly measured with Babinet's compensator) λ the wavelength of light used and 'l' is the length of propagation of light through the sample, which is the thickness of the fluid film,

The birefringence is measured with different applied magnetic field values for the chemically synthesized as well as mechanically milled samples. The same experimental set up is employed to study the variation of birefringence with sample volume fraction also.

7.2.4 Linear dichroism:

The intensities of transmitted light with planes of polarization parallel and perpendicular to the applied field are measured using photo multiplier tube. The corresponding intensities for the zero fields is also measured.

Hence the change in absorbance of the sample caused by turning the magnetic field on for the parallel light beam is

$\Delta A_{\parallel} = -\ln(I_{\parallel} / I_0)$ \hfill (1)

Where $I_{\parallel}$ is the transmitted intensity when the magnetic field is turned on and I_0 is the intensity of transmitted light with zero field.

Similarly for the plane of polarization perpendicular to the field direction

$\Delta A_{\perp} = -\ln\left(\dfrac{I_{\perp}}{I_0}\right)$ \hfill (2)

The intrinsic dichroism of the sample can be calculated using the formula

$$\Delta K = (\Delta A_{||} - \Delta A_{\perp})(\frac{\lambda}{4\pi l}) \qquad (3)$$

Where λ is the wavelength of the source used and l is the thickness of the sample.

7.2.5 Faraday rotation

Faraday rotation is measured using the standard ellipsometer arrangement. In this configuration applied field is longitudinal. Initially the light is made circularly polarized with the quarter wave plate placed in the optical path after polarizer make the linearly polarized waves into circularly polarized by adjusting the quarter wave plate and analyzer together to obtain a null signal in the output. So we used magnetic poles with a hole of diameter 2mm drilled through them. The angular setting of the analyzer (θ) is adjusted to obtain a minimum photo multiplier output. Now with the application of the field the analyzer is readjusted for a minimum photo multiplier output and from these readings the rotation of plane of polarization of light $\Delta\theta$ is calculated.

7.2.6 Faraday ellipticity

The experimental arrangement of ellipticity is the same adopted for the measurements of Faraday rotation. The analyzer and quarter wave plate are adjusted to obtain a minimum photomultiplier output with and without the application of the magnetic field. From these readings the changes in readings of analyzer ($\Delta\theta$) and quarter wave plate ($\Delta\phi$) are calculated. Hence the faraday electricity is

$$E_F = \tan(\Delta\theta - \Delta\phi) \qquad (4)$$

7.3 Results and discussions

All the prepared samples are phase pure, nanometric, dense, devoid of any settled particles and show good magnetic response. They exhibit spiking when subjected to a perpendicular magnetic field. The magnetisation seems to be decreasing with increasing the doping of nickel. This is attributed to the reduction in particle size with the increase in the doping concentration of nickel.

From the results of XRD studies, it is evident that there is a reduction in particle size with an increase in doping concentration of nickel. This may be due to the replacement of the Fe^{2+} ions with ionic radius 74pm by the Ni^{2+} ions with ionic radius 69pm. A typical X ray diffraction spectrum is depicted in Fig 1.
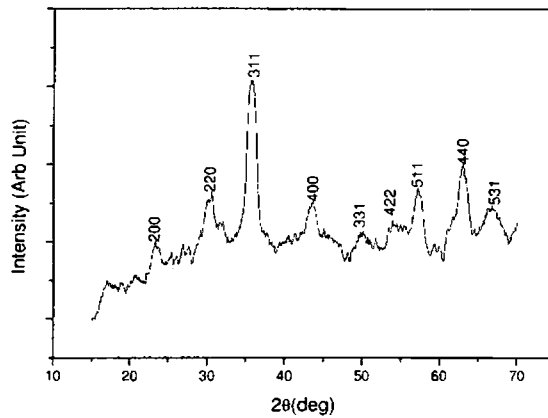
Fig 1. XRD spectrum of Fe₃O₄ ferrofluid sample

Linear Dichroism

The measurements of dichroism are carried out using a ferrofluidic thin film with thickness of 50μm. The absorbance for the ordinary and extra ordinary rays are measured with the plane of polarisation of the laser beam parallel and perpendicular the direction of the applied field. These are found to be in agreement with the theoretically predicted behaviour within the limit of experimental errors.

The theory predicts that, when the plane of polarization of light is perpendicular to the direction of the applied magnetic field, the absorptions for the ordinary and the extra ordinary rays are related as

$\Delta A_{||} = -2\Delta A_{\perp}$.

If the Polariser is rotated so that the plane of polarization of light is parallel to the direction of the field, the theory [5] predicts that

$\Delta A_{||} = -\Delta A_{\perp}$

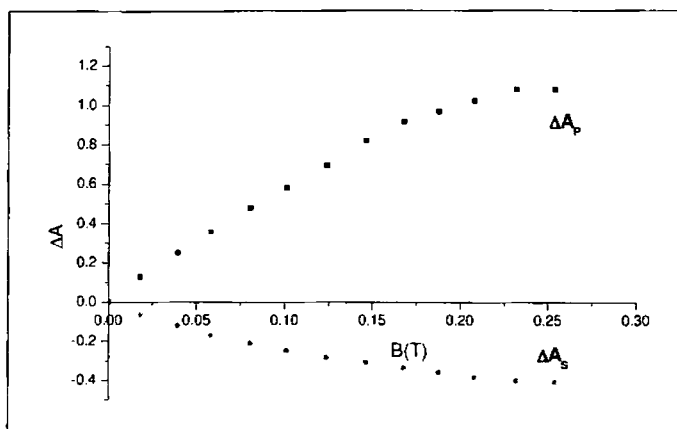This condition is also satisfied by the experimental observations. (Fig. 2)

Fig 2 Absorbance for perpendicular field shown by ferrofluid ($Ni_{0.1}$)

The intrinsic dichroism of the samples was determined. It tends saturate at higher fields [6].

The dichroism effects in any colloidal suspensions may originate from the intrinsic anisotropy or the shape anisotropy of the individual particles, which are suspended in the base fluid.   In a magnetic fluid to which a magnetic field is applied, the real physical process likely to occur are that some pre existing aggregates align along the direction for the applied field and with increasing fields, these clusters grow in size resulting long periodic chains, which are responsible for strong magneto optical properties.

The dichroism of a sample can be explained by the modified version of the classical oscillating dipole model. Here we assume that magnetic particles are optically isotropic spherical and behave like permanent magnetic dipoles forming a linear head to tail aggregates due to static magnetic forces between them. In the electric field of a laser beam (polarized) these individual particles may be considered as oscillating dipoles, which interact with one another, which is symmetric depending upon the orientation of the aggregates to the direction of the light polarization [17]. The asymmetry produces an optical anisotropy, which is the key reason for dichroism in ferrofluids.

According to this model, the anisotropy in refractive index is given by

$$\Delta n \approx \frac{1}{2} n_1 C (\chi_\parallel - \chi_\perp)[1 - \frac{3}{x}\coth(x) + \frac{3}{x^2}] \tag{5}$$

where C=N V_p and   x= 2μH/kT,
N is the number of particles, V_p is the volume of the particles and n_1 is the refractive index of the carrier.

177

So the refractive index change depends mainly on the orientation of the particles and the applied magnetic fields.

In the weak field region, we can approximate this in to,

$$\Delta n = \frac{15}{2} n_1 C(\chi_{||} - \chi_{\perp}) x^2 \qquad (6)$$

which is linearly proportional to the square of the applied field strength in the low field approximation and the anisotropy in the susceptibility.

In the ferrofluid samples belonging to the series $Ni_x Fe_{1-x} Fe_2 O_4$, the linear dichroism decreases with an increase in Nickel doping up to $x = 0.6$ in the series and then shows an increase for the sample $x = 0.7$. (Fig. 3)
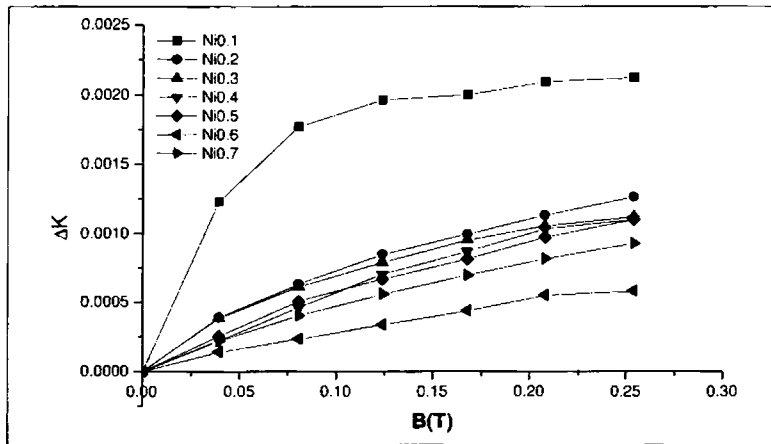

Fig. 3 Linear dichroism in co-precipitated $Ni_x Fe_{1-x} Fe_2 O_4$ series

This is due to the variation in magnetisation of these samples with the variation of nickel doping. This can be explained using the Neel's two sublattice model and spin canting taken together into account.

In this model, it is assumed that in spinel ferrites, the magnetic moments are distributed in two sublattices and the effective magnetisation is got by the interaction of the two.

The saturation magnetization (M_s) of the ferrofluids can be theoretically calculated by employing Neel's two sublattice model with known concentration. In this model, it is assumed that the ferrimagnetic properties arise as a result of the interaction of the tetrahedral (A) and octahedral (B) sublattices. A general cation distribution for the series is assumed and is as follows.

$[Fe^{3+}, Fe^{2+}_{1-x}]_A [Ni_x, Fe^{3+}]_B O_4^{2-}$, where 'x' varies from 0.1, 0.2, 0.3, 0.4 0.5, 0.6 and 0.7.

The magnetic moment of ferrites is due to the interactions of the moments of the ions in A and B sites and the moment value for the bulk sample using the Neel's two sublattice model is given by

$$\mu = M_A - M_B \tag{7}$$

where M_A is the total magnetic moment of the A site and M_B that of the B site. The saturation magnetization of the samples is calculated by employing the formula

$$M_s = \frac{5585\mu}{Mol.wt} \tag{8}$$

A graph is plotted with calculated saturation magnetization (M_s) against the composition 'x'. This shows a linear decrease with the 'x' value in the series $Ni_xFe_{1-x}Fe_2O_4$ up to x =0.4 and increases there after which is shown in Fig. 4.
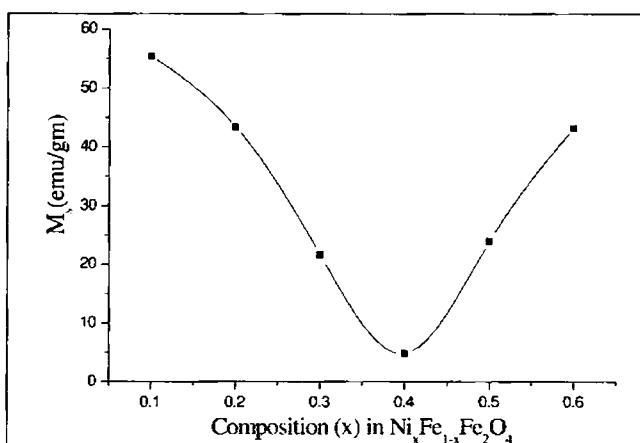

Fig. 4 Composition vs calculated saturation magnetisation M_s

This effect can be visualized by the spin canting model. In spinel ferrites, there are three types of interactions as per Neel's two-sublattice theory. One the A-A interactions, second, the BB interactions and the third A-B interactions. In a ferromagnetic material like Fe_3O_4, the addition of 'Ni' will increase the BB interactions, as Ni always prefers B sites. Then the anti parallel arrangement of spins will then be distorted a little and 'canting of spins' occur. This decreases effective magnetic moment of the sample. As the doping increases, the B-B interaction dominates and the canting of spins becomes a maximum and then it reaches a minimum value of magnetisation for the sample. After that the spin canting goes in opposite direction and the effective spin increases and the magnetic moment also increases in case of Ni doping

In nanoparticles there is a chance of cation redistribution often and that is why the Neel's two sublattice theory is not valid here in this case. Also here as the particles

are in ultrafine regime, the dependence on grain size plays a dominant role in determining all the magneto-optical properties and instead of magnetisation, we have to account for the magnetic moment here.

Faraday Rotation

Magnetic field induced Faraday rotation is measured for all the synthesized samples using 50µm sample cell. From the graph (Fig. 5) it is clear that Faraday rotation decreases with the increase in Ni concentration upto x=0.6 instead of x=0.4.

Faraday rotation is an intrinsic property of a crystal which can rotate the plane of polarisation of light with the application of an applied magnetic field. Normally the rotation is proportional to the applied magnetic field strength if the optically active materials is non magnetic or paramagnetic.

However in magnetic materials magneto-optical effects become more pronounced because of the magnetization of individual moments. When magnetic field is applied to ferromagnetic/ferromagnetic materials, the rotation is dependant on the saturation magnetization of the sample and the rotation curve behaves in a similar fashion as compared the magnetization curve of the sample. In a multidomained material, due to domain wall motion in presence of applied magnetic field, the domains could be observed by this method. Here in our system of experiment, the magnetic particles used are single domain and superparamagnetic so that the coercivity and remanance tends to zero values. Hence magnetization cycle becomes non lossy. Hence the only parameter here comes into play is the magnetization of individual moments and the interaction of them in the medium.

Faraday rotation curve has been plotted in magnetizing and demagnetizing modes in the positive half cycle for magnetite sample. This shows that the samples possess almost zero loop loss, which once again proves their superparamagnetic nature. However a complete tracing of the hysteresis loop was not possible due to the nonavailability of a magnet with dual power supply so that field could not be reversed in the negative half cycle.

To probe deeply into the interacting/non interacting nature of the individual moments inside the fluid, Faraday rotation curves have been recorded for magnetite ferrofluids with varying carrier concentration. The investigation carried out on magnetite samples under various concentration of the magnetic particles in the fluid shows that the samples with very high dilution can be treated as system of non interacting particles and the Faraday rotation spectra could be fitted to the magnetization values for these fluids. However in moderate concentration interaction effects come into play and the signal is very high when plotted for normalized concentrations. So diluted magnetic systems only shows ideal Faraday rotation curves as predicted by theory.

As the suspended particles are magnetic in nature, Faraday rotation angle will depend on the domain structure and magnetic moment of the fine magnetic particles. So rotation will be dependant on the saturation magnetisation of the sample.

In our system of samples it is observed that the rotation is decreasing with increase in Ni doping and then increase in x=0.7. (Fig.6)
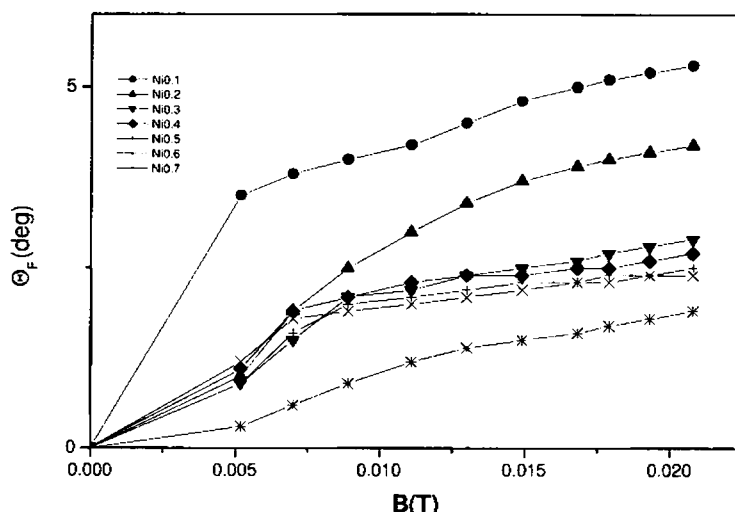

Fig. 5 Faraday rotation in $Ni_xFe_{1-x}Fe_2O_4$ ferrofluids

This peculiar behaviour can be explained by using Neel's two sublattice model as in the case of linear dichroism.

Faraday Ellipticity

Ellipticity is a consequence of Faraday rotation in general as the Faraday rotation changes the circularly polarized light in to the elliptically polarized light. Faraday rotation is a consequence of anisotropy of the particles and so is the faraday ellipticity. If dimer structures are there, there is a definite chance of a change in the c/a ratio of the 'cubic' crystal. As the decrease in magnetization accounts for a low Faraday rotation, the ellipticity also decreases with decrease in magnetization. It also tends to saturate at higher fields. (Fig. 6)
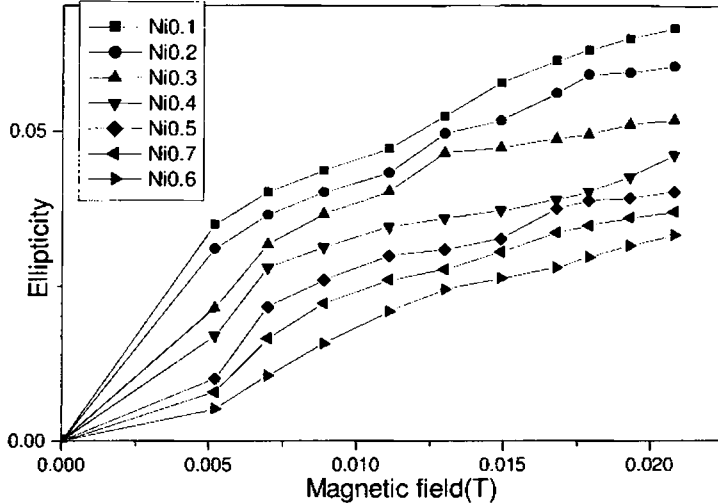
Fig. 6 Faraday Ellipticity for $Ni_xFe_{1-x}Fe_2O_4$ ferrofluids

The maximum magnetic field is quite low so that many of the samples are not reaching the saturation values in both the Faraday rotation and Faraday ellipticity.

The Faraday Ellipticity is also decreases with increase in nickel doping up to 0.6 and then increases for 0.7 due to spin canting.

Birefringence studies

In the present investigation, magnetite ferrofluids were synthesized both by direct co-precipitation (insitu surfactant coating) method, and by co precipitation and surfactant coating aided by high energy ball milling (HEBM)} techniques. Their structural, magnetic and magneto-optical properties namely birefringence and dichroism are evaluated and the results are compared. The comparison of such a system for the present investigation is to study the effect of anisotropy (which will be greater for the ferrofluids synthesized by HEBM) in shape and size, on the magneto-optical properties. Attempts are made to explain the observed effects based on a theoretical model. The effect of aggregation, and shape anisotropy are also discussed. Also the effect of nickel doping on the birefringent properties are also investigated.
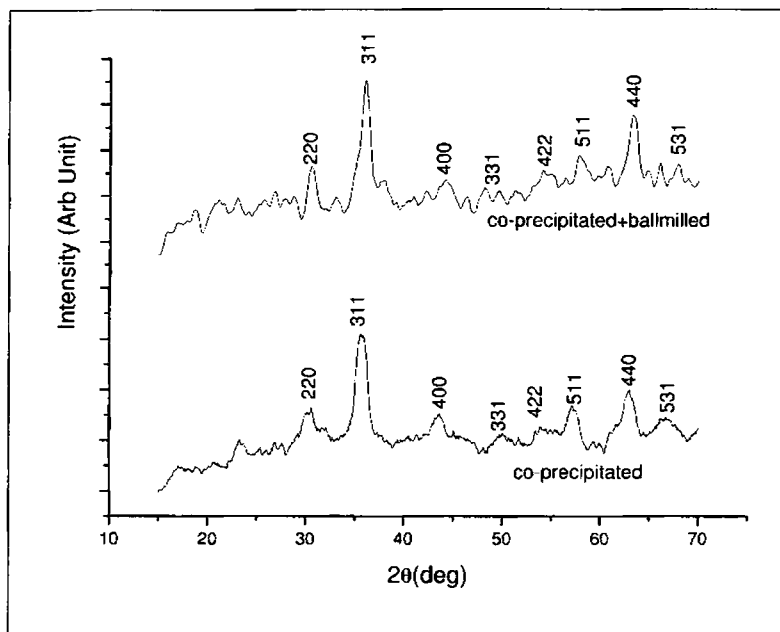
Fig. 7 XRD spectrum of representative sample Fe₃O₄

The X ray diffraction spectrum (Fig.7) shows that the samples are phase pure with semi amorphous nature and the estimation of the average grain size from the line broadening of the central maxima points to the fact that the grain size is of the order of 80 Å for all the chemically synthesized ferrofluid samples. However the samples synthesized by co-precipitation aided by HEBM, show signatures of higher strain and lattice contraction in addition to the presence of small traces of αFe_2O_3 present as impurity. Grain size of the ferrofluid samples synthesized by employing this modified procedure also lies in the range 85 Å which is quite comparable to that of the ferrofluids synthesized by conventional route.
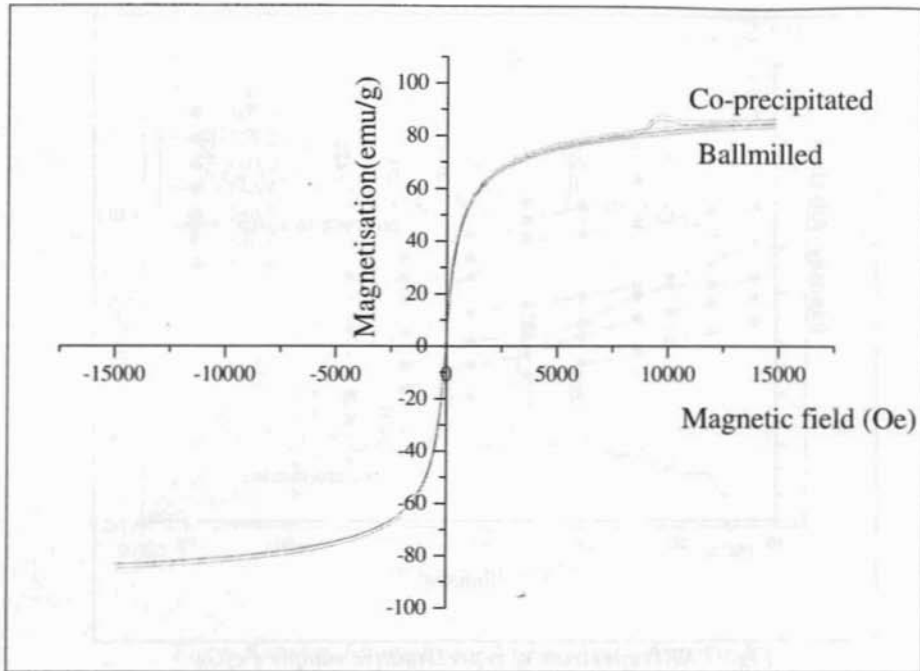
*Fig. 8 Magnetization curve in the ferrofluid samples synthesized by HEBM
(normalized volume fraction=1 ie, the precursor powder samples)
and co-precipitation* $[Fe_3O_4]$

The magnetization curves for the magnetite samples (Fig. 8) synthesized both by the precipitation method and by the ball milling process shows near zero loop loss showing their single domain/superparamagnetic nature in general. The saturation magnetization values of these ferrofluids seems to be unaffected by the ball milling process to a certain extent and the sample shows closely comparable magnetic parameters. However there are reports of change in magnetization during HEBM process due to cation redistribution [13]. Such a remarkable change is not observed in this case may be because of the lower milling time of~ 1 hour.

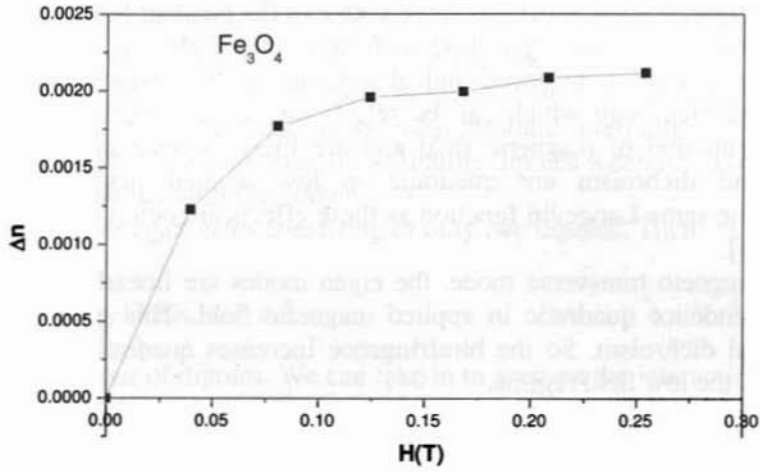Their magneto optical investigations show that the birefringence is enhanced by an order in ball milled ferrofluids.

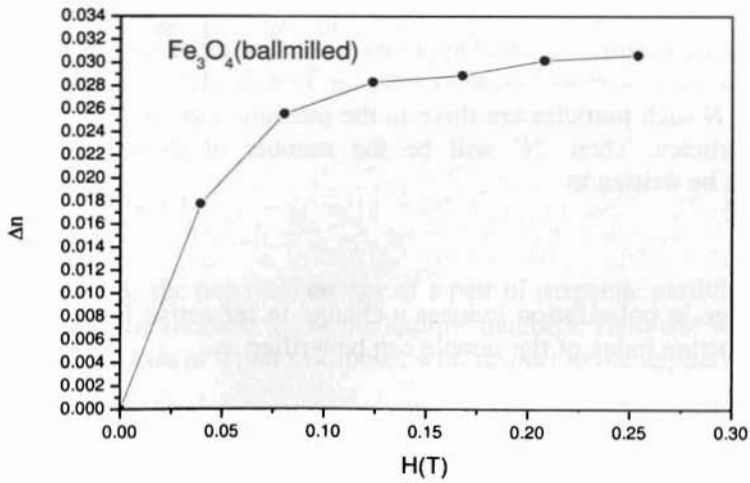*Fig 9 Birefringence in chemically synthesised ferrofluids.*

Fig. 10 Birefringence in ballmilled ferrofluids.

The application of magnetic field in these ferrofluids induces magneto-optical anisotropy, which mainly contributes to the birefringence and dichroism [5]. In the longitudinal configuration, in which the wave vector of the incident light is directed along the applied magnetic field, the eigen modes of the electric field are circularly polarized waves [13]. The difference in speed and absorption of these waves induces circular birefringence and dichroism which can be related to Faraday rotation and ellipticity, which are odd function of magnetic field and are linear in magnetic field while the birefringence and dichroism are quadratic in low applied magnetic fields both proportional to the same Langevin function as these effects are determined by transverse magnetic field [5].

In the magneto transverse mode, the eigen modes are linearly polarized waves making the dependence quadratic in applied magnetic field. This gives rise to linear birefringence and dichroism. So the birefringence increases quadratically with applied magnetic field in the low field regime.

Magneto optical properties shown by these smart fluids depend only on the magnetic fine particles which are suspended inside the base liquid. According to Rayleigh theory [14], particles that are small compared to the wavelength of light will behave like oscillating dipoles when irradiated by a light beam. Excited dipole moments of the particle has the following relationship with local electric field vector of the laser

$$p = \varepsilon_0 \alpha E \qquad (9)$$

where 'α' is the polarisability, 'p' the Dipole moment. For an anisotropic medium, 'α' is a tensor.

Consider N such particles are there in the medium and assume no aggregation is there for the particles. Then 'N' will be the number of dipoles so that the total polarization P can be written as

$$P = Np \qquad (10)$$

The change in polarization induces a change in refractive index of the medium. The complex refractive index of the sample can be written as

$$N^2 = (1 + N \langle \alpha \rangle) \qquad (11)$$

where $\langle \alpha \rangle$ is the average polarizability which can be calculated using a statistical distribution which can be related to the distribution of particle size of the particles. For nanosized particles whose size is much lower than the wavelength of the laser used

$$K^2 = \omega^2 \mu_0 \varepsilon_1 (1 + N \langle \alpha \rangle) \qquad (12)$$
$$n^2 = n_1^2 (1 + N \langle \alpha \rangle) \qquad (13)$$

where ε_1 is the dielectric constant, n_1 is the refractive index of the carrier. So far we have been discussing about the isolated particles. But in dense ferrofluids, magnetic particles form linear aggregates due to the magnetostatic interparticle interactions. The particle in an aggregate forms an array of oscillating dipoles when acted on by an electric field. The dipoles interact with each other.

Now consider aggregates consisting of only two dipoles. Then

$$E_p = \frac{1}{4\pi\varepsilon_1 |r_0|^3} [3(p.r_0)r_0 - p_0] \qquad (14)$$

Consider a pair of dipoles. We can take in to account the interaction effects of the dipole moments p_1 and p_2.

$$p_1 = \varepsilon_1 \alpha_p (E + E_{p2}) \qquad (15)$$
$$p_2 = \varepsilon_1 \alpha_p (E + E_{p1})$$

So interaction of two dipoles produces an anisotropic polarizability giving rise to magnetic field induced optical effects. The complex refractive index now becomes a tensor with its diagonal values non-vanishing. Now the anisotropy in refractive index is given by: $\Delta n = n_z - n_y$

$$\Delta n \approx \frac{1}{2} n_1 N(\alpha_X - \alpha_\perp) \int (\cos^2\theta - \sin^2\theta \sin^2\phi) f(\theta, \phi) d\theta . d\phi \qquad (16)$$

where $f(\theta, \phi)$ denotes the orientation of the particles which obey a Boltzmanian function. $f(\theta, \phi) = A \exp(U / kT)$ and

$$A \int \exp(\frac{U}{kT}) d\theta . d\phi = 1 \qquad (17)$$

$U = -2\mu H \cos\theta$, which is the potential energy of a pair of magnetic particles constituting a dipole having a magnetic moment 2μ in the applied magnetic field and θ is the azimuthal angle of the symmetry axis of a pair of dipoles with respect to the applied field.

$$\Delta n \approx \frac{1}{2} n_1 N(\alpha_X - \alpha_\perp)[1 - \frac{3}{x}\coth(x) + \frac{3}{x^2}] \qquad (18)$$
$$\Delta n \approx \frac{1}{2} n_1 C(\chi_\Pi - \chi_\perp)[1 - \frac{3}{x}\coth(x) + \frac{3}{x^2}]$$

where C=N v_p and x= 2μH/kT, So the refractive index change depends mainly on the orientation of the particles and the applied magnetic fields. The birefringence for a non agglomerated ferrofluid can be fitted to the second Langevin function

$$\Delta n_{ef} = 1 - \frac{3}{x}\coth(A) + \frac{3}{x^2}$$ (19)

where, the quantity x= (MVH/kT),
with V=(π/6) D^3, H is the magnetizing field. Thus birefringence varies as H^2 in low applied magnetic field values and in higher applied field values the value tends to saturate.

In a log normal distribution function, with the particle size = 70 Å, with σ = 0.36, the distribution function for the particle size can be written as

$$P(D) = \frac{\exp(2\sigma^2)}{D_{avg}\sqrt{2\pi}} \exp \frac{-\ln^2(D/D_{avg})}{2\sigma^2}$$

Using the distribution function, the birefringence can be theoretically calculated using the second Langevin's function and the fit for monomer with the experimental result is given in Fig.11 , which is in a good agreement with that of the co-precipitated ferrofluids.

The ball milled ferrofluids however does not agree well with the monomer fit and the fit for a dimer (N=2.4) is rather in good agreement with the experimental data in the case of ball milled ferrofluids (Fig. 12). This large enhancement in magneto-optical signal cannot be attributed to the change in magnetization or grain size as they are obtained in nice agreements.
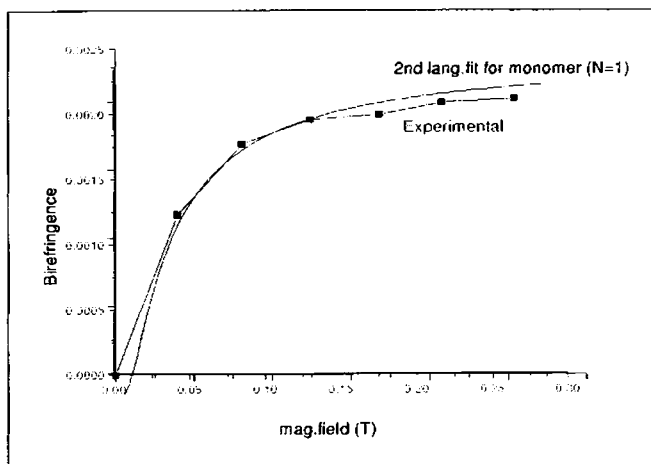
F Fig . 11 Langevin curve fitting and experimental birefringence values ς
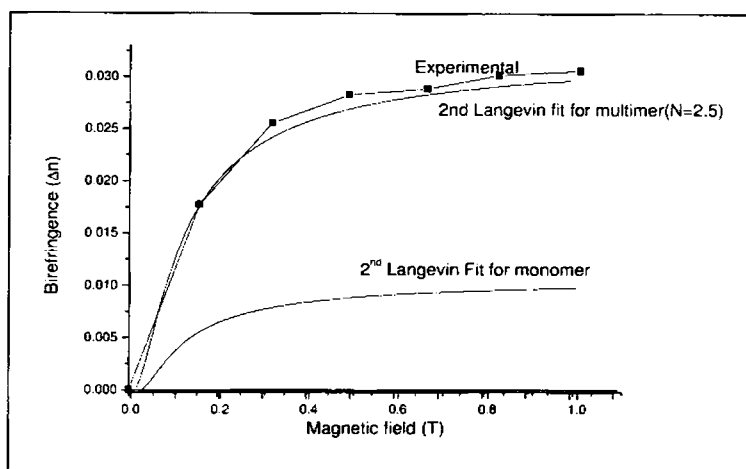*(fit for monomer) for chemically synthesised magnetite*

Fig. 12 Langevin curve fitting and experimental birefringence values
(fit for multimer N=2.5) for ballmilled Fe₃O₄.

This enhancement of birefringent signals is due to the stress and strain induced in course of ball milling. In course of ball milling there can be deviation from spherical shape to oblate which results enhanced magneto-optical signals because of the large change in polarisability induced out of the non-sphericity of individual particles. Thus the

magneto-optical signals could be deliberately enhanced by a modified synthesis procedure aided by HEBM.

Birefringence in $Ni_xFe_{1-x}Fe_2O_4$ ferrofluids

The evaluation of structural parameters becomes important to understand the contribution of structural anisotropy (shape anisotropy) in the context of the magneto-optical properties exhibited by ferrofluids. Hence the lattice parameter is evaluated for all the samples belonging to the series $Ni_xFe_{1-x}Fe_2O_4$ assuming cubic symmetry. The variation of lattice parameter with composition (x) (Fig. 13) is in accordance with the Vegards law [12]. However, the lattice appears to shrink in the case of ball milled $Ni_xFe_{1-x}Fe_2O_4$ samples probably because of the high impact imparted to the fine powder samples during milling.
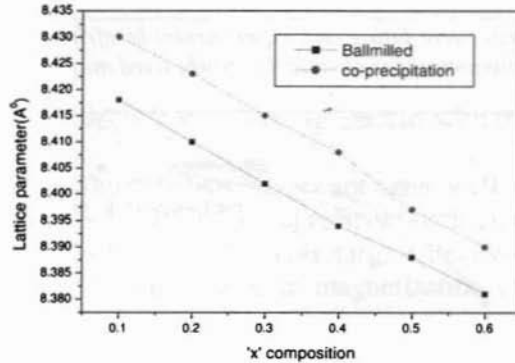

Fig. 13 Variation of lattice parameter with composition in chemically synthesized and ball milled ferrofluids

The AFM studies on ferrofluid samples shows that the synthesized ferrofluid samples are in ultra fine form and the cluster formation is a minimum with a lesser line width for the particle size.

The TEM images on the ball milled fine particles belonging to the series $Ni_xFe_{1-x}Fe_2O_4$ show that the particles are ultra fine with particle size varying from 60Å to 100Å. The electron diffractogram is also recorded and the planes were identified which matches well with the data obtained from the X Ray Diffraction Analysis. Typical TEM diffractogram is depicted in Fig. 14
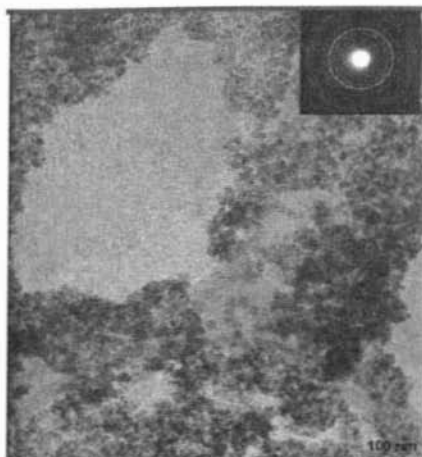
*Fig. 14 TEM Image of a representative ferrofluid sample (dried)
Inset - Electron Diffraction spectrum.*

The magnetization curves for the samples belonging to the series $Ni_xFe_{1-x}Fe_2O_4$ (Fig. 15) synthesized both by the precipitation method and by the ball milling process agrees well with the magnetisation values predicted by Neel's Two sublattice model when plotted for normalized concentration (Fig.16). The magnetisation values of these ferrofluids seems to be unaffected by the ball milling process to an extent. However there are reports of change in magnetisation during HEBM process [13]. Such a remarkable change is not observed in this case may be because of the lower milling time of 3 hours.
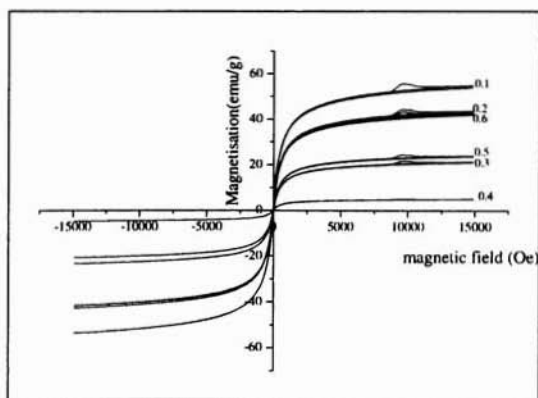
Fig. 15 Variation of magnetisation in the ferrofluid samples synthesized by HEBM (normalized volume fraction=1 ie, the precursor powder samples)
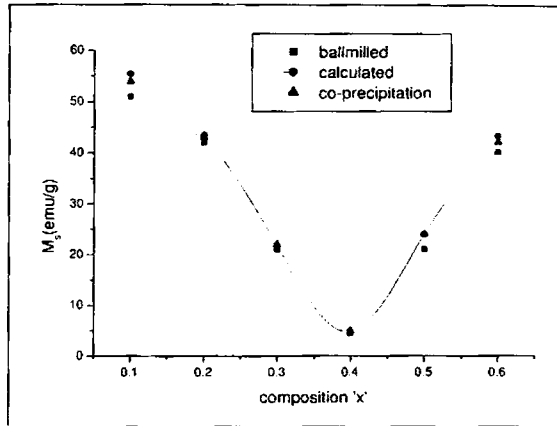
Fig. 16 Saturation magnetization M_s (emu/gm) vs composition 'x'
In $Ni_xFe_{1-x}Fe_2O_4$

Their magneto optical investigations show that the birefringence decreases in the series $Ni_xFe_{1-x}Fe_2O_4$ from x=0 to x=0.7 (Fig. 17 and Fig. 18).

Fig 17 Birefringence in chemically synthesized ferrofluids. $\left[Ni_xFe_{1-x}Fe_2O_4 \right]$

Fig. 18 Birefringence in ball milled ferrofluids.

Fig. 19 Birefringence vs H²

The variation of birefringence signal (saturation value) is in accordance with the variation pattern of the magnetisation in the series $Ni_xFe_{1-x}Fe_2O_4$ for both chemically synthesized and ball milled ferrofluids.
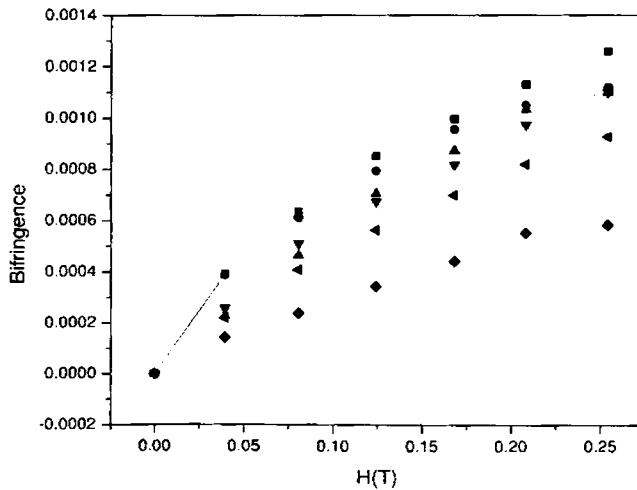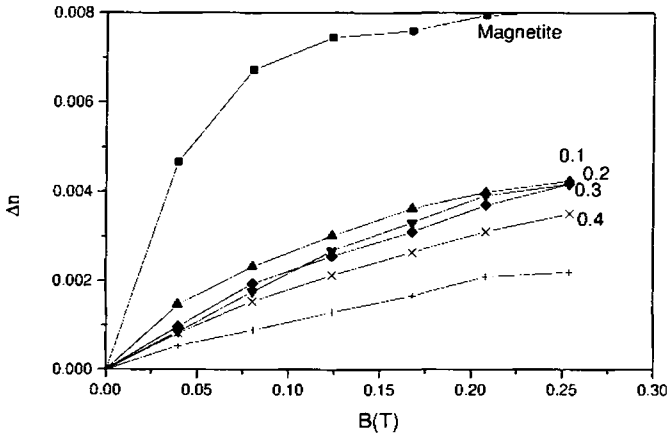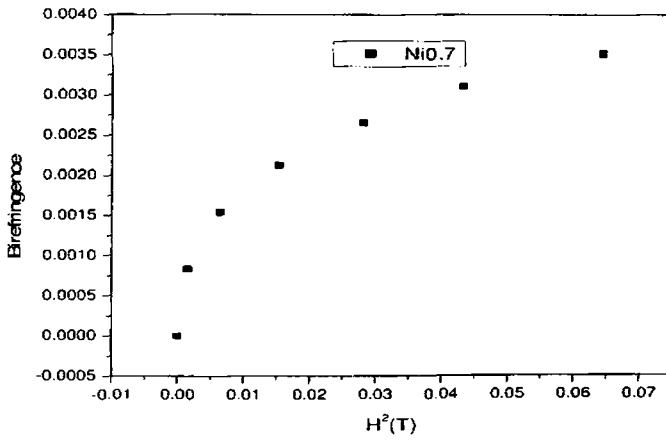
Calculation of anisotropy, dielectric permittivity from magneto-optical properties
Evaluation of magneto-optical parameters provides us set of data that could be employed for the calculation of effective anisotropy, dielectric tensor etc.

$$\Delta n_s = \frac{2\pi C_v}{n_0}(g_1 - g_2)G,$$

Where G depends on coupling and typical values of 'G' is 0.33 for kerosene based fluids, C_v is the volume concentration of ferrofluids, 'n_0' is the refractive index of base fluid, Δn_s is the saturating value of birefringence, (g_1-g_2) is the average optical anisotropies. The equation is valid only for lower concentrations.

Here saturating value of birefringence is calculated by extrapolating the unsaturated curves for the second Langevin function and effective anisotropy is calculated.

Chemically synthesized

Table 7.1.1 Composition vs anisotropy (co-precipitated ferrofluids)

Composition	Anisotropy
0	0.0215
0.1	0.0205
0.2	0.020
0.3	0.0185
0.4	0.018
0.5	0.0165
0.6	0.0155
0.7	0.0160

Table 7.1.2 Composition vs anisotropy (Ball milled ferrofluids)

Composition	Anisotropy
0	0.0355
0.1	0.0325
0.2	0.0320
0.3	0.0315
0.4	0.0305
0.5	0.0300
0.6	0.0295

Estimation of magneto-optical diameter from birefringence measurements

Measurement of birefringence in ferrofluids provide valuable information about their structural, magnetic and optical characters. Apart from the evaluation of optical anisotropy the birefringence data could be successfully employed for the evaluation of magnetic diameter of the individual grains suspended inside the ferrofluid system.

$$\Delta n = \Delta n_s \psi$$

$$\Delta n = \Delta n_s \int_0^\infty \psi f(y) \, dy$$

Where f(y) can assume a log normal distribution of the form

$$f(y) = \frac{1}{y\sigma(2\pi)^{1/2}} \exp\{-[Ln(y)]^2/2\sigma^2\}$$

where σ is the standard deviation.

Low field limit

$$\psi = \mu^2 B^2/15\, k^2 T^2$$

$$\psi = I^2 V^2 B^2/15\, k^2 T^2.$$

$$\Delta n = \Delta n_s \frac{I^2 B^2 \pi^2 D^6}{15 k^2 T^2 .36} \int_0^\infty y^6 f(y) \, dy$$

$$V = \pi D^3/6 = \pi D^3 y^3/6.$$

$$K = \frac{d(\Delta n)}{d(B^2)} = \frac{\Delta n_s I^2 \pi^2 D^6}{15 k^2 T^2 .36} \int_0^\infty y^6 f(y) \, dy$$

High field limit

$$\psi = 1 - 3kT/\mu B.$$

However the calculation of magnetic diameter from the birefringence data can cause errors because of the Neel rotation of individual particles when the grain size is reduced below a 10 nm.

Magnetic diameter calculated from the magneto-optical data is found to be less than that of the original grain size. This is because in ultra fine systems, there can be non collinear spins giving rise to a magnetic dead layer. The surfactant layer coating in the fluid system over count the grain size in TEM as well as XRD measurements. However the variation of grain size is in accordance with that measured through TEM and XRD measurements.

Table. 2 Grain size variation in ferrofluids based on $Ni_xFe_{1-x}Fe_2O_4$

x	Grain size (TEM)	Grain size birefringence
0	83	69
0.1	81	67
0.2	80	64
0.3	76	61
0.4	68	59
0.5	60	56
0.6	53	45
0.7	57	49

7.4 Conclusion

The magneto-optical characterization of the ferrofluid samples synthesized by both routes show that the assumption of a "system of identical spherical particles" fails in the case of fluids synthesized with high energy ball milling of the fine particle precursors. Thus size and shape anisotropy enhancement is occurred by the ball milling process thereby increasing the birefringent signal which confirms our earlier assumption of inducing the formation of oblate particles with enhanced magneto-optical signals. The low and high energy limits of the birefringence are discussed showing their quadratic dependence on M_s (saturation magnetization), H (magnetic field) and V (particle volume) at lower applied field. The birefringence measurements on chemically synthesized samples were satisfactorily fitted to the standard second Langevin function for monomer fit which hints towards to the spherical non aggregates. The ball milled ferrofluids shows anomalous behaviour and the birefringence is enhanced by an order and the fit for dimer in the standard Langevin fit is good for the milled ferrofluid samples. This large enhancement in birefringence signal with high energy ball milling can find enormous application potential. Thus birefringence can be employed as tool to gauge the quality of the ferrofluids.

References

1. Ronald .E. Rosenweig , Ferro hydrodynamics, Cambridge University Press 1985
2. E. Hasmonay, J Depeyrot, J. Appl.Phys. **88**, No 11 (Dec. 2000), 6628.
3. A.F Bakuzis, M.F Da Silva, P.C Morais, L.S.F Olavo, and K. Skeff Neto, J. Appl. Phys **87**, (5), March 2000, 2497.
4. H.C Yang, I.J Jang, H.E Horng, J.M Wu, Y.C Chiou, Chin-Yih-Hong, J. Magn. Magn. Mater. **201**, (1999), 215.
5. M. Xu and P.J Ridler, J. Appl. Phys. **82** (1), (1997 July), 326.
6. H.E Horng, Chin-Yih-Hong, H.C Yang, I.J Jang, S.Y Yang, S.L Lee, and I.C Kuo, J. Magn. Magn. Mater. **201**, (1999), 215.
7. S. Taketomi, Jpn. J. Appl. Phys, **22**(1983) 1137.
8. H.E Horng, Chin-Yih-Hong, S.Y Yang, and H.C Yang, J. Phys. And Chem. Solids, **62** (2001) 1749.
9. Sutharia G.M, Siblini.A, Blanc-Mignon. M.F, Jorat. L, Parekh. K, Upadhyaya R.V, Mehta R.V, and Noyel. B, J. Magn. Magn. Mater **234**, (2001) 90.
10. V.S. Abraham, S. Swapna Nair, S. Rajesh, U.S. Sajeev and M.R. Anantharaman, Bull. Mater. Sci. **27** (2) (April 2004) 155.
11. B.D Cullity Addison Wesley Publishing company, 1978.
12. J. Smit and H.P.G Wijn, Ferrites (Philips Technical Library) 1959.
13. S. D. Shenoy, P. A. Joy, M R Anantharaman J. Magn. Magn. Mater, **269** (2004) 217.
14. Eugene Hecht and Alfred Zajac, Optics, Addisson Wesley Publishing Company, London, 1979.

Magneto-optical.......

CHAPTER 8

Electrical Characterisation $Ni_xFe_{1-x}Fe_2O_4$ and $Zn_xFe_{1-x}Fe_2O_4$ Ferrofluids and a study on the magnetic field dependence of the capacitance– Evidence for Neel's like particles

This chapter describes the results obtained from the electrical characterisation of ferrofluids. Two different systems of ferrofluids were employed for their electrical characterisation, both derivatives of magnetite. Concentration, composition, and frequency dependence of dielectric permittivity was evaluated. Effect of an applied magnetic field on their dielectric properties have been studied in detail and the enhancement in the capacitance values has been attributed to the presence of more Neel like particles in the fluid system than the Brown particles usually present in colloids. Also their permittivity as well as permeability has been evaluated in the X band using a capillary method and their compositional variation has been studied. These measurements also show that the fluids can act as a microwave absorber.

8.1 Introduction

Ferrites belong to the class of magnetic dielectrics because of their high resistivity and low loss. They are widely employed as filters, antennas, transformer cores, and read/write heads for high-speed digital tape due to the coexistence of a very high permittivity as well as permeability in these system of materials[1–3]. Dielectric characteristics of ferrites depends markedly on preparative conditions, chemical composition, method of preparation, grain size, and the ratio of Fe^{2+}/Fe^{3+} ions and defects in lattices [4,5]. A systematic study on the dielectric properties including the ac electrical conductivity can throw light into the behaviour of localized electric charge carriers and hence can lead to the understanding of the Physics of electric conduction and dielectric polarization in ferrites systems. Ferrite systems such as Nickel ferrites are well-known for their high frequency applications. Nickel ferrites are well studied by various researchers [6-11]. However most of the literatures on the electrical and magnetic properties are in the micron regime.

Ferrofluids are stable colloidal suspensions of nanomagnetic particles usually having single domain superparamagnetic characteristics [12-15]. Stability against agglomeration and settling has been taken care during the synthesis technique. They can act as a system of non-interacting magnetic domains. They find extensive applications in versatile fields like in rotary sealing, pressure sensors, loud speaker coolants, display devices etc[16,17]. In the absence of an external magnetic field they exhibit usual properties of a stable colloid while in the presence of an applied magnetic field, their magnetic, optical and electrical properties could be greatly modified which throws open a new area in nanomaterials whose underlying Physics has not been investigated in detail by researchers and thus become quite important from the fundamental as well as technological point of view.

The electrical properties are important for ferrites and ferrofluids containing ferrites not only from the application point of view but also from the fundamental point of view [18-23]. Evaluation of ac conductivity reveals wealth information as regard the usefulness of these materials for various applications. Moreover the study of ac electrical conductivity sheds light on the behaviour of charge carriers under an ac electric field, their mobility and the mechanism of conduction [24-25]. The conductivity studies on ferrites carried out by various researchers prove its semi conducting behaviour and also prove the dependence of electrical conductivity on preparation condition, sintering time, temperature and the type of impurities present.

Microwaves are detrimental to human kind as well as to the electronic circuits they employed in our day to day life. In the former, microwaves affect the human tissues while in the latter they can interfere and produce noise in the electronic circuit [26-29]. So it is essential that they be prevented from coming out of a microwave based device as well as to stop them from getting in to it.

. Electromagnetic interference (EMI) – a specific kind of environmental pollution, is drawing more attention recently, due to the explosive growth in the utilisation of electrical and electronic devices in industrial, commercial and military applications. To provide adequate solutions for the EMI problem, the shielding and/or absorbing of the electromagnetic field is considered. There has been considerable interest in recent years in the applications of magnetic materials to the problem of microwave absorber design [27,28]. This is because, if a material with lossy dielectric is imparted a magnetic permeability by appropriate means, the absorbing characteristics of the material can be greatly modified .The modulation of the absorbing characteristics is based on the electromagnetic theory. The cardinal principle based on which absorbers are designed is the surface impedance.

Surface impedance can be written as

$$Z = \sqrt{\frac{\mu_r}{\varepsilon_r}} \tanh [\, j \frac{2\pi}{\lambda} \sqrt{\mu_r \, \varepsilon_r} \, t], \qquad\qquad 8.1$$

where μ_r and ε_r are the complex permittivity and permeability of the composites of thickness t. The reflection coefficient is expressed as

$$R \, (dB) = 20 \log \frac{Z-1}{Z+1} \qquad\qquad 8.2$$

Ferrites are materials, which can satisfy the above criteria; because the composition in a particular ferrite material can be altered to tailoring the magnetic permeability and dielectric permittivity. There has been considerable efforts from the microwave engineers to model an absorber for optimum performance

Ferrites are already known for their microwave absorption in UHF and VHF band. As evident from theory, the most important property that governs electromagnetic absorption is the dielectric permittivity and magnetic permeability at the desired bandwidth operation. The dielectric permittivity depends on the grain size,

composition, and concentration of ferrite materials in ferrofluids. In this chapter, the results of such studies are presented. The data generated in the X-band are analysed for permittivity and permeability measurements which determines the microwave absorption properties of these materials at that bandwidth of frequency.

In the present investigations, ferrofluids belong to the series $Ni_xFe_{1-x}Fe_2O_4$ and $Zn_xFe_{1-x}Fe_2O_4$, which were pre-characterised structurally have been analysed to study their electrical characterisation. Frequency, concentration and compositional dependence of dielectric properties have been investigated and have been explained with the support of existing theories. Also their permittivity and permeability were evaluated in the X band using a capillary method and the results are analysed. Also ferrofluids were analysed for their "magneto-dielectric" characteristics. Variation of capacitance in presence of an applied magnetic field shows the presence of Neel like particles suspended in these fluids.

8.2 Experimental techniques

Dielectric Measurements of $NiFe_2O_4$

Designing of a dielectric cell for liquids
A home made dielectric cell had been designed for the dielectric characterisation of ferrofluids samples. A parallel plate capacitor has been designed and fabricated with two copper plates as electrodes which were separated in space and the spacing was adjusted to be much low as compared to the area of the plates to have the parallel plate approximation. Measurement had been carried out using four probe method. Entire set-up was placed in a glass container in which the parallel plate capacitor can be placed vibration free with a stopper. Ferrofluid samples were added to the container till the plates are completely immersed in fluids.

The dielectric measurements of ferrofluid samples were carried out by using a homemade cell and an HP 4285A Impedance Analyser. The cell was standardized by using test samples of pure water, lead and fringe capacitance was eliminated by employing a procedure suggested by Ramasastry *et al* [30]. The capacitance C_1 of the parallel plate capacitor for fixed spacing of 1.5 mm was calculated first with air as the dielectric the medium and then with the ferrofluids as the medium C_2. The dielectric permittivity (ε_r) of the samples were calculated using the relation,
$$\varepsilon_r = C_1/C_2 \qquad\qquad 8.3$$

The complete experimental set-up and details of the dielectric measurements are explained in Chapter3.

8.3. Results and discussions

8.3.1Dielectric properties of ferrofluids
Frequency dependence
The dielectric behaviour of ferrofluids containing nickel and zinc derivatives of magnetite with change in frequency is depicted in Fig. 1a, and Fig. 1b (in the frequency in the range 100KHz to 8MHz). Here in the ferrofluid systems, the dielectric properties obey Maxwell Wagner type of dielectric dispersion in the given frequency range. Representative curves have been fitted for the Maxwell Wagner theory of dielectric dispersion and it fits moderately well for the samples, with a small discrepancy arising out of the colloidal nature of the fluid. Their ferrite counter parts exhibit excellent Maxwell Wagner type dispersion.

The variation of dielectric constant with frequency reveals the dispersion due to Maxwell-Wagner type[31-32], interfacial polarisation in agreement with Koops phenomenological theory of dielectric dispersion [33].The dielectric permittivity decreases with increasing frequency reaching a constant value for all the samples. The mechanism of dielectric polarisation in ferrites is similar to that of conduction process [34]. By electron exchange between $Fe2^+\leftrightarrow Fe^{3+}$,one obtains local displacement of electrons in the direction of applied field and these electrons determine the polarisation. The polarisation decreases with increase in frequency and then reaches a constant value due to the fact that, beyond a certain frequency of external field the electronic exchange $Fe^{2+}\leftrightarrow Fe^{3+}$ cannot follow the alternating field.

High values of dielectric permittivity at low frequencies are due to the predominance of the species like Fe^{2+} ions, interfacial dislocation pile ups, oxygen vacancies, grain boundary defects [31,32], while the decrease in dielectric permittivity with frequency is natural because of the fact that any species contributing to polarisability is bound to show lagging behind the applied field   d higher frequencies.

Koops [33] was among the first to study the frequency depe   of dielectric permittivity and dispersion of ferrites. He interpreted the   by considering the dielectric as an inhomogeneous medium of a Maxwell- Wa   ype. The high values of ε could be explained on the basis of Maxwell- Wagi   n ory, which is a result of the inhomogeneous nature of dielectric structure. This   ric structure is supposed to be composed of two layers. The first layer is the lar   te grains of fairly well conducting materials,   parated by the second th   r (grain boundaries) of relatively poor co   ins. The grain bounda   found to be effective at lower frequencies, while the ferrite grains are more e at higher frequencies [34-35]. Maxwell-Wagner model thus explain the decr. permittivity as the frequency increases.

A general relation of the following form explains the variation of diele constant with frequency

$$\varepsilon'' =(r-r')(\varepsilon'\times\omega) \qquad\qquad 8.4$$

where ε' and ε" are the real and imaginary parts of the dielectric constant and r and r' are the ac and dc conductivity respectively and ω is the frequency at which ac conductivity is measured.

The resistivity of ferrites decrease with increase in temperature. Anantharaman *et al* reported the same variations of dielectric permittivity with temperature in Ni-Zn ferrites[36] The high dielectric permittivity at lower frequencies found at high temperature may be explained in the presence of the permanent dipole moments indicating a small effective charge separation. Such a small charge separation must be due to asymmetry in the fields experienced by either oxygen ion or metallic ions. This could arise in the case of oxygen ions three B-site and one A-site neighbours, or in the case of A-site ion through a distortion of its surrounding oxygen tetrahedron [37].Similar results have been also reported by Josylu et al [38] in case of mixed ferrites.
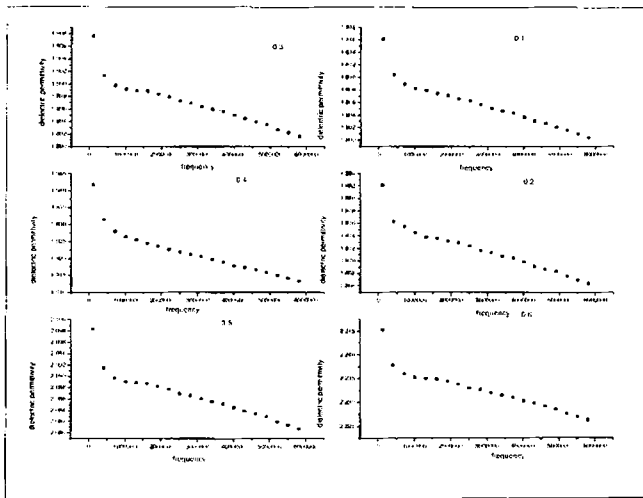

Fig. 1a Variation of dielectric constant with frequency in nickel doped derivatives of ferrofluids.
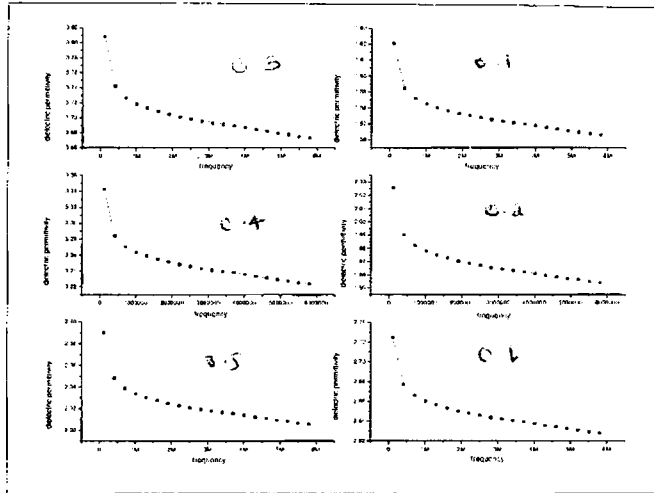
Fig. 1b Variation of dielectric constant with frequency in zinc doped derivatives of ferrofluids.

<u>Compositional dependence.</u>

To investigate the effect of dopant amount in the magnetite lattice, ferrofluids with varying amount of nickel, as well as zinc as dopant materials were investigated through dielectric measurements. Although the dispersion of dielectric permittivity in the MHz range are almost in accordance with the Maxwell Wagner type in all the fluid systems, there is an increase in dielectric constant exhibited by all the ferrofluid samples with increasing amount of dopants. Magnetite in its pure form is a highly symmetric crystal with any exchange from Fe_{2+} to Fe_{3+} will again result in similar state giving degenerate states. The existence of a foreign atom in the magnetite lattice will change the polarisability and hence an enhancement of dielectric permittivity is observed. Also lattice contraction occurring in the ultra fine systems also contribute to the enhanced permittivity.

Here a discrepancy is noted for the sample with composition 'x=0.7' where the permittivity decreases.
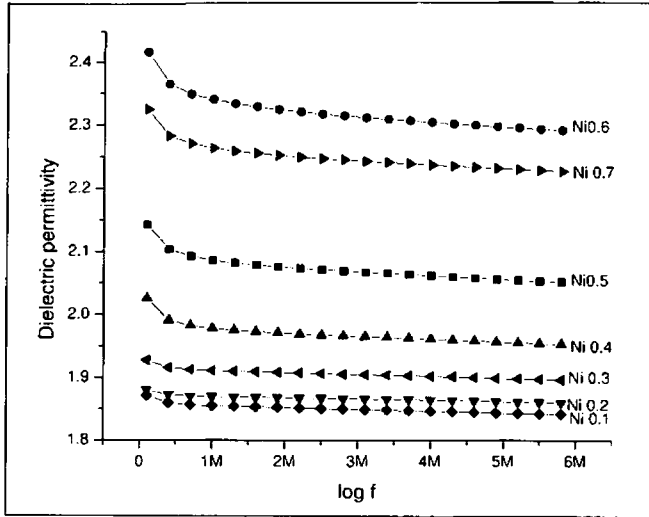
*Fig..2aVariation of dielectric permittivity of ferrofluids
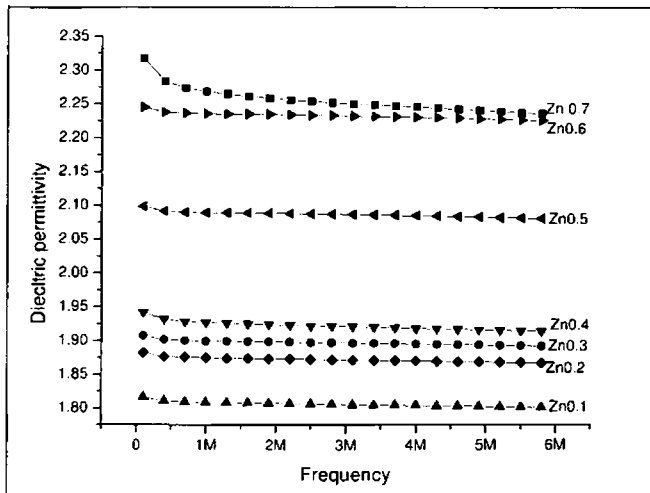with composition 'x in $Ni_xFe_{1-x}Fe_2O_4$*

*Fig. 2bVariation of dielectric permittivity of ferrofluids
with composition 'x in $Zn_xFe_{1-x}Fe_2O_4$*

The absolute values of the dielectric permittivity of the composites are found to be greater than that of the carrier kerosene, but less than that of the pure ferrite material. Maximum dielectric constant is observed for the maximum concentration as per our expectation. Thus ferrofluids with desired permittivity can be synthesised by varying the concentration of the sample.

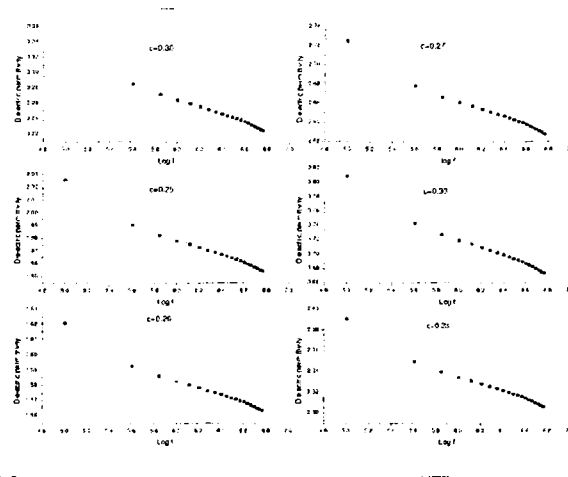*Concentration dependence.*

Fig. 3 Concentration dependence of permittivity in ferrofluids

To investigate the effect of individual dipole-dipole interaction in the value of dipolar polarisability, dielectric characterisation have been performed in varying concentration of the ferrite materials in the carrier fluid. In diluted systems, the suspended particles will be non interacting there by limiting the value of dielectric permittivity in the mixture like state.

For, a mixture of m component the dielectric permittivity ε^* is connected by a relation, where Log ε^* is given by

$$\sum_{i=1}^{m} y_i \log \varepsilon_i \qquad\qquad 8.5$$

Where ε^* is the dielectric permittivity of the mixture and y is the weight fraction of the component. For a two-component system the relationship can be written as

$$\log \varepsilon^* = y_1 \log \varepsilon_1 + y_2 \log \varepsilon_2 \qquad\qquad 8.6$$

where ε^* is the dielectric constant of the composite, ε_1 ,y_1 and ε_2 ,y_2 are the dielectric constant and weight fractions of the matrix and the filler component respectively.

Another mixture equation of the form

$$\varepsilon^{*} = \frac{\varepsilon_1 \varepsilon_2}{\varepsilon_1 y_2 + \varepsilon_2 y_1} \qquad\qquad 8.7$$

is also found to be useful in predicting the loading dependence of dielectric constant of the RFC. However in ferrofluid samples the logarithmic relations hold good in moderate concentrations.

However in highly concentrated ferrofluid system, there is a large deviation from the expected behaviour because of the strong dipole-dipole interaction. In Faraday rotation also such a behaviour is exhibited in a highly concentrated system. This can be explained by considering the fluid system as a collection of fine suspension of previously formed aggregates and in presence of an applied magnetic field, they will align which can change the dipole-dipole interaction and polarisation which can enhance the magnetic susceptibility which is not in accordance with the normal superparamagnetic model which greatly underestimates the value of initial susceptibility. Modified mean field model [39] can support the large enhancement in polarization and dielectric permittivity value in concentrated ferrofluid system.

Magnetic field dependence
An enhancement of capacitance/dielectric permittivity is observed for all the samples with the application of an external magnetic field (*Fig. 4a* to *Fig.4c*).
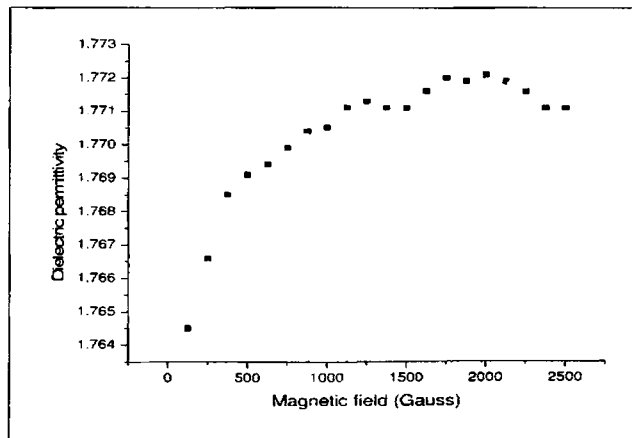

Fig. 4 a Variation of dielectric permittivity with applied magnetic field in (Fe₃O₄)ferrofluids
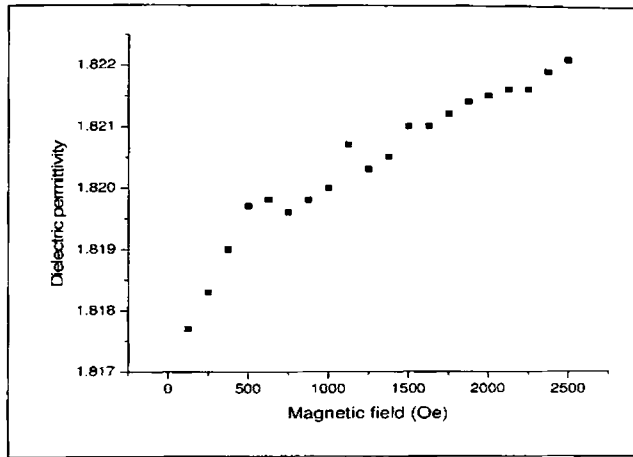
Fig. 4 b Variation of dielectric permittivity with applied magnetic field in (Zn $_{0.2}$ Fe $_{0.8}$Fe$_2$O$_4$) ferrofluids
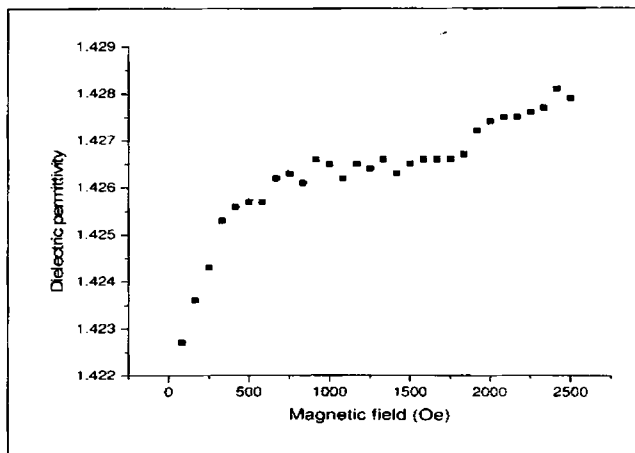
Fig. 4 c Variation of dielectric permittivity with applied magnetic field in (Zn $_{0.4}$Fe $_{0.6}$Fe$_2$O$_4$) ferrofluids

This is due to the independent Neel rotation of magnetic dipoles in a diluted ferrofluid. In a ferrofluid, in the absence of magnetic field, the particles exhibit constant zig-zag Brownian motion with in the whole volume of ferrofluid. However with the application of an external field, particles oppose this zig-zag motion and try to get aligned with in the applied magnetic field. This spin rotation will chance the dipolar polarisation and hence initially there is a comparatively large variation in capacitance and after that with moderate applied field, the dipolar polarisation is not varying there after and hence no change in permittivity is observed there after.

8.3.2 *Permittivity in the X band and Microwave absorption*

Microwaves constitute only a small portion of the electromagnetic spectrum, but the applications have become increasingly important to investigate the material properties. Measurement of material properties like permeability, permittivity, and conductivity will serve as a tool for investigating the intermolecular and intra molecular mechanisms of compounds.

Bethe and Schwinger suggested the cavity perturbation theory for the first time. According to them, the perturbation was caused by the insertion of small dielectric sample in to the cavity and by a small deformation of the boundary surface of the cavity. By quantifying the perturbation occurred, various material properties can be measured. The fundamental idea is that the change in the overall configuration of the electromagnetic fields upon the introduction of the sample must be low. Based on this assumption, detailed derivation of the perturbation equation for the frequency shift upon introduction of a sample into a cavity was given by Waldron and Harrington.

The permittivity and permeability of a material in general is a complex quantity such as $\varepsilon_r = \varepsilon_r' - j\varepsilon_r''$ and $\mu = \mu' - j\mu''$. The real and imaginary part of the permittivity are obtained from the perturbation equation for the frequency shift as,

$$\varepsilon_r' + 1 = \frac{(f_0 - f_s) \, V_c}{2 f_s \quad V_s}$$

$$\varepsilon_r'' = \frac{V_c}{4 V_s} \left(\frac{1}{Q_s} - \frac{1}{Q_0} \right)$$

Here Q_0 and f_0 represent the quality factor and resonance frequency of the cavity in the unperturbed condition respectively. Q_s and f_s are the corresponding parameters of the cavity loaded with the sample.

To study the dielectric properties of liquid, a container is required. For this purpose, a capillary tube of low- loss, fused silica is used. If the frequency shift is measured from the resonance frequency f_t of the cavity loaded with an empty capillary tube rather than that with an empty cavity alone, the above equation becomes

$$\varepsilon_r' + 1 = \frac{(f_t - f_s) \, V_c}{2 f_s \quad V_s}$$

$$\varepsilon_r'' = \frac{V_c}{4 V_s} \left(\frac{1}{Q_s} - \frac{1}{Q_t} \right)$$

Here, Q_t represent the quality factor of empty tube.

Similarly, the real and part of the complex permeability is given by,

$$\mu_r + 1 = \left(\frac{\lambda_g^2 + 4a^2}{8a^2} \right) \frac{(f_t - f_s) V_c}{f_s V_s}$$

where f_s and f_t are the resonant frequencies of the cavity with the sample and with the empty tube, respectively and a represent the λ_g is the guided wavelength and is given by
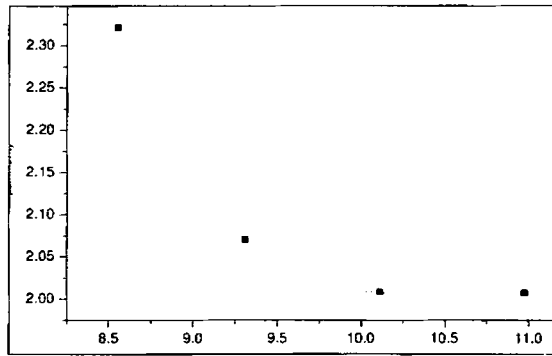
$$\lambda_g = \frac{2d}{p}$$

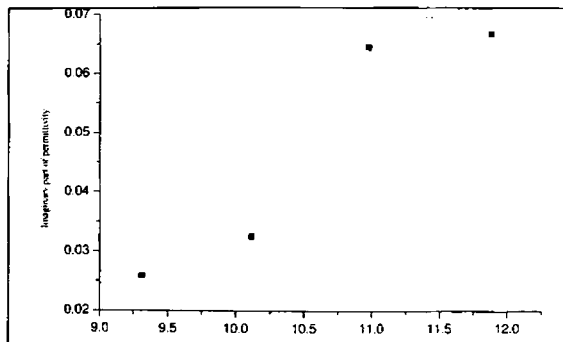*Fig.5a Permittivity of $Zn_{0.4}Fe_{0.6}Fe_2O_4$ ferrofluid*

Fig. 5b Imaginary part of permittivity for $Zn_{0.1}Fe_{0.9}Fe_2O_4$ ferrofluid
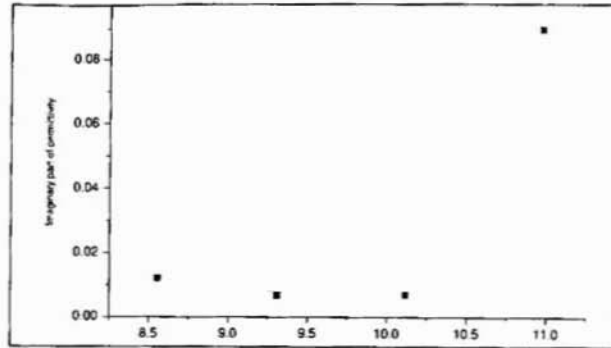
Fig. 5c Imaginary part of Permittivity for $Zn_{0.4}Fe_{0.6}Fe_2O_4$ ferrofluid
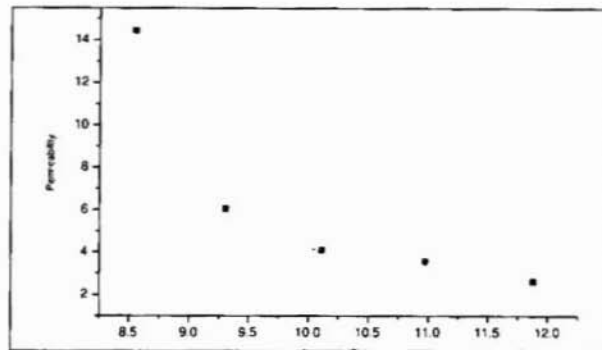
Fig. 5d Permeability for $Zn_{0.4}Fe_{0.6}Fe_2O_4$ Ferrofluid

The samples show microwave absorption properties and the permeability values found out using the capillary method agrees well with the reported values. Also permittivity measurements are in good agreement with that measured in the MHz regime. Also their microwave absorption properties make them ideal candidates for many devices for microwave applications including in cell phones.

8.4 Conclusion

Dispersion of permittivity is of Maxwell Wagner type with slight variation due to Brownian motion of the colloidal system. Permittivity increases with increase in dopant concentration due to the enhanced dipolar polarisation. Diluted ferrofluid system behaves like a collection of independent dipoles, while concentrated systems show discrepancy due to their mutual interaction. In presence of an applied magnetic field change in dipolar polarisation due to the independent Neel rotation results in the enhanced capacitance in the low applied fields which saturates abruptly. Coaxial cavity resonator has been employed for the determination of permittivity in the X band. Permeability measurements were also carried out in the X band using

perturbation technique. The coaxial cavity resonators measurements at frequencies below the cut off could also be carried out by changing length of the centre conductor.

References

1. D.Y.Kim, Y.C.Chung, T.W.Kang and H.C.Kim, IEEE Trans. Magn., **32.** No.2 (1996)
2. Mingzhong Wu,Huahul He,Zhensheng Zhao and Xi Yao J.Phy. D.Appl.Phys.**33**(2000)2398
3. Hyung Do Choi, Hwan Woo Shim, Kwang Yun Cho, Hyuk Jaee Lee, J.App. Poly. Scie, **72**, (1999) 75
4. John L. Wallace, IEEE Trans. on Magn, **29.** No.6 (1993)
5. Morihiko Matsumoto and Yoshimori Miyata, IEEE Trans. on Magn. vol. 33 No.6 November(1997)
6. Renachao Che, Yongqing Li, Zhaohui Chen, Hongji Lin, J. Materials Science Letters **18** (1999) 1963-1964.
7. Praveen Sing, T C Goel, Indian Journal of Pure and Applied Physics.**38**.(March 2000) 213
8. Yoshimori Miyata and Morihiko Matsumoto IEEE Trans. Magn. **33.** No.5, September1997.
9. J.Y. Shin and J.H.Oh, IEEE Trans. on Magn, **29**, No.5, (September1993)
10. Hombach, V.Meier, K;Burkhardt, M;Kuhn;Kuster,N, IEEE Trans. on Micr.Theory Technol **44** (1996),1865.
11. Rao K and Zhao B J.Univ.Electron.Sci.Technol.China **23** (1994) 478.
12. Ronald .E. Rosenweig , Ferro hydrodynamics, Cambridge University Press, 1985.
13. B.M Berkovsky, V.S Medvedev., M.S Krakov, Magnetic fluids; Engineering applications, Oxford university press. 1993
14. J. Deperiot, G. J Da Silva C.R Alves, Braz. J. Phys. **31**, (3) (Sept 2001), 390
15. Helen W Davies and Patrick Llewellian, J. Phys. D; Appl. Phys, **13** (1980) 2327.
16. R.K Bhat, Indian J. Eng. Mater. Scie. **5**, (Dec 1998), 477.
17. H.E Horng, Chin Yin Hong, H.C. Yang, I J Jang, S.Y Yang, J.M Wu, S. I Lee, F. C Kuo, J. Magn. Magn. Mater, **201**(1999) 215.
18. H M Musal. Jr. and DC Smith. IEEE Trans. on Magn, **26** no 5 (September) 1990, 1462.
19. K.A Malini, E.M. Mohammed , S.Sindhu, P. Kurian, M.R. Anantharaman, Plastics, Rubber and Composites 2002 **31** No.10 449
20. KJ Chul Han Hyung Do Choi, Tak Jin Moon,Wang Sup Kim, Kyung Yong Kim, Journal of Material Science 30 (1995) 3567-3571.
21. K.W.Wagner, Amer, Phys.**40** (1973) 317
22. Nelson,S,Krazewski,A,You, T.J Micropower Electro energy 1991,26,45.
23. B.T. Lee and H.C. Kim, J.Phys.D. Appl.Phys. (1994)
24. M.Pal, P.Brahma and D.Chakravorthy, Journal of Physical Society of Japan, **63.** Nov.9, (September 1994) 3356.
25. Seyed Abdullah MIRTAHERI, Tetsuya Nizumoto, The transactions of the IEICE,.**E.73**, No.10, October 1990.

26. D.Y.Kim, Y.C.Chung, T.W.Kang and H.C.Kim, IEE Transactions on Magnetics,. **32**. No.2 (1996)

27. Mingzhong Wu, Huahul He Zhensheng Zhao and Xi Yao J.Phy. D.Appl.Phys. **33** (2000) 2398

28. Hyung Do Choi,Hwan Woo Shim, Kwang Yun Cho, Hyuk Jaee Lee.Journal of Applied Polymer Science, **72**. (1999) 75

29. John L. Wallace, IEE Transactions on Magnetics,. **29**. No.6(1993)

30. Ramasastry C and Syamasundra Rao, J.Phys.E.Sci.Instrum.12(1979) 1023

31. I.C.Maxvell,Electricity and Magnetism, vol.1,Oxford   univ.Press,Newyork(1973) 828.

32. 29). K.W.Wagner, Amer.Phyis. **40** (1973) 317.

33. C.G.Coops, Phys. Rev **83** (1951) 121.

34. L.T.Rabinkin,Z.I.Novikora.Ferrites,146 Izv. Acad. Nauk,USSR,Minsk 1960

35. B.K.Kunar,G.S.Srivastava,J.Appl.Phys.**70**(1994)6115.

36. E.M. Mohammed, K.A. Malini, P. Kurian, M.R. Anantharaman, Mat. Res. Bull **37** (2002) 753

37. K.J.Standley, oxide Magnetic Materials, Clarendon Press, Oxford,1962, 323

38. O.S.Josylu, J.Sobhanadri, Phys.Stat.Sol.A **59** (1980) 323.

39. A.F. Pshenichnikov, J. Magn. Magn. Mater. **145**, (1995) 319

CHAPTER 9

Effect of Quantum Confinements and alloying on the Optical Properties of Ferrofluids Synthesized via Chemical Routes

This chapter presents the studies carried out on the optical properties of ferrofluids based on magnetite. The effect of nickel alloying is studied and the effect of quantum confinement and alloying is investigated.

Magnetite based ferrofluids have been synthesized by chemical co-precipitation and their structural characterization have been carried out using X-Ray Diffraction. Micro structural characterization as well as grain size estimation has been carried out by TEM techniques, which revealed the ultrafine nature of the suspended particles. The synthesized ferrofluids were characterized optically by absorption spectra taken in three different ways to eliminate the effect of carrier liquid and surfactant coating. The optical band gap determined by Tauc plots is found to be blue shifted by 0.81 eV for magnetite based ferrofluids which is explained on the basis of exciton confinement in the weak regime. The addition of Ni on the lattice further reduces the grain size and enhances the blue shift up to 1.31 eV and the observations were interpreted in terms of the combined effect of alloying and grain size variation. By carefully varying the grain size and doping percentage, possibility of obtaining a more optically transparent ferrofluid is proposed which is quite important from the application point of view.

9.1 Introduction:

Transparent magnetic materials finds extensive application potential in versatile fields like Xerox technology, magneto-optical recording, magnetic field controlled optical modulators, magneto-optical displays and switching devices [1,2,3]. Aerogel based transparent magnetic materials have been proposed now a days which is rather too weekly magnetic to be used for any applications [4].

With the advent of nanotechnology, it is known that both the optical and magnetic properties could be greatly modified if the synthesized particles are in ultra fine regime. The optical properties of the materials change dramatically when the grain size is reduced to the order of Bohr radius limit. Semiconductor nanocrystallites are recently studied for their excellent optical properties due to the quantum confinement effects. It is reported first in CdSe nanocrystals that in the strong quantum dot confinement a shift of 1.54 eV in energy band gap is exhibited [5]. Also the enhanced blue shift due to weak exciton confinement is reported in γ Fe_2O_3 nanocrystals [6]. A strong and dot like confinement can occur if the grain size could be further reduced below Bohr radius of the material which can enhance the quantum confinement effects to a higher order.

Magnetic properties also change with the ultra fine nature of the grains. Normally materials exhibit single domain and superparamagnetic characteristics at the nanolevel. However if the grain size is reduced further, thermal energy contribution becomes higher which can randomize the spins giving negligible value of   magnetization and thus becomes non favorable from the application point of view.

Alloying with any other metals is also found to enhance the blue shift in Ni doped CdTe nanocrystalline thin films [7]. However such a technique is never found to be employed in enhancing the optical transparencies of a magnetic material. Ferrofluids are stable colloidal suspension of ultra fine magnetic particles in a suitable base fluid [8]. They are ideal candidates to study the magnetism and optics at the nanolevel. However, due to the reduction in magnetization with reduction in grain size of the order of 40 Å, alternative methods have to be employed to enhance the optical transparencies other than the grain size reduction.

Studies on the size effects or alloying effects on the optical properties possess problems and careful methods of preparation have been employed so as to prepare magnetic fluids having high saturation magnetization values with least possible grain size (50-65Å) and a narrower size distribution. Here attempts are made to and the effect of Nickel doping on the optical band gaps of these magnetic fluids have been dealt in detail. The grain size estimation using XRD is well supported by the TEM and AFM measurements.

Semiconductor nanocrystals
It has been very helpful for the Physics of nanocrystals to employ the simplified models to trace the effects originating from the three dimensional spatial confinements. An extension of the effective mass approximation towards the spatially confined structures leads to a particle in a box problem and provides a way to calculate the properties of nanocrystals that are not possible to analyze by other means. Hence in nanocrystals, "crystal to nanocluster approximation" and "single molecule to quantum dot" approximations are examined for their respective employment in our system with known particle diameters.

Excitons
Excitons are quasiparticles formed by the elementary excitations of the system consisting of real particles[9]. By this approach electrons in the conduction band can be considered as the primary elementary excitation of the electrons in the crystal. This will lead to a quasi particle *hole* in the valence band with a proper quasi momentum providing a quasi effective mass. Hence the ground state of an electron is a vacuum state and the first excited state is the creation of one electron-hole pair. Electrons and holes can be described by Fermi Dirac statistics. Ideal excitation produces the electrons and holes with

216

no attraction. However there is a coulomb attraction for electrons and holes which results in the formation of a quasi particle called an exciton. Exciton possess a Bohr radius of

$$a_B = \frac{\varepsilon \eta^2}{\mu e^2} = \varepsilon \frac{m_0}{\mu} 0.53 \overset{\circ}{A}$$

As the reduced electron mass is smaller than electron mass and dielectric constant is larger several times than in vacuum, the excitons possess large Bohr radius as compared to the ground state of hydrogen atom although they hydrogen like states.

Quantum confinements

In semiconductors, the de Broglie wavelength of an electron and a hole and the Bohr radius of an exciton may be considerably larger than the lattice along the confinement direction. For d=0, complete confinement occurs with zero dimensional structure which differs from quantum wells and wires and the density of states is a discrete delta function resulting in the finite motion in all three dimensions with finite number of atoms and elementary excitations in each quantum dot. This gives strong confinements.

Weak and strong exciton confinements

Weak confinement regime corresponds to a region when the particle radius is small, but a few times greater than exciton Bohr radius. In this quantization of exciton centre of mass occurs. In strong confinement, in contrary to the hydrogen like Hamiltonian, the appearance of potential does not allow the centre of mass motion and the motion of a particle with reduced mass to be considered independently. Strong confinements are resulted only when the grain size is several times less than the exciton Bohr radius and this grain size distribution is quite narrow.

A heavy hole and a light hole

A heavy hole and a light hole can be differentiated by their energy curves. Light holes have a sharp energy band and the energy parabola by the first approximation will be steeper, while the heavy hole has a broader energy curve. Their density of states are very high in normal crystals and there by influencing all the optical properties exhibited by these crystals. Light holes are lesser in number and their density of states are thus very low and unless the grains fall in dot regime, ie, when the grain size becomes much below the Bohr radius limit of excitons, the properties of the crystal wont be much affected by their presence. However, in the highly confined regime, light holes also results in the formations of excitons with a very small effective mass for the hole, there by changing the energy shift towards the blue region. Electron-Heavy hole pair exciton has almost the same effective mass in all semiconductors, while the excitons formed by a light hole and electron has varying effective mass in different crystals.

Generally if there is a triplet and singlet level, triplet states provide high momentum and hence higher effective mass to the exciton, thus the hole is a heavy hole, while the singlet state gives rise to a light hole.

In the present investigation, ultra fine magnetic materials (magnetite) are synthesized and pre-coated with a surfactant while in the synthesis process and they were dispersed in hydrocarbon based carrier to obtain ferroluids. Quantum confinement induced blue shift in energy band gap have been studied in detail by various researchers in semiconductors like Si, ZnO, CdS, CdTe etc. However such an attempt was never carried out in magnetic nanoparticles in which there are vast probabilities of tuning band gap towards the blue regime to obtain transparent magnetic material which is the dream goal of researchers working in the area of magnetic materials since their invention due its application potential. Here an attempt is made towards enhancing the optical transparency of magnetic nanoparticles by the grain size dependant quantum confinement and the effect of alloying with nickel in magnetite on the confinement effects is studied. To the best of our knowledge, such an attempt of obtaining transparent magnetic material was never reported so far.

9.2 Experimental Techniques:
9.2.1 Preparation of magnetite ferrofluids:
The magnetite ferrofluid samples were synthesized by standard co-precipitation of aqueous solutions of 2M $Fe(NO_3)_3$ $9H_2O$ and 1M $FeSO_4$ $7H_2O$ at room temperature at a pH of 11.5 and insitu coating is provided with oleic acid and the wet slurry is washed with acetone and finally dispersed in kerosene.

9.2.2 Doping
Insitu doping with Ni was carried out using the standard co-precipitation technique using xM $NiSO_4$ $7H_2O$, 1-xM $FeSO_4$ $7H_2O$, 2M $Fe(NO_3)_3$ $9H_2O$ for the synthesis of ferrofluids belonging to the series $Ni_xFe_{1-x}Fe_2O_4$ where 'x' was varied from 0.1 to 0.7.

9.2.3 XRD Studies
The synthesized ferrofluids have been dried by the reversible flocculation technique using acetone and the slurry was dried in room temperature. The XRD spectra of the samples were recorded on an X-ray diffractometer (Rigaku D-max-C) using Cu Kα radiation (λ=1.5406Å). The particle size was estimated by employing Debye-Scherer's formula,

$$D = \frac{0.9\lambda}{\beta\cos\theta},$$

<div align="right">9.1</div>

where λ = Wave length of X-ray used, β = FWHM in radians of the XRD peak with highest intensity, D = particle diameter, θ = glancing angle.

9.2.4. Transmission Electron Microscopy (TEM)

The synthesized ferrofluids have been dried by washing with acetone and were analyzed for their grain size and grain size distribution using transmission electron microscopy (TEM). The electron diffraction (ED) spectrum was also recorded and the lattice planes were identified using the ED spectrum. Here a thin specimen is irradiated with an electron beam of uniform current density. Electrons are emitted from an electron gun and illuminate the specimen through a two or three stage condenser lens system. The electron intensity distribution behind the specimen is magnified with a three or four stage lens system and viewed on a fluorescent screen. The image can be recorded by direct exposure of a photographic film.

9.2.5. Optical studies

Optical absorption spectrum was recorded using a Hitachi U-3410 UV-VIS-NIR spectrophotometer for the pure as well as nickel doped magnetite based ferrofluid samples and the band gap was determined for all the synthesized samples. Using three different procedures.

a) The synthesized ferrofluids were encapsulated in between two optically smooth and ultrasonically cleaned glass substrates and absorption spectrum was taken with a similar slide with the base fluid and surfactant as the reference.

b) The ferrofluids were dip coated on an optically smooth glass slide and the optical absorption spectrum was recorded with the surfactant-base fluid dip coated slide as the reference.

c) Ferrofluids were taken in a standard quartz cuvette and absorption spectrum was recorded with a similar cuvette with the base fluid and surfactant as the reference.

In order to calculate the band gap (assuming direct band gap), it may be noted that for a semiconductor, the absorption coefficient near the band edge is given by

$$\alpha = \frac{A(h\nu - E_g)^{1/2}}{h\nu} \qquad\qquad 9.2$$

where A is a constant and E_g is the energy band gap.

When $\alpha h\nu = 0$, $E_g = h\nu$.

So using an extrapolation to the X axis of the pot of "$(\alpha h\nu)^2$ vs $h\nu$", gives the band gap of the material if it is a direct transition which is the Tauc plots .

9.3. Results and Discussions

X Ray diffraction spectra (Fig. 1) of ferrofluids shows that synthesized particles are in the ultra fine regime.
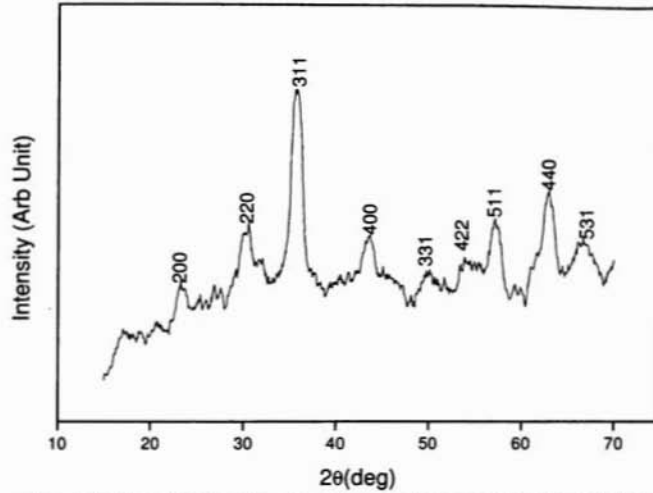
Fig. 1 X Ray Diffraction Spectrum of <u>magnetite</u> ferrofluids

Lattice planes were identified using both XRD and Electron diffraction (ED) spectrum. Exact grain size and size distribution were estimated using Transmission Electron Micrograms. Representative TEM micrographs are depicted in Fig. 2.
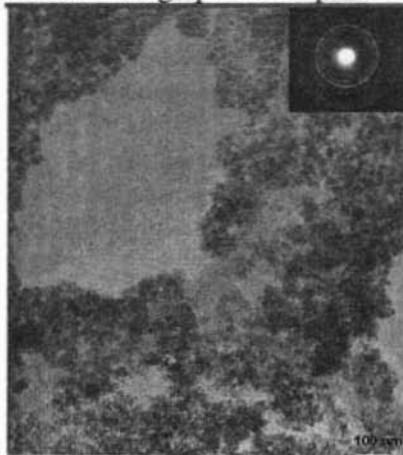
Fig. 2 TEM Image of a representative ferrofluid sample (dried)
Inset - Electron Diffraction spectrum. $\left(N_{0.1} Fe_{0.9} Fe_2 O_4 \right)$

The TEM images shows that the grain size distribution is narrow and grain sizes are in the range 55-70Å. Lattice planes were also calculated using the Electron Diffraction Spectrum. (Inset Fig. 2)

220

The grain sizes for all the samples have been estimated and plotted for all compositions (Fig. 3).

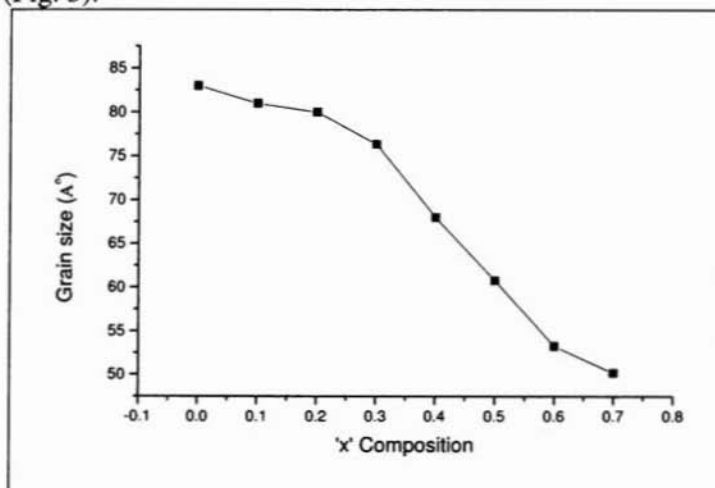*Fig. 3 Grain size vs composition in $Ni_xFe_{1-x}Fe_2O_4$ (0 corresponds to Fe_3O_4)*

Lattice parameters were evaluated and plotted for the variation in 'x' in the series $Ni_xFe_{1-x}Fe_2O_4$ (Fig. 4) using X ray diffraction data. The lattice parameter variation is as per Vegard's law and parameter shows a linear decrease with increasing nickel doping.
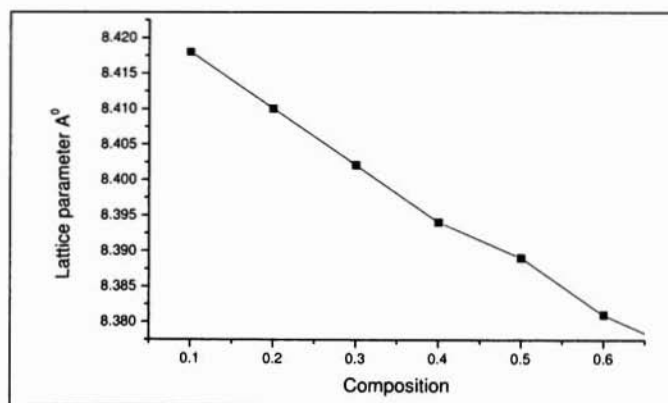

Fig. 4 Lattice Parameters vs Composition

221

The optical absorption spectra of the pristine and the doped samples were recorded. Absorption spectra of magnetite ferrofluids obtained using different techniques are provided (Fig. 5)
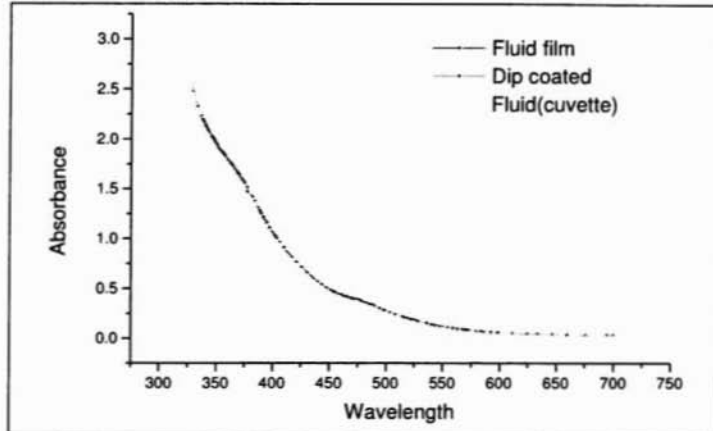
Fig. 5. Absorption spectra recorded for magnetite ferrofluids

Their optical band gaps were determined using Tauc plots [9] and they are plotted for all the samples in the series (Fig. 6). However the error in the calculation of band gap using Tauc plots may vary from 0.01 eV to 0.08 eV which may be much higher comparing with the shift in energy band gap. So a more accurate way for the determination of band gap using a first differential analysis [10] is employed which could be applicable for both the direct and indirect transitions. Energy band gap is determined by this method and plotted for all the $Ni_xFe_{1-x}Fe_2O_4$ samples (Fig. 7) where 'x' varies from 0 to 0.7 in steps of 0.1.
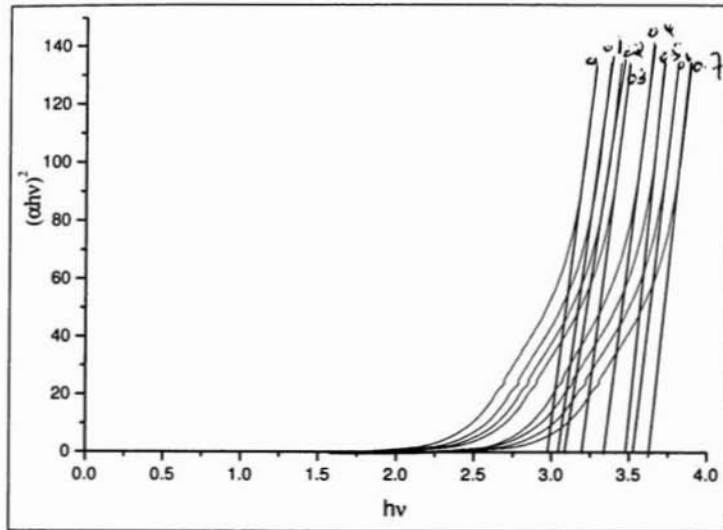
Fig. 6 Optical band gap variation of using Tauc plots ($N_x Fe_{1-x} Fe_2 O_4$)

A large blue shift in energy band gap of 0.81 eV for the undoped samples (E_g=3.01 eV) is observed as compared to the bulk value. The details are included in table 1. Doping with nickel enhanced the blue shift up to 3.71 eV.

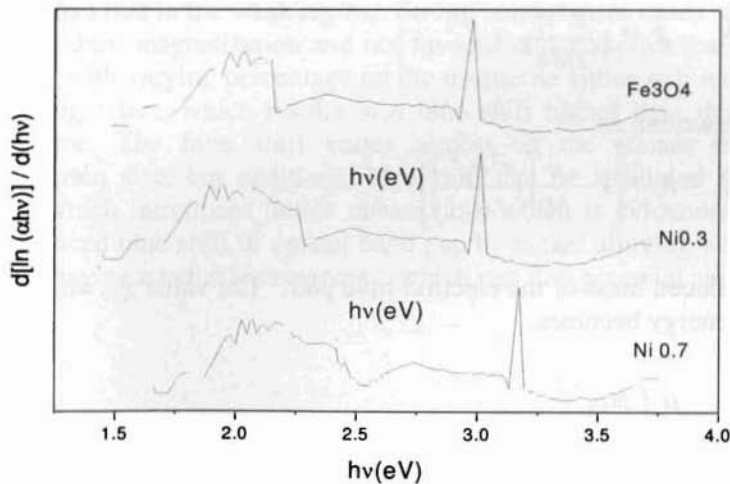*Fig. 7 First derivative of the graph with 'hv' plotted along X-axis and ln(αhv) plotted along Y-axis of representative ferrofluids.*

Optical absorption spectrum of many of the nanocrystalline semiconductors exhibits a blue shift due to the quantum confinements [11-16]. The confinements in these nanostructured semiconductors could be broadly divided into two extremes, namely the strong and the weak confinement. In the strong confinement regime, the grain size is less than $2a_0$ where a_0 is the exciton Bohr radius of the material and in the weak confinement regime, the grain size is larger than $4a_0$. In between these limiting cases, both electron and hole confinement and their Coulomb interaction should also be considered.

Strong quantum confinement will occur only if the grain size distribution is very narrow and the particle could be compared as a molecule in its orbital level in which a quantum dot like confinement occurs if the nanocrystallite grain size is less than the Bohr radius of the material.

In the weak confinement regime, quantisation of exciton centre of mass comes into play. Starting from the dispersion law of an exciton in a crystal, the energy of a free exciton is replaced by a solution derived for a particle in a spherical potential well [17]. The energy of an exciton in the weak confinement case is then of the form

$$E_{nml} = E_g - \frac{Ry^*}{n^2} + \frac{\eta^2 \chi_{ml}^2}{2Ma^2}$$
9.3

E_g is the bandgap, Ry^* is the Rydberg's constant.
For the lowest state (n=1, m=1, l=0) the energy can be expressed as

$$E_{1s1s} = E_g - Ry^* + \frac{\pi^2 \eta^2}{2Ma^2}$$
9.4

which could be rewritten as,

$$E_{1s1s} = E_g - Ry^* \left[1 - \frac{\mu}{M} \left(\frac{\pi^2 a_B^2}{a} \right) \right]$$
9.5

where μ is the reduced mass of the electron-hole pair. The value $\chi_{10} = \pi$, and the relation for confinement energy becomes,

$$\Delta E_{1s1s} = \frac{\mu}{M} \left(\frac{\pi a_B}{a} \right)^2 Ry^*$$
9.6

which is, however, small compared with Ry^* so far as
$$a >> a_B$$
holds. This is the quantitative justification of the term "weak confinement".

Taking into account of photon absorption which can create an exciton with zero angular momentum, the absorption spectrum will then consist of a number of lines corresponding to states with l=0. therefore, the absorption spectrum can be derived from eqn 9.3 with $\chi_{m0}=\pi m$ radius, using eqn 9.6 confinement energy can be written as

$$E_{sh} = \frac{h^2 \pi^2}{2m_{eff}R^2},$$
9.11

where R is the nanocrystalline radius and m_{eff} is the effective mass of the exciton in weak confinement. Thus confinement energy is clearly a function of the nanoparticle radius and varies as $1/R^2$.

The exciton of 1s electron-heavy hole has comparable values of effective mass m_{eff} for almost all the semiconductors and thus the energy shift variation becomes a function of the nanoparticle radius in the weak confinement regime.

The addition of nickel in the lattice of magnetite will reduce the effective mass m_{eff} due to the difference in heavy whole energy spectra resulting from the alloying owing to the difference in the orbital hybridization and spin momenta.

9.4. Conclusion:

Careful control of grain size the co-precipitation parameters like pH and temperature ensured the synthesis of smallest possible magnetic grains. *Insitu* capping by the surfactant oleic acid prevents further grain growth. Their optical absorption spectrum shows a high blue shift of 0.81 eV in band gap due to quantum confinement effects, which are higher than that in the weak regime. Strong confinement needs still lower grain size, which may reduce magnetization and not favored under application point of view. Addition of nickel with varying percentage on the magnetite lattice still reduces the band gap by the alloying effect, which results in a blue shift higher than that in the weak confinement regime. The blue shift varies almost as the square inverse of the nanocrystallite's grain size, but additional blue shift can be attributed to the alloying effect of nickel, which introduces lattice contraction, which is evidenced by the XRD studies. This enhanced blue shift in optical band gap by nickel alloying will enable us to obtain ferrofluids having a better transparency, which can find potential applications.

References

1. Marcos Zayat, Francisco del Monte, Maria del Puerto Morales, Gregorio Rosa, Hector Guerrero, Carlos J. Serna and David Levy 2003 *Adv.Mater.* **15** 1809
2. M. Gich *et.al* 2003 *Appl.Phys.Lett* **82** 4307
3. Zhou Z H, Xue J M, Chan H S O and Wang J 2001 *J.Appl.phys.* **90** 4169
4. del Monte F, Morales M P, Levy D, Fernandez A, Ocana M, Roig A, Molins E, O'Grady K and Serna C J 1997 *Langmuir* **13** 3627

5. George C Hadjipanayis and Richard W Siegel, *Nanophase materials-synthesis, properties and applications*, kluwer Academic Publishers, London, 432

6. Swapna S Nair, Mercy Mathews, M.R. Anantharaman, Chem. Phys. Lett, 2005, (In Press)

7. O. Alvarez-Fregoso, J.G. Mendoza- Alvarez, and O. Zelaya-Angel, J. Appl. Phys, **82** (2), (1997 July), 708

8. Ronald .E. Rosenweig , Ferro hydrodynamics, Cambridge University Press 1985

9. Richard Turton, *The Physics of Solids*, Oxford University Press, New York (2000)

10. S. Chakrabarti, D. Ganguli, S. Chaudhuri, Physica E **24** 333 (2004).

11. R.V. Kamat and B Patrick, J.Phys.Chem, **96**, (1992) 6829,

12. I Bedja, S.Hotchandani, P.V.Kamat, J. Phys.Chem, **97**, (1993) 11064,

13. J.Bedja, S Hotchandani, P.V kamat, **98,** (1994) 4133,

14. D.E Skinner, D.P.J Colombo, J.J Caveleri, R.M Bowman, J.Phys.Chem, **99**, (1995) 7853,

15. J.G Zhang, R.H.O' Neil, T.W Robertie, J.Phys.Chem, **98,** (1994) 3859,

16. J.Z Zhang, R.H.O' Neil, T.W Roberti, J.L McGowan, J.E Evans, Chem. Phys. Lett, **218,** (1994) 479

17. M.Xu and P.J Ridler, J. Appl. Phys. **82** (1), (1997 July), 326

CHAPTER 10

Non linear Optical Properties of Ferrofluids Investigated by Z Scan Technique.

This chapter gives a general outline of the optical nonlinearity shown by materials, and it also deals with the nonlinear optical properties of ferrofluids measured by open aperture Z-scan technique. Magnetite based ferrofluids were investigated for their non linear properties like induced scattering, multiphoton absorption etc and the observation were linked with the general non linear optical theories and the data were fitted for multiphoton absorption coefficients.

Surfactant coated ferrofluids based on magnetite and nickel doped magnetite have been synthesized by the co-precipitation process, with oleic acid as the surfactant and kerosene as the carrier. The colloidal suspensions contain nanosized particles of approximately 80 Å diameter, with a number density of the order of $10^{22}/m^3$. Optical nonlinearities associated with the samples have been studied in the nanosecond and femtosecond excitation domains, employing the open aperture Z-scan technique. Excited state multi photon absorption and induced scattering are found to be responsible for the observed optical limiting in the nanosecond domain, while electronic nonlinearities dominate in the femtosecond regime, which were fitted for three photon absorption. The wavelength and concentration dependence of the limiting also is investigated.

10.1 Introduction

Ferrofluids are stable colloidal suspensions of nanomagnetic materials suspended in a suitable base fluid [1]. These rheological fluids have attracted the attention of scientists and engineers due to their possible applications in versatile fields. Surfactant separated ferrofluids assume significance due to their ease of preparation, and greater stability against agglomeration. This stability is achieved by coating the fine magnetic particles with molecules like oleic acid, which have a polar head, thereby ensuring that the ultrafine particles are separated. Thus a stable colloidal suspension is obtained, with the suspended fine particles executing constant Brownian motion [2].

Magnetite ferrofluids are the oldest and widely used ferrofluids due to their very high saturation magnetization, which finds enormous applications in a variety of fields [3]. Due to their good thermal stability and stability against agglomeration, these smart fluids have been extensively used in many engineering applications such as in loud speaker coils and pressure sensors. Fluid dynamics of ferrofluids in the presence of an applied magnetic field is governed by the modified Bernoulli's equation, given by

$$1/2\rho v^2 + \rho g h + P - \mu_0 \int M dH = constant$$

where the additional term arises due to the interaction of individual magnetic moments with the applied magnetic field [1]. In the absence of an external magnetic field, the equation will be reduced to the standard Bernoulli's equation. The magnetic field induced structural anisotropy of ferrofluids leads to many special magneto-optical properties like field induced optical birefringence, linear and circular dichroism, Faraday rotation and ellipticity. They also show many field independent properties like zero field birefringence [4-8].

Ever since powerful laser systems became commercially available, there has been a growing need for the protection of human eyes and optical sensors from intense laser radiation. The development of optical limiters has received significant attention in this regard. An ideal optical limiter should be transparent to low energy laser pulses, and opaque at high energies. Several organic and inorganic compounds have been found to exhibit good optical limiting properties [9-15]. Nanomaterials such as metal and semiconductor nanoparticles also have been investigated in much detail [16-22]. However, the same has not been reported for ferrofluids so far. In fact, it is the physical and chemical stability of ferrofluids, which is an important attribute for an optical limiter, which prompted us to investigate their optical limiting properties.

We employed the technique of Z-scan, which is a simple and highly sensitive method widely used for the determination of nonlinear optical constants of materials. The present samples have been irradiated using 7 ns (532 nm), and 100 fs pulses (400 nm and 800 nm). The wavelength, concentration and pulse width dependence of the limiting process is investigated.

The Z- Scan Experiment

Characterization of the nonlinear optical properties of materials is of utmost interest in several fields of physics, both from the fundamental and the applied points of view. In particular, great effort has been devoted to the determination of the third-order nonlinear optical susceptibility, $\chi^{(3)}$, responsible for phenomena such as third harmonic generation or optical phase conjugation. In media with inversion symmetry (such as gases, liquids and non-crystalline materials), third order nonlinearity is the lowest order nonlinearity allowed under the electric-dipole approximation. Third harmonic generation, phase conjugation, saturation, self-focusing, optical Kerr effect, and two-photon absorption can all be attributed to this optical nonlinearity. There has been a great deal of research directed to investigating these phenomena in various materials and in pursuing their application. The nonlinear intensity index of refraction n_2 and the two-photon absorption coefficient β are normally used to quantitatively characterize these kinds of self-action nonlinear optical behavior. Many experimental techniques have been developed to measure the magnitude and dynamics of third order nonlinearities. Two most commonly

used methods are Degenerate Four Wave Mixing (DFWM) and beam distortion measurements (Z-scan). DFWM directly measures the third order nonlinear susceptibility and usually involve a complicated experimental set up. The Z-scan method utilizes the self-focusing effects of the propagation beam to measure the nonlinear refractive index. The most commonly used method to extract β, is the nonlinear transmittance method which measures the transmittance of the laser medium as a function of the laser's intensity.

Among the many methods of measuring $\chi^{(3)}$, the Z-scan technique is the simplest and deserves the most attention. As stated above, the Z-scan technique is a simple and popular experimental technique to measure intensity dependent nonlinear susceptibilities of materials. Moreover, it is a highly sensitive single beam technique for measuring both non-linear refractive index and nonlinear absorption coefficients for a wide variety of materials. In this method, the sample is translated in the Z-direction along the axis of a focused Gaussian beam, and the far field intensity is measured as function of sample position. Analysis of the intensity versus sample position Z-scan curve, predicated on a local response, gives the real and imaginary parts of the third order susceptibility. In this technique the optical effects can be measured by translating a sample in and out of the focal region of an incident laser beam. Consequent increase and decrease in the maximum intensity incident on the sample produce wavefront distortions created by nonlinear optical effects in the sample being observed. Moving the sample along a well defined focused laser beam, and thereby varying the light intensity in the sample one obtains the z-scan. By varying the size of an aperture kept in front of the detector, one makes the z-scan transmittance more sensitive or less sensitive to either the real or imaginary parts of the nonlinear response of the material, i.e., nonlinear refractive index and nonlinear absorption, respectively. The z-scan method is an experimental way to obtain informations on nonlinear refractive index and nonlinear absorption properties of materials. With nonlinearity, here we simply mean the intensity dependent response of the material, which can be used to obtain an optical limiting device, either by nonlinear refraction or by nonlinear absorption such as TPA or three photon absorption.

The other widely used technique, degenerate four-wave mixing (DFWM), involves a far more complex experimental apparatus but provides several advantages. The fact that the setup includes temporal and spatial overlapping of three separate beams permits increased flexibility, such as the possibility of measuring different tensor components of $\chi^{(3)}$, and a straight forward study of temporal behavior.

When the Z scan was originally devised, it was used to characterize the nonlinear susceptibility of transparent bulk materials. Nevertheless, its use has now been extended to the study of a wide variety of samples. In particular, it is often used to study absorbing media. Among the latter, its use for the assessment of materials consisting of semiconductor or metal crystallites of nanometer size embedded in dielectric matrices has

been very common. These composites are currently the object of intensive research, their most direct application being related to their high third-order nonlinear susceptibility, $\chi^{(3)}$, which makes them promising candidates for the development of all-optical switching devices.

Z-scan is based on the principles of spatial beam distortion and offers simplicity as well as very high sensitivity. There are two types of Z-scan techniques, namely, the **'Closed aperture'** Z-scan and the **'Open aperture'** Z-scan.
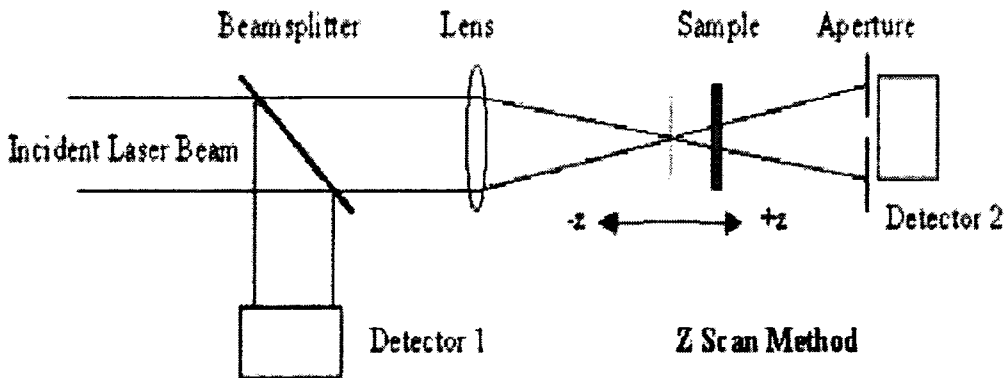
The Z-scan experimental setup

Fig. 1.1 Schematic of Z scan experimental set-up

In a typical experimental setup, a lens initially focuses a laser beam with a transverse Gaussian profile. The sample, the thickness of which is kept less than the Rayleigh range, is then moved along the axial direction of the focused beam in such a way that it moves away from the lens, passing through the focal point. At the focal point, the sample experiences the maximum pump intensity, which will progressively decrease in either direction of motion from the focus. A suitable light detector is placed in the far field and the transmitted intensity is measured as a function of the position of the sample, to obtain the open aperture Z-scan curve. Then an aperture of suitable S value is placed closely in front of the detector, and the experiment is repeated to obtain the closed aperture Z-scan. The absorptive nonlinearity is first determined from the open aperture data, and then the refractive nonlinearity is determined from the closed aperture data.
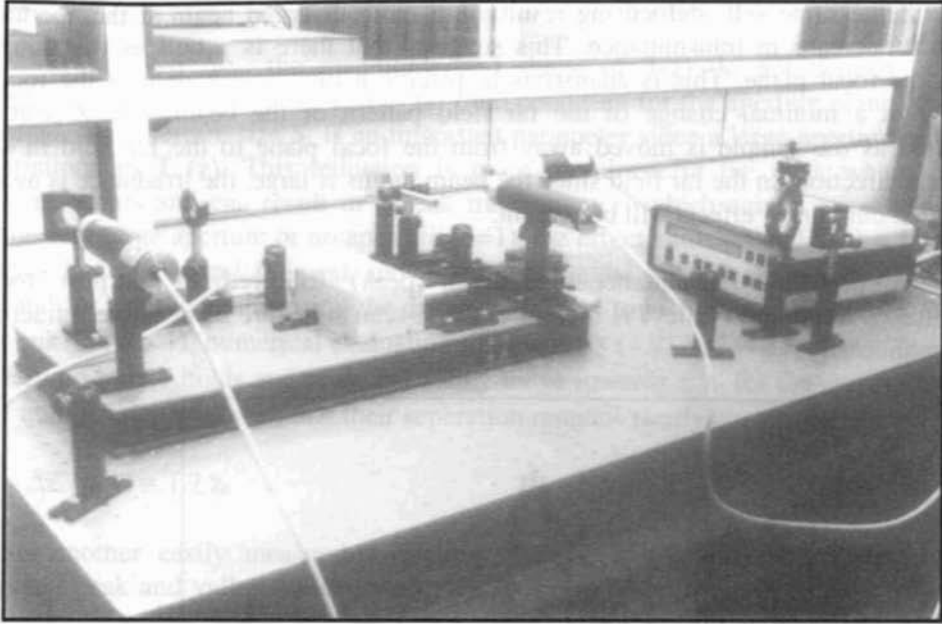
Fig. 1.2 A Photograph of the Z-scan experimental setup in the nanosecond laser pulses

Closed Aperture Z-Scan:

In this method, a single Gaussian beam in tight focus geometry is allowed to pass through a non-linear medium.The sample is moved along the z-direction so that it passes through the focal region of the beam. The transmitted beam is passed through an aperture placed in the far field, and then measured by the detector, for different values of sample position z. This method gives quantitative information on the non-linear refraction of the sample.

Assume, for example, a material with a negative non-linear refractive index and a thickness smaller than the diffraction length of the focused beam (a thin medium). This can be regarded as a thin lens of variable focal length. Starting the sample scan from a distance far away from the focus and close to the lens (negative z), the beam irradiance is low and negligible non-linear refraction occurs. Hence the transmittance (D_2/D_1) remains relatively constant. As the sample is brought closer to the focus, the beam irradiance increases, leading to self-lensing in the sample (As the sample is moved towards the focus, the intensity increase, since the width of the beam decreases towards the focus and the entire energy concentrates into a small area.). A negative self-lensing prior to focus will tend to collimate the beam, causing a beam narrowing at the aperture, which results in an increase in the measured transmittance. When the sample passes the focal plane to

positive z, the same self -defocusing results in a more diverged beam at the aperture, causing a decrease in transmittance. This suggests that there is a null as the sample crosses the focal plane. This is analogous to placing a thin lens at or near the focus, resulting in a minimal change of the far field pattern of the beam. The Z-scan is completed as the sample is moved away from the focal plane to the far field in the positive z direction. In the far field since the beam radius is large, the irradiance is again low so that only linear effects will be present.

A prefocal transmittance maximum (peak) followed by a post focal transmittance minimum (valley) is therefore, the Z-scan signature of negative refractive index nonlinearity.
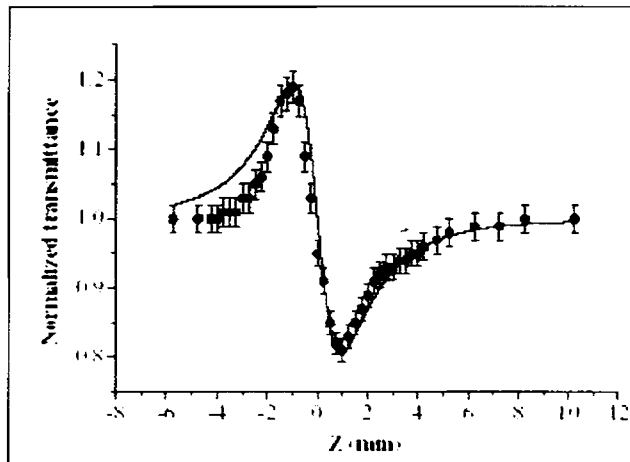

Fig. 1.3 A typical closed aperture z- scan curve

Positive nonlinear refraction, following the same analogy, gives rise to the opposite valley-peak configuration. It should be noted here that the sensitivity to nonlinear refraction is due to the presence of the aperture, and removal of the aperture will completely eliminate the effect. Thus an extremely useful feature of the Z-scan method is that the sign of the nonlinear index is immediately obvious from the data. Furthermore, its magnitude can also be readily estimated using a simple analysis for a thin medium. For a transparent nonlinear medium, the Z-scan curve will be symmetrical about the z = 0 point. However, if absorptive non-linearities are present, the symmetry will be lost. For example, multiphoton absorption will suppress the peak and enhance the valley, while saturable absorption leads to the opposite effect.

232

For a given $\Delta\phi_0$, the magnitude and shape of T(z) do not depend on the wavelength or geometry as long as the far field condition for the aperture plane ($d \gg z_0$) is satisfied. The aperture size S, is an important parameter since a large aperture reduces the variations in T (z). This reduction is more prominent in the peak where beam narrowing occurs and can result in a peak transmittance, which cannot exceed (1- S). Thus for very large aperture or no aperture (S=1), the effect vanishes and T(z) = 1 for all z and $\Delta\phi_0$. For small $|\Delta\phi_0|$, the peak and valley occur at the same distance with respect to focus, and for a cubic nonlinearity, the distance is found to be 0.86 z_0. With larger phase distortions ($|\Delta\phi_0| > 1$), numerical evaluation of equations (4.9) and (4.11) shows that this symmetry no longer holds and peak and valley move towards $\pm$ z for the corresponding sign of nonlinearity($\pm\phi_0$) such that their separation remains nearly constant given by,

$$\Delta Z \, (p, v) \cong 1.7 \, z_0 \qquad\qquad 10.1$$

There is another easily measurable quantity, $\Delta T_{(p,v)}$, is the difference between the normalized peak and valley transmittance: T_p-T_v. For a given order of nonlinearity, the curves $\Delta T_{(p,v)}$ versus $|\Delta\phi_0|$ exhibits universality, i.e., they are independent if laser wavelength, geometry(as long as the far field condition is met) and the sign of nonlinearity.For all aperture sizes, the variation of $\Delta T_{(p,v)}$ is found almost linearly dependent on $|\Delta\phi_0|$ as given by the equation,

$$\Delta T_{(p,v)} \approx 0.406 \, (1\text{-S})^{\,0.25} \, |\Delta\phi_0| \,, \qquad \text{for } |\Delta\phi_0| \leq \pi \qquad 10.2$$

which can be used to estimate the non-linear refractive index. If the experimental apparatus and the data acquisition system are capable of resolving transmittance changes of $\Delta T_{(p,v)} \cong 1 \, \%$, then a phase change corresponding to a wavefront distortion as low as λ/250 can be measured. Achieving such sensitivity, however, requires relatively good optical quality of the sample under study.

These equations were obtained based on a cubic nonlinearity (i.e. a $\chi^{(3)}$ effect). A similar analysis can be performed for higher order nonlinearities. Regardless of the order of nonlinearity, the same qualitative features are to be expected from the Z-scan analysis. For a fifth order effect, assuming a thin sample and using the GD approach, the peak and valley are found to be separated by $\cong$1.2 z_0 as compared to 1.7 z_0 obtained for the third order effect.

Open Aperture Z-scan:

Large refractive nonlinearities in materials are commonly associated with a resonant transition, which may be of single, or multiphoton nature. The non-linear absorption in such materials arising from either direct multiphoton absorption, saturation of the single photon absorption, or dynamic free carrier absorption have strong effects on the measurements of non linear refraction using the Z-scan technique. Clearly, even with nonlinear absorption, a Z-scan with a fully opened aperture (S=1) is insensitive to non-linear refraction.

In the Open Aperture Z-scan Technique, the sample transmission for different z values is measured as before, but the aperture is removed from the set up. The absorptive non-linearity will be a maximum at the focal plane. For example, in the case of two-photon absorption, the transmittance will be a minimum and in the case of saturable absorption, the transmittance will be a maximum. The open aperture Z-scan curve is symmetrical about the focus (z=0).
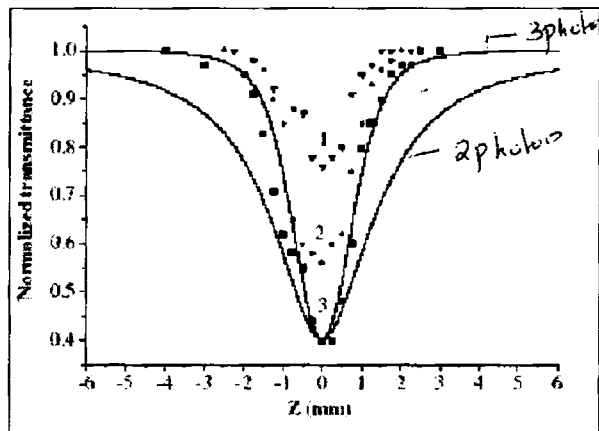

Fig 1.4 Open aperture z- scan at different intensities ((1). 2.2×10^{11}W/cm^2 ,(2).3.2×10^{11}W/cm^{-2}., (3).4×10^{11}W/cm^{-2}.). Dashed line is a theoretical fit for two photon absorption and solid line is a theoretical fit for the three-photon absorption at the intensity of 4×10^{11}W/cm^{-2}.

Although this method has several advantages, disadvantages of this technique include the fact that it requires a high quality Gaussian TEM$_{00}$ beams for absolute measurement. The analysis must be different if beam is non-Gaussian. Sample distortions or wedges, or a tilting of the sample during translation can cause the beam to walk off the far field aperture. This produces unwanted fluctuations in the detected signal. Even if these are kept under control, beam energy jitter will produce the same effect. A second reference arm may be employed to subtract out the effects of beam jitter.

234

10.2 Experimental techniques

Synthesis

Precursor fine particles of magnetite were synthesized by cold co-precipitation from the aqueous solutions of $FeSO_4 \, 7H_2O$ and $FeCl_3$ taken in the molar ratio 1 M and 2 M respectively. The exact preparation details have been explained in the chapter Experimental Techniques. Stability criteria are explained in chapter 2, theoretical Concepts.

Characterization

X-ray diffraction patterns of the dried precursor samples and that of the ferrofluid were recorded in an X-ray diffractometer (Rigaku D max-C) using Cu Kα radiation (λ=1.5406 Å), and planes were identified using the JCPDS tables [23]. The X ray diffraction spectrum of the magnetite ferrofluids is depicted in figure 1. The average particle sizes of these powder samples were estimated from the Debye Scherrer's formula

$$D = \frac{0.9\lambda}{\beta \cos \theta} \qquad\qquad 10.3$$

where λ is wave length of X-ray used, β is the FWHM of the XRD peak with the highest intensity, and D is the particle diameter.

10.3 Results and discussions

From the measured line broadening the particle size is calculated to be around 90Å, and the planes are identified. The lattice parameter 'a' has been evaluated assuming cubic symmetry, and its value is found to be 8.314 Å.

The optical absorption spectrum of the magnetite-based ferrofluids is shown in Fig. 2.2. The absorbance gradually decreases through the visible, towards the IR region. A weak absorption band can be seen around 490 nm. In order to calculate the band gap (assuming direct band gap), it may be noted that for a semiconductor, the absorption coefficient near the band edge is given by

$$\alpha = \frac{A(h\nu - E_g)^{1/2}}{h\nu} \qquad\qquad 10.4$$
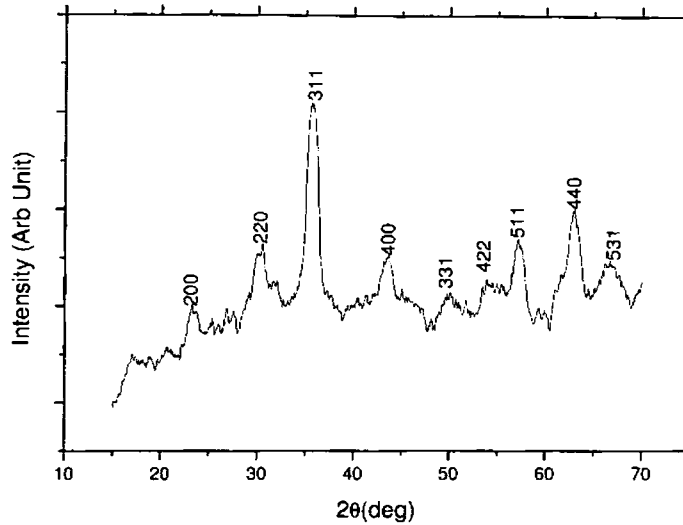
Fig .2.1. X Ray Diffraction Spectrum of magnetite ferrofluids.

where A is a constant and E_g is the energy band gap. When $\alpha h\nu = 0$, $E_g = h\nu$, and therefore, using an extrapolation the energy bandgap is determined to be 3.1 eV (Details in chapter9).
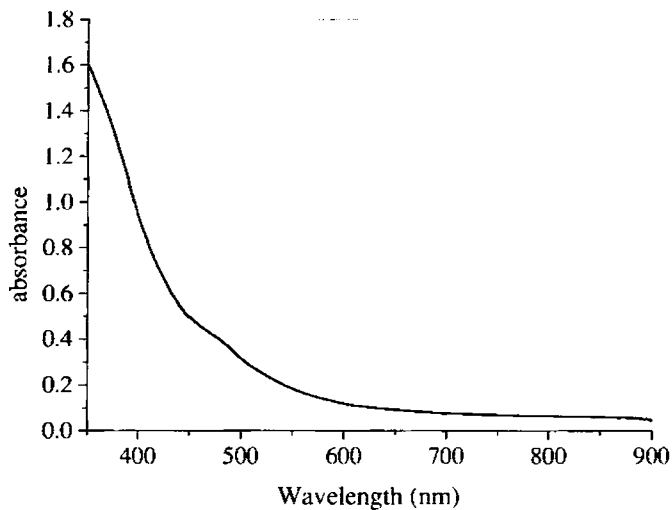

Fig.2.2: Linear absorption spectrum of the ferrofluid sample FF1.

Non Linear Optical Studies

Non linear optical measurements were carried out using laser pulses of 7 ns as well as 100 fs durations (FWHM). Nanosecond pulses at 532 nm were obtained from a frequency-doubled Nd:YAG laser, while femtosecond pulses at 800 and 400 nm were obtained from a Ti:Sapphire CPA laser (TSA-10, Spectra Physics) equipped with a harmonic generator. Samples were taken in a 1 mm cuvette. The laser pulses were plane polarized with a Gaussian spatial profile. The intensity dependent light transmission through the sample was measured using an automated z-scan set-up. In the z-scan technique, the laser beam is focused using a lens, and the sample is moved along the beam axis (z-axis) from one side of the focus to the other, through the focal point. At each position z, the sample sees a different laser fluence, and the fluence will be a maximum at the focal point (where z is taken as zero). An energy meter placed after the sample measures the position dependent (ie, fluence-dependent) transmission through the sample [24]. In our experiment we added another detector, which is a photo multiplier tube (PMT), to record scattered radiation from the sample. The PMT is kept at a radial distance of 5 cm from the beam axis. Both the PMT and the cuvette are mounted on the same translation stage, so that they remain at the same relative distance throughout the scan.

For all the three wavelengths used, the samples show a minimum transmission around the beam focus, showing that the nonlinearity is of the optical limiting type. In general, optical limiting in media can arise from different types of processes like nonlinear refraction, two-photon absorption, excited state absorption and induced light scattering. Two-photon absorption is an intensity dependent process, in which two photons of the exciting radiation are absorbed simultaneously. On the other hand, excited state absorption is a sequential process in which an absorbed photon initially raises the molecule to an excited state of finite lifetime, from where it absorbs one more photon to reach a terminal level. In the case of induced light scattering, in transparent media it is usually caused by the microplasma formed due to laser-induced dielectric breakdown. In absorbing colloidal suspensions it can be of thermal origin as well. Here the particles absorb laser light and heat the liquid so that the local temperature exceeds the ambient temperature, resulting in transient refractive index changes. If the temperature exceeds the liquid's boiling point, microbubbles also will be generated. As a result of these, light will get scattered at high input fluences. Such induced scattering contributes to optical limiting in a number of materials, including carbon black [25] and carbon nanotube [26] suspensions, and metal nanoparticles [27,28]. The PMT kept off-axis in our z-scan experiment monitors the normal as well as induced scattering from the sample.

The causes of limiting being so diverse, we have studied the samples at two different concentrations, in addition to the pure base fluid. Samples having linear

transmissions of 0.5 and 0.75 at the respective wavelengths are employed for all measurements. When excited with low energy nanosecond pulses, the base fluid kerosene shows very little limiting and the ferrofluid suspensions show a moderate limiting behaviour (Fig. 2.4).

Pure kerosene exhibits weak two-photon absorption, and the two-photon absorption coefficient β is calculated to be equal to 5 x 10^{-12} m/W from numerical fits to the experimental data. However, data from the samples seem to fit to a three-photon absorption process, given by the equation [21]

$$T = \frac{(1-R)^2 \exp(-\alpha L)}{\sqrt{\pi} p_0} \int_{-\infty}^{+\infty} \ln\left[\sqrt{1 + p_0^2 \exp(-2t^2)} + p_0 \exp(-t^2) \right] dt \qquad 10.5$$

where $p_0 = [2\gamma(1-R)^2 I_0^2 L_{eff}]^{1/2}$. Here T is the transmittance, R is the Fresnel reflection coefficient at the sample-air interface, α is the absorption coefficient, L is the sample length, and I_0 is the peak on-axis intensity incident on the sample.
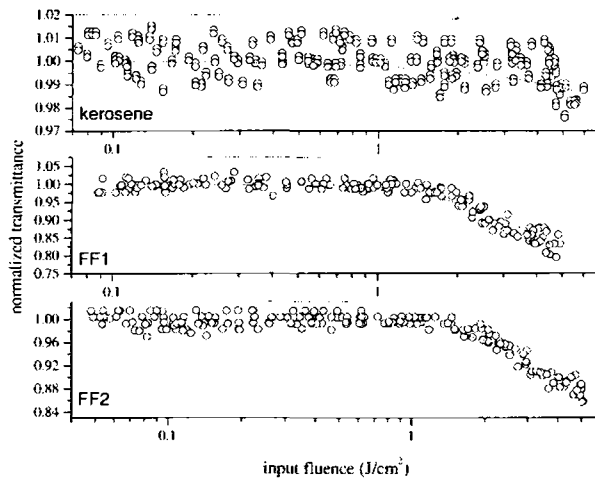

Fig. 2.4: Fluence dependent transmission of the base fluid and the samples at 7ns laser pulse excitation. Excitation wavelength is 532 nm, and the maximum laser fluenceused is 6 J/cm². The linear transmissions of FF1 and FF2 are equal to 0.5. Kerosene is transparent at this wavelength. Circles denote experimental data, and the solid curves are theoretical fits (see text).
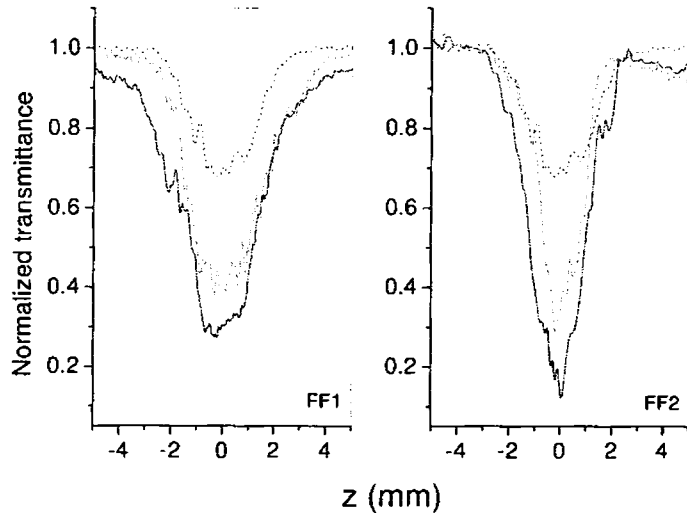
238

Fig. 2.5: Concentration dependence of the Z-scans obtained for the ferrofluid samples at 7ns laser pulse excitation. Excitation wavelength is 532 nm. Laser fluence is approximately 20 J/cm^2 at z=0. Sample linear transmissions are, Solid line – 0.5, and Dashed line – 0.75. Dotted line – pure kerosene.

L_{eff} is given by $[1-exp(-2\alpha L)]/2\alpha$. The three-photon absorption coefficients γ are found to be 7.5 x $10^{-23}m^3/W^2$ and 5 x $10^{-23}m^3/W^2$ respectively, for FF1 and FF2. The above values of β and γ are applicable in the limit of moderate laser excitation, at the specified concentrations. As seen from Fig.5, at higher fluences a stronger, concentration dependent limiting effect is observed.

Fig. 2.6 shows the Z scan curves obtained with femtosecond pulses, for the excitation wavelength of 800 nm.

Limiting in the base fluid is substantially increased, though it is less than that exhibited by the samples. However, when the excitation wavelength is changed to 400 nm, there is practically no difference between the limiting efficiency of the pure base fluid and the ferrofluid suspensions (Fig.2.7).

Fig. 2.6: Z scan curves obtained for the ferrofluid samples at 100 fs, 800 nm laser pulse excitation. Sample linear transmissions are, Solid line – 0.5, and Dashed line – 0.75. Dotted line – pure kerosene.
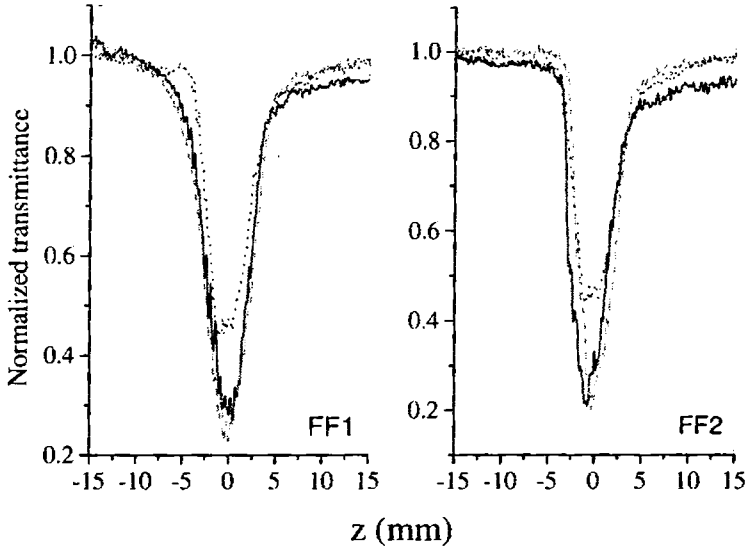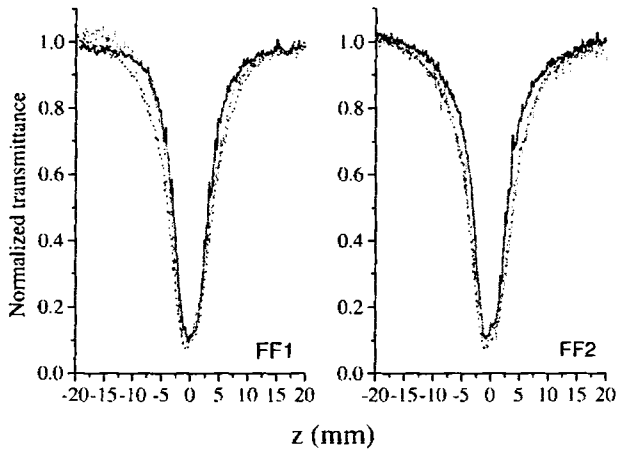

Fig. 2.7: Z scan curves obtained for the ferrofluid samples at 100 fs, 400 nm laser pulse excitation. Sample linear transmissions are, Solid line – 0.5,
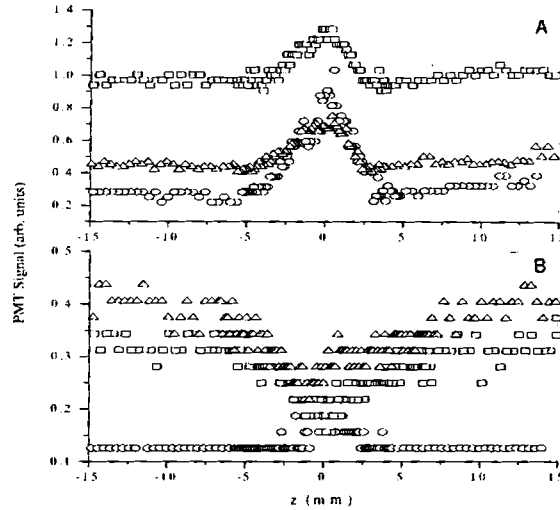
Dashed line – 0.75. Dotted line – pure kerosene.

Fig. 2.8: Signals obtained from the PMT detector, kept off-axis in the z-scan experiment. Plot A is for nanosecond excitation (532 nm) and plot B for femtosecond excitation (400 nm). Circles denote pure base fluid (kerosene), squares are for FF1, and triangles for FF2. Both FF1 and FF2 have a linear transmission of 0.5.

Fig. 2.8 gives the signals recorded by the PMT as a function of the sample position z. When the sample is away from the beam focus a background scattering can be seen, which is a minimum for pure kerosene and more for the ferrofluid suspensions.

In the nanosecond regime the signal amplitude goes up near the beam focus, indicating the occurrence of induced scattering. In the pure base fluid this may be caused by the microplasma, whereas in the samples it can also be of the thermal origin. The thermally induced transient refractive index change is given by

$$\Delta n_0 = (dn_0/dt)F_0\alpha/2\rho C_v \qquad\qquad 10.6$$

where dn_0/dt is the thermo-optic coefficient, F_0 is the laser fluence, ρ is the density and C_v is specific heat at constant volume. The induced scattering amplitude is found to be the highest in the base fluid, and lesser in the suspensions, even though optical limiting in the suspensions is substantially higher than that seen in the base fluid (Fig. 2.5). Therefore nanosecond optical limiting in the ferrofluids cannot be fully accounted for by induced scattering. Moreover, numerical fitting to the data (Fig. 2.4) shows that in the samples an

241

effective fifth order nonlinearity is manifested even at relatively lower pump fluences. Since there are no compelling reasons for a higher order process like three-photon absorption to be dominant in these systems, what is more likely is that there are sequential excited state absorption events, in which free carriers take an active part. The collective effect of such events will appear in the form of higher order processes. For example, a $\chi^{(5)}$ nonlinearity of the $\chi^{(3)}:\chi^{(1)}$ type has been observed in semiconductors [30]. For metal nanoparticles, photoexcitation of free carriers has been discussed previously by Kamat et.al.[18], and the role of free carriers in enhancing their nonlinear absorption also has been discussed [31]. Recently we have observed the same behaviour in molecular metal clusters as well [results to be published].

In the femtosecond excitation case the PMT signal behaves differently, as the ultrashort pulse is too fast to register any thermal scattering events. Some induced scattering is observed in the base fluid, but the suspensions do not show any nonlinear increase in the scattering level. In fact at the highest intensities, rather a decrease in the signal level is observed. The reason for this decrease is not well understood now, but it clearly shows that induced scattering does not contribute to femtosecond optical liming under the present experimental conditions. Considering the very short timescale and the high intensities involved, instantaneous nonlinearities like two-photon and multiphoton absorption should be responsible for the limiting. As seen from Fig.2.7 limiting is the best in the pure base fluid, and the addition of the ferrofluid does not improve the inherent optical limiting of kerosene in the femtosecond regime.

10.4 Conclusions

Magnetite based ferrofluids synthesized by co-precipitation technique with oleic acid as the surfactant and kerosene as the carrier, are characterized by optical absorption and X ray diffraction measurements. The absorptive nonlinearities have been studied, and the wavelength, fluence, concentration and pulse width dependence of the nonlinear transmission have been investigated. Results indicate that induced scattering and excited state absorption contribute to the observed optical limiting in the nanosecond excitation regime. On the other hand, in the femtosecond regime, pure electronic effects are responsible for the limiting. Due to their good thermal stability, resistance against agglomeration and long shelf life, ferrofluids will be potential candidates for optical limiting applications.

References

1. Ronald .E. Rosenweig , *Ferro hydrodynamics*, Cambridge University Press 1985
2. Berkovsky B.M, Medvedev V.S., Krakov M.S., *Magnetic fluids; Engineering applications*, Oxford university press. 1993
3. R.K Bhat, *Indian J. Eng. Mater. Scie.* 5, (Dec 1998), 477.

4. J. Smit and H.P.G Wijn, *Ferrites* (Philips Technical Library) 1959
5. J.Deperiot, G. J Da Silva C.R Alves *Brazilian J. of Phys.* 31, No 3 (Sept 2001), 390
6. E. Hasmonay, J Depeyrot, *J. Appl.Phys.* **88**, No 11 (Dec. 2000), 6628.
7. G. M Sutharia and R.V Upadhyaya *Indian J. Eng. Mater.Scie.* **5**, (Dec 1998), 347.
8. K.T. Wu, P.C. Kuo, Y.D. Yao and E.H Tsai, *IEEE trans. Magn*, **37** No.4, (2001). 2651.
9. Helen W.Davies and Patrick Llewellian, *J. Phys. D, Appl. Phys*, **12**, 1979, 1357.
10. S Couris, E. Koudoumas, A A Ruth and S. Leach, *J.Phys.B, At.Mol.Opt.Phys.* **28** (1995) 4537.
11. Tutt L W and Kost A *Nature* **356** (1992),225
12. kost A Tutt L W, Klein M B Dougherty T K, and Elias W, *Opt. Lett*, **18** (1993) 334.
13. Mc Lean D. G, Sutherland R L, Brant M.C, Brandelik D M, Fleitz P A and Pottenger T, *Opt Lett*, **18** (1993) 858.
14. Lin F, Zhao J, Luo T, Jiang M, Wu Z, Xie Y, Qian Q and Zeng H *J. Appl. Phys*, **74** (1993) 2140.
15. Justus B L, Kafafi Z H, and Huston A L, *Opt. Lett*, **18** (1993) 1603.
16. R.Philip, G.Ravindra Kumar, N.Sandhyarani, T.Pradeep, *Phys.Rev.B.* **62** (2000) 13160
17. S.Link, C.Burda, Z.L.Wang, M.A.El-Sayed, *J.Chem.Phys.* **111** (1999) 1255
18. P.V.Kamat, M.Flumiani, G.V.Hartland, *J.Phys.Chem.B.* **102** (1998) 3123
19. C.Zhan, D.Li, D.Zhang, W.Xu, Y.Nie and D.Zhu, *Opt.Mat.* **26** (2004) 11
20. K.S.Bindra, S.M.Oak and K.C.Rustagi, *Opt.Commun.* **124** (1996) 452
21. H.P.Li, C.H.Kam, Y.L.Lam, and W.Ji, *Opt.Commun.* **190** (2001) 351
22. A.A.Said, M.Sheik Bahae, D.J.hagan, T.H.Wei, J.Wang, J.Young, and E.W.Van Stryland, *J.Opt.Soc.Am.B.* **9** (1992) 405
23. JCPDS-ICDD C 1990 10-319
24. M. Sheik Bahae, A. A Said and Van Stryland, *Opt. Lett.* **14**, (1989) 955
25. L. W. Tutt, T. F. Boggess, *Prog.Quant.Electron.* **17** (1993) 299
26. S. R. Mishra, H. S. Rawat, S. C. Mehendale, K. C. Rustagi, A. K. Sood, R. Bandopadhyay, A. Govindaraj, C. N. R. Rao, *Chem.Phys.Lett.* **317** (2000) 510
27. L.Francois, M.Mostafavi, J.Belloni, J.F.Delouis, J.Delaire, P.Feneyrou, *J. Phys.Chem.B.* **104** (2000) 6133
28. Anija M., Jinto Thomas, Navinder Singh, Sreekumaran Nair, Pradeep T. and Reji Philip, *Chem. Phys. Lett.* **380**, 223 (2003)
29. *Handbook of Nonlinear Optics*, by R.L.Sutherland, Marcel Dekker (NY) 1996
30. M. Sheik Bahae, A. A Said and Van Stryland, *IEEE J.Quant.Electron.*
31. C.Zhan, D.Li, D.Zhang, W.Xu, Y.Nie and D.Zhu, *Optical Materials* **26** (2004) 11

CHAPTER 11
Conclusion

With the emergence of nanotechnology, physics at the surface of materials is increasingly becoming complex. In magnetism and nanomagnetic materials it is the surface magnetism and surface spins which is playing a dominant role in determining the overall magnetism exhibited by these materials. Quantum mechanics plays a lead role in understanding the surface physics of magnetic materials and new phenomenon like quantum tunneling, quantum magnetization, spin polarized tunneling and superparamagnetism are some among them. Understanding these phenomena on the nanolevel leads to tailoring the properties of materials.

From a fundamental point of view, many surface phenomena are not well understood and investigations on materials are a perennial activity in the realm of material science. As far as material scientists are concerned understanding the nanophysics of these magnetic materials is synonymous with manipulating material properties for various applications.

Material scientists are equally aware of the deleterious effects of high surface area in the sense that large surface area leads to high surface activity and hence some of the useful properties are invariably lost. So the task before physicists is to advantageously employ the quantum size effects for making better materials for various applications. The need for arresting the surface activity by passivation and capping is a rich area in Physics. The last decade witnessed an unprecedented research activity in this regime. This has further fuelled multidisciplinary activity involving physicists, chemists, material scientists and engineers. The fruits of these research activities are slowly emerging and new materials like Diluted Magnetic Semiconductors, negative refractive index material, Magnetic Fluids are born. New products based on giant magnetoresistance, spintronics and others have started hitting the markets.

Though ferrofluids were invented in the 1960's the potential of these materials in realizing various applications have gained momentum only now and a host of devices are conceived based on magnetic fluids. The importance of magnetic nanocomposites as well as ferrofluids is that they are ideal templates for studying magnetism at the nanolevel, which assumes high priority.

This investigation presented in this thesis is such an attempt in delving in to the physics of materials at the nanolevel and to suggest newer applications of nano magnetic materials. Some of the important inferences drawn out of this investigation are listed in this chapter. The scope for further work and the need for rectifying some of the lacunae in this study are also dealt with.

Magnetic nanomaterials with in the grain size limit 100Å serves as ideal templates to study the quantum size effects on their structural and magnetic properties. If

such nanoparticles could be synthesized with in the Bohr radius limit of the material their band structure as well as optical properties could be greatly modified by grain size dependant quantum confinement effects.

Magnetic nanocomposites are composite materials in which the fine particles are magnetic materials. It was possible to synthesize nanocomposites based on sulphonated polystyrene and gamma ferric oxide by a simple process of ion exchange. Normally *insitu* chemical synthesis of nanocomposites does not yield the required magnetisation and the process of cycling was successfully employed to increase the net magnetisation of the composite. The pores present in the matrix determine the size of the particle and this provides a natural capping for the material which is trapped inside the pores. the pores size limit the nucleation and the growth process and the pore density determines the net saturation magnetisation of the composite. In this investigation a magnetic composite with a near theoretical limit of ~16emu/g was achieved by employing this novel synthesis technique.

The incorporation of maghemite in the polystyrene matrix often results in superparamagnetic particles and hence control of coercivity of these particles is often not possible. It was thought that since γFe_2O_3 is a vacancy ordered spinel and cobalt being a octahedral site cation, it was doped *insitu* into the γFe_2O_3 lattice. The coercivity as well as the saturation magnetisation could be manipulated by cobalt incorporation.

For this, the method of ion exchange was modified and the procedure for the precipitation of maghemite nanocomposite was standardised and optimised. The magnetization can be increased by cycling process in which more vacant sites in the polymer matrix can be made to occupy the vacancies. A pristine superparamagnetic composite was imparted a coercivity of 30 Oe via this preparation route. Turning of coercivity was possible by varying the dopant concentration of cobalt.

The optical characterization was carried out by the absorption spectroscopy with a view to studying the quantum confinement effects as well as to investigate in detail the nature of confinement that is responsible for its peculiar behaviour.

Optical properties of nanomagnetic materials is another interesting area and tuning of the transparency of magnetic material by finite size effect materials was adopted. An in depth study in to the tuning of band gap was carried out and it was found that the bandgap of these composites could be tuned. Evidence for blue shifts was extracted through these investigations.

It was found that absorption edge of ultra fine γ-Fe_2O_3-polystyrene magnetic nanocomposites synthesized by chemical route was blue shifted by an amount of 0.64eV due to weak exciton confinement. Strong confinement can result in a theoretical blue shift of around 1.45eV (in a quantum dot like confinement); but that may reduce the magnetic properties because of the grain size reduction to an order of 10-20 Å and thus not favoured under application point of view. Thus transparent magnetic nanocomposites (in

the visible range) could be synthesized by size reduction of the order of the Bohr radius limits, which can throw open a wide field with versatile application potential. Also tuning of optical bandgap was reported for the first time in these magnetic nanocomposites by doping with Co and the spectrum gets red shifted more and more with increased doping and finally gets saturated due to the formation of a complete dopant level in the intermediate stage.

Scope exists for the synthesis of ultra fine magnetic materials in any porous network by this route with an ion exchange resin. Also by controlled oxidation, magnetic materials like CrO_2 which are hard to synthesize under normal conditions can be attempted by appropriate modification of this synthesis route.

Synthesis of metal nanoparticles especially of a material with high c/a ratio is rather difficult because of their high surface activity due to the enhanced surface area when synthesized at the nanolevel. Due to its inherent magneto-crystalline anisotropy, cobalt like metals even in its ultrafine form possess moderate to high coercivity. Also their optical as well as electrical properties are remarkably modified if their grain size could be reduced below 50Å.

High surface area, self protected elementary cobalt nanoparticles could be successfully synthesized inside the natural pores of polystyrene by a novel simple, cost effective reduction process. They are impurity free except for the shell formation of cobalt oxide at the surface. The magnetization and coercivity could be enhanced by repeating the precipitation cycles by opening more and more inner pores. Initial reactions are centered at the surface thereby reducing the yield due to surface oxidation. By repeating the precipitation cycles, inner pores are exposed and the yield of metal nanoparticles is enhanced. Also the synthesis of high surface area cobalt by a simple technique by growing them inside the natural pores of polymers can throw a new area of applications including their catalytic application for the synthesis of carbon nanotubes. Scope exists for further modification of the synthesis technique to obtain a more pure self protected nanometal magnet with slightly modifying the experimental parameters with the addition of $NaBH_4$ in excess with a provisions to provide a nitrogen atmosphere for controlling the oxidation process.

Scope for further work exists in synthesizing magnetic metal nanoparticles with cubic structure like Fe and Ni inside any porous material by the same method. They are assumed to be in superparamagnetic state with zero coercivity and hysteresis. Evaluation of their optical properties probed through optical absorption and photoluminescence spectroscopy, will throw light on the exact nature of quantum confinement effects. As the pore diameter is the limiting factor in the determination of the particle diameter, molecular sieves with pore diameters of the order of 10Å-20Å can be employed as templates for the synthesis of ultra fine magnetic metal powders which could be self protected inside the sieves. This can be ideal systems for studying the structure,

microstructure, magnetism and optics especially strong quantum confinement effects at these dot dimensions.

Ferrofluids were synthesized by various routes and the synthesis conditions are optimized with careful control over the grain size and size distribution. Carrier fluid as well as surfactant could be exchanged by reversible as well as irreversible flocculation techniques. Their structural, as well as microstructural characterization have been carried out by employing techniques like X Ray diffraction, transmission electron microscopy, electron diffraction, and atomic force microscopy. These studied confirms that their grain sizes lie well with in 80Å.

Complex behaviour was observed in the field induced laser transmission through ferrofluid thin films belonging to the series $Ni_xFe_{1-x}Fe_2O_4$. The diffracted light intensity is increased by the application of the magnetic field while the intensity of the central spot decreases. The output intensity of the central spot decreases in a linear manner till the saturation occurs in the cluster formation and this saturation field is dependent on the saturation magnetization (M_s) value of the ferrite powder precursors used for the ferrofluid synthesis. Tuning of the maximum sensing capability of these films can be achieved by controlling the 'x' values in the series $Ni_xFe_{1-x}Fe_2O_4$.

A full fledged magneto-optical laboratory was set up for the evaluation of dichroism, birefringence, and faraday rotation. The same set up can now be upgraded for studying magneto optical Kerr rotation (MOKE) in thin films and liquid films. The magneto-optical characterization of the ferrofluid samples synthesized by both routes show that the assumption of a "system of identical spherical particles" fails in the case of fluids synthesized with high energy ball milling of the fine particle precursors. Thus size and shape anisotropy enhancement occurred by the ball milling process increases the birefringent signal which confirms our earlier assumption of inducing the formation of oblate particles and thereby enhanced magneto-optical signals. The low and high energy limits of the birefringence are discussed indicating their quadratic dependence on M_s (saturation magnetization), H (magnetic field) and V (particle volume) at lower applied field. The birefringent measurements on chemically synthesized samples were satisfactorily fitted to the standard second Langevin function for monomer fit which hints towards to the spherical non aggregates. The ball milled ferrofluids shows anomalous behaviour and the birefringence is enhanced by an order and the fit for dimer in the standard Langevin fit is good for the milled ferrofluid samples. This large enhancement in birefringence signal with high energy ball milling can find enormous application potential. Thus birefringence can be employed as tool to gauge the quality of the ferrofluids.

Dielectric properties measured in the MHz as well as GHz regime show that dielectric constant increases with concentration in a normal way in low concentrations. But the permittivity values are very high for highly concentrated samples. Here the

248

concept of Brown like particles are no more found to be valid, and their behaviour could be fitted for Neel like particles. They are good microwave absorbers and can be used as a microwave absorbing lubricant in electromagnetic circuits and mobile phones which is quite important and the property that could be exploited in the coming century. Their magnetic field induced capacitance change measured is an added evidence for Neel like particles whose free rotation and oblation in applied magnetic field make the capacitance values magnetic field sensitive.

Careful control of grain size, the co-precipitation parameters like pH and temperature ensured the synthesis of smallest possible magnetic grains. *Insitu* capping by the surfactant oleic acid prevents further grain growth. Their optical absorption spectrum shows a high blue shift of 0.81 eV in band gap due to quantum confinement effects which are higher than that in the weak regime. Strong confinement needs still lower grain size which may reduce magnetization and not favored under application point of view. Addition of nickel with varying percentage on the magnetite lattice still reduces the band gap by the alloying effect, which results in a blue shift higher than that in the weak confinement regime. The blue shift varies almost as the square inverse of the nanocrystallite's grain size, but additional blue shift can be attributed to the alloying effect of nickel which introduces lattice contraction which is evidenced by the XRD studies. This enhanced blue shift in optical band gap by nickel alloying will enable us to obtain ferrofluids having a better transparency which can find potential applications.

The absorptive nonlinearities have been studied, and the wavelength, fluence, concentration and pulse width dependence of the nonlinear transmission have been investigated. Results indicate that induced scattering and excited state absorption contribute to the observed optical limiting in the nanosecond excitation regime. On the other hand, in the femtosecond regime, pure electronic effects are responsible for the limiting. Multiphoton absorption processes with a small accumulative non linearity is found to be responsible for their high optical limiting. Due to their good thermal stability, resistance against agglomeration and long shelf life, ferrofluids will be potential candidates for optical limiting applications.

As far as the potential applications of these nanocomposites are concerned they can serve as good candidate for magnetic refrigeration applications. If the same *insitu* method of incorporation of guest nanoparticles in a host matrix can be modified, thin films based on nylon and metal nanoparticles could be made. Ferrofluidic thin films can be tried as field induced gratings. Stable ferrofluidic thin films can also be used as a magnetic resonator in microwave circuits.

Most of the envisaged objectives of these investigations could be fructified. However, there is still enough room at the bottom which is unexplored and that needs to be illuminated. Hypotheses become theories and with the passage of time theories

become obsolete. Materials turn outdated and so the road to tomorrow is always full of further opportunities. Here too, there are gaps and these gaps are to be plugged. There exists ample scope for further investigations in understanding the material physics at the nanolevel.

As the old saying goes, "change is something which remains constant in the universe and here too, constants of new changes are necessary for delving more and more about less and less".

Annexure1-Publications

1. Effect of Cobalt Doping on The Magnetic Properties of Superparamagnetic γ-Fe_2O_3 - Polystyrene Nanocomposites, *Swapna.S.Nair*, Mercy Mathews, P.A. Joy[s], S. D Kulkarni and M.R. Anantharaman, Journal of magnetism and magnetic materials, **283,** (2004) 344

2. Magnetic field induced assembling of nanoparticles in ferrofluidic liquid thin films based on $Ni_xFe_{1-x}Fe_2O_4$, V.S. Abraham, *S. Swapna Nair*, S. Rajesh, U.S Sajeev and M.R Anantharaman, Bull. Mater. Science, **27** (2), 2004, 165.

3. Evidence For Blue Shift By Weak Exciton Confinement And Tuning of Band gap In Superparamagnetic Nanocomposites, *Swapna S Nair*, Mercy Mathews And M.R Anantharaman, Chemical Physics Letters, 406 (2005) 398

4. Finite Size Effects On The Structural and Magnetic Properties Of Sol-Gel Synthesized $NiFe_2O_4$ Powders, M.George, A.M. John, *S. S. Nair*, P.A. Joy, M.R. Anantharaman , J. Magn. Magn. Mater, 302, **(2006)**190

5. Magnetic Field Induced Cluster Formation And Variation Of Magneto-Optical Signals In Zinc Substituted Ferrofluids *S.Swapna Nair*, S. Rajesh, V.S Abraham, and M.R Anantharaman, J.Magn.Magn.Mater, In Press.

6. Structural Magnetic and electrical properties Of Sol-Gel Synthesized $LiFe_2O_4$ fine particles, M.George, *Swapna.S.Nair*, A.M. John, P.A. Joy, M.R. Anantharaman , J. Phys.D: Apply.Phys, **39,** (2006) 900.

7. Magneto-Optical Properties of $Ni_xFe_{1-x}Fe_2O_4$ Ferrofluids, *Swapna S Nair*, Francis Xavier, M.R Anantharaman, Thin Solid Films, Under revision

8. Initial investigations on the SHI irradiation on the structural, magnetic and microstructural characterisation of $Fe_{40}Ni_{38}B_{18}Mo_4$ thin films, Hysen Thomas, *Swapna.S.Nair*, R.V.Ramanjunan, P.A Joy, D.K Awasti, M.R Anantharaman, Thin Solid Films, Under revision .

9. Effect of high energy ball milling on the birefringent signals of magnetite ferrofluids, *Swapna.S.Nair*, Francis Xavier, M.R Anantharaman J. Phys, Cond.matt. Under review

10. Alloying induced enhanced quantum confinement and blue shift in magnetite ferrofluids, *Swapna.S.Nair*, Francis Xavier, M.R Anantharaman, Appl. Phys. Lett, Under minor revision

Conference Papers

1. Magnetic And Optical Properties Of Nanocomposites Based On Gamma Ferric Oxide With And Without Cobalt , Mercy Mathews, *Swapna S Nair,* K A Malini, P A Joy, M R Anantharaman, International conference on Recent Advances in Inorganic materials, IIT Bombay, 11-13 Nov, 2002.

2. Optical studies on ferrofluidic thin films. S. *Swapna Nair, S.* Rajesh, V.S. Abraham, M.R. Anantharaman, Recent Advances in the Nanotechnology of ferrofluids, National Physical Laboratory, New Delhi, Dec. 22-24, 2002.

3. Structural and magnetic properties of thin films based on finemet alloys, M.R. Anantharaman, S. Deepa, *S. Swapna Nair,* P.A. Joy, and R.V Ramanujan, Materials processing for advanced applications, Singapore.

4. Modification of Magnetic and Electrical properties of $Ni_xFe_{1-x}Fe_2O_4$ by polymer surface coating, M.R. Anantharaman, P.A. Joy, *S. Swapna Nair,* U.S Sajeev and V. Sooraj. International conference in inorganic materials, Andwerp, Belgium.

5. Surface modification of magnetic nanoparticles by RF plasma polymerisation, V. Sooraj, U.S Sajeev, *S. Swapna Nair,* M.R.Anantharaman. National symposium on Instrumentation 28, Vallabhai University, Panth nagar, Utharanchal, Nov. 1-3, 2003.

6. Structural and magnetic properties of cobalt-polystyrene nanocomposites synthesized by chemical route, *Swapna. S. Nair,* P.A joy, and M.R Anantharaman, Materials Research Society Of India Symposium, National Chemical Laboratory Pune, Feb 9-11, 2005.

7. Magneto-Optical Properties of $Ni_xFe_{1-x}Fe_2O_4$ Ferrofluids, *Swapna S Nair,* Francis Xavier, M.R Anantharaman, ICMAT International Conference Singapore, July 3rd to July 9th 2005

8. Initial investigations on the SHI irradiation on the structural, magnetic and microstructural characterisation of $Fe_{40}Ni_{38}B_{18}Mo_4$ thin films, Hysen Thomas, *Swapna.S.Nair,* R.V.Ramanjunan, P.A Joy, D.K Awasti, M.R Anantharaman, ICMAT International Conference, Singapore, July 3rd to July 9th 2005.

9. Alloying induced enhanced quantum confinement in $Ni_xFe_{1-x}Fe_2O_4$ ferrofluids, *Swapna.S.Nair,* Francis Xavier and M.R Anantharaman OMTAT international conference, Cochin, Nov. 2005